KA-BROADBAND SATELLITE COMMUNICATION USING CYCLOSTATIONARY PARABOLIC BEAMFORMING

by

PAUL LUSINA

A thesis submitted to the
Department of Electrical and Computer Engineering
in conformity with the requirements
for the degree of Master of Science

Queen's University
Kingston, Ontario, Canada
August 1997

Abstract

The purpose of this document is to investigate the design of a broadband satellite system which operates at the Ka frequency band. A channel model was developed which indicated that the satellite link would be noise limited and slowly time varying.

Cyclostationary beamforming using the Cross-SCORE (Self Coherent Property Restoral) algorithm on a high gain multi-feed parabolic antenna array was considered. The slowly time varying channel environment allowed for a long correlation time. This application of SCORE is in contrast to existing work which uses linear arrays in interference limited environments with short correlation times.

A novel technique of front-end filtering was applied to the SCORE algorithms to improve the convergence rate. This resulted in a reduction of the noise power input to the beamformer which improved the performance. A phase bias was also introduced by the filter which degraded the performance of the system under certain conditions. A second filtering technique which used of phase compensation to eliminate the phase bias improved performance. Robustness tests of the Cross SCORE algorithm showed that the technique was highly sensitive to errors in the characteristic cyclic frequency of the signal. Beamforming gains were shown to be dependent on the parabolic antenna array geometry.

The design of a Ka broadband satellite system is feasible. However, large gain terrestrial antennas or high transmission power levels may be necessary to insure reliable performance.

Acknowledgements

I would like to thank my thesis supervisor Dr. Steven Blostein. His insight and enthusiasm about this project made the research highly rewarding. I would also like to thank him for his advice and support with respect to my application to the University of Ulm, Germany and for his interest in my extra-curricular hobbies.

Thanks to my lab mates, especially Mark Earnshaw who's technical experience was key in overcoming many computer and system problems throughout my two years at Queen's.

Thanks is extended to my family. Their support of my interests and confidence in my abilities helped me through the difficult times. Their enthusiasm and love made the distance from Kingston to Pickering much smaller.

Finally, I would like to dedicate this thesis to the memory of my Grandmother, whose kindness, generosity and humour throughout my life will always be remembered. Thoughts of her will forever bring our family closer together.

This work was supported by the Canadian Institute for Telecommunications Research and the School of Graduate Studies and Research at Queen's University.

Contents

Abstract ii

Acknowledgements iii

List of Tables xiii

List of Figures xv

List of Symbols xxiii

1 Introduction 1

1.1 Motivation 1

1.2 Thesis Contributions 3

1.3 Presentation Outline 4

2 Antenna Dimension and Coverage Area Calculations 6

2.1 Literature Search 6

2.1.1 Antenna for Military Satellite Communications 7

2.1.2 Performance of Contour Shaped Beam Antennas 7

2.1.3 The Orion Satellite Antenna Sub-System 9

2.1.4 TOPEC/Poseidon Project 9

2.1.5 Personal Handheld Communications via Ka and L/S band Satellites 11

2.2 Antenna Design and Satellite Coverage Area 11

2.2.1 Aperture Taper and Sidelobe Level 12

2.2.2 Beamwidth 12
2.2.3 Gain Loss 14
2.2.4 Offset Height 14
2.2.5 Maximum Scan Angle 14
2.3 Calculated Dimension for the Reflector Antenna 15
2.3.1 Reflector Diameter 15
2.3.2 Focal Length 15
2.3.3 Gain 15
2.3.4 Reflector Angle 16
2.3.5 Feed Directivity Value (Q) 16
2.3.6 Element Size and Spacing 17
2.3.7 Antenna Design Summary 17
2.4 Feed Location Calculation 19
2.5 Beam Distortion due to Frequency Distribution 20
2.6 Degradation in Performance for Off Focus Beams 22

3 Link Budget Calculation for the Ka-Band Geostationary Satellite 27
3.1 Ka-Band Link Budget Contributions 27
3.1.1 Physical Link Parameter Summary 29
3.1.2 Earth/Satellite EIRP 30
3.1.3 Free Space Loss 31
3.1.4 Gaseous Losses 31
3.1.5 Rain Attenuation 32
3.1.6 Temperature 32
3.1.7 Bandwidth Calculation 32
3.2 FDMA System 33
3.3 Link Budget Calculation 33
3.3.1 Hardware Specifications 34
3.3.2 Frequency Parameters 34
3.3.3 Target Latitude and Longitude 34

3.3.4 Height above Sea Level 35
3.3.5 Outage Percentage 35
3.3.6 Antenna Gain Reduction 35
3.3.7 System Interference 35
3.3.8 Temperature Parameters 36
3.3.9 Channel Guard Bands 36
3.3.10 Pulse Design 37
3.3.11 Base Band Channel 37
3.3.12 Ionospheric Effects 37
3.3.13 E_b/N_o Requirements 37
3.4 Comparison with L Band Voice System 40

4 Cyclostationary Beamforming and On-Board Processing 42
4.1 Motivation for Digital Beamforming and On-Board Processing 42
4.1.1 Reference-Based Beamforming 43
4.1.2 Location-Based Beamforming 44
4.1.3 Property Restoral/Blind Beamforming 44
4.2 Motivation for the Cyclostationary Property Restoral Technique . . . 45
4.3 Theoretical Background for Cyclostationary Analysis 46
4.3.1 Fraction of Time Probability Measure 47
4.4 Second-Order Cyclostationariy 50
4.4.1 Cyclic Autocorrelation Function 51
4.5 Cyclic Temporal Correlation Coefficient 53
4.6 Spectral Correlation Density Function 53
4.7 Frequency-Shift Filtering (FRESH) 54
4.8 The Cyclic Signal Model Environment 55
4.9 Blind Cyclic Spatial Filtering Algorithms 57
4.9.1 Spectral Coherence Restoral Blind Beamforming Algorithms (SCORE) 57
4.9.2 The Cyclic Adaptive Beamforming Algorithm 62

4.9.3 Castedo Algorithm 63
4.9.4 PHASE Algorithm 64
4.9.5 Signal Subspace Techniques 65

5 The Modeled Channel 67

5.1 Signal Model and Test Environment 67
5.1.1 Binary Phase Shift Keying 68
5.1.2 Raised Cosine Pulse Shaping 70
5.1.3 Array Configuration 71
5.1.4 Complex Gaussian Noise Model 71
5.1.5 Signal Model Representation 73
5.1.6 SINR Calculation, and Optimal Beamforming SINR 73
5.2 Performance Evaluation Parameters 75
5.2.1 Gaussian Noise Level Test Scenario 75
5.2.2 Interference Test Scenario 77
5.2.3 Carrier Frequency Jitter 77
5.2.4 Offset Frequency Error Test 78
5.2.5 Filter Bandwidth Test 78
5.2.6 Simulation Test Environment Conditions 79

6 Cyclostationary Beamforming with Broadband Front End Filtering, and Array Response Estimation 80

6.1 Front End Filter Motivation 80
6.2 Filtering Effect on Cyclic Spectral Correlation 83
6.2.1 Unfiltered Noise Sample Model 85
6.2.2 Ideal Filter Model 88
6.2.3 Non-Ideal Filter Model 90
6.2.4 Time Averaging Computation 92
6.2.5 Effect of Filtering on Time Averaging 95
6.2.6 Effect of Filtering on the Noise Power 96

6.2.7 Limit as the Filter Bandwidth Approaches Infinity 96
6.2.8 Limit as the Filter Bandwidth Approaches Zero 97
6.2.9 Finite Time Fourier Transform 98
6.2.10 Summary of Filtering's Effects on Beamforming 99
6.3 Cyclostationary Array Response Estimation 101
6.4 Front End Filtered SCORE Beamforming Techniques 103
6.4.1 SCORE Algorithm (SCORE) 106
6.4.2 Filtered SCORE Algorithm (F-SCORE) 106
6.4.3 Phase Compensated SCORE Algorithm (PC-SCORE) 106
6.4.4 Array Estimated SCORE (A-SCORE) 107
6.4.5 Filtered Array Estimated SCORE (FA-SCORE) 107
6.5 Transitional Filter Design 107

7 SCORE Algorithm Simulation Results 112

7.1 Introduction 112
7.2 Cyclostationary Array Estimation Performance of the Linear and Parabolic Antenna Configuration 113
7.3 Effect of Array Initialization 118
7.4 Performance Comparison between Cross SCORE and Least Squares SCORE 119
7.4.1 Summary of Filtered Least Square and Cross SCORE algorithm Comparison 127
7.5 Comparison of the Parabolic and Linear Arrays 127
7.6 Beam Pattern Performance 128
7.7 SCORE Algorithm Convergence Performance 130
7.7.1 Effect of Filter Bandwidth on Convergence Performance . . . 130
7.8 Effect of Noise on Convergence Performance 137
7.8.1 Convergence Rate Deterioration due to Noise 139
7.8.2 SCORE Convergence Limit due to High Noise 139
7.8.3 Cross SCORE Noise Performance Summary 139

7.9 Effect of Interference on Convergence Performance 143
7.10 Frequency Jitter Noise Performance 143
7.11 Frequency Offset Convergence Performance 149
7.12 Direction of Arrival Effect on the Parabolic Antenna 153
7.13 Performance Summary of Filtered SCORE Algorithms 159

8 Conclusions and Future Work **161**

8.1 Conclusions on the Geostationary Satellite Channel 162
8.2 Conclusions on Antenna Design 162
8.3 Conclusions on SCORE Algorithm Simulation Performance 163
8.3.1 SCORE Algorithm Performance Summary 166
8.4 Conclusions on Array Estimation using Cyclostationarity 166
8.4.1 Conclusions on Cyclostationary Array Estimation for the Linear Array 168
8.4.2 Conclusions on Cyclostationary Array Estimation for the Parabolic Antenna 168
8.5 Final System Design Proposal 169
8.5.1 Phase-Compensated SCORE Algorithm 169
8.5.2 Link Budget 169
8.5.3 Receiver Antenna 170
8.5.4 Uplink System Limits 170
8.5.5 Downlink System Limits 170
8.5.6 System Robustness 172
8.5.7 Proposed System Specification Modifications and Performance Observations 172
8.6 Suggested Future Areas of Investigation 172
8.6.1 Channel Simulation Model 173
8.6.2 Antenna and Feed Plane Design 173
8.6.3 Noise Performance Limit 173
8.6.4 Interference Performance 174

8.6.5 Frequency Jitter Performance 174
8.6.6 Offset Frequency Error 174
8.6.7 Filter Optimization 174
8.6.8 Cyclostationary Array Estimation 175
8.6.9 Low Earth Orbit Satellite Applications 175
8.6.10 Terrestrial Applications 176
8.6.11 Algorithm Optimization 176

A Antenna Design and Simulation Methods **177**
A.1 Calculation of the Offset Parabolic Reflector Dimensions 177
A.2 Design Procedure 179
A.3 Approximate Radiation Pattern 181
A.4 Antenna Pattern Program 182
A.4.1 Parabolic Antenna Theory and Approximations 182
A.4.2 Parameter Specification 183
A.5 Feed Design 183
A.5.1 Maximum Theoretical Efficiency of Multiple Beam Antennas . 184
A.5.2 Beamwidth of Antenna Feed Elements 184
A.5.3 Wide Band Techniques for Antenna Feeds 186
A.6 Filter Implementation 188
A.7 Transitional Filter Design 190
A.8 Butterworth Pole Location 190
A.9 Bessel Pole Location 191

B Satellite Footprint Calculations **193**

C Beam Patterns for Off Focus Feeds **198**

D Communications Model Background **202**
D.1 Statistical Channel Model of the Carrier at the Ka Frequency Band . 203
D.2 Ionospheric Effects 205

D.2.1 Refraction/Direction of Arrival Variation 205
D.2.2 Faraday Rotation 205
D.2.3 Group Delay 206
D.2.4 Phase Advance 206
D.2.5 Doppler Frequency 207
D.2.6 Dispersion 207
D.2.7 Ionospheric Scintillation 208
D.2.8 Summary of Ionospheric Effects 208
D.3 Clear Air Effects 209
D.4 Tropospheric Scattering 209
D.5 Antenna Gain Reduction 209
D.6 Absorptive Effects 210
D.6.1 Absorption due to Oxygen 210
D.6.2 Absorption due to Water 211
D.6.3 Total Gaseous Attenuation due to Absorption 212
D.7 Tropospheric Scintillation Effects 213
D.8 Attenuation Effects 213
D.8.1 Attenuation Prediction Models 214
D.9 Downlink Degradation 219
D.10 Frequency Scaling 221
D.11 Fading Statistics 223

E Coordinate System Transformations 226

E.1 Earth Centered System 226
E.2 Satellite Centered System 228
E.3 Perspective Projection View of the Earth 228
E.4 Coordinate Transform 229
E.5 Local Coordinate System 231
E.6 Satellite / Earth Geometry 233

F Calculation of Satellite Feed Coordinates **236**

Bibliography **241**

Vita **246**

List of Tables

1.1 Satellite System Design Specifications 2

2.1 Dimensions for 45 GHz Military Antennas 7
2.2 Dimensions and Performance of European Contour Shaped Antennas 8
2.3 Parameters for the Orion Satellite System 9
2.4 Parameters for the TOPEC/Poseidon Project 10
2.5 Specifications for the Ka Personal Handheld Communications System 11
2.6 Formula Specifications for the Offset Parabolic Antenna Design . . . 18
2.7 Calculations for the Offset Parabolic Antenna Design 19
2.8 Beamwidth Distortion due to Frequency 22
2.9 Gain and Location Data for Sample Coverage Areas 25

3.1 Link Budget Parameters: FDMA System 38
3.2 Link Budget Calculations: FDMA System 39
3.3 Up Link Performance Comparison:Ka System with L Band System . 40
3.4 Down Link Performance Comparison:Ka System with L Band System 40

5.1 Feed locations for the Parabolic Antenna array simulation 72
5.2 Default Simulation Parameters 75
5.3 Variable Simulation Parameters 76
5.4 Test Environments for Beamforming Techniques 79

6.1 Sample Transitional Filter Data and Calculations 108

7.1 Direction of Arrival Information for the Parabolic Antenna: $\tau = 0.23°$ $\phi = 4.21°$ 154
7.2 Direction of Arrival Information for the Parabolic Antenna: $\tau = 0.0°$ $\phi = 3.5°$ 154

8.1 SCORE SINR Convergence Summary: Parabolic Antenna 167
8.2 SINR Calculations of Proposed Satellite System 171

A.1 Antenna Parameters for the Offset Parabolic Antenna Program . . . 183
A.2 Feed Parameters for the Offset Parabolic Antenna Program 183

D.1 Statistical Data on Carrier Envelope Under Various Weather Patterns 204
D.2 Calculation Summary of Ionospheric Effects 208
D.3 Fading Duration Statistics: 15 dB Attenuation Threshold 223
D.4 Fading Duration Statistics: 20 dB Attenuation Threshold 224

List of Figures

2.1 a) Diagram of Antenna Parameters b) Diagram of Beampattern Parameters 13

2.2 Satellite Footprint Coverage of Canada, Dimensions in λ 20

2.3 Feed Plane Element Location for Coverage of Canada 21

2.4 Foot Print Distortion at 21 MHz 23

2.5 Foot Print Distortion at 19 MHz 23

2.6 Feed Location for Off Focus Beam Pattern Foot prints 24

2.7 Beam Pattern of Feed 1 26

2.8 Beam Pattern of Feed 6 26

3.1 Diagram of Atmospheric Effects on the Channel 28

3.2 Allocation of Channels at the Ka Band 36

5.1 Signal Processing before Beamforming 68

5.2 a) Signal spectrum at the Ka Band. b) Analogue down conversion of desired channel to the wide band anti-aliasing filter. c) Digitally sampled spectrum of the desired channel. 69

6.1 a) Received waveform magnitude before filtering b) Received waveform magnitude after filtering 82

6.2 Processing Steps for Beamforming 86

6.3 a) Frequency Domain of the Noise Variance. b) Time Domain of Noise Samples. 87

6.4 a) Frequency domain magnitude of an ideal filter pulse. b) Frequency domain phase of an ideal filter pulse. c) Time domain impulse response of an ideal filter. 89
6.5 a) Frequency domain magnitude of an non-ideal filter. b) Frequency domain phase of an non-ideal filter. 91
6.6 Components of a filter with non-ideal phase response 92
6.7 Comparison of a ideal and non-ideal filter pulse in response showing pulse widening. 93
6.8 a) SCORE beamforming implementation b) F-SCORE beamforming implementation c) PC-SCORE beamforming implementation 104
6.9 d)A-SCORE beamforming implementation e) FA-SCORE beamforming implementation 105
6.10 Plot of S plane Poles and Zeros for Butterworth, Bessel, Transitional Filters 109
6.11 Plot of the Normalized Magnitude for Butterworth, Bessel, Transitional Filters 109
6.12 Plot of the Normalized Phase for Butterworth, Bessel, Transitional Filters 110

7.1 Cyclic Array Estimation Linear Array SINR Test LNNB: Received SINR=-12 dB. *-: Optimum SINR, x-:Single Element SINR. 113
7.2 Cyclic Array Estimation: Element # 1 Phase Convergence Test LNNB: Received SINR=-12 dB. *-: Optimum Angle 114
7.3 Cyclic Array Estimation: Element # 5 Phase Convergence Test LNNB: Received SINR=-12 dB. *-: Optimum Angle 115
7.4 Cyclic Array Estimation Linear Array SINR Test HNNB: Received SINR=-36 dB. *-: Optimum SINR, x-:Single Element SINR. 115
7.5 Cyclic Array Estimation Parabolic Antenna: Element # 1 Phase Convergence Test HNWB: Received SINR=-36 dB. *-: Optimum Angle . 116

7.6 Cyclic Array Estimation Parabolic Antenna: Element # 5 Convergence Test HNWB Received SINR=-14 dB. *-: Optimum Angle 117
7.7 Performance Comparison of Array Initialization for SCORE Algorithms. *-: Optimum SNR, x-: Single Element SNR 120
7.8 LS-SCORE Linear Array SINR, Test LNNB. Received SNR=-12 dB. *-: Optimum SINR, x-:Single Element SINR. 122
7.9 Cross-SCORE Linear Array SINR, Test LNNB. Received SNR=-12 dB. *-: Optimum SINR, x-:Single Element SINR. 123
7.10 LS-SCORE Converged SINR Linear Array Noise Performance: Test LNNB. *-: Optimum SINR, x-:Single Element SINR 123
7.11 Cross-SCORE Converged SINR Linear Array Noise Performance: Test LNNB. *-: Optimum SINR, x-:Single Element SINR 124
7.12 LS-SCORE Parabolic Antenna SINR, Test LNNB. Received SNR=-36 dB. *-: Optimum SINR, x-:Single Element SINR. 124
7.13 Cross-SCORE Parabolic Antenna SINR, Test LNNB. Received SNR=-36 dB. *-: Optimum SINR, x-:Single Element SINR. 125
7.14 LS-SCORE Converged SINR Parabolic Antenna Noise Performance: Test LNNB. *-: Optimum SINR, x-:Single Element SINR 125
7.15 Cross-SCORE Converged SINR Parabolic Antenna Noise Performance: Test LNNB. *-: Optimum SINR, x-:Single Element SINR 126
7.16 CS-SCORE Parabolic Antenna Beam Pattern, Test LNNB. Received SNR=-36 dB. *-: Optimum SINR. 128
7.17 CS-SCORE Parabolic Antenna Beam Pattern, Test LNNB. Received SNR=-36 dB. *-: Optimum SINR. 129
7.18 Cross SCORE Parabolic Array SINR, Test LNNB: Received SNR=-36 dB. Filter BW= .05Hz. *-: Optimum SINR, x-: Single Element SINR 131
7.19 Cross SCORE Parabolic Array SINR, Test LNWB: Received SNR=-36 dB. Filter Bandwidth= .2 Hz *-: Optimum SINR, x-: Single Element SINR 132

7.20 Cross SCORE Parabolic Array SINR, Test LNNB: Received SNR=-42 dB. Filter Bandwidth= .05 Hz *-: Optimum SINR, x-: Single Element SINR 133

7.21 Cross SCORE Parabolic Array SINR, Test LNWB: Received SNR=-42 dB. Filter Bandwidth= .2 Hz *-: Optimum SINR, x-: Single Element SINR 133

7.22 Cross SCORE Parabolic Antenna SINR, Test LNNB: Received SNR=-40.4 dB. Filter Bandwidth= .4 Hz *-: Optimum SINR, x-: Single Element SINR 134

7.23 Cross SCORE Steady-State for SINR Parabolic Antenna, Test LNNB: Received SNR=-40.4 dB. *-: Optimum SINR, x-: Single Element SINR 135

7.24 Cross SCORE Steady State for SINR Parabolic Antenna, Test HNNB: Received SNR=-47 dB. *-: Optimum SINR, x-: Single Element SINR 136

7.25 Cross SCORE Steady-State for SINR Linear Array, Test LNNB: Received SNR=-12 dB. *-: Optimum SINR, x-: Single Element SINR . 137

7.26 Cross SCORE Steady State for SINR Linear Array, Test HNNB: Received SNR=-22 dB. *-: Optimum SINR, x-: Single Element SINR . 138

7.27 Cross-SCORE Parabolic Array SINR, Test LNWB. Received SNR=-36 dB. *-: Optimum SINR, x-: Single Element SINR 140

7.28 Cross-SCORE Parabolic Array SINR, Test LNWB. Received SNR=-42 dB. *-: Optimum SINR, x-: Single Element SINR 141

7.29 Cross-SCORE Parabolic Array SINR, Test LNWB. Received SNR=-50 dB. *-: Optimum SINR, x-: Single Element SINR 142

7.30 Cross-SCORE Steady State SINR Parabolic Antenna Noise Performance: Test LNWB. *-: Optimum SINR, x-: Single Element SINR . 142

7.31 Cross SCORE Parabolic Antenna Array SINR, Test LNNB. Interference Frequency=.245 Hz with the desired offset frequency at .25 Hz. *-: Optimum SINR, x-: Single Elements SINR. 144

7.32 Cross SCORE Parabolic Antenna Array SINR, Test LNNB: Interference Frequency=.2 Hz with the desired offset frequency at .25 Hz. *-: Optimum SINR, x-: Single Elements SINR. 145

7.33 Cross SCORE Parabolic Antenna SINR, Test LNWB: Jitter Deviation= 0.04 % of Carrier Offset Frequency (2 kHz). *-: Optimal SINR, x-: Single Element SINR. 146

7.34 Cross SCORE Parabolic Antenna SINR, Test HNWB: Jitter Deviation= 0.04 % of Carrier Offset Frequency (2 kHz). *-: Optimal SINR, x-: Single Element SINR. 147

7.35 Cross SCORE Parabolic Antenna SINR, Test LNNB: Jitter Deviation= 0.2 % of Carrier Offset Frequency (10 kHz). *-: Optimal SINR, x-: Single Element SINR. 148

7.36 Cross SCORE Parabolic Array SINR, Test LNWB: Frequency Error = 0.04 % of Carrier Offset Frequency (2 kHz). *-: Optimum SINR, x-: Single Element SINR. 150

7.37 Cross SCORE Parabolic Array SINR, Test LNWB: Frequency Error = 0.2 % of Carrier Offset Frequency (10 kHz). *-: Optimum SINR, x-: Single Element SINR. 151

7.38 Cross SCORE Parabolic Array SINR, Test HNWB: Frequency Error = 0.04 % of Carrier Offset Frequency (2 kHz). *-: Optimum SINR, x-: Single Element SINR. 152

7.39 Cross SCORE Parabolic Antenna Performance: $\tau = 0^\circ$ $\phi = 3.5^\circ$. Received SINR=-36 dB. *-: Optimum SINR, x-: Single Element SINR. 155

7.40 Cross SCORE Parabolic Antenna Performance: $\tau = 0^\circ$ $\phi = 3.5^\circ$. Received SINR=-42 dB. *-: Optimum SINR, x-: Single Element SINR. 155

7.41 Cross SCORE Parabolic Antenna Performance: $\tau = 0^\circ$ $\phi = 3.5^\circ$. Received SINR=-50 dB. *-: Optimum SINR, x-: Single Element SINR. 156

7.42 Cross SCORE Steady State SINR Parabolic Antenna Noise Performance: $\tau = 0°$ $\phi = 3.5°$. Received SINR=-50 dB. *-: Optimum SINR, x-: Single Element SINR. 157
7.43 Cross SCORE Parabolic Antenna Beam Pattern: $\tau = 0°$ $\phi = 3.5°$. Received SINR=-50 dB. *-: Optimum SINR. 158

A.1 Offset Parabolic Antenna Schematic 178
A.2 Simple Diagram of a Patch and Planar F Antenna 186
A.3 Broad and Narrow band Filter Schematic for Message and Carrier Recovery 189

B.1 Earth-Satellite Geometry for the Calculation of Beam Footprints . . . 194

C.1 Beam Pattern of Feed 1 198
C.2 Beam Pattern of Feed 2 199
C.3 Beam Pattern of Feed 3 199
C.4 Beam Pattern of Feed 4 200
C.5 Beam Pattern of Feed 5 200
C.6 Beam Pattern of Feed 6 201

D.1 Effect of Elevation Angle on Oxygen and Water attenuation at = 20 GHz 211
D.2 Effect of Frequency on Oxygen and Water attenuation 212
D.3 Schematic of Absorption Mechanisms 214
D.4 Effect of Elevation on Rain Attenuation 215
D.5 Effect of Frequency on Rain Attenuation 216
D.6 Effect of Height Above Sea Level on Rain Attenuation 217
D.7 Effect of Percent Outage Level on Rain Attenuation 218
D.8 Down Link Degradation Mechanism 219
D.9 Antenna Noise Schematic 220

E.1 Earth Coordinate system Geometry 227

E.2 Satellite Coordinate system Geometry 228
E.3 Satellite Coordinate system Geometry 229
E.4 Local Coordinate system Geometry 232
E.5 Satellite-Earth Geometric relationship 234

F.1 Earth-Satellite Target Geometry 236
F.2 Antenna Feedplane Geometry, Y-Plane 237
F.3 Antenna Feed Plane Geometry, XZ-Plane 238
F.4 Geometry of Polar Coordinate Transform 240

List of Symbols

C/N	$\Rightarrow$	Carrier to noise power ratio (dBm)
P_t	$\Rightarrow$	Power transmitted (mW)
G_{Sat}	$\Rightarrow$	Satellite Antenna Gain (dB)
G_{Ea}	$\Rightarrow$	Earth Antenna Gain (dB)
L	$\Rightarrow$	Total Loss (dB)
N_t	$\Rightarrow$	Thermal Noise (dB)
A_A	$\Rightarrow$	Antenna apperature (m^2)
η_s	$\Rightarrow$	Spillover efficiency
η_o	$\Rightarrow$	Manufacturing efficiency
η_i	$\Rightarrow$	Illumination efficiency
λ	$\Rightarrow$	Wavelength (m)
SCORE	$\Rightarrow$	SCORE simulation algorithm
F-SCORE	$\Rightarrow$	Filtered SCORE simulation algorithm
FA-SCORE	$\Rightarrow$	Filtered Array Estimated SCORE simulation algorithm
A-SCORE	$\Rightarrow$	Array Estimated SCORE simulation algorithm
PC-SCORE	$\Rightarrow$	Phase Compensated SCORE simulation algorithm
Array	$\Rightarrow$	Cyclic Array Estimation Algorithm
F-Array	$\Rightarrow$	Filtered Cyclic Array Estimation Algorithm
PC-Array	$\Rightarrow$	Phase Compensated Cyclic Array Estimation Algorithm
LNNB	$\Rightarrow$	Low Noise Narrow Band
LNWB	$\Rightarrow$	Low Noise Wide Band
LNNB	$\Rightarrow$	High Noise Narrow Band
HNWB	$\Rightarrow$	High Noise Wide Band

F	$\Rightarrow$	Parent parabola focal length (λ)
h	$\Rightarrow$	Height to center of reflector A (λ)
l_{ant}	$\Rightarrow$	Reflector focal length (λ)
SL	$\Rightarrow$	Sidelobe Level (dB)
Ω_1	$\Rightarrow$	angle of x-z plane with reflector base (degrees)
Ω_2	$\Rightarrow$	angle of x-z plane with reflector tip (degrees)
Ω_3	$\Rightarrow$	angle of x-y plane with reflector center (degrees)
h_1	$\Rightarrow$	offset height with respect to x-y plane (λ)
D	$\Rightarrow$	Diameter of parent parabola ($lambda$)
D_1	$\Rightarrow$	Diameter of reflector parabola (λ)
θ'	$\Rightarrow$	the angle of the ray originating at the focus with respect to the x-z componenet of the antenna boresight (λ)
θ_1	$\Rightarrow$	3 dB angle (degrees)
λ	$\Rightarrow$	Wavelength
$\triangle$	$\Rightarrow$	aperature taper (dB)
ET	$\Rightarrow$	edge taper (dB)
θ_3	$\Rightarrow$	maximum scan angle (degrees)
BDF	$\Rightarrow$	beam deviation factor
N	$\Rightarrow$	Number of feeds.
A_{ant}	$\Rightarrow$	center of the reflector
d_{ant}	$\Rightarrow$	element spacing (λ)
Q	$\Rightarrow$	Quality factor
f_{hp}	$\Rightarrow$	Half power frequency
f_o	$\Rightarrow$	Center frequency (Hz)
R_f	$\Rightarrow$	Resistance of the feed Ω
f_o	$\Rightarrow$	Center frequency (Hz)
P_{trans}	$\Rightarrow$	Complex Poles of the transitional filter
P_{Btt}	$\Rightarrow$	Complex Poles of the Butterworth filter
P_{Bss}	$\Rightarrow$	Complex Poles of the Bessel filter
W_{Btt}	$\Rightarrow$	Weighting factor of the Butterworth filter

W_{Bss} $\Rightarrow$ Weighting factor of the Bessel filter

ϵ_{Btt} $\Rightarrow$ Butterworth scale factor for transfer function

k_{Btt} $\Rightarrow$ Transfer function of Butterworth filter

A_{Btt} $\Rightarrow$ Attenuation function of Butterworth filter

N_{Btt} $\Rightarrow$ Number of poles for Butterworth filter

$N_{Bss|i}$ $\Rightarrow$ Bessel filter polynomial, odd powers of frequency

$M_{Bss|i}$ $\Rightarrow$ Bessel filter polynomial, even powers of frequency

q_i $\Rightarrow$ coefficients for the Bessel filter transfer function

τ_{Bss} $\Rightarrow$ delay of Bessel filter

k $\Rightarrow$ Boltzman's constant $(1.38 \cdot 10^{-23} J/K)$

T_e $\Rightarrow$ Noise temperature of Earth station (degrees K)

B $\Rightarrow$ Base band of signal (Hz)

T_s $\Rightarrow$ Sky noise temperature (degrees K)

P_s $\Rightarrow$ Satellite power (dB)

P_e $\Rightarrow$ Earth station power (dB)

G_s $\Rightarrow$ Satellite antenna gain (dB)

G_e $\Rightarrow$ Earth station antenna gain (dB)

L $\Rightarrow$ Link losses (dB)

L_w $\Rightarrow$ Weather losses (dB)

L_g $\Rightarrow$ Gaseous losses (dB)

L_f $\Rightarrow$ Free space losses (dB)

$EIRP$ $\Rightarrow$ Equivilant Isotropic Radiated Power (dB)

f $\Rightarrow$ frequency (Hz)

N $\Rightarrow$ number of electrons $/m^3$

B_{av} $\Rightarrow$ average strength of earth's magnetic field (Wb/m^3)

dl $\Rightarrow$ incremental distance through plasma. (m)

TEC $\Rightarrow$ Total Electron Content (electrons$/m^2$)

ϕ_{fd} $\Rightarrow$ Faraday rotation (rad)

$\triangle t_i$ $\Rightarrow$ group delay (sec)

δt_{gd} $\Rightarrow$ group delay across message bandwidth (sec)

$\frac{\phi_{pa}}{dt}$ $\Rightarrow$ rate of change of phase advance (rad/sec)

$\triangle\phi_{pa}$ $\Rightarrow$ phase advance (rad)

f_D $\Rightarrow$ Doppler frequency (Hertz)

ϕ_{pd} $\Rightarrow$ phase dispersion (rad)

γ_w $\Rightarrow$ water attenuation coefficient (dB/km)

ρ_w $\Rightarrow$ water vapour (g/m^3)

γ_o $\Rightarrow$ oxygen attenuation coefficient (dB/km)

h_o $\Rightarrow$ effective oxygen height (km)

h_w $\Rightarrow$ effective water vapour height (km)

h_{wo} $\Rightarrow$ effective water vapour scale coefficient

h_s $\Rightarrow$ height above sea level (km)

h_R $\Rightarrow$ height of rain (km)

L_s $\Rightarrow$ slant path (km)

L_g $\Rightarrow$ horizontal slant path length (km)

r_x $\Rightarrow$ rain intensity reduciton factor

k_r $\Rightarrow$ rain attenuation coefficient

α_r $\Rightarrow$ rain attenuation power term

θ_{el} $\Rightarrow$ earth station elevation

γ_r $\Rightarrow$ specific rain attenuation (dB/km)

A_g $\Rightarrow$ effective water vapour scale coefficient

$A_{x|R}$ $\Rightarrow$ attenuation level for a specific outage percent

$R_{0.01}$ $\Rightarrow$ Point rainfall rate for the location for 0.01 percent of an average year (mm/hr)

T_{sys} $\Rightarrow$ System noise temperature. ($^\circ K$)

T_A $\Rightarrow$ Noise temperature incident on antenna. ($^\circ K$)

T_r $\Rightarrow$ Receiver noise temperature ($^\circ K$)

T_c $\Rightarrow$ Cosmic noise temperature ($^\circ K$)

T_m $\Rightarrow$ Temperature of the medium ($^\circ K$)

σ_f $\Rightarrow$ Feed transmissivity factor

A_{sky} $\Rightarrow$ Total atmospheric attenuation (dB)

A_g $\Rightarrow$ Gaseous attenuation (dB)

RAS $\Rightarrow$ rain attenuation statistical ratio

ACA $\Rightarrow$ attenuation due to clear air (dB)

f_u $\Rightarrow$ upper frequency (Hz)

f_l $\Rightarrow$ lower frequency (Hz)

G $\Rightarrow$ gravitational constant ($6.67 \cdot 10^{-11}$)

M $\Rightarrow$ earth mass (kg) ($5.976 \cdot 1024$)

P $\Rightarrow$ earth period (sec) (86, 164)

R $\Rightarrow$ earth mean radius (km) (6371)

$\vec{f}$ $\Rightarrow$ intersection point of ray from satellite with earth.

$\vec{t}$ $\Rightarrow$ ray from satellite to intersection point f.

$\vec{s}$ $\Rightarrow$ ray from the earth center to the satellite.

A_T $\Rightarrow$ the target satellite point on the earth.

A'_T $\Rightarrow$ projection of the satellite point on the earth x-y plane

d_1 $\Rightarrow$ distance from satellite position S to target location A.

d_2 $\Rightarrow$ distance from satellite position S to target projection A'_T.

μ_{es} $\Rightarrow$ earth satellite longitudinal position

μ_{eA} $\Rightarrow$ earth aim point longitudinal position

ρ_{eA} $\Rightarrow$ earth aim point latitudinal position

θ_{bw} $\Rightarrow$ spherical coordinate of ray $\vec{t}$ in $z_a y_a$ plane restricted by beam width

ϕ_{bw} $\Rightarrow$ spherical coordinate of ray $\vec{t}$ in $z_a x_a$ plane restricted by beam width

μ_{ef} $\Rightarrow$ intersection point of satellite ray's longitudinal position

ρ_{ef} $\Rightarrow$ intersection point of satellite ray's latitudinal position

x_e, y_e, z_e $\Rightarrow$ earth cartesian coordinates

x_L, y_L, z_L $\Rightarrow$ local cartesian coordinates

x_s, y_s, z_s $\Rightarrow$ satellite cartesian coordinates

ρ_e, μ_e $\Rightarrow$ earth spherical coordinates

θ_s, ϕ_s $\Rightarrow$ satellite spherical coordinates

$\vec{r}, \vec{s}, \vec{t}$ $\Rightarrow$ orientation vectors for cartesian coordinate transform

$\vec{i}, \vec{j}, \vec{k}$ $\Rightarrow$ basis vectors for earth cartesian system

$\vec{l}, \vec{m}, \vec{n}$	$\Rightarrow$	basis vectors for earth local system
$\mathbf{A}$	$\Rightarrow$	cartesian transformation matrix
a_i	$\Rightarrow$	element of cartesian transformation matrix
M_i	$\Rightarrow$	scalar magnitudes of transformation matrix
α_{es}	$\Rightarrow$	azimuth angle of earth to satellite
ϵ_{es}	$\Rightarrow$	elevation angle of earth to satellite
BDF	$\Rightarrow$	beam deviation factor.
γ_r	$\Rightarrow$	angle reflected off of the reflector
α_a	$\Rightarrow$	angle of the feed plane normal with the zy satellite plane
θ_r	$\Rightarrow$	angle reflected off of the reflector in the yz plane
τ_a	$\Rightarrow$	angle of rotation of the antenna coordinates with respect to the satellite system in the xz plane
N_f	$\Rightarrow$	normal vector of feed plane
$\vec{x_{da}}, \vec{y_{da}}, \vec{z_{da}}$	$\Rightarrow$	direction vector with respect to cartesian coordinates
$\vec{V_d}$	$\Rightarrow$	direction vector with respect to cartesian coordinates
$\vec{x_{ra}}, \vec{y_{ra}}, \vec{z_{ra}}$	$\Rightarrow$	cartesian coordinates of ray reflected off of reflector
$\vec{v_r}$	$\Rightarrow$	cartesian coordinates of ray reflected off of reflector
Ω_a	$\Rightarrow$	angle of reflection of incident ray for an on focus beam in the xz plane of the antenna
t_{feed}	$\Rightarrow$	scaling parameter to find the intersection point of the ray with the feed plane
Γ_{feed}	$\Rightarrow$	angular component of the polar intersection point on the feed plane
ϵ_{feed}	$\Rightarrow$	radial component of the polar intersection point on the feed plane
u	$\Rightarrow$	dummy frequency
ζ	$\Rightarrow$	Fourier frequency
T_{FA}	$\Rightarrow$	Fourier Time average period
v_l	$\Rightarrow$	filtered signal
$x(t)$	$\Rightarrow$	unfiltered signal
$s(t)$	$\Rightarrow$	deterministic desired signal
f_c	$\Rightarrow$	desired signal frequency

$|A_{sig}|$ $\Rightarrow$ deterministic desired signal magnitude

$|A_{sinc}|$ $\Rightarrow$ $sinc(\cdot)$ attenuation factor

$|A_{filt}|$ $\Rightarrow$ filter attenuation factor

ψ $\Rightarrow$ deterministic phase of desired signal

$i(t)$ $\Rightarrow$ deterministic interference signal

ϱ $\Rightarrow$ deterministic phase of interference signal

$|I|$ $\Rightarrow$ deterministic interference magnitude

$n(t)$ $\Rightarrow$ random noise vector

$|\mathbf{N}_l(t,f)|$ $\Rightarrow$ white Gausian noise $N(0,\sigma_n)$ from element l.

ξ $\Rightarrow$ uniformly distributed noise phase $[-\pi, pi]$

$h(t)$ $\Rightarrow$ time domain response of filter

$|H(f)|$ $\Rightarrow$ frequency response magnigude of filter

$\chi(f)$ $\Rightarrow$ frequency phase response of filter

B_{filt} $\Rightarrow$ filter bandwidth

B_{FA} $\Rightarrow$ Fourier time average filter bandwidth

$\gamma_{T_{FA}}$ $\Rightarrow$ coefficient for the sinc function of the finite time Fourier transform

$\gamma_{T_{FA}}$ $\Rightarrow$ maximum magnitude of the finite time Fourier transform with $T_{FA} = 0$

β_{filt} $\Rightarrow$ phase error constant of the filter

$N_{B_{FA}}$ $\Rightarrow$ number of discrete frequencies for in the interval $\pm B_{FA}$.

δ_ξ $\Rightarrow$ filter phase error due to β_{filt}

$\Upsilon_{N_{\triangle t},K}$ $\Rightarrow$ Correlation coefficient sum.

$\overline{\mu}$ $\Rightarrow$ time averaged mean

$v_c(i-k)$ $\Rightarrow$ correlation between elements.

Chapter 1

Introduction

1.1 Motivation

There is an increasing demand for broadband services which will provide reliable transmission of information. Multi-media applications including data and video require large bandwidths and low error rates for satisfactory performance. This demand will exceed the present services in existence today, and there will be increasing problems finding the required frequency spectrum to provide the bandwidth for broadband services. Below is a summary of some of the obstacles that the design and deployment of a broadband system will have to overcome.

- An accurate model of the channel environment must be developed which will predict how the transmitted signals would be degraded.
- High frequency spectral bands will have to be used to provide the necessary bandwidth for the system.
- In order to keep the transmitter and receiver small, power resources must be conserved.
- The system must be robust to component failure, and errors introduced by the channel.
- The service provided to the coverage area must be uniform.

- A dynamic access scheme needs to be considered which will adapt to changes in the user location, and in the channel environment.

To meet these system requirements a geostationary satellite system is proposed. The target specifications of this system are presented in Table 1.1.

Parameter	Specification
Downlink Frequency	20 GHz
Uplink Frequency	30 GHz
Coverage Area	Canada
BER	10^{-5}
Number of Users	100
Bit Rate	2 Mbps
Uplink Transmitter Power	1 W
Downlink Transmitter Power	1 W
User Location	Portable

Table 1.1: Satellite System Design Specifications

In order to meet these specifications, the following techniques will be employed:

- The Ka frequency band will be used. The spectrum at this frequency is presently unallocated, and has the necessary size to support a broadband service. Bandwidth will not be a limiting parameter.

- A multi-beam geostationary satellite will provide the necessary coverage. This satellite system will use a parabolic antenna to increase the SNR of the signal.

- Beamforming will be investigated using the Spectral Self Coherence Property Restoral technique (SCORE). A new technique using front end filtering and array estimation will be applied to the SCORE algorithm to improve performance and robustness.

The use of the Ka frequency band has the advantage of providing the necessary spectrum. The drawback is that higher frequencies suffer more from attenuation due to free space losses and atmospheric attenuation. The present literature is only beginning to focus on characterizing the Ka frequency band, and there is very little long term data available for modeling.

The multi-beam parabolic antenna configuration seeks to compensate the high attenuation resulting from using the Ka frequency band. The parabolic antenna offers a large gain. Parabolic antenna construction can be light-weight which will keep the payload of the system small.

The use of beamforming is aimed at maximizing the satellites resources. A beamforming algorithm will allow for agile formation of spot beams which can adaptively focus on a user's location, and respond to a time varying channel environment. The ability to dynamically focus the satellite beam could be used to reduce power and hardware requirements, or to increase the system performance.

The SCORE algorithm is seen as ideal for the satellite beamforming application. This algorithm uses the cyclostationary properties of the desired signal to beamform. As a result, no synchronization, training sequences, or array calibration are needed.

1.2 Thesis Contributions

This thesis has investigated several new areas with respect to satellite beamforming.

- A channel model for the Ka frequency band is constructed. This channel shows that the FDM access system proposed in this thesis is noise limited. Access schemes studied in present literature are usually interference limited.

- The Least Squares and Cross SCORE algorithm are applied to a parabolic antenna array under high noise conditions (SNR < -30 dB). Previous work using SCORE had always employed linear arrays in interference limited environments, under low noise conditions (SNR > 0 dB).

- Front-end filtering is employed to isolate the desired offset carrier frequency needed for beamforming. Front-end filtering was shown to improve the performance of the SCORE algorithms in high noise environments.

- An estimation technique of the array response is presented. This algorithm maximizes the real component of the cyclic autocorrelation value between antenna elements by introducing a delay. The delay corresponds to a phase shift which can be calculated. The cyclic array estimation technique was shown to work for SNR levels of about -12 dB on linear arrays.

- Initialization of the antenna elements to an estimate of the array response was shown to have no significant effect on the convergence rate of the SCORE algorithms.

1.3 Presentation Outline

There are two distinct areas of research in this thesis. The first aspect focuses on the modeling of the satellite link at the Ka frequency band. The second section deals with the beamforming algorithms and the test scenarios.

Chapter 2 presents the design and calculation of the parabolic antenna which will be used in the satellite link. Based on the design of the antenna, a uniform coverage area of Canada is calculated. This coverage area provides information on the amount of physical hardware needed.

The system link budget is calculated in Chapter 3. The significant channel attenuation factors for the link are presented for the Ka frequency band.

Chapter 4 presents the theory behind the cyclostationary algorithms. Several different cyclostationary beamforming techniques are briefly presented.

The signal model for the simulations is described in Chapter 5. This includes the noise modeling, modulation format, and simulation parameters. The selected parameters for evaluating the robustness of the SCORE algorithms are also presented.

A technique of combining front-end filtering with cyclostationary beamforming is presented in Chapter 6. A method of array response estimation is outlined, and the simulation conditions are defined. The final section of this chapter deals with the design of the transitional filter to be used in the simulations.

Chapter 7 presents the results of the beamforming algorithm performance under the test conditions chosen. Conclusions based on these test results are presented in Chapter 8.

Appendix A, B and C present a calculation of the antenna design, coverage area calculations and performance values. A detailed account of the channel model design is presented in Appendix D.

Reference coordinate system derivations and translations are presented in Appendices E and F.

Chapter 2

Antenna Dimension and Coverage Area Calculations

This chapter outlines the calculation of the antenna dimensions and the required hardware to provide uniform coverage of Canada. The antenna will be designed to work at the Ka band frequency and will provide broadband services to the coverage area. These models are used to determine worst case conditions within the coverage area. The antenna gain and array patterns based on the calculated antenna dimensions are used in all beamforming simulations and in link budget calculations.

A detailed presentation of the design procedures, and approximations used in generating the antenna dimensions and beampatterns is presented in Appendix A.

Models and reference systems used in calculating the satellite foot print coverage, and feed location calculations are presented in Appendices B and E.

2.1 Literature Search

In order to get an idea of the parameters of the system which are physically realizable using current technology, an extensive search was done on satellite projects which are already designed or implemented. The result of this search provided guidelines in selecting the physical antenna parameters.

2.1.1 Antenna for Military Satellite Communications

In the paper by Rao [33], a satellite antenna was designed, and a prototype constructed which used a feed array of 121 Potter horn feed elements to cover a circular region of 8° radius at 45 GHz modulating frequency. The design used 1° spot beams which were grouped into a hexagonal septet to form a "virtual" feed and a resulting beam footprint. This allowed beamforming to take place by weighting these feeds.

The system achieved a beam crossover level of 3 dB, and a sidelobe level of 25 dB below the peak gain. The interference nulling capability achieved nulls of 32 dB below the main lobe. The satellite dimensions are shown bellow in units of wavelength.

Dimension	Measurement (λ)
Diameter	83.4
Focal Length	140
Offset Height	22.36
Feed Horn Size	2.1
Gain (dB)	43.1

Table 2.1: Dimensions for 45 GHz Military Antennas

2.1.2 Performance of Contour Shaped Beam Antennas

There are several European satellite systems which employ shaped reflectors which result in contour beam patterns. The design has the advantage of being practically simple to implement, and the reduced number of feeds greatly reduces the mass of the system. This design did not give the flexibility of multiple access and beamforming which is the thrust of this thesis. Below are a list of existing, or designed contour beam systems which can be used to compare the performance of the multi-beam system proposed in this thesis [30].

Mission	# Beams	Tx Band (GHz)	Rx Band (GHz)	Gain (dB)	Sidelobe (dB)	Antenna Size (λ)
EutelSat III	1	11.7	14.25	34	-	80
DRS	2	19.0	28.75	23	-	76
EuroSat	7	12.1	-	35	35	120
Hispanic	2	11.2	-	34	27	75

Table 2.2: Dimensions and Performance of European Contour Shaped Antennas

2.1.3 The Orion Satellite Antenna Sub-System

This satellite project operates at the Ku band and uses two beam forming networks to service America and Europe. The feed array is used to re-configure the antenna beam patterns. The design accounts for antenna feed coupling. The system links with ground terminals which use a 1.2 m rooftop antenna system. The satellite link uses 100 W of power for each feed. Below is a summary of the design specifications [43].

Parameter	American Beam	European Beam
Diameter (λ)	91.6	57.7
Focal Length (λ)	75.7	47.7
Offset (λ)	8	47.7
Tx Band (GHz)	11.95	12.1
Rx Band (GHz)	14.25	14.25
Gain (dB)	41	41
Feed Horns	12	8

Table 2.3: Parameters for the Orion Satellite System

The power requirements and the size of the receiving antenna make this style of design poor for the portable low power system proposed in this thesis.

2.1.4 TOPEC/Poseidon Project

This project's objective is to accurately measure and collect data from the earth's oceans. Below is a summary of the significant parameters of the satellite. [47]

The largest power drain of this system comes from the traveling wave tube amplifier (70 W). The signal processor is the next largest power user (37.4 W).

Power requirement data from this project indicate that a significant amount of the satellite's resources will have to be allocated to running the digital beamforming hardware.

Parameter	Measurement
Frequency (GHz)	13.6
Antenna Diameter (λ)	68
Peak Power (W)	232
Gain (dB)	43.9

Table 2.4: Parameters for the TOPEC/Poseidon Project

2.1.5 Personal Handheld Communications via Ka and L/S band Satellites

Design guidelines for portable voice systems operating in the Ka and L/S frequency bands are presented in [13]. The following information is given for the Ka band system.

Frequency (GHz)	20
3 dB Beamwidth	0.3
Antenna Diameter (λ)	333
Antenna Gain (dB)	51.8
Transmitter Power (W)	7.8
Total number of cells	260
Total Power (W)	9192.91

Table 2.5: Specifications for the Ka Personal Handheld Communications System

This system is designed to provided almost complete coverage of the United States during clear sky conditions. During rain conditions a L band sub system (which suffers less from rain fades) takes over. The draw back of this system is the high number of feeds required, and the large power demands of the system.

2.2 Antenna Design and Satellite Coverage Area

One of the goals of this thesis is to provide a system which would service all of Canada. Simulations for coverage areas were made using designed programs, based on geometric relations and approximations. These calculations are only first order [38], and do not incorporate detailed physical effects in antenna construction. Second-order effects are not considered crucial to the system due to the fact that the cyclic beamforming algorithms do not rely on the physical geometry of the system, and provide adaptive beamforming weights to changing environmental conditions.

Calculations for the geometry of the offset parabolic antenna, a pattern of satellite footprints to provide coverage of Canada, and the corresponding feed locations for these footprints are presented in the following sections.

Preliminary calculations for the offset parabolic antenna are made using the design formulas presented in A.1, and the beampattern is verified using the program developed by [11] (section A.4). The basic antenna design will cover Canada using a hexagonal grid of antenna feeds. While this may not be the optimum configuration for beamforming, it will offer a system that can be used for comparison with conventional single beam per user systems, and will be able to show the relative gain due to beamforming alone in these systems. The following subsections briefly define some of the design parameters and their effect on the antenna design. Figure 2.1 shows some of the significant antenna design dimensions and beampattern terms.

2.2.1 Aperture Taper and Sidelobe Level

The antenna's aperture taper measures the relative power level of the electric field at the center of the reflector with the power at the edge of the reflector. This in turn determines the sidelobe level of an antenna. The sidelobe level is the magnitude of the second maximum point after the mainlobe maximum. Low sidelobe levels are desired to minimize the chance of amplifying signals which are not in the target area.

The sidelobe level directly influences the aperture taper, which in turn controls the size of the reflector. Levels ranging from 20 dB to 30 dB below the peak lobe gain are used in existing systems. A specification of 27 dB was chosen for this project.

The 27 dB level gives the optimum edge taper performance for aperture efficiency as presented in [26]

2.2.2 Beamwidth

The beamwidth of the antenna greatly affects the antenna gain, and the size of the reflector. The smallest practical beam that can be focussed accurately from a geostationary satellite is 0.2°. The beamwidth is a parameter that is dependent on the

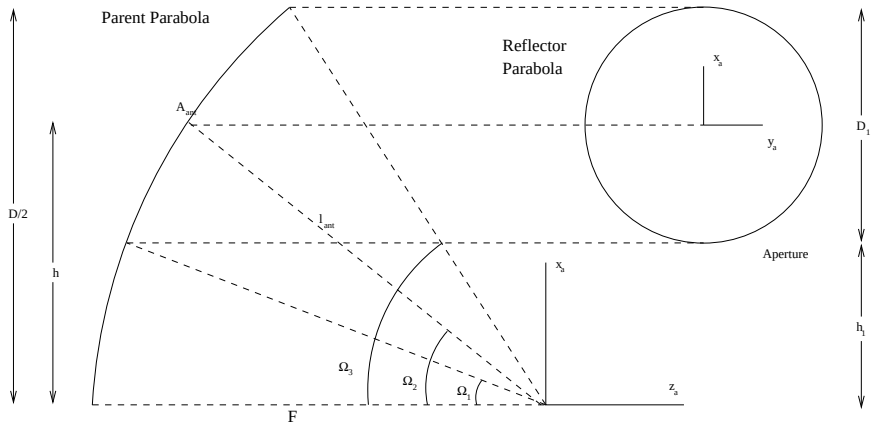

Figure 2.1: a) Diagram of Antenna Parameters b) Diagram of Beampattern Parameters

frequency of the transmitted signal. For this reason all calculations are done in terms of wavelengths, and then scaled to standard SI units depending on the frequency of the application.

Since the largest possible gain is desired for this application, the 0.2° limit was chosen as the design parameter.

2.2.3 Gain Loss

The gain loss parameter refers to the reduction in the main lobe gain as the antenna feed is moved off of the focus of the x-z plane of the feed coordinate system (Appendix F). The chosen gain loss greatly affects the focal length of the antenna and indirectly affects the necessary size of the feed. A small gain loss results in a long focal length and a larger, more directive feed.

The gain loss selected for this application is 0.1 dB. This level was found to give a low loss while resulting in physical dimensions comparable to dimensions found in the literature.

2.2.4 Offset Height

The offset height is defined as the number of wavelengths that the bottom edge of the reflector is positioned above the y-z plane. This height is usually determined by the size and orientation of the feed plane.

An offset height of 2λ was found to provide enough clearance for the feed plane.

2.2.5 Maximum Scan Angle

The maximum scan angle is determined by the required coverage area of the system. It is the largest angle in the x-z plane within the coverage area. The maximum scan angle affects the focal length of the satellite.

The maximum scan angle for Canada was calculated. The antenna was directed toward a target location of 94.7° Longitude and 51.4° Latitude. These dimensions

required a scan angle of 0.77° to provide coverage of Canada.

2.3 Calculated Dimension for the Reflector Antenna

Once the design parameters were selected, the antenna dimension calculations were made. It was found that for these parameters, an antenna with dimensions comparable to those found in literature was possible. Below is a comment on the significance of some of the calculated values.

2.3.1 Reflector Diameter

Present satellite systems have reflector parabolas approximately 3 m in diameter. It was found that using the above design parameters that the downlink antenna (20GHz operating frequency) would have the dimension of 2.5 m and the uplink (30 GHz operating frequency) would have the dimension of 1.67 m.

2.3.2 Focal Length

The focal lengths over 2.0 m are difficult to deploy. The design formulas indicated that the focal length for the Uplink and Downlink antennas were 1.809 m and 1.206 m respectively. The shorter focal length also required a less directive, and smaller feed.

2.3.3 Gain

The antenna gain was calculated using the antenna program developed in [11]. The maximum achieved gain calculated was for the on focus feed, (feed position (0,0)), was found to be 53.4 dB. The lowest gain for the coverage area was found to be 48.1 dB at a focal plane location of $x = 1.165\lambda$ and $y = -8.869\lambda$.

The pointing error associated with the 0.2° beamwidth is not expected to be significant for the beam forming application due to the fact that the calculated beam will adjust to optimize the desired signal based on the direction of arrival.

The above calculated gain is comparable to the reflector antennas of existing systems.

It was noticed during beamforming simulations that only two or three feed elements made significant contributions to the combined signal depending on the location of the target on the earth. Simulations were run using larger beamwidths with lower gains to determine if such a system would have a better performance. The motivation was that the larger beamwidths would allow more elements to contribute to the sum after beamforming. The conclusion to this design was that the loss of gain could not be compensated by the broader beamwidths of the adjacent elements. Further investigation is needed in the area of optimizing the location of the antenna feeds for the purpose of coverage and beamforming.

2.3.4 Reflector Angle

This is the angle that the center of the reflector makes with the focus and the z-y plane of the satellite coordinate system. The feed plane is oriented perpendicular to this angle.

The reflector angle was calculated to be 39°. This exceeds the recommended design for the formulas which is $0° < \theta_{ref} < 30°$. In order to decrease this angle it would have been required to increase the focal length beyond practical dimensions.

The plotted beam patterns displayed no degradation in performance with respect to the sidelobe levels or the gain due to the reflector angle.

2.3.5 Feed Directivity Value (Q)

The feed Q value controls the directivity of the antenna feed, and is responsible for the edge taper. A more directive feed is required for long focal lengths or for low gain

losses. The required Q value for this configuration was found to be 6.62. Details of this calculation are presented in Section A.3.

2.3.6 Element Size and Spacing

The paper [33] offered a method for calculating the element size for a specific Q value based on the Potter Horn feed configuration.

The element size for the above designed antenna was calculated to be 0.903 λ. This size was found to be small enough to fit on the feed plane and provide coverage of Canada. Different feed plane technologies, such as planar feeds, may also be able to produce smaller feeds while still providing the necessary performance criteria.

A design was constructed which grouped feeds closer together than one wavelength. The combined feed patterns for this system were found to be worse than those for the larger element spacing design. This behavior was explained in the paper by Lam et al. [24]

2.3.7 Antenna Design Summary

An offset parabolic antenna was designed which gives a minimum gain of 48.1 dB for the furthest off focus antenna feed while giving a side lobe level of 27 dB below the peak lobe. This gain was achieved for beamwidth of 0.2°.

Reflector size and focal length for both Uplink and Downlink designs were within the dimensions of existing satellite systems. The feed size which resulted from the calculations was small enough to fit on the feed plane while providing enough coverage to service any location in Canada.

This design will be used for all systems to be studied in this thesis.

Parameter	Specification
Side Lobe (SL) (dB)	27
θ_{3dB} (deg)	0.2
Gain Loss (dB)	0.1
Height (λ)	2
Max Scan θ_3 (deg)	.77

Table 2.6: Formula Specifications for the Offset Parabolic Antenna Design

Parameter	Calculation
Reflector Diameter (λ)	166.8
Uplink Reflector Diameter (m)	1.668
Downlink Reflector Diameter (m)	2.502
Length to Focus (λ)	120.6
Uplink Length to Focus (m)	1.206
Downlink Length to Focus (m)	1.809
Gain Max Feed (dB)	53.4
Gain Min Feed (dB)	48.1
Reflector Angle (deg)	39
Feed Q value	6.62
Element Size (λ)	0.903

Table 2.7: Calculations for the Offset Parabolic Antenna Design

2.4 Feed Location Calculation

Feed locations were calculated to provide uniform coverage of Canada using a 0.2° beam width for a 3 dB beam contour. The beam distortion due to the curvature of the earth was not considered significant to the free space loss of the system.

Seventy feeds are required to provide the necessary coverage. The beams are spaced laterally by approximately 1 λ. This is sufficient distance required for the feed size calculated in the antenna design section. The beam spacing depends on the reflector tilt angle and the calculated focal length. The target center for the satellite was chosen to be 51.4° Latitude, and 94.3° Longitude. This corresponds to the geographic center of Canada. Plots of the beam coverage area and the distribution of feeds on the feed plane may be referenced in Figures 2.2, and 2.3.

For the broadband satcom application, the goal of systems with beamforming is to incorporate a less dense collection of feeds and to dynamically control the array

so as to give comparable or better coverage using less hardware as compared to the single feed per sector design.

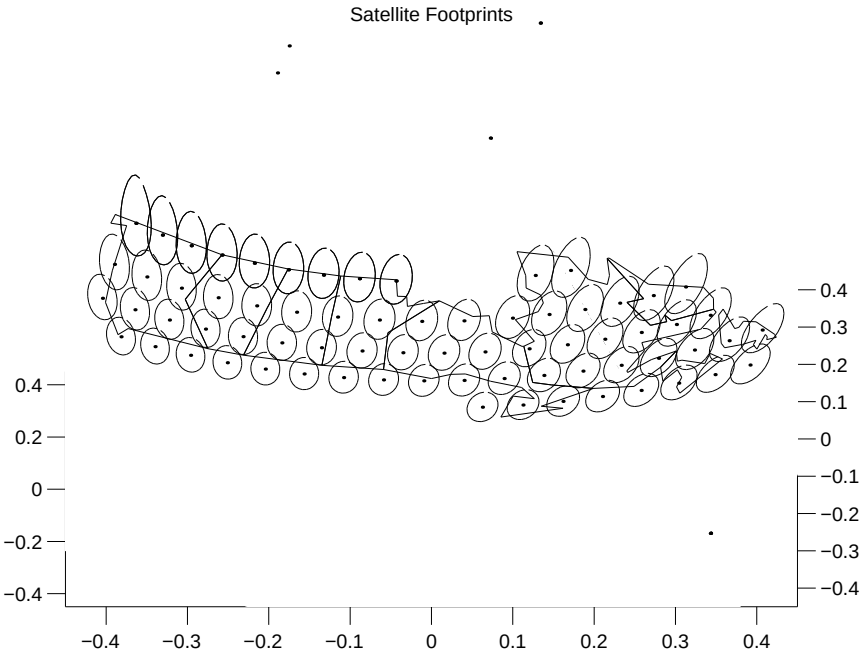

Figure 2.2: Satellite Footprint Coverage of Canada, Dimensions in λ

2.5 Beam Distortion due to Frequency Distribution

Each antenna must support a signal frequency bandwidth of +/- 1 GHz of the designed center frequency. Since the relative spacing of the antenna geometry determines the performance of the satellite, this change in frequency will result in some beam distortion.

By calculating the relative change in the antenna dimensions due to the change in frequency, plots were produced showing the resulting new beamwidth. The deviations around 20 GHz were relatively more significant than around 30 GHz, and only these frequency extremes are presented.

The 19 GHz signal resulted in a relative decrease in the antenna dimensions which

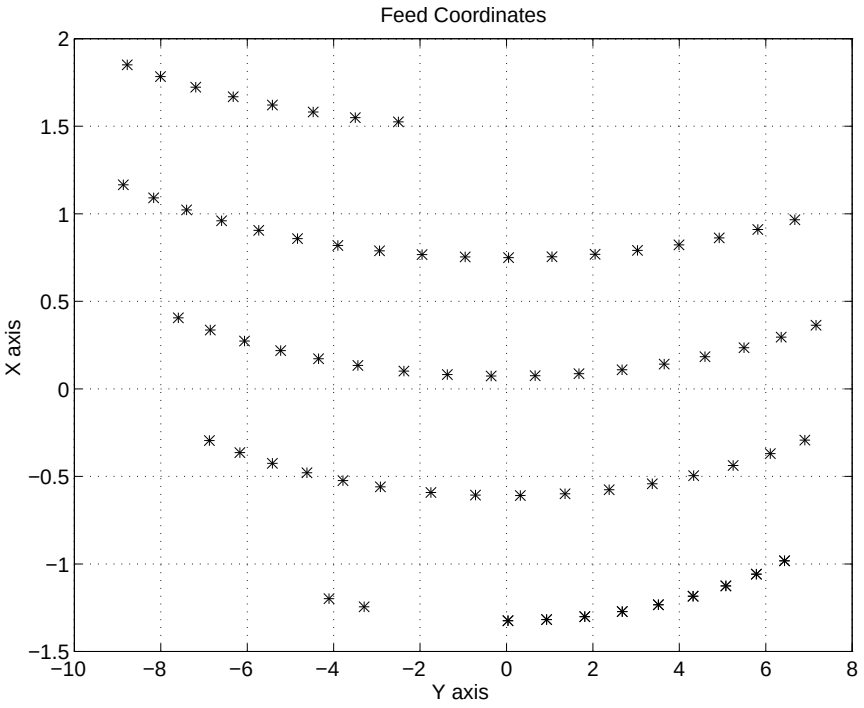

Figure 2.3: Feed Plane Element Location for Coverage of Canada

resulted in a broader beamwidth and a lower gain. In this case the beamwidth increased to 0.22°. Simulation plots showed that this deviation was not significant. Conversely, the 21 GHz signal resulted in a relative increase in the antenna dimensions which resulted in a narrower beam width and a higher gain. The beamwidth decreased to 0.191° Again, simulations showed that the change did not significantly affect coverage area or preformance. Plots of the distortion due to frequency of the beam foot prints may be referenced in Figures 2.4 and 2.5.

The 29 and 31 Ghz signals resulted in a new 3 dB beamwidth of 0.206° and 0.194° respectively. The beam distortion for the coverage area was less than that for the 20 GHz carrier, and was therefore not considered significant.

Frequency (GHz)	Beamwidth (deg)
19	0.211
20	0.200
21	0.191
29	0.206
30	0.200
31	0.194

Table 2.8: Beamwidth Distortion due to Frequency

2.6 Degradation in Performance for Off Focus Beams

When a feed is displaced from the geometric focus, the resulting electromagnetic field no longer arrives at the feed with a coherent phase. This produces a decrease in the effective gain of the antenna.

Six antenna feed locations were chosen from the feed plane. Five of the feed locations (1-5) corresponded to beam footprints on the edge of the coverage area. The 6th location corresponded to the focal point of the feed. The program by Duggan [11] was used to calculate the beam patterns.

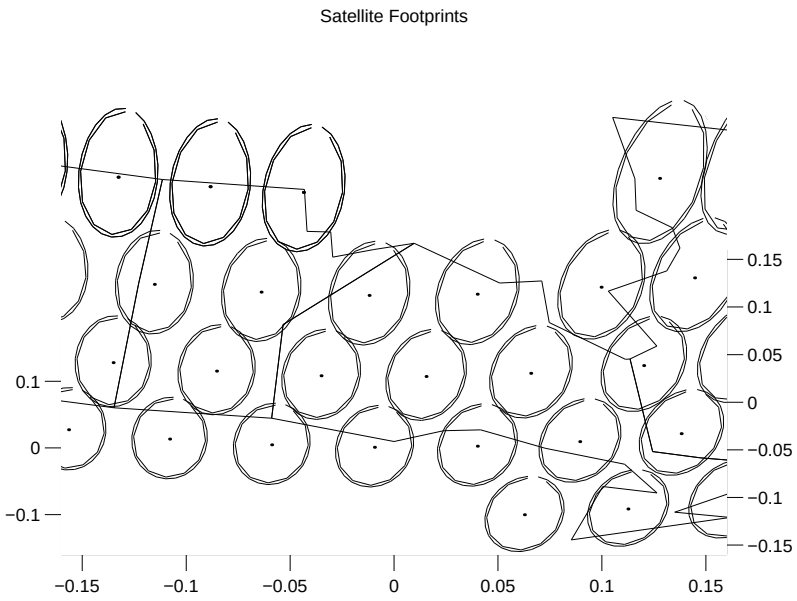

Figure 2.4: Foot Print Distortion at 21 MHz

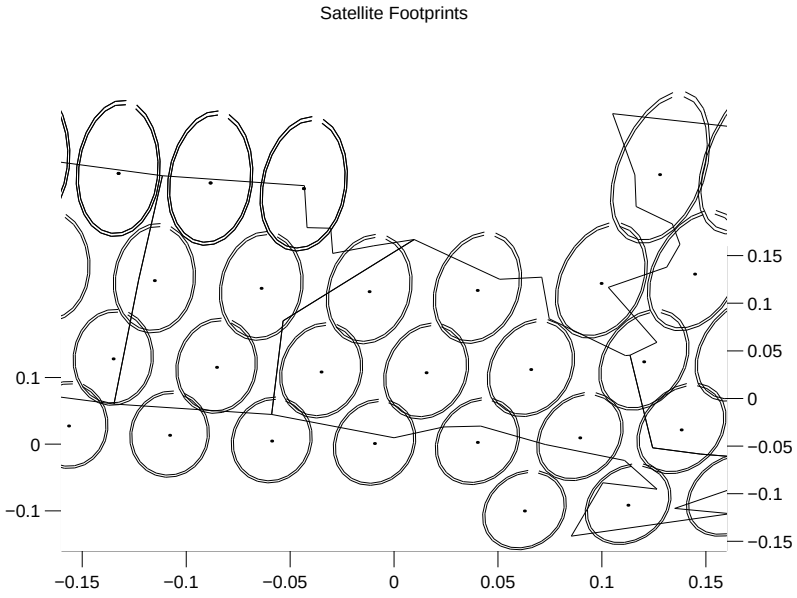

Figure 2.5: Foot Print Distortion at 19 MHz

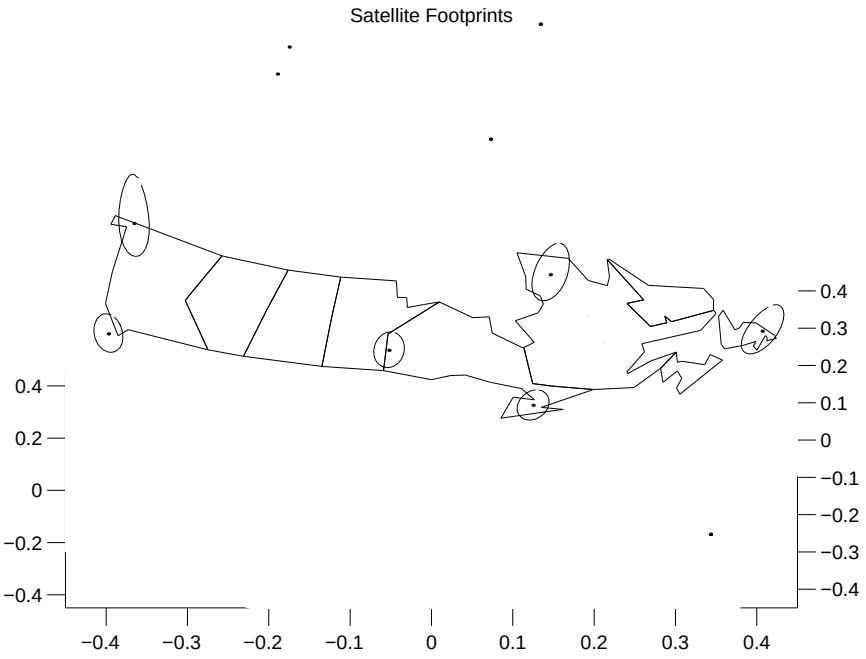

Figure 2.6: Feed Location for Off Focus Beam Pattern Foot prints

It was found that the on-focus feed had the largest gain (53.4 dB), while the worst gain was from feed number 1 (48.1 dB). This feed location was used in the link budget calculation as a worst-case scenario.

The coverage area of these feeds and their location on the feed plane may be referenced in Section 2.6. The corresponding antenna gain patterns for the worst feed may be referenced in Section 2.7. The optimal on-focus feed may be referenced in Section 2.8. Remaining plots of the other feed locations are presented in Appendix C

Beam Number	Longitude (degrees)	Latitude (degrees)	x_{plane} λ	y_{plane} λ	Tilt (degrees)	Max θ	Max dB
1	53	47.5	1.165	-8.869	-0.53	3.696	48.1
2	137	60	-0.976	6.481	0.42	-2.800	49.9
3	126	47.5	0.989	6.985	-0.45	-2.857	49.75
4	80	44	1.557	-3.745	-0.67	1.524	52.1
5	73	60	-1.227	-3.642	0.49	1.451	52.25
6	94.8	51.4	0	0	0.00	0.00	53.4

Table 2.9: Gain and Location Data for Sample Coverage Areas

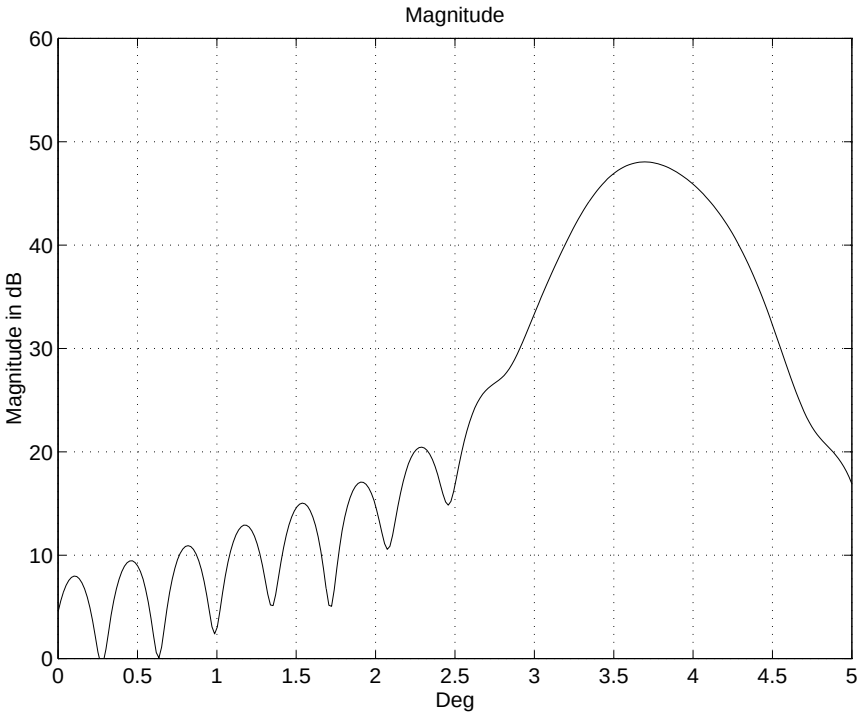

Figure 2.7: Beam Pattern of Feed 1

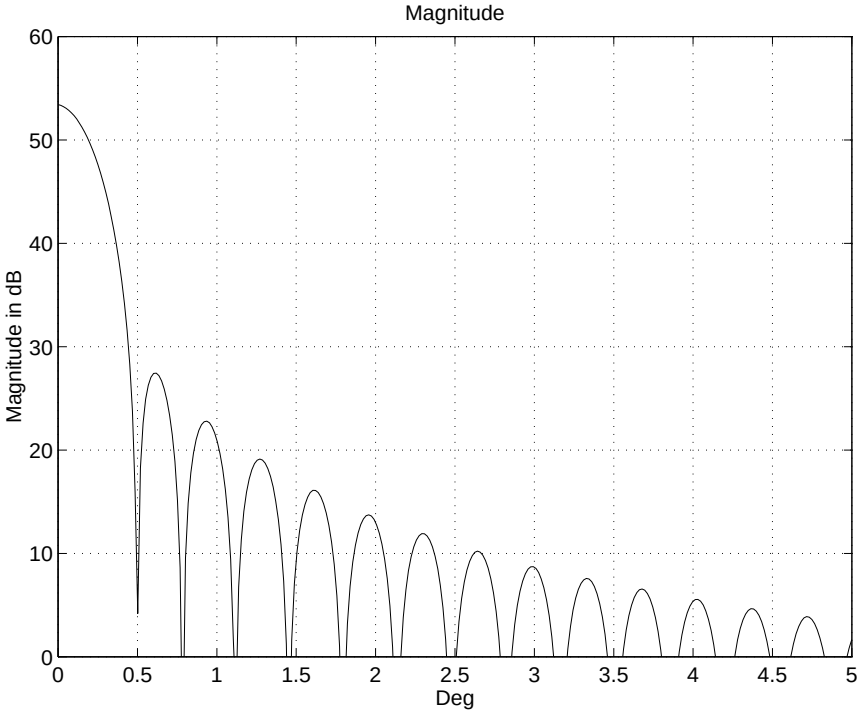

Figure 2.8: Beam Pattern of Feed 6

Chapter 3

Link Budget Calculation for the Ka-Band Geostationary Satellite

Based on the coverage area and the antenna design calculated in Chapter 2, a link budget was determined for the proposed broadband satellite system operating at the Ka frequency. This chapter details some of the first-order effects contributing to the link budget.

3.1 Ka-Band Link Budget Contributions

The link budget is the calculation of the signal energy in the channel. This budget determines the number of users that can be supported by the system, and the quality of service that can be provided.

Figure 3.1 shows the factors in the Link calculations. Only the most significant of these factors were incorporated in a first order Link Budget calculation. The Link Budget can be calculated using the following formula:

$$\frac{C}{N_t} = P_t + G_{Sat} + G_{Ea} - L - 10\log(N_t) \tag{3.1}$$

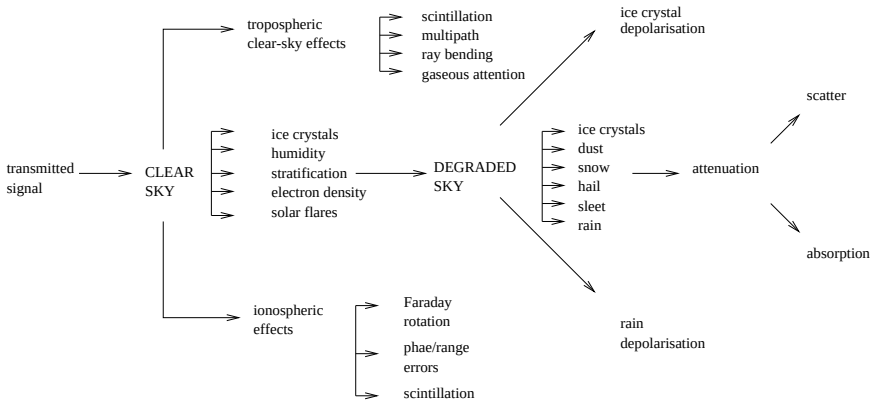

Figure 3.1: Diagram of Atmospheric Effects on the Channel

C/N $\Rightarrow$ Carrier to noise power ratio (dBm)

P_t $\Rightarrow$ Power transmitted (mW)

G_{Sat} $\Rightarrow$ Satellite Antenna Gain (dB)

G_{Ea} $\Rightarrow$ Earth Antenna Gain (dB)

L $\Rightarrow$ Total Loss (dB)

N_t $\Rightarrow$ Thermal Noise (dB)

The remainder of this section provides a summary of the calculation of the parameters, and a comparison with values from literature.

3.1.1 Physical Link Parameter Summary

To begin the calculation of the link budget several parameters must be determined including frequency, link direction, satellite position, and target location.

The system is to be operated in the Ka frequency range (20-30 GHz). This band is presently unallocated, and can provide the necessary bandwidth. The frequencies near 22 GHz were avoided for this system because these values were close to the resonant frequency of water (Section D.6). This resonance would cause a large amount of signal attenuation.

Specifying up/down link directions in the calculation are needed to determine the worst path. In general, atmospheric attenuation increases with the increase of frequency. Furthermore the thermal noise in each link is also different due to the Downlink Degradation factor (section D.9). As a result, one link direction will be more attenuated than the other. Attenuation may be compensated from the earth station using an increase of transmit power or by more complex receiver or antenna design. A satellite system would typically not have these resources due to payload and power limitations. Based on this reasoning, the downlink was given the lower frequency band (20 GHz).

The geometry of the link is determined by the satellite and the earth latitude and longitude coordinates. Typically, coverage will not be guaranteed for target locations greater than 70° latitude. Points at this latitude have an elevation angle below 10°.

Attenuation increases greatly at these latitudes (Section D.6.3).

3.1.2 Earth/Satellite EIRP

The Equivalent Isotropic Radiated Power (EIRP) for the earth and the satellite are calculated using the following formulas:

$$EIRP = G_t + P_t \tag{3.2}$$

where G_t is the transmitter antenna gain, and P_t is the transmitter power.

The typical antenna gain values found in literature for existing Ka and Ku band satellites ranges from 25 - 45 dB. This gain is given by:

$$G_t = \frac{4\pi(A_A \eta_s \eta_o \eta_i)}{\lambda^2} \tag{3.3}$$

$A_A \Rightarrow$ Antenna aperture (m^2)

$G_t \Rightarrow$ Transmitter antenna gain (dB)

$P_t \Rightarrow$ Transmitter power (dBW)

$\eta_s \Rightarrow$ Spill-over efficiency

$\eta_o \Rightarrow$ Manufacturing efficiency

$\eta_i \Rightarrow$ Illumination efficiency

$\lambda \Rightarrow$ Wavelength (m)

In addition, the antenna efficiency is decreased by non-ideal properties such as surface blemishes, however the limiting factor in efficiency for a multi-beam antenna is due to the Stein Limit which is 50 % [10] (Section A.5.1).

The maximum gain that could be achieved while giving reasonable reflector dimensions and coverage footprints was 53.4 dB for on focus feed. Gains above this resulted in very large antennas, with very small beam footprints which would require many feeds to cover the desired geographic area.

3.1.3 Free Space Loss

The free space loss is the loss due to the distance that the transmitted signal must travel through free space. This is found using the following formula:

$$L_{fs} = (\frac{\lambda}{4\pi r})^2 \tag{3.4}$$

Where r is the radius from the source. The radius is determined by the satellite and target coordinates. This loss was found to be the largest single contributor to signal attenuation. The large distances required for Geostationary orbit which result in high free space losses are one of the major drawbacks of this system.

3.1.4 Gaseous Losses

The calculations of the gaseous losses are done based on the CCIR model presented in [3] (Section D.6). These losses are not significant at lower frequencies, but in the Ka band they should be considered. The major gases which contribute to attenuation are oxygen and water. The CCIR model [3] is used to calculate the gaseous attenuation of the system. Water has a resonance frequency at approximately 22 GHz which makes this frequency undesirable. Water attenuation depends largely on the atmospheric conditions specified by temperature, atmospheric water vapor, and precipitation conditions. A value of 7 g/m^3 was used as quoted from [3] for the water vapor. Correction constants were used in the attenuation formulas to correct for temperature ranges. Two different constants were used in determining the equivalent atmospheric height of water vapor for rainy and clear sky conditions. The resonant frequency of Oxygen is at approximately 60 GHz. This frequency is well outside of the bandwidth being investigated. A detailed calculation of Oxygen attenuation is presented in Appendix D

3.1.5 Rain Attenuation

The rain attenuation model used was the CCIR model (Section D.8). The values generated using this method have been shown to have a good correlation with measured values [3] while requiring a minimal amount of statistical data. The CCIR divides the world into different regions based on rain fall statistics. Canada falls mainly in regions E and C. Region E was chosen for determining the rainfall model as a pessimistic parameter. This rainfall area has a precipitation rate exceeding 22 mm/h for 0.01 % of the year [3].

3.1.6 Temperature

Several different temperatures are significant in the calculation of the system temperature. These include the receiver temperature, the cosmic temperature, the ground temperature and the medium temperature. The direction of the link is also important. In the downlink, the earth station sees cool sky. As the signal passes through the atmosphere, some of the energy of the signal is absorbed and retransmitted as thermal noise. This effect is quantified in the downlink degradation factor (section D.9) which has been shown to increase the attenuation by as much as 2 dB.

3.1.7 Bandwidth Calculation

The bandwidth section of the link calculation provides information which is specific to the type of system proposed. This includes the uplink and downlink band frequency, the information bandwidth, the size of the guard bands and the type of pulse used. This information gives a bit energy over signal and noise ratio. Depending on the modulation scheme used, this would correspond to a particular bit error rate as well as the number of channels available.

3.2 FDMA System

This system has the basic configuration that will be used as a baseline for comparison with other beamforming systems. The FDMA scenario has no beamforming. The down link is considered the most critical direction due to the limitations of satellite power, mass and receiver complexity. The system is noise limited. This is a result of the large amount of attenuation on both desired and interference signals, and from the frequency separation of signals which allows for front- end filtering. Interferers from other systems at the Ka band are not anticipated in the signal environment.

The statistical models on which the link budget has been based show that the channel is slowly time varying. Experimental results from [27] support the slowly time varying model.

Each user is assigned a unique frequency for the uplink and the downlink. The link budget for this system shows the major losses in the link and the amount of additional gain that would be required due to channel coding and beamforming to make the system feasible. The system is compared with the link analysis performed by Karimi for a low bit rate (9600 bps) voice system operating at L-band [21].

A more detailed explanation of the link budget calculations is presented in the following sections.

3.3 Link Budget Calculation

The link budget is a calculation which shows the expected carrier to noise ratio of the system under the specified conditions. This ratio is directly related to the E_b/N_o [3]. From this calculation a prediction of the bit error rate and the reliability of of service can be determined.

The following sections outline the values chosen for the input parameters and the calculations which result.

3.3.1 Hardware Specifications

Hardware losses for both the uplink and the downlink were estimated at 2.0 dB for the each receiver and 0.2 dB for each feed. These were the values presented in [3]. The satellite gain was calculated using the designed parabolic antenna presented in the previous section. The power for each downlink signal was limited to 1 Watt due to power constraints on the satellite.

The earth antenna gain was set at 0 dB and the earth transmitter was given a power of 1 Watt. In this way the design of the satellite system alone can be evaluated and the necessary gain needed from the earth station to make the system feasible can be determined.

3.3.2 Frequency Parameters

Frequencies in the Ka frequency band were chosen because this band has not yet been allocated. There is a large amount of available bandwidth which could support high data rate services.

Frequency has a direct effect on the power of the received signal due to rain attenuation and free space loss. Free space loss increases at a rate of inverse distance squared. The frequency scaling method presented by [25] (section D.10) was used for frequencies +/- 1 GHz for the up and downlink frequencies of 30 and 20 GHz.

3.3.3 Target Latitude and Longitude

The target latitude and longitude were selected based on the coverage area of the feed with the worse gain as calculated in the antenna design section (Feed # 1). The geographical coordinates of feed # 1 correspond to 47.5° Latitude and 53.0° Longitude. The satellite Latitude position must be situated on the equator 0° in order to maintain a geostationary position. The Longitude position of the satellite was chosen to be 94.7° which is the geographic center of the coverage area.

3.3.4 Height above Sea Level

A target's height above sea level affects the attenuation due to the free space loss, as well as the effect of rain on the slant path of the signal. A height of 0.2 km was selected for the elevation of the target.

3.3.5 Outage Percentage

The outage percentage is a statistical calculation which is used to predict the percentage of time that atmospheric attenuation exceeds a certain threshold (Section D.8). This calculation is based on the CCIR attenuation model as presented in [3]. The model is dependent on the geographic parameters as well as the frequency of the signal.

An outage percent probability of 0.01 % was used for this system. The 0.01% level is the value derived from measured systems. Other percent outage levels must be calculated indirectly using a scaling method.

The 0.01 % level gives a statistical prediction that the attenuation due to rain will exceed the calculated threshold only 0.01 % of the year.

3.3.6 Antenna Gain Reduction

For an antenna design having a beam width of 0.2° and servicing a location having an elevation angle of 20° the antenna gain reduction was found to be 0.5 dB [3].

3.3.7 System Interference

In the FDMA system, no interference from other users was modeled. This is due to the fact that all users occupy a unique frequency and from the fact that channels are spaced with 1 Mhz guard bands at the upper and lower edges of each channel. Broadband front-end filtering would provide additional attenuation to interfering signals. The narrow beamwidth of the antenna and low side lobe levels tend make user signals in other geographic areas very weak relative to the desired signal. For this

reason, the FDMA system is seen to be noise-limited. Further justification for this assumption is presented through simulations in Chapter 7.

3.3.8 Temperature Parameters

Summer temperatures were estimated for the system to give a worst-case scenario. Temperatures were selected based on those found in literature and through personal communication with system designers. The selected parameters are presented in chart form in the link analysis summary.

The temperature values chosen significantly affect the amount of attenuation which results from the downlink degradation factor (Section D.9).

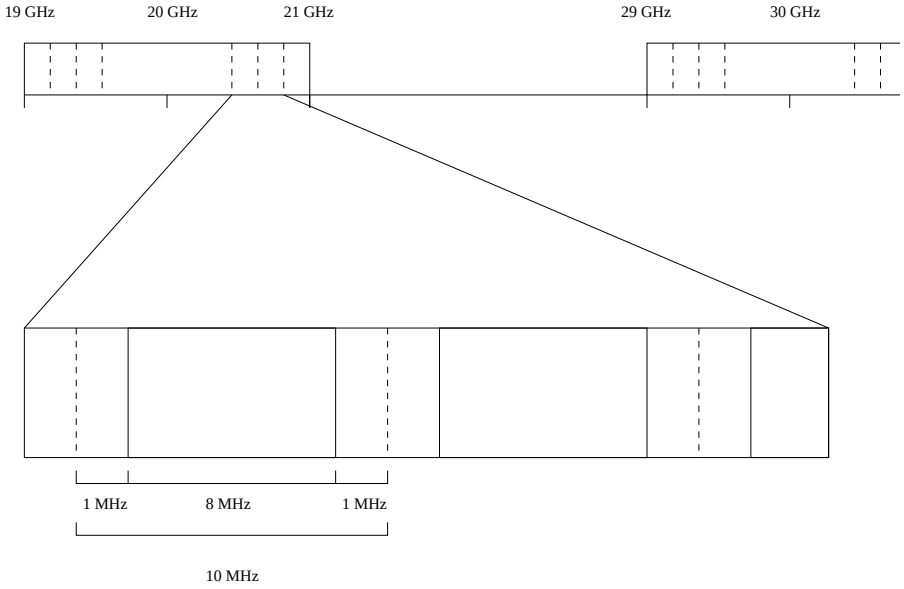

Figure 3.2: Allocation of Channels at the Ka Band

3.3.9 Channel Guard Bands

In order to decrease the interference from other users, guard bands of 1 MHz are placed between each channel. A schematic of the frequency allocation is given in figure 3.2.

3.3.10 Pulse Design

A binary phase shift keying pulse was used to transmit data. This scheme simplifies the recovery of the message signal at the receiver.

To minimize intersymbol interference a 100 % raised cosine pulse was selected. This effectively doubles the bandwidth of the system. The increase in bandwidth is not seen as a problem due to the large amount of unallocated bandwidth in the Ka band.

3.3.11 Base Band Channel

The basic information rate was selected for 2 Mbps. The 2 Mbps rate will allow for high data rate transfer as well as image transmission.

3.3.12 Ionospheric Effects

The major parameter controlling the effect of the the ionosphere are the Total Electron Count (TEC=$\#/m^3$) and the frequency. The TEC value of 10^{17} was used [3]. The ionospheric effects are not seen as significant with respect to signal distortion. The reason for the small influence of the ionosphere on the signal is due to the inverse frequency dependence on the degradation parameters. A detailed description of the ionospheric effects are presented in Appendix D. The ionospheric effects were not considered further.

3.3.13 E_b/N_o Requirements

The E_b/N_o level was selected to give a Bit error rate (BER) of 10^{-5} for binary phase shift keying pulses. This level corresponds to an E_b/N_o of 10 [40]. Additional gain from beamforming and coding would be expected to increase this level to give data quality performance of 10^{-6} or better.

Satellite Rx Loss (dB)	2
Satellite Feed Loss (dB)	0.2
Satellite Gain (dB)	48
Satellite Power (dBW)	0
Earth Rx Loss (dB)	2
Earth Feed Loss (dB)	0.2
Earth Gain (dB)	0
Earth Power (dBW)	0
Target Latitude (deg)	47.5
Target Longitude (deg)	53.0
Satellite Longitude (deg)	94.8
Earth Feed Temp ($^\circ K$	300
Sat Feed Temp ($^\circ K$)	200
Earth Temp ($^\circ K$)	300
Sat Temp ($^\circ K$)	200
Sky Temp ($^\circ K$)	2
Medium Temp ($^\circ K$)	290
Ground Temp ($^\circ K$)	300
Guard Band (MHz)	1
Base Band (MHz)	2
Raised Cosine %	100
TEC ($\#/m^2$)	10^{17}
Height above Sea (km)	0.2
Outage (%)	0.01
Aperture Degradation (dB)	0.5
Interference Noise (dB)	0.0
H_2O Vapor (ρ), (g/m^3)	7.0

Table 3.1: Link Budget Parameters: FDMA System

Calculation	19 GHz	20 GHz	21GHz	29 GHz	30 GHz	31 GHz
Satellite EIRP (dBW)	45.8	45.8	45.8	45.8	45.8	45.8
Earth EIRP (dBW)	-2.2	-2.2	-2.2	-2.2	-2.2	-2.2
Elevation Angle (deg)	22.59	22.59	22.59	22.59	22.59	22.59
Free Space Loss (dB)	210.69	211.14	211.56	214.37	214.66	214.95
O_2 Attenuation (dB)	0.15	0.15	0.16	0.26	0.27	0.29
H_2O Attenuation (dB)	0.42	0.66	1.04	0.44	0.42	0.40
Gaseous Loss (dB)	0.57	0.81	1.21	0.70	0.69	0.70
Rain Attenuation (dB)	11.33	12.98	14.76	23.21	25.39	27.69
System Temp ($^\circ K$)	572.70	578.96	583.49	485.99	485.97	485.96
DWN Degradation (dB)	2.15	2.03	1.84	0.00	0.00	0.00
Noise Power (dB)	-201.02	-200.97	-200.94	-201.73	-201.73	-201.73
Noise Bandwidth (MHz)	8	8	8	8	8	8
Total Loss (dB)	228.24	230.47	232.87	241.71	244.17	246.76
Total Gain (dB)	43.6	43.6	43.6	43.6	43.6	43.6
Carrier / Noise, E_b/N_o (dB)	-49.64	-51.91	-54.35	-62.39	-64.86	-67.45
Channel Bandwidth (MHz)	10	10	10	10	10	10
Number of Channels	200	200	200	200	200	200
Bandwidth Available (GHz)	2	2	2	2	2	2
Required Eb/No (dB)	10	10	10	10	10	10
E_b/N_o Margin (dB)	-59.64	-61.91	-64.35	-72.39	-74.86	-77.45
Max Dispersion (deg)	0.027	0.027	0.027	0.027	0.027	0.027
Max Dispersion (psec)	0.008	0.008	0.008	0.008	0.008	0.008
Phase Delay (deg)	24.24	24.24	24.24	24.24	24.24	24.24
Group Delay (psec)	6.734	6.734	6.734	6.734	6.734	6.734

Table 3.2: Link Budget Calculations: FDMA System

3.4 Comparison with L Band Voice System

There is significantly more loss resulting in the broadband scenario proposed as compared to voice band systems which operate at lower frequencies. In order to illustrate the source of these differences, a comparison was made with the 9.6 kbps voice band system proposed by [21].

Parameter	1.6 GHz	30 GHz	Difference
Bit Rate	9.6 kbps	2 Mbps	
Free Space Loss (dB)	188.38	214.66	26.28
Noise Power (dB)	-158.34	-141.73	22.61
Weather Attenuation (dB)	0.1	26.08	25.98
Total Major Attenuation Factors (dB)	30.14	105.01	74.87

Table 3.3: Up Link Performance Comparison:Ka System with L Band System

Parameter	2.0 GHz	20 GHz	Difference
Bit Rate	9.6 kbps	2 Mps	
Free Space Loss (dB)	190.11	211.14	21.03
Noise Power (dB)	-157.11	-140.96	22.15
Weather Attenuation (dB)	0.1	13.79	13.69
Total Major Attenuation Factors (dB)	33.1	89.97	56.87

Table 3.4: Down Link Performance Comparison:Ka System with L Band System

As this analysis shows that the major factors contributing to the system attenuation as compared to the lower frequency and data rate system are the free space loss, the noise power (which is a function of the data rate and noise power bandwidth) and the attenuation due to weather.

The values affecting the magnitude of this attenuation are the result of the desired frequency band the of the service required. Practical receiving antennas are limited

to a gain of approximately 50 dB due to size constraints, construction and pointing errors. It is anticipated that beamforming will allow for an increase in the signal to noise ratio which would make this system less costly.

Chapter 4

Cyclostationary Beamforming and On-Board Processing

The underlying principles behind the cyclostationary beamforming techniques, and a summary of existing cyclostationary algorithms will be presented.

A brief summary of the advantages of beamforming and on board processing will be discussed, and the advantages of cyclostationary algorithms over other beamforming techniques will be summarized.

4.1 Motivation for Digital Beamforming and On-Board Processing

On-Board Processing deals with the general topic of improving the received signal of the system in question before it is retransmitted to the desired user. Three forms of on-board processing take the form of regenerative repeaters, adaptive power control, and antenna beamforming.

This thesis will investigate the area of digital beamforming method of on-board processing as applied to the geostationary satellite mobile communications environment at the Ka frequency band. Digital Beamforming can offer the following advantages in a communications environment:

- Adaptive beams may be dedicated to individual users using antenna arrays.
- Power can be efficiently focused on a target area to improve the satellite system's efficiency.
- The beamforming array can adapt to variations in the user traffic levels
- The increased efficiency of power usage could translate into reduced hardware requirements and payload expense.
- Frequency reuse may be increased as a result of narrower adaptive beams which reduce interference from adjacent channels.
- Beamforming may offer robustness to the system in the event of component failure.

There are three general methods of beamforming being actively investigated in the present literature. The following sections briefly introduce the basic principles of these methods, and relate their application to the satellite system under investigation. For a more complete account of beamforming, tutorial papers by Van Veen and Buckley [41] and the text by Monzingo and Miller [28] may be referenced.

4.1.1 Reference-Based Beamforming

In reference based beamforming, a know signal which is highly correlated with the desired data and uncorrelated with interference signals is transmitted. This reference signal often takes the form of a known transmitted training sequence. Beamforming weights are calculated based on the reference signal using a variety of algorithms, the most common of which are Least Mean Square, and Direct Matrix Inversion. The major drawback of the reference-based beamforming method is the power and bandwidth resources that are taken up by the reference signal. In the satellite environment, this power cost is highly undesirable.

4.1.2 Location-Based Beamforming

Location-based beamforming relies on knowledge of the direction of arrival of the desired signal and the interference signals. Using this information, optimum beam weights may be calculated to suppress the interference, and boost the desired signal. This technique relies on algorithms which reliably estimate the direction of both the desired and interference signals. This is often done on the basis of eigen-vector analysis, such as the Multiple Signal Classification algorithm (MUSIC) [36] Most of these direction estimation algorithms require accurate knowledge of the type of interference, and the geometry of the array manifold.

In the portable satellite communications environment, weather patterns are constantly changing, and the ability to characterize the system once deployed is difficult. These disadvantages would make knowledge of the interference environment difficult, and the array geometry calibration less robust.

4.1.3 Property Restoral/Blind Beamforming

The property restoral beamforming technique focuses on maximizing inherent properties of the desired signal which are already present during transmission. Typically these characteristic signal properties are degraded by noise and interference. Algorithms are employed which beamform to restore these properties in the signal. It is assumed that by restoring the characteristic properties, the entire message signal is improved. Two techniques of property restoral are the Constant Modulus algorithm [37], and Cyclostationary Property Restoral technique [2].

The most obvious advantage of this type of beamforming is that there is no need for a reference signal, or accurate knowledge of the interference environment. Only accurate knowledge of the property to be restored is needed.

4.2 Motivation for the Cyclostationary Property Restoral Technique

Cyclostationary theory and techniques have been pioneered in various works by Gardner [16] [14]. Cyclostationarity exploits the behavior that most man-made signals exhibit a high degree of correlation with characteristic frequency shifted versions of themselves. Through selected weighting and summing of the signal at these frequencies, the cyclic correlation coefficient can be calculated. This coefficient is a measure of the similarity between the received signal and the frequency shifted signal. By adjusting antenna element weight coefficients to maximize this property, beamforming can be done to improve the reception of the entire message signal.

The advantages which result from the cyclostationary method are many. The beamforming algorithms are blind. They require no knowledge of the transmitted waveform. No training signal is needed and no knowledge of the noise and interference statistics are necessary. It is not necessary to calibrate the algorithm with measurements of the array manifold. The cyclostationary algorithms do not increase bandwidth or power requirements of the signal, and no synchronization is needed with the transmitter, which is a highly prohibitive requirement for the long distances and time delays involved in satellite communication. The only knowledge that is needed is the cyclic frequency of the chosen signal to be restored.

The major drawback of the cyclostationary algorithms are their high computational requirements and their slow convergence rate. Present literature has focused mainly on developing computationally efficient algorithms in SINR environments in the range of 0 to 20 dB [34] [2]. The focus of investigation for this thesis is on modifying existing algorithms to work in the geostationary satellite environment at the Ka band where SINR levels may be as low as -110 dB (Table 3.2) without antenna gains.

4.3 Theoretical Background for Cyclostationary Analysis

The theory of Cyclostationary analysis first began to receive attention in 1972 with Gardner's PhD. thesis [14]. Over the past 25 years, his original presentation which focused on real time series properties of cyclostationarity, has been extended to include complex time series and has been linked with statistical theory. Areas of application for cyclostationarity are being developed in the areas of array processing, transmitter/receiver optimization, blind channel equalization and identification.

Cyclostationarity exists in a signal if and only if a finite amplitude sine wave is produced when the original signal is multiplied by a non-linear n-th order transformation. This is calculated through temporal processing. A signal, $x(t)$, exhibits second order (n=2) cyclostationarity at the cyclic frequency α if and only if its delay product waveform, $y(t)$, exhibits a spectral line at this frequency.

$$y(t) = x(t)x(t-\tau) \tag{4.1}$$

Higher order non-linearities with a multiple lag parameters (ie. $\tau_1, \tau_2, ...$) will generate spectral lines for higher order cyclostationary time series. For wide sense stationary signals, a spectral line is only observed for the case $\alpha = 0$.

The cyclic spectrum is defined as all cyclic frequencies α where the signal exhibits a spectral line. Cyclic spectrums of man-made signals are often unique. Therefore, the unique cyclic spectrum of the desired signal may be exploited resulting in the rejection of noise and interferers, and enhancement of the desired signal.

Processing of the cyclostationary spectrum is done using time series analysis. As a result, the desired signal must be ergodic in nature, which will allow the ensemble average to equal the time average in the limit as the averaging time goes to infinity. Fortunately, most communications signals and environments are ergodic in nature.

The next section presents a brief outline of the theory and motivation behind cyclostationarity. Many of the results are presented without proof or justified by

appeal to the analogous well known property in a stochastic environment.

The cyclic theory presented by Gardner is based on the extension of Wiener's time-series analysis to cyclostationary signals of arbitrary order. Using this approach, temporal and spectral moments, higher order moments, bias, variance and Cramer-Rao bounds may be calculated. The application to this thesis is to provide a theoretical justification for the second order cyclostationary equations used in the beamforming algorithms applied. A full presentation of the following theory may be referenced in [16]. The "$\hat{\cdot}$" notation is used to distinguish between time-series measures and the related probabilistic measures.

4.3.1 Fraction of Time Probability Measure

Let the event indicator be defined as

$$I[x - x(t)] \triangleq \begin{cases} 1, & \mathrm{x(t) < x} \\ 0, & \mathrm{x(t) > x} \end{cases} \tag{4.2}$$

The time averaging of the event indicator results in the fraction-of-time probability distribution.

$$\hat{F}^0_{x(t)} \triangleq \hat{E}^0\{I[x - x(t)]\} \tag{4.3}$$

Where the time-averaging operator $\hat{E}^0$ is defined as:

$$\hat{E}^0\{h(t)\} \triangleq \lim_{Z\to\infty} \frac{1}{2Z} \int_{-Z}^{Z} h(t + t')dt' \tag{4.4}$$

Where $h(t)$ is any time dependent signal.

The joint fraction-of-time probability distribution may be generalized for the set of variables $\mathbf{x} \triangleq \{x(t + t_1), x(t + t_2), ...x(t + t_n)\}$

$$\hat{F}^0_{\mathbf{x}(t)} \triangleq \hat{E}^0\{\prod_{j=1}^{n} I[x_j - x(t + t_j)]\} \tag{4.5}$$

The joint fraction of time probability density which results when (4.5) is differentiable.

$$\hat{f}^0_{\mathbf{x}(t)}(\mathbf{x}) = \frac{\partial^n}{\partial x_1, \partial x_2, ... \partial x_n} \hat{F}^0_{\mathbf{x}(t)}(\mathbf{x}) \tag{4.6}$$

The following theorem results from the Fraction-of-Time formulation of the time signal x, which is based upon the parallel stochastic process principle, the "Fundamental Theorem of Expectation". It states:

Theorem 1 (Fundamental Theorem of Time-Averaging)

For every time-invariant function $g(\cdot)$ for which $\hat{E}^0\{g[\mathbf{x}(t)]\}$ exists,

$$\hat{E}^0\{g[\mathbf{x}(t)]\} = \int g(\mathbf{x}) \hat{f}^0_{\mathbf{x}(t)}(\mathbf{x}) d\mathbf{x} \tag{4.7}$$

This theorem shows that the time averaging operator $\hat{E}^0\{\cdot\}$ can be thought of as the temporal expectation operator. It may also be shown [34] that the $\hat{E}^0\{\cdot\}$ may remove residual terms in the time-averaged equation. Therefore $\hat{E}^0\{\cdot\}$ is also referred to as the constant component extractor.

In the probabilistic environment, the joint density of a cyclostationary stationary process is periodic in t. Similarly the Fraction-of-time probability density function is also periodic in t. In order to extend the principle of the constant component extractor to a polyperiodic function, consider the time series Fraction-of- Time probability density $\hat{F}^0_{\mathbf{x}(t)}(\mathbf{x})$ which is a polyperiodic function of t. This function can be expanded in a Fourier series as

$$\hat{F}^0_{\mathbf{x}(t)}\mathbf{x}(t) = \sum_\alpha \hat{F}^0_{\mathbf{x}(0)}(\mathbf{x}) e^{i2\pi\alpha t} \tag{4.8}$$

$$= \sum_\alpha \hat{F}^\alpha_{\mathbf{x}(t)}(\mathbf{x}) \tag{4.9}$$

Here $\hat{F}^\alpha_{\mathbf{x}(0)}(\mathbf{x})$ are the Fourier series coefficients, and α denotes the cyclic frequency. The sinusoidal components of $\hat{F}^\alpha_{\mathbf{x}(t)}(\mathbf{x})$ may be given by:

$$\hat{F}^{\alpha}_{\mathbf{x}(t)}(\mathbf{x}) \triangleq Z \overset{\lim}{\rightarrow} \infty \frac{1}{2Z} \int_{-Z}^{Z} \hat{F}^{0}_{t+t'}(\mathbf{x}) e^{-i2\pi\alpha t'} dt' \tag{4.10}$$

$$= \hat{E}^{0}\{\hat{F}^{0}_{\mathbf{x}(t)}(\mathbf{x}) e^{-i2\pi\alpha t'}\} e^{i2\pi\alpha t'} \tag{4.11}$$

$$\triangleq \hat{E}^{\alpha}\{\hat{F}^{0}_{\mathbf{x}(t)}\} \tag{4.12}$$

The general sinewave component extractor may be written as:

$$\hat{E}^{\alpha}\{\cdot\} \triangleq \hat{E}^{0}\{(\cdot) e^{-i2\pi\alpha t}\} e^{i2\pi\alpha t} \tag{4.13}$$

Using this definition of the sinewave component extractor, the multiple periodicities of a time series may be extracted by:

$$\hat{E}^{\alpha}\{\cdot\} \triangleq \sum_{\alpha \in \{\alpha\}} \hat{E}^{\alpha}\{\cdot\} \tag{4.14}$$

The set of $\{\alpha\}$ frequencies which are extracted represent the harmonics of the reciprocals of the underlying multiple periodicities in the signal. Finally, the expression for the polyperiodic Fraction-of-Time Probability distribution for a time-series with multiple periodicities becomes:

$$\hat{F}^{\alpha}_{\mathbf{x}(t)} \triangleq \hat{E}^{\alpha}\{\prod_{j=1}^{n} I[x_j - x(t + t_j)]\} \tag{4.15}$$

The polyperiodic Function of Time density which results is:

$$\hat{f}^{\alpha}_{\mathbf{x}(t)}(\mathbf{x}) = \frac{\partial^n}{\partial x_1, \partial x_2, \ldots \partial x_n} \hat{F}^{\alpha}_{\mathbf{x}(t)}(\mathbf{x}) \tag{4.16}$$

Theorem 2 (Fundamental Theorem of Polyperiodic Component Extraction)

For every time-invariant function $g(\cdot)$ for which $\hat{E}^{\alpha}\{g[\mathbf{x}(t)]\}$ exists:

$$\hat{E}^{\alpha}\{g[\mathbf{x}(t)]\} = \int g(\mathbf{x}) \hat{f}^{\alpha}_{\mathbf{x}(t)}(\mathbf{x}) d\mathbf{x} \tag{4.17}$$

The strict sense definitions of cyclostationarity follow from the preceding theorem. Define $\{\alpha\}$ to be the set of all cycle frequencies for which $\hat{F}^{\alpha}_{\mathbf{x}(t)} \neq 0$ [34].

Stationarity: A time series $x(t)$ is stationary if and only if its joint fraction of time probability density $\hat{F}^{\alpha}_{\mathbf{x}(t)} \neq 0$ exists and is independent of the parameter t. In this case $\{\alpha\} = \{0\}$

Cyclostationarity: A time-series $x(t)$ is cyclostationary with period T_0 if and only if its fraction of time probability density $\hat{F}^{\alpha}_{\mathbf{x}(t)} \neq 0$ exists, and is periodic in t with period T_o. In this case, the cyclic spectrum $\{\alpha\}$ is composed of all harmonics of $1/T_0$.

Polycyclostationarity: A time-series $x(t)$ is cyclostationary with period $T_0, T_1, T_2...$ if and only if its fraction of time probability density $\hat{F}^{\alpha}_{\mathbf{x}(t)} \neq 0$ exists, and is polyperiodic in t with periods $T_0, T_1, T_2, ...$ In this case, the cyclic spectrum is the set of all the harmonics of each fundamental period.

The following section will build upon the theorems and definitions presented as applied to second order cyclostationary time-series.

4.4 Second-Order Cyclostationariy

The second order polyperiodic cyclostationary waveform can be generated as follows:

$$y_\tau(t) = x(t+\tau/2)x(t-\tau/2) \tag{4.18}$$

From the theorems and definitions presented in Section 4.3 , the following terms are obtained from the polyperiodic component extractor

$$\tilde{E}^{\alpha}\{y_r(t)\} = \sum_{\{\alpha\}} \tilde{E}^{0}\{y_r(t)e^{-i2\pi\alpha t}\}e^{i2\pi\alpha t} \tag{4.19}$$

$$= \sum_{\{\alpha\}} \tilde{R}^{\alpha}_{xx}(\tau)e^{-i2\pi\alpha(t-\tau/2)} \tag{4.20}$$

Here the $\sim$ notation refers to continuous time series, and the omission of this symbol refers to discrete time series.

In Equation (4.20)

$$\tilde{R}^{\alpha}_{xx}(\tau) \triangleq E^0\{x(t+\tau/2)x(t-\tau/2)e^{-i2\pi\alpha t}\} \tag{4.21}$$

is the Fourier series coefficient of the additive sine-wave component of $y_r(t)$ with frequency α. For the discrete case this formula is modified to:

$$R^{\alpha}_{xx}(\tau) \triangleq E^0\{x(t)x(t-\tau)e^{-i2\pi\alpha t}\}e^{-i2\pi\alpha\tau} \tag{4.22}$$

It is important to stress that the above quantities are time-averaged. The constant component extraction operation will be defined as:

$$\langle\cdot\rangle_{\infty} = \lim_{Z\to\infty}\frac{1}{2Z}\int_{-Z}^{Z}(\cdot)dt \tag{4.23}$$

For the discrete case the formula is modified to:

$$\langle\cdot\rangle_{\infty} = \lim_{Z\to\infty}\frac{1}{2Z+1}\sum_{-Z}^{+Z}(\cdot) \tag{4.24}$$

4.4.1 Cyclic Autocorrelation Function

The quantity $\tilde{R}^{\alpha}_{xx}(\tau)$ may be interpreted in three ways which offer insight into the measure produced.

1 $\tilde{R}^{\alpha}_{xx}(\tau)$ may be interpreted as the Fourier coefficients of the additive sine-wave components of the delay product waveform of $x(t)x(t-\tau)$. This was shown in section 4.3.

2 The conventional autocorrelation function

$$R^{0}_{xx}(\tau) = \langle x(t)x(t-\tau)\rangle_{\infty} \tag{4.25}$$

can be shown to be a specific case of $\tilde{R}^{\alpha}_{xx}(\tau)$. This may be done by setting $\alpha = 0$ and using the time averaging notation presented in Equations (4.23), (4.24) for the constant component extractor E. Therefore, $\tilde{R}^{\alpha}_{xx}(\tau)$ may be thought of as a generalized autocorrelation function, and will be referred to as the cyclic autocorrelation function. For complex signals, it is also useful to define the conjugate cyclic autocorrelation function $\tilde{R}^{\alpha}_{xx^*}(\tau)$ which may be applied in some algorithms to obtain different cyclic spectra from a signal.

The cyclic correlation and conjugate cyclic correlation functions are shown below.

$$\mathbf{R_{xx}}^{\alpha}(\tau) = \langle \mathbf{x}(t)\mathbf{x}^*(t-\tau)e^{-j2\pi\alpha t}\rangle_{\infty} e^{j\pi\alpha\tau} \tag{4.26}$$

$$\mathbf{R_{xx^*}}^{\alpha}(\tau) = \langle \mathbf{x}(t)\mathbf{x}(t-\tau)e^{-j2\pi\alpha t}\rangle_{\infty} e^{j\pi\alpha\tau} \tag{4.27}$$

$$\tag{4.28}$$

3 If the input time function is frequency translated via:

$$u(t) = x(t)e^{-i\pi\alpha t} \tag{4.29}$$

$$v(t) = x(t)e^{+i\pi\alpha t} \tag{4.30}$$

it is easy to show that the conventional cross-correlation function can be made equal to the cyclic cross correlation function.

$$R_{uv}(\tau) = \langle u(t)v^*(t-\tau)\rangle_{\infty} \tag{4.31}$$

$$= R^{\alpha}_{xx}(\tau) \tag{4.32}$$

Equation (4.32) gives a quantitative measure of the amount of correlation of the signal x at the cyclic frequency α.

4.5 Cyclic Temporal Correlation Coefficient

The cyclic temporal autocorrelation coefficient may be generated by normalizing the the cyclic autocorrelation function with respect to the autocorrelation function of $x(t)$ for the time lag $\tau = 0$. This produces the cyclic temporal correlation coefficient.

$$\gamma_{xx}^{\alpha}(\tau) \triangleq \frac{R_{xx}^{\alpha}(\tau)}{R_{xx}(0)} \tag{4.33}$$

The feature strength is defined as the magnitude of equation (4.33)

The value of (4.33) is $0 \leq \gamma_{xx}^{\alpha}(\tau) \leq 1$. This quantity is the measure that is maximized in the existing cyclic correlation algorithms. It should be noted that (4.33) is complex-valued. Therefore its argument can be used to distinguish between different signals of the same magnitude which may allow algorithms to select signals with the same cyclic frequencies arriving from different directions.

Similarly the cyclic temporal cross correlation coefficient may be generated for two time sequences $x(t)$ and $y(t)$ by:

$$\gamma_{xy}^{\alpha}(\tau) \triangleq \frac{R_{xy}^{\alpha}(\tau)}{R_{xy}(0)} \tag{4.34}$$

4.6 Spectral Correlation Density Function

Gardner in [17] has related the time domain performance of the cyclic correlation coefficient to the frequency domain. This is be done by passing the frequency translated signals $u(t)$ and $v(t)$ through an ideal bandpass filter at the center frequency f. The average power is measured at the output, and the result is normalized by the bandwidth. This results in the spectral correlation density function:

$$S_{xx}^{\alpha} \triangleq \lim_{B \to 0} \frac{1}{B} \left\langle \left[h_B^f(t) \otimes u(t) \right] \left[h_B^f(t) \otimes v(t) \right]^* \right\rangle \tag{4.35}$$

where $\otimes$ denotes convolution and h_B^f is the ideal bandpass filter.

Gardner in [16] relates the cyclic power spectral density function of S_{xx}^{α} to the cyclic auto correlation function. The result is similar to the "Wiener-Khinchin Theorem" in the probabilistic framework, which relates the autocorrelation function of a signal as the Fourier transform of the power spectral density.

Theorem 3 (Cyclic Wiener Relation) [34]

The spectral correlation density function, $S_{xx}^{\alpha}(f)$, and the cyclic autocorrelation function, $R_{xx}^{\alpha}(\tau)$ are related by the Fourier transform pair:

$$S_{xx}^{\alpha}(f) = \int_{-\infty}^{\infty} R_{xx}^{\alpha}(\tau) e^{-i2\pi f\tau} d\tau \tag{4.36}$$

$$R_{xx}^{\alpha}(\tau) = \int_{1/2}^{1/2} S_{xx}^{\alpha}(f) e^{i2\pi f\tau} df \tag{4.37}$$

$$\tag{4.38}$$

A summary of the above terms are given below:

$\tilde{R}_{xx}^{\alpha}(\tau)$ $\Rightarrow$ Fourier series coefficients of the continuous time series $x(t+\tau/2)x(t-\tau/2)$ at frequency α

$R_{xx}^{\alpha}(\tau)$ $\Rightarrow$ Fourier series coefficients of the discrete time series $x(t)x(t-\tau)$ at frequency α

S_{xx}^{α} $\Rightarrow$ Spectral correlation density function

$\gamma_{xx}^{\alpha}(\tau)$ $\Rightarrow$ Temporal Correlation Coefficient.

Work by Gardner [16] has developed a method of cyclic Wiener Filtering which uses knowledge of the spectral structure of the channel to develop optimum filtering weights. This technique is briefly outlined below.

4.7 Frequency-Shift Filtering (FRESH)

FRESH filtering is a recently developed class of filters based on the optimal minimum mean-squared filtering of polycyclostationary time-series signals. The filter is made up of two processors that filter the input signal and its complex conjugate. Filtering is done using a set of linear time-varying frequency shifters, and linear time-invariant filters. The linear-conjugate-linear frequency shift (LCL-FRESH) filter obtains its

input values from solving a multi-variate Wiener filtering problem based on the application of theorem 3. This filtering allows the desired signal to be separated from spectrally overlapping interference using the spectral redundancy inherent in the excess bandwidth of the signal.

The computation of the variables in FRESH filtering requires knowledge of the frequency spectrum of the interference signals and the desired signal, such as the baud rate, carrier frequency, and number of interferers. For an adaptive application of the FRESH filter, some known training sequence must be supplied for the purpose of updating the variables.

4.8 The Cyclic Signal Model Environment

The notation introduced in this section is summarized below:

$\mathbf{n} \Rightarrow$ independent, identically distributed , spatially and temporally incoherent white Gaussian noise samples.

$\mathbf{d}(\Phi) \Rightarrow$ array response of the desired signal.

$\mathbf{a} \Rightarrow$ array response of the interference signals.

$\Phi_l \Rightarrow$ direction of arrival of the l^{th} signal with frequency spectrum L_α

$\Theta_m \Rightarrow$ direction of arrival of the l^{th} interference signal.

$\mathbf{D}(\mathbf{\Theta}) \Rightarrow J \times L_\alpha$ Array manifold for the desired signal vectors $\mathbf{s}(t)$.

$\mathbf{A}(\mathbf{\Phi}) \Rightarrow J \times M$ Array manifold for the interference vectors $\mathbf{i}(t)$.

The signal observed for a J-element antenna is defined as:

$$\mathbf{x}(t) = \sum_{l=1}^{L_\alpha} \mathbf{d}(\Theta_l) s_l(t) + \sum_{m=1}^{M} \mathbf{a}(\Phi) i_m + \mathbf{n}(t) \tag{4.39}$$

$$= \mathbf{D}(\mathbf{\Theta})\mathbf{s}(t) + \mathbf{A}(\mathbf{\Phi})\mathbf{i}(t) + \mathbf{n}(t) \tag{4.40}$$

In the above equation, $L_\alpha, l = 1, ...L_\alpha$ represents the number of desired signals s_l with cyclic spectra α. There are also M interferers $i_m(t), m = 1, ..., M$ which do not have the cyclic spectrum α.

In the equation (4.40), a matrix form is used where:

$$\mathbf{D}(\mathbf{\Theta}) \triangleq [\mathbf{d}(\Theta_1), \mathbf{d}(\Theta_2), ...\mathbf{d}(\Theta_{L_\alpha})]_{J \times L_\alpha} \quad (4.41)$$

$$\mathbf{A}(\mathbf{\Phi}) \triangleq [\mathbf{a}(\Phi_1), \mathbf{a}(\Phi_2), ...\mathbf{a}(\Phi_M)]_{J \times M} \quad (4.42)$$

$$\mathbf{s}(t) \triangleq [s_1(t), s_2(t), ...s_{L_\alpha}(t)]^T_{L_\alpha \times 1} \quad (4.43)$$

$$\mathbf{i}(t) \triangleq [i_1(t), i_2(t), ...i_M(t)]^T_{M \times 1} \quad (4.44)$$

$$(4.45)$$

The autocorrelation matrix of $x(t)$ is given by:

$$\mathbf{R_{xx}}(\tau) = \mathbf{D}(\mathbf{\Theta})\mathbf{R_{ss}}(\tau)\mathbf{D}^\dagger(\mathbf{\Theta}) + \mathbf{A}(\mathbf{\Phi})\mathbf{R_{ii}}(\tau)\mathbf{A}^\dagger(\mathbf{\Phi}) + \sigma_n^2\mathbf{I} \quad (4.46)$$

The term $\sigma_n^2 = \langle |n_j|^2 \rangle_\infty$, and $\mathbf{I}$ is the identity matrix, and $(\cdot)^\dagger$ is the conjugate-transpose operator.

The advantage of the computing the cyclic autocorrelation of the vector $\mathbf{x}(t)$ at cyclic frequency α is demonstrated below:

$$\mathbf{R_{xx}}^\alpha(\tau) \triangleq \langle \mathbf{x}(t)\mathbf{x}^\dagger(t-\tau)e^{i2\pi\alpha t} \rangle_\infty e^{i2\pi\alpha\tau} \quad (4.47)$$

$$= \mathbf{D}(\mathbf{\Theta})\mathbf{R_{ss}}^\alpha(\tau)\mathbf{D}^\dagger(\mathbf{\Theta}) + \mathbf{A}(\mathbf{\Phi})\mathbf{R_{ii}}^\alpha(\tau)\mathbf{A}^\dagger(\mathbf{\Phi}) + \mathbf{R_{nn}}^\alpha(\tau) \quad (4.48)$$

$$= \mathbf{D}(\mathbf{\Theta})\mathbf{R_{ss}}^\alpha(\tau)\mathbf{D}^\dagger(\mathbf{\Theta}) \quad (4.49)$$

By exploiting the spectral self-coherence property of the desired signal, the interference and noise terms of the above equation go to zero as the time averaging approaches infinity. This leaves only the signals with the cyclic spectrum of α to be processed using a beamforming algorithm. This is a very different approach than to the MUSIC-type algorithms [2] which use the classic autocorrelation function and resort to eigenvalue decomposition to determine the beamforming weights of all signals which are spatially coherent (same direction of arrival).

4.9 Blind Cyclic Spatial Filtering Algorithms

Since the theory behind cyclic time series is still relatively new, its application to this beamforming is also quite new. There are four major techniques of beamforming to date which employ cyclostationarity: SCORE (Spectral Coherence Restoral) [2], the Cyclic Adaptive Beamformers [46], the Phase algorithm [34], and finally the Castedo algorithm [34]. Recent investigation into signal subspace techniques have also been applied to existing algorithms [5], and the motivation for this technique will be briefly discussed below.

The performance of all these algorithms may be measured with respect to the optimal beamforming weights. The optimal weights in terms of maximizing signal to noise and interference (SINR) are given by [41]:

$$\mathbf{w}_{1,opt} = \beta \mathbf{R_{xx}}^{-1} \mathbf{d}(\Theta_1) \tag{4.50}$$

Where $\mathbf{w}$ is the optimal beamforming weight vector.

4.9.1 Spectral Coherence Restoral Blind Beamforming Algorithms (SCORE)

All SCORE algorithms aim at maximizing the spectral self-coherence of a single frequency at the output of the beamformer using the principle of cyclostationarity. There are a variety of cost functions which give rise to different algorithms with specific advantages and applications. Least Squares SCORE and Cross SCORE are the two techniques which are dealt in detail in this thesis.

4.9.1.1 Least-Squares SCORE

The Least-Squares SCORE is the simplest algorithm which employs spectral self-coherence. This technique is applicable to the rank $L_\alpha = 1$ environment where there is only one signal with the frequency spectrum α.

The first step in the LS-SCORE algorithm is to define the reference signal:

$$u(t) \triangleq \mathbf{c}^{\dagger} \cdot \mathbf{x}^{(*)}(t-\tau)e^{i2\pi\alpha t} \tag{4.51}$$

This reference signal has a component which is correlated with the desired signal ($s(t)$) and a component which is uncorrelated ($\mathbf{i}(t), \mathbf{n}(t)$) The optional conjugation operator $(\cdot)^{(*)}$ is employed depending on the type of spectral self-coherence to be exploited. The value of the control vector $\mathbf{c}$ is a fixed constant, and does not affect the performance of the algorithm.

The beamforming weights are found by performing a least squares minimization of the distance between the reference signal and the output signal $y(t)$:

$$y(t) \triangleq \mathbf{w}^{\dagger} \cdot \mathbf{x}(t) \tag{4.52}$$

This results in the requirement:

$$\min_{\mathbf{w}} \langle |y(t) - u(t)|^2 \rangle_N \tag{4.53}$$

Here N is the number of samples of x available to the algorithm.

The familiar optimal solution to (4.53) as $N \rightarrow \infty$ is [34]:

$$\mathbf{w}_{opt} \rightarrow \mathbf{R_{xx}}^{-1} \cdot \mathbf{r_{xu}} \tag{4.54}$$

$$= \mathbf{R_{xx}}^{-1}\mathbf{R_{xx}}^{\alpha}(\tau)\mathbf{c}e^{-j\pi\alpha\tau} \tag{4.55}$$

$$\tag{4.56}$$

For this application of the LS-SCORE algorithm, it is assumed that the interference and the noise terms are not spectrally coherent at the frequency spectrum α and that only one desired signal has the frequency spectrum α. Therefore $\mathbf{R_{xx}}^{\alpha}(\tau) = \mathbf{d}(\Theta_1)\mathbf{d}^{\dagger}(\Theta_1)R_{ss}^{\alpha}$ is a rank-one matrix. 4.56 reduces to:

$$\mathbf{w}_{opt} = [\mathbf{d}^{\dagger}(\Theta_1)R_{ss}^{\alpha}\mathbf{c} \cdot e^{-j\pi\alpha\tau}]\mathbf{R_{xx}}^{-1}\mathbf{d}(\Theta_1) \tag{4.57}$$

$$= \beta\mathbf{R_{xx}}^{-1}\mathbf{d}(\Theta_1) \tag{4.58}$$

Where β is a complex-valued constant.

Therefore as $N \rightarrow \infty$ the Least Squares SCORE algorithm converges to the SINR optimal beam weight.

The main advantage of the Least Squares score is its computational simplicity. The cost for this simplicity is a slow convergence rate. Analysis done in [34] attributes the slow convergence rate to the weak feature strength or spectral self-coherence generated by the algorithm, and its inability to quickly reject strong interferers.

An improvement to the Least Squares SCORE algorithm is to adaptively modify the control vector $\mathbf{c}$. This give rise to the Cross Score algorithm.

4.9.1.2 Cross SCORE Algorithm

The Cross SCORE algorithm uses the received signal $y(t)$ and the reference signal $u(t)$ to adaptively update both the control vector $\mathbf{c}$ and the weight vector $\mathbf{w}$. The algorithm maximizes the temporal cross-correlation coefficient, $|\gamma_{yu}^{\alpha}(\tau)|^2$ defined analogously to equation (4.33) resulting in the following cost function:

$$\max_{\mathbf{w},\mathbf{c}} |\gamma_{yu}^{\alpha}(\tau)|^2 \quad \Leftrightarrow \quad \max_{\mathbf{w},\mathbf{c}} \frac{|\mathbf{w}^{\dagger}\mathbf{R_{xx}}^{\alpha}(\tau)\mathbf{c}|^2}{[\mathbf{w}^{\dagger}\mathbf{R_{xx}}\mathbf{w}][\mathbf{c}^{\dagger}\mathbf{R_{xx}}\mathbf{c}]} \tag{4.59}$$

The Rayleigh Quotient cost function for $\mathbf{w}$ arises when $\mathbf{w}$ in (4.59) is fixed. The maximal value for $\mathbf{c} = \mathbf{R_{xx}}^{-1}\mathbf{R_{xx}}^{\alpha\dagger}(\tau)\mathbf{w}$ is substituted:

$$\max_{\mathbf{w}} \frac{\mathbf{w}^{\dagger}\mathbf{R_{xx}}^{-1}(\tau)\mathbf{R_{xx}}^{\alpha\dagger}(\tau)\mathbf{w}}{\mathbf{w}^{\dagger}\mathbf{R_{xx}}\mathbf{w}} \tag{4.60}$$

By solving a standard eigenvalue problem, solutions to Equation (4.60) may found. The solution to the Cross Score algorithm is achieved using the optimal expression for $\mathbf{c}$, and by using the pair of eigenvectors corresponding to the maximum eigenvalues of the two equations below:

$$\mathbf{R_{xx}}^{\alpha}(\tau)\mathbf{R_{xx}}^{-1}\mathbf{R_{xx}}^{\alpha\dagger}(\tau)\mathbf{w} = \lambda\mathbf{R_{xx}}\mathbf{w} \tag{4.61}$$

$$\mathbf{R_{xx}}^{\alpha}(\tau)\mathbf{R_{xx}}^{-1}\mathbf{R_{xx}}^{\alpha\dagger}(\tau)\mathbf{c} = \lambda\mathbf{R_{xx}}\mathbf{c} \tag{4.62}$$

Typically, the solution of the above equations requires computationally expensive eigenvector methods. However, for the $L_\alpha = 1$ environment, the iterative Power Method [6] may be employed:

Theorem 4 (Power Method)

Given a diagonalizable $n \times n$ matrix $\mathbf{A}$ with eigenvectors $\mathbf{e}_1, \mathbf{e}_2, ...\mathbf{e}_n$ and corresponding eigen values $\lambda_1, \lambda_2, ...\lambda_n$, and assuming $|\lambda_1| \geq |\lambda_2| \geq ... \geq \lambda_n$, then for an arbitrary non-zero vector v_1 with a component in the direction $\mathbf{e}_1$, the iterated vector $\mathbf{v}_m = \mathbf{A} \cdot \mathbf{v}_{m-1}$ will converge as $m \rightarrow \infty$, to

$$\mathbf{A}^m \mathbf{v}_m \rightarrow \lambda_1^m \mathbf{e}_1 \tag{4.63}$$

$$\lambda_1 = m \overset{lim}{\rightarrow} \infty \frac{\|\mathbf{v}_m\|}{\|\mathbf{v}_{m-1}\|} \tag{4.64}$$

By applying the Power Method to the Cross SCORE algorithm, the following iterations for $\mathbf{w}$ and $\mathbf{c}$ are obtained.

$$\mathbf{w}_{m+1} = g_w \mathbf{R_{xx}}^{-1} \mathbf{R_{xx}}^{\alpha}(\tau) \mathbf{c}_m \tag{4.65}$$

$$\mathbf{c}_{m+1} = g_c \mathbf{R_{xx}}^{-1} \mathbf{R_{xx}}^{\alpha}(\tau) \mathbf{w}_m \tag{4.66}$$

$$g_w = \frac{1}{\|\mathbf{w}_m\|^{1/2}} \tag{4.67}$$

$$g_c = \frac{1}{\|\mathbf{c}_m\|^{1/2}} \tag{4.68}$$

where g_w and g_c are normalization constants.

In the general rank L_α environment, techniques can be applied which will allow for the extraction of other signals with the frequency spectrum α which correspond to the smaller eigen values of the matrix. Each eigenvalue will correspond to a unique spectral self coherence magnitude i.e., $\lambda_l = |\gamma^{\alpha}_{s_l s_l}(\tau)|^2$. This is achieved provided the number of signals with spectrum α are less than or equal to the number of elements in the antenna array, that is $L_\alpha \leq J$. This behavior is demonstrated by simulations in [35] and [34]. These simulation results show that the performance of the Cross SCORE in the L_α interference environment is always inferior, but this performance

degradation is minimal if the direction of arrival of the different signals Θ_k and Θ_l are approximately orthogonal, i.e., $\mathbf{d}^\dagger(\Theta_k) \cdot \mathbf{d}^\dagger(\Theta_l) \approx 0$.

4.9.1.3 Auto SCORE

Auto-SCORE algorithms rely solely on the property restoral principle. The spectral or conjugate spectral self- coherence property is restored by adapting one weight vector based on the beamformer output. The cost function to be maximized is

$$\max_{\mathbf{w}} |\gamma^{\alpha}_{yu^{(*)}}(\tau)| \quad \Leftrightarrow \quad \max_{\mathbf{w}} \frac{|\mathbf{w}^\dagger \mathbf{R}_{\mathbf{x}\mathbf{x}^{(*)}}{}^{\alpha}(\tau)\mathbf{w}^{(*)}|}{\mathbf{w}^\dagger \mathbf{R}_{\mathbf{x}\mathbf{x}}\mathbf{w}^{(*)}} \tag{4.69}$$

The performance of the Auto SCORE in the $L_\alpha = 1$ environment converges to the optimal beamforming weights. In environments where $L_\alpha > 1$ the performance is closely resembled by the Cross SCORE algorithm performance. One of the major drawbacks of the Auto SCORE algorithm, is the fact that a local maximum may be produced in its solution. For more detail on the Auto SCORE algorithm [2] and [1] may be referenced. The Auto SCORE was not considered for the application to the satellite channel model.

4.9.1.4 Phase SCORE

The aim of the Phase SCORE algorithm is to develop a method where the defining eigen-equation is equal to the complex valued spectral correlation coefficients $\gamma_{s_l s_l}(\tau)$ of the desired signal. This technique preserves the self coherent phase of the spectral correlation coefficients. This allows the algorithm to distinguish between different signals which may have the same cyclic frequency α and the same spectral correlation magnitude. It is only required that signals have a different delay, or carrier phase.

Phase SCORE is a sub-optimal approach based on a modification to the non-conjugate Auto-SCORE algorithm. The defining eigenequation for Phase SCORE is given by:

$$\mathbf{R_{xx}}^{\alpha}(\tau)\mathbf{w} \quad = \quad \lambda \mathbf{R_{xx}}\mathbf{w} \tag{4.70}$$

The phase score algorithm is not applied to the satellite environment in this thesis. Further development of Phase SCORE performance is presented in [34], [2] and [35].

4.9.2 The Cyclic Adaptive Beamforming Algorithm

The Cyclic Adaptive Beamforming Algorithms (CAB) are based using the cyclic properties of the desired signals to extract a weight vector $\mathbf{w}$ which is a scalar multiple of the steering vector $\mathbf{w}(\Theta_1)$ of the desired signal. The goal in designing the CAB algorithm was to present an alternative set of cyclic beamforming algorithms which would converge more quickly than SCORE, especially in the mobile communications environment and which would perform well in the case where the desired signal is much stronger than the interference and noise signals. Restriction of the CAB algorithm to a high SINR signal environment disqualifies it from further consideration for the satellite environment. Simulation results performed by Rollins [34] demonstrates the degradation in CAB performance in a low SINR environment. Furthermore, Rollins shows that CAB algorithms converge to beamforming weights which yield SINR values several dB below the optimum values in an interference environment modeled by Equation (4.50). He accounts for this from the fact that the scaled version of the steering vector produces a maximal ratio combiner [44] whereas SCORE algorithms produce optimal combiners.

Three types of CAB algorithms have been developed by Wu et. al.. [46], [45] and are presented for reference.

4.9.2.1 Basic CAB Algorithm

The basic CAB algorithm converges to the scaled version of the steering vector with a complexity of order $O\{J\}$, where J is the number of elements of the antenna array and as $N \rightarrow \infty$, where N is the number of samples. The CAB may also extract

multiple signals with the cyclic frequency spectra α, provided the direction of arrival of the signals are approximately orthogonal.

4.9.2.2 Constrained CAB Algorithm (C-CAB)

C-CAB exploits the property that the CAB algorithm converges to a scaled version of the steering vector. The $\mathbf{w}_{CAB}$ estimation of the direction of arrival of the desired signal is used as an input to the linearly-constrained minimum variance (LCMV) beamforming algorithm [41]. The computational complexity of this problem is of order $O\{J^2\}$

4.9.2.3 Robust CAB Algorithm (R-CAB)

The R-CAB algorithm has a modified cost function that reduces the effect of small perturbations in $\mathbf{R_{ii}}$ and $\mathbf{d}(\Theta_l)$. R-CAB requires an estimation of $\mathbf{R_{ii}}$ which requires the complexity of order $O\{J^3\}$.

4.9.3 Castedo Algorithm

This algorithm is based upon the observation that cyclostationary signals exhibit spectral lines in the frequency domain when passed through non-linear transforms. The algorithm attempts to minimize the mean square error of these spectral lines with a known generated reference tone corresponding to one of the spectral lines α [7]. Spectral lines are generated by the non-linear transform $(\cdot)^p$ where $p \geq 2$ at the following frequencies:

$$
\begin{aligned}
y(t) &= \hat{E}^{\alpha}\{x^p(t)\} && (4.71)\\
&\triangleq \hat{E}^{0}\{x^p(t)e^{-i2\pi\alpha t}\}e^{i2\pi\alpha t} && (4.72)\\
&= m_{px}^{\alpha}e^{i2\pi\alpha t} && (4.73)
\end{aligned}
$$

Cyclic beamforming weights may be calculated by using the following cost function:

$$\mathcal{J} \quad = \quad \langle |e^{i2\pi\alpha t} - y^p(t)|^2 \rangle_\infty \tag{4.74}$$

Here, the beamformer output is the scalar $y(t) = \mathbf{w}^\dagger \mathbf{x}(t)$

The Equation (4.74) may be minimized using the method of steepest descent, resulting in the iteration:

$$\mathbf{w}(t+1) \quad = \quad \mathbf{w}(t) - \mu \nabla_{\mathbf{w}(t)} \mathcal{J} \tag{4.75}$$

In 4.75 μ represents the step-size parameter, and $\nabla_{\mathbf{w}(t)}\mathcal{J}$ represents the gradient of $\mathbf{w}$. This results in the following iterative algorithm for finding the beam weights:

$$\mathbf{w}(t+1) \quad = \quad \mathbf{w}(t) + \mu \epsilon^*(t) y^{p-1}(t) \mathbf{x} \tag{4.76}$$

Where the error signal is the term $\epsilon = e^{i2\pi\alpha t} - y^p(t)$.

The performance of the Castedo algorithm is highly dependent upon the stationary points which are generated under different signal environments. A summary of the conditions for optimal convergence are presented in [7] and [34]

4.9.4 PHASE Algorithm

A new PHASE algorithm has been proposed by Cui in [9] for application in a wireless indoor environment. In the Phase algorithm, the output of each array element is spectrally correlated. A reference signal $u_j(t) = x_j(t)e^{-2\pi\alpha t}$ is applied to the steering vector.

$$\mathbf{r}_j^\alpha \quad \triangleq \quad \langle \mathbf{x}(t) u(t) \rangle_N \tag{4.77}$$

This results in a set of cyclic correlation vectors, in which the rank $L_\alpha = 1$ environment converges towards a scaled replica of the steering vector $\mathbf{d}(\Theta_1)$. Each

weight vector $\mathbf{w}_j = \mathbf{R_{xx}}^{-1}\mathbf{r}_j^{\alpha}$ obtained in this manner is equivalent to a uniquely scaled Least Squares SCORE weight vector. The final step in the algorithm is to average these weight vectors to obtain a single vector:

$$\mathbf{w} = \mathbf{R_{xx}}^{-1} \cdot \frac{1}{J}(\mathbf{r}_1^{\alpha} + \mathbf{r}_2^{\alpha} ... + \mathbf{r}_j^{\alpha}) \tag{4.78}$$

This formulation of the Phase algorithm has been shown to have a faster convergence rate and larger final SINR, as compared to the Auto SCORE. Furthermore, it requires no eigenvalue decomposition in finding the weight vectors. [34] [9].

4.9.5 Signal Subspace Techniques

In investigations by Biedka [5] on the SCORE algorithms, he observed that if the number of array elements are increased while keeping the averaging time for the algorithm constant, a degradation in the performance of the final SINR of the signal was observed. This behavior is may be explained using signal space arguments: The maximum SINR at the beamformer is obtained from Equation (4.50). Eigenvalue decomposition reduces this relation to:

$$\mathbf{R_{xx}}^{-1}\mathbf{d}(\Theta) = \left[\mathbf{Q}_s\mathbf{\Lambda}_s^{-1}\mathbf{Q}_w^{\dagger} + \frac{1}{\sigma_n^2}\mathbf{Q}_s\mathbf{Q}_w^{\dagger}\right]\mathbf{d}(\Theta) \tag{4.79}$$

$$= \mathbf{Q}_s\mathbf{\Lambda}_s^{-1}\mathbf{Q}_w^{\dagger}\mathbf{d}(\Theta) \tag{4.80}$$

Where in the above equation:

$\mathbf{Q}_s \Rightarrow$ eigenvectors of the matrix $\mathbf{R_{xx}}$

$\mathbf{\Lambda} \Rightarrow$ eigenvalues of the matrix $\mathbf{R_{xx}}$

In equation (4.80), the vector $\mathbf{d}$, which lies in the signal subspace is orthogonal to the noise subspace, and the optimal weight vector also lies in the signal subspace.

The degradation in convergence rate for the SCORE algorithms occurs when more elements are added to the array for a fixed sample time. Performance degradation results from the increased sensitivity of the SCORE algorithms to errors in the finite sample estimation of the cyclic autocorrelation matrix $\mathbf{R_{xx}}$. Even small perturbations

in the estimation of the noise matrix may cause large errors in the inverse of the cyclic autocorrelation matrix $\mathbf{R_{xx}}^{\alpha}$.

Biedka's solution to this problem is to constrain the weight vector to lie in the signal subspace by using a low rank approximation to $\mathbf{R_{xx}}$ [5]. Simulations by Biedka show that the Subspace constrained SCORE algorithms exhibit significant improvements in convergence rates, compared to the standard SCORE algorithms.

The drawback to this approach is the relatively high complexity with directly computing the eigen value decomposition of the signal space which is of order $O(J^3)$. New techniques in subspace tracking may improve computational efficiency. For a brief summary of signal subspace techniques, see reference [34].

4.9.5.1 Rank-1 Power Phase SCORE Algorithm

Recent work by Rollins [34] has applied the signal sub-space method to the Phase SCORE, and has incorporated the power method technique for arriving at the signal weights in the rank $L_{\alpha=1}$ environment. In his study, Rollins shows that the asymptotic values reached by Cross-SCORE and the Power Phase SCORE are the same. The Power Phase-SCORE method is given by:

$$\mathbf{w}(1, opt) \quad = \quad g_w(t)\hat{\mathbf{R}}_{\mathbf{xx}}^{-1}\hat{\mathbf{R}}_{\mathbf{xx}^{(*)}}^{\alpha}(\tau)\mathbf{w}(t) \tag{4.81}$$

The matrix $\hat{\mathbf{R}}_{\mathbf{xx}}^{-1}$ is the signal sub-space constrained estimate of the autocorrelation of x. The major advantage of this algorithm over the Cross SCORE algorithm, is the need to adapt only one vector, which greatly reduces the complexity of the beamformer.

Chapter 5

The Modeled Channel

In this chapter, the signal model for the experimental performance evaluation will be presented based on the statistical models, and the empirical measurements discussed in previous chapters. The next section deals with a description of the algorithms that will be simulated, and an account of the different environments that will be used to test the robustness of the algorithms under different conditions.

5.1 Signal Model and Test Environment

All calculations of the signal frequencies are normalized with respect to the sampling frequency of the system. Sampling frequencies would have to be greater than 20 MHz based on the channel spectrum proposed in Section 3.3.

The signal processing will go through several stages. The first stage will be the analogue downconversion from the Ka frequency band. The desired channel will then be frequency translated into the range of a broad band filter equal to half of the sampling frequency. This filter will eliminate distortion due to aliasing during the digital conversion as well as removing undesired signals from the waveform. These steps will not be simulated in this thesis. A whitening filter may be necessary at this stage to whiten the coloured noise generated by the broad band filter. Figure 5.1 shows the stages of the above steps. From this point on, the processing will depend upon the proposed beamforming algorithm.

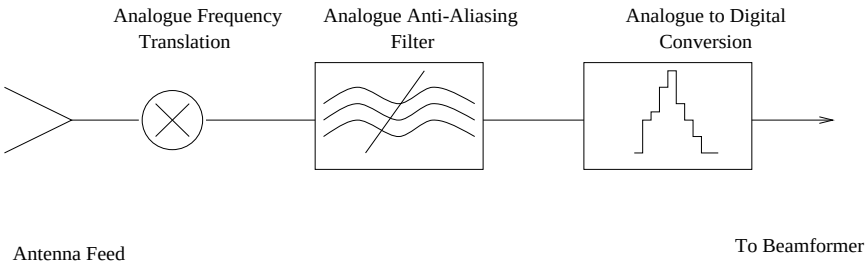

Figure 5.1: Signal Processing before Beamforming

It is important to remember that the offset frequency of the carrier must not be removed during frequency translation. This would remove the characteristic cyclic frequency of the signal needed for the beamforming algorithms. Figure 5.2 graphically illustrates the conversion in the frequency domain.

5.1.1 Binary Phase Shift Keying

The signal method chosen was Binary Phase Shift Keying. It was selected for a variety of reasons, the first of which is its simplicity for decoding. The antipodal nature of the signal constellation also provides the greatest signal distance between different symbols, which will reduce the probablily of error in a high noise environment. The BPSK format provides cyclostationarity at self-coherent frequencies at baud rate multiples, and at a unique conjugate self-coherence frequency at $2f_c$. Simulations were run using the conjugate self-coherent technique [2] [34]. This will allow offset frequencies to be assigned to different channels, and will allow these frequencies to be used in the cyclostationary beamforming algorithms.

The cyclic signal strength parameter generated using conjugate self-coherent technique produces a temporal cyclic correlation coefficient of unity. In contrast, cyclostationary frequencies which are multiples of the baud rate produce temporal cyclic correlation coefficients of $1/6$. This smaller value results in a much slower convergence rate than for the offset carrier case [34]. Furthermore, assigning signals different baud rates for identification purposes would greatly increase the complexity of the receiver in signal recovery, and would not allow the convenience of frequency translation in

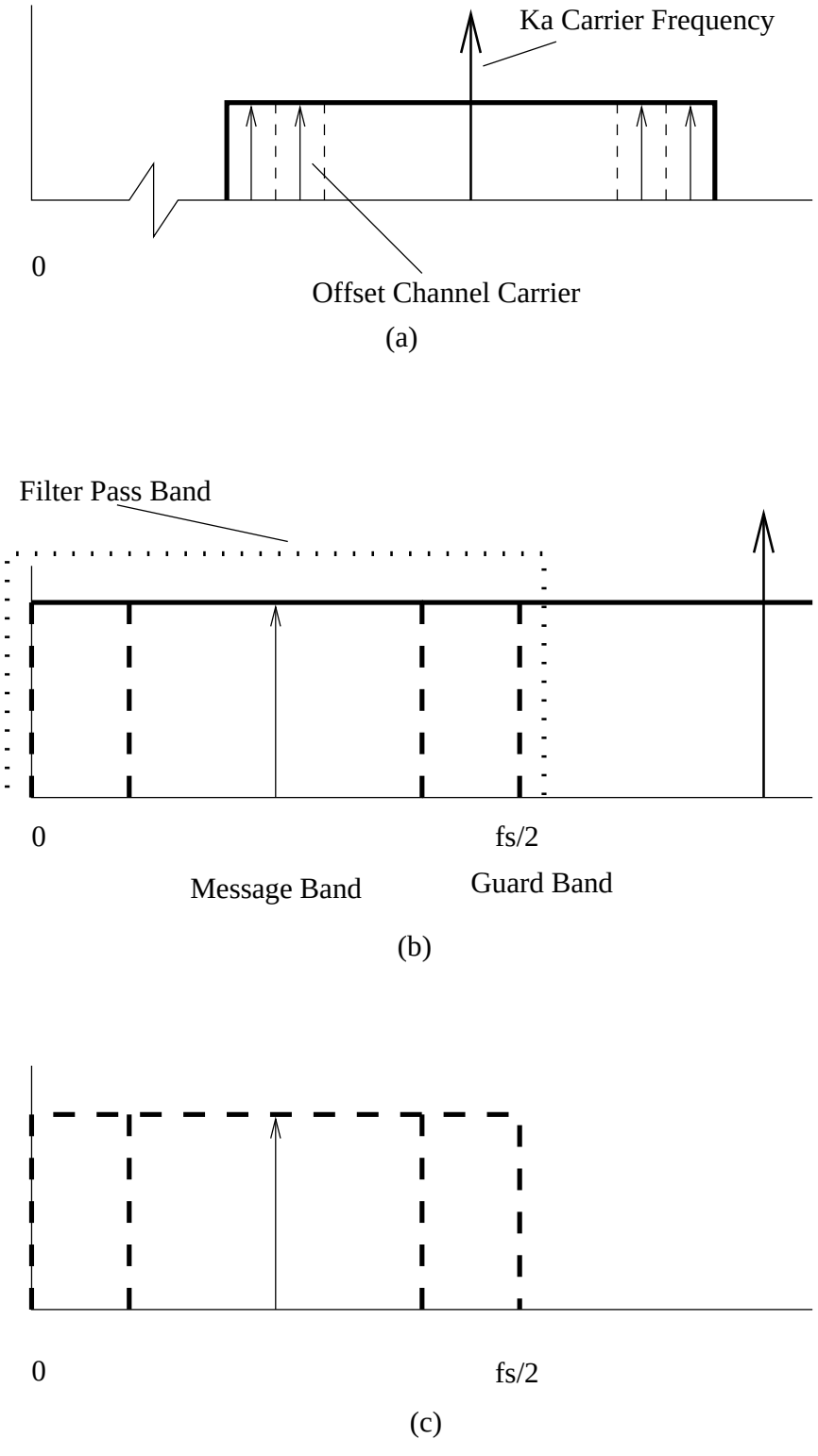

Figure 5.2: a) Signal spectrum at the Ka Band. b) Analogue down conversion of desired channel to the wide band anti-aliasing filter. c) Digitally sampled spectrum of the desired channel.

positioning the desired channel for the anti-aliasing filter.

A detailed derivation of the calculation of the cyclic spectra of BPSK and other modulation schemes are reported in [16].

5.1.2 Raised Cosine Pulse Shaping

The raised cosine pulse was chosen for pulse shaping [32]:

$$p(t) = \frac{sin(\pi t/T_p)}{\pi t/T_p} \frac{cos(\beta \pi t/T_p)}{1 - 4\beta^2 t^2/T_p^2} \tag{5.1}$$

$p(t) \Rightarrow$ pulse waveform as a function of time.

$T_p \Rightarrow$ pulse period.

$\beta \Rightarrow$ percent roll off factor.

The excess bandwidth was selected at 100 %. This value was chosen because at the Ka frequency band, bandwidth is not a limiting factor in the system design. The 100 % bandwidth selection makes the system more robust to sampling jitter and intersymbol interference effects. These robustness considerations are not directly investigated in this thesis.

In the simulations, the pulses were computed over 5 signal periods. This number was selected as a compromise between computational speed for the simulation, as well as in providing sufficient accuracy in channel modeling.

5.1.3 Array Configuration

Two types of arrays were investigated. The first array was a five-element linear array, with half-element spacing. This geometry was chosen for its simplicity in calculation of the array response vector for any given direction of arrival. This basic model allowed for easy verification of the output of the beam weights produced by the various algorithms.

In the second array, a multiple-feed parabolic reflection antenna was calculated using the dimensions of the antenna calculated in Section 2.2. A feed matrix was then simulated using a parabolic array response program [11]. The target location on the earth was selected to have a longitude of 53 degrees, and a latitude of 47.5 degrees. This corresponds to the worst case location in the coverage area as calculated in Section 2.6.

A 5-element array was used for the purpose of beamforming on the parabolic antenna. The earth coordinates of the target corresponded to 1.1λ in the x-direction, and -8.9λ in the y-direction on the satellite feed plane. The method for the calculation of the feed location may be referenced in the Appendix F The geometry of the remaining 4 points were spaced one wavelength apart in a square pattern around the center point. The one wavelength spacing was selected to satisfy the requirements of Section 2.3.6.

The geometry of the selected locations are presented in the Table 5.1

5.1.4 Complex Gaussian Noise Model

An additive white Gaussian noise model was used in the channel simulation. White noise was considered the best model for the representation of the system noise which primarily was a result of atmospheric conditions, and thermal radiation from the earth and the satellite system. The noise vector was generated using a Gaussian distributed envelope of various noise power levels. The phase of the generated points were evenly distributed between 0 and 2π. The noise at each antenna element was considered independent and identically distributed.

Feed #	x-plane Coordinate λ	y-plane Coordinate λ
1	0	-9
2	1	-10
3	-1	-10
4	1	-8
5	-1	-8

Table 5.1: Feed locations for the Parabolic Antenna array simulation

Based on the calculation of the satellite link budget presented in Table 3.2, the noise power was found to be -200.94 dBW at 20 GHz, and -201.73 dBW at 30 GHz. This resulted in a SNR value of -51.91 dB for the 20 GHz downlink, and 64.8 dB for the 30 GHz uplink including the parabolic antenna gain.

5.1.5 Signal Model Representation

Based on the modeling considerations presented above, the following signal model was generated for the signal received at the antenna. This signal model was presented in Equation (4.40) and is reproduced here for reference.

$$\mathbf{x}(t) = \sum_{l=1}^{L_\alpha} \mathbf{d}(\Theta_l) s_l(t) + \sum_{m=1}^{M} \mathbf{a}(\Phi) i_m + \mathbf{n}(t) \tag{5.2}$$

$$= \mathbf{D}(\mathbf{\Theta})\mathbf{s}(t) + \mathbf{A}(\mathbf{\Phi})\mathbf{i}(t) + \mathbf{n}(t) \tag{5.3}$$

5.1.6 SINR Calculation, and Optimal Beamforming SINR

The equation for the SINR is calculated based on the above model [11]

$$SINR = \frac{\sigma_d^2 \cdot \|\mathbf{w}^\dagger \mathbf{d}(\Theta)\|^2}{\mathbf{w}^\dagger \mathbf{A}(\mathbf{\Phi}) \mathbf{R_{ii}} \mathbf{A}^\dagger(\mathbf{\Phi}) \mathbf{w} + \sigma_n^2 \|\mathbf{w}\|^2} \tag{5.4}$$

$\sigma_d^2 \Rightarrow$ desired signal power

$\sigma_n^2 \Rightarrow$ noise power

$\mathbf{A}(\mathbf{\Phi}) \Rightarrow$ interference array matrix

$\mathbf{d}(\Theta) \Rightarrow$ desired signal direction vector

$\mathbf{w} \Rightarrow$ beamforming weight vector

$\mathbf{R_{ii}} \Rightarrow$ interference correlation matrix

To compare the performance of the beamformers, the optimal SINR of the message signal was calculated in closed-form with the known interference direction and noise power parameters without filtering. Using these known values, the autocorrelation matrix $\mathbf{R_{xx}}$ was calculated using the following steps:

The IID white Gaussian noise component of $\mathbf{R_{xx}}$ was calculated resulting in the following matrix.

$$\begin{bmatrix} \sigma_n^2 & 0 & 0 & \rightarrow & 0 \\ 0 & \sigma_n^2 & 0 & \rightarrow & 0 \\ 0 & 0 & \sigma_n^2 & 0 & 0 \\ \downarrow & & & & \\ 0 & 0 & \rightarrow & 0 & \sigma_n^2 \end{bmatrix} \tag{5.5}$$

Next, the component of the autocorrelation of the desired signal was calculated based on the known phase delays of the relative elements. This resulted in the complex matrix below.

$$\begin{bmatrix} \sigma_d^2 & \sigma_d^2 e^{j2\pi(\theta_1-\theta_2)} & \sigma_d^2 e^{j2\pi(\theta_1-\theta_3)} & \rightarrow & \sigma_d^2 e^{j2\pi(\theta_1-\theta_j)} \\ \sigma_d^2 e^{j2\pi(\theta_2-\theta_1)} & \sigma_d^2 & \sigma_d^2 e^{j2\pi(\theta_2-\theta_3)} & \rightarrow & \sigma_d^2 e^{j2\pi(\theta_2-\theta_j)} \\ \sigma_d^2 e^{j2\pi(\theta_3-\theta_1)} & \sigma_d^2 e^{j2\pi(\theta_3-\theta_2)} & \sigma_d^2 & \rightarrow & \sigma_d^2 e^{j2\pi(\theta_3-\theta_j)} \\ \downarrow & & & & \\ \sigma_d^2 e^{j2\pi(\theta_n-\theta_1)} & \sigma_d^2 e^{j2\pi(\theta_n-\theta_3)} & \rightarrow & \sigma_d^2 e^{j2\pi(\theta_n-\theta_{j-1})} & \sigma_d^2 \end{bmatrix} \tag{5.6}$$

Finally, the interference matrix was calculated in the same manner as for the desired signal except the phase offsets were scaled by the difference in wavelength which resulted from the different carrier frequency. This is indicated by the ϕ' notation where ϕ is the direction of arrival of the interferer. Only one interferer was considered.

$$\begin{bmatrix} \sigma_i^2 & \sigma_i^2 e^{j2\pi(\phi_1'-\phi_2')} & \sigma_i^2 e^{j2\pi(\phi_1'-\phi_3')} & \rightarrow & \sigma_i^2 e^{j2\pi(\phi_1'-\phi_j')} \\ \sigma_i^2 e^{j2\pi(\phi_2'-\phi_1')} & \sigma_i^2 & \sigma_i^2 e^{j2\pi(\phi_2'-\phi_3')} & \rightarrow & \sigma_i^2 e^{j2\pi(\phi_2'-\phi_j')} \\ \sigma_i^2 e^{j2\pi(\phi_3'-\phi_1')} & \sigma_i^2 e^{j2\pi(\phi_3'-\phi_2')} & \sigma_i^2 & \rightarrow & \sigma_i^2 e^{j2\pi(\phi_3'-\phi_j')} \\ \downarrow & & & & \\ \sigma_i^2 e^{j2\pi(\phi_n'-\phi_1')} & \sigma_i^2 e^{j2\pi(\phi_j'-\phi_3')} & \rightarrow & \sigma_i^2 & \sigma_i^2 e^{j2\pi(\phi_j'-\phi_j')} \end{bmatrix} \tag{5.7}$$

These three matrices were summed and inverted. The resulting $\mathbf{R_{xx}}^{-1}$ was substituted into Equation (4.50) along with the known desired signal direction to produce

the optimal beam forming weights.

5.2 Performance Evaluation Parameters

Several different test scenarios were chosen to compare the new techniques under different conditions. The default environment and algorithm parameters which were selected for the different test conditions are presented in Table 5.2. Table 5.3 is a list of the variable test condition values. The test conditions are outlined below.

Total Number of Samples	2^{14}
Number of Samples/$\mathbf{R_{xx}}^{\alpha}$	2^{7}
Number of Symbols	3276
Number of Elements	5
# of Power Method Iterations	50
% Raised Cosine	100
# of Pulse Overlap Periods	5
Carrier Signal Magnitude	1 V
Offset Frequency of Carrier (Normalized)	.25 Hz
Interference Magnitude	1
Message Signal Period (Normalized)	.2 Hz

Table 5.2: Default Simulation Parameters

5.2.1 Gaussian Noise Level Test Scenario

In this test, the noise power of the environment is altered while the other test conditions remain the same. The purpose of this test was to compare the performance of different algorithms under different noise levels. This is considered the most critical test environment.

Interference Frequency	$(f_c - 10^{-4})$, $(f_c - 5 \cdot 10^{-4})$ $(f_c - 10^{-3})$, $(f_c - 15 \cdot 10^{-3})$
Band Pass Filter Width (Normalized)	0.4, 0.3, 0.2, 0.1, 0.05
Carrier Jitter Deviation Variance	10^{-8}, $2.5 \cdot 10^{-7}$, 10^{-6}, $2.5 \cdot 10^{-5}$
Noise Vector Magnitude (Parabolic)	36.3, 40.4, 43.2, 45.3, 47.0, 48.5, 49.7, 51.7, 52.6
Noise Vector Magnitude (Linear)	0, 12.0, 18.1, 21.6, 24.1, 26.0, 27.6

Table 5.3: Variable Simulation Parameters

5.2.2 Interference Test Scenario

Interference is not considered to be a crucial performance measure in the noise limited environment of the satellite channel. It has been included to get an idea of the effect an interferer would have on the algorithm. The variable which is altered in this test is the frequency of the interferer. The interference to noise ratio (INR) for the simulations were 0 dB.

5.2.3 Carrier Frequency Jitter

The crucial property of the received signal is the offset carrier frequency. It is possible that this tone may be corrupted through several mechanisms. This may include jitter in the transmitter/ receiver oscillator, or as a result of weather conditions. The effect of an error in the carrier frequency has not been investigated in any of the literature produced to date. The frequency jitter is generated by selecting a variance level for a Gaussian distribution. This distribution is added to the frequency of the sinusoidal component of the received message. Different variances are tested and compared. A more realistic method of testing this condition would be modeling the jitter in terms of a drift of the carrier frequency. This may result from thermal fluctuations of the oscillator, and is the most common mechanism of jitter. This was not attempted in this thesis. The received signal is modified as follows:

$$s(t_j) = m(t_j)e^{(j2\pi(f_c+\sigma_j)t_j)}; \tag{5.8}$$

$s(t) \Rightarrow$ transmitted signal

$m(t) \Rightarrow$ message signal

$\sigma_j \Rightarrow$ Gaussian jitter frequency distribution

5.2.4 Offset Frequency Error Test

In this test scenario the offset frequency of the carrier is miss-matched with the receiver cyclic frequency. In this case the desired signal is seen as an interferer. The longer the convergence time, the greater the chance of rejection of the desired signal by the beamforming algorithm. It is likely that the satellite and receiver oscillators will be slightly different, therefore this test is seen as fairly significant in determining the application of the cyclic algorithms to the satellite environment. One method proposed by [2] to minimize the effect of frequency mismatch, is to weight the significance of the received data points in calculating the cyclic correlation matrix $\mathbf{R_{xx}}^{\alpha}$ based upon the time that the sample is received. The problem with this technique in the satellite environment is that long correlation times are needed to reject the high noise level, and by weighting the data, the necessary level of noise rejection may not be possible.

5.2.5 Filter Bandwidth Test

The variable in this test scenario is the bandwidth of the front-end filter. This test examines the effect of the distortion of the received signal which is caused by the filter on the beamforming algorithm under different noise levels, and different filter band widths to determine whether it is worth optimizing the bandwidth.

5.2.6 Simulation Test Environment Conditions

Four basic test environments were chosen to characterize the performance of the algorithms. Single interferers were used in the interference tests. The variables in each environment are listed below for reference:

Test Condition	Default Noise Power Parabolic (dB)	Default Noise Power Linear (dB)	Default Bandwidth	Notes
LNNB	40.4	12.0	.05	
LNWB	40.4	12.0	.2	Filtering not tested
HNNB	47.0	21.6	.05	Filtering not tested
HNWB	47.0	21.6	.2	Noise not tested

Table 5.4: Test Environments for Beamforming Techniques

Where the above acronyms represent:

LNNB $\Rightarrow$ Low Noise Narrow Band

LNWB $\Rightarrow$ Low Noise Wide Band

HNNB $\Rightarrow$ High Noise Narrow Band

HNWB $\Rightarrow$ High Noise Wide Band

Chapter 6

Cyclostationary Beamforming with Broadband Front End Filtering, and Array Response Estimation

Two novel techniques are introduced for the purpose of beamforming in a high noise environment. The first of which is front end filtering the received signal before beamforming to reduce the magnitude of the noise power. The second technique investigated uses the time lag between array elements to calculate the array response of the system. Array response estimation is expected to reduce the time to convergence of the algorithms.

6.1 Front End Filter Motivation

As demonstrated in Table 3.2, the Ka broadband satellite system is a noise-limited environment. This places a different emphasis on beamforming algorithms than in in the case of interference limited environments. Preliminary calculations using the large gain of a parabolic antenna indicate that a large amount of power or gain from the earth station (up to 74.86 dB, Table 3.2) would be required to produce a SINR ratio sufficiently strong to provide a reliable link in most weather conditions. (i.e. an outage rate of 0.01 %)

The literature to date has focused on cyclic beamforming environments where the system is interference limited and the relative SINR is high, typically 0 - 20 dB. These systems were applied to lower frequency earth based applications where there is interference from other systems, or in multi-path environments.

Filtering was considered as a method to reduce the noise in the system. The FRESH filtering technique employs cyclostationarity (Section 4.7) but is mainly designed for eliminating interference in the system. It is also computationally expensive.

We propose basic front end digital filtering for the Ka satellite environment, in combination with beamforming. Cyclostationarity works on the principle of rejecting frequencies which are not equal to the cyclic frequency α. The algorithm's ability to reject other frequencies is dependent on the relative power of the desired signal and the interference.

In Section 5.1.1 the cyclic frequency will be chosen to be twice the conjugate of the offset frequency of the channel of interest. Since this is the only signal parameter upon which the cyclic beamforming algorithms depend, all the other frequencies of the received signal may be attenuated for the purpose of beamforming. This includes the signal information as well as noise and interference. Only the carrier component must be preserved at each antenna element. Once the beamforming weights are calculated, they may be applied to the unfiltered signal, yielding the beamforming gain. A sketch of this technique in the frequency domain is presented in Figure 6.1.

Front end filtering may be seen as a method of altering the noise subspace of the system. From this perspective, the front end filter reduces the magnitude of the frequency components in the noise sub-space while leaving the signal sub-space ideally unaffected.

Front end filtering avoids the need for eigenvalue decomposition or detailed knowledge of the noise environment and may offer a simple method of improving cyclostationary beamforming algorithms.

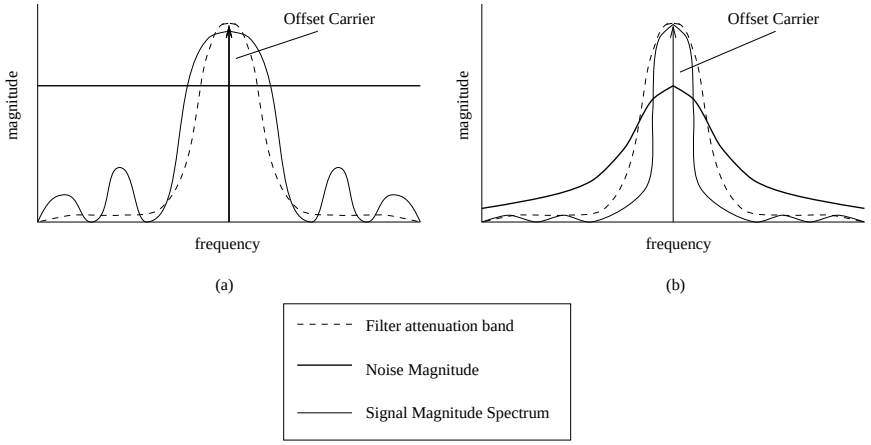

Figure 6.1: a) Received waveform magnitude before filtering b) Received waveform magnitude after filtering

6.2 Filtering Effect on Cyclic Spectral Correlation

The effect of filtering on a cyclic signal is presented below in the frequency domain in terms of the spectral correlation of a signal. The calculation of the spectral correlation is related to the cyclic autocorrelation calculation (Section 4.6), which is directly related to the performance of cyclic beamforming algorithms (Section 4.9). The presentation of the derivation relies on concepts presented in Section 4.

The following models will be used throughout this chapter.

$$x_l(t) = s(t, f_c)e^{j\psi_l} + \sum_k i_{l|k}(t)e^{j\varrho_l} + n(t) \tag{6.1}$$

where $x_l(t)$ is the received signal from antenna element l. The terms ψ_l and ϱ_l are the corresponding array phase factors which effect the desired and interference signals, respectively. The interference is modeled as being deterministic sinusoids with frequencies $f_k \neq f_c$ where f_c is the offset carrier frequency of the desired signal ($L_\alpha = 1$ signal environment, Section 4.9.1). Interference terms are identical in magnitude such that $|I_k| = |I|$. The white noise is represented by $n(t)$. It has an independent Gaussian distributed magnitude $\mathbf{N}(t)$ with mean $\mu_{n_*} = 0$ and variance $\sigma^2_{n_*n_*}$, and an independent uniformly distributed phase $\xi(t)$ from $[-\pi, \pi]$ over all frequencies. The signal model definitions are summarized below:

$$s(t, f_c) = |A_{sig}|e^{j2\pi f_c t} \tag{6.2}$$

$$i_k(t, f_k) = |I|e^{j2\pi f_k t} \tag{6.3}$$

$$n_l(t, f) = |\mathbf{N}_l(t, f)|e^{j\xi_l(t)} \tag{6.4}$$

The filtered signal $v(t)$ is obtained by convolving the received signal $x(t)$ by the filter $h(t)$.

$$v_l(t) = h(t) \otimes x_l(t) \tag{6.5}$$

$$h(t) = \int_{-\infty}^{\infty} |H(f)| e^{j\chi(f)} e^{j2\pi ft} df \tag{6.6}$$

$$\tag{6.7}$$

The filter parameters are bounded in the following manner.

$$|H(f)| = \begin{cases} |A_{filt}| < 1 & f \neq f_c \\ 1 & f = f_c \end{cases} \tag{6.8}$$

$$\tag{6.9}$$

To show the mechanism of how the cyclic correlation process works, the spectral content of the signal is calculated for the frequency ζ [15]. The signal is represented in terms of its finite-time Fourier transform shown below:

$$V_{l|T_{FA}}(t,\zeta) \triangleq \int_{t-T_{FA}/2}^{t+T_{FA}/2} v_l(u) e^{-j2\pi\zeta u} du \tag{6.10}$$

The term T_{FA} is the is the Fourier averaging time period. Two spectral components at frequencies $\zeta = f+\alpha/2$ and $\zeta = f-\alpha/2$ from arbitrary antenna elements can be correlated by integrating over the correlation averaging time $\triangle t$, and normalizing each signal by $\sqrt{T_{FA}}$. Here, f is the midpoint between the frequency separation α [15].

$$S^{\alpha}_{v_l v_k|T_{FA}}(f)_{\triangle t} \triangleq \frac{1}{\triangle t} \int_{-\triangle t/2}^{\triangle t/2} \frac{1}{\sqrt{T_{FA}}} V_{l|T_{FA}}(t, f+\alpha/2) \cdot \frac{1}{\sqrt{T_{FA}}} V^{*}_{k|T_{FA}}(t, f-\alpha/2) dt \tag{6.11}$$

The ideal spectral correlation coefficient may be found by letting the limit of $\triangle t \to \infty$ and $T_{FA} \to \infty$.

$$S^{\alpha}_{v_l v_k}(f) \triangleq \lim_{T_{FA}\to\infty} \lim_{\triangle t\to\infty} S^{\alpha}_{v_l v_k|T_{FA}}(f)_{\triangle t} \tag{6.12}$$

The order of the limit is important. As $\triangle t \rightarrow \infty$ all random terms are averaged to their mean value. As $T_{FA} \rightarrow \infty$, the Fourier integral results in the rejection of all frequencies except for $f = \zeta$.

If the order of the limit is changed, the limit $T_{FA} \rightarrow \infty$ would decompose the signal $v_l(t)$ into a discrete summation of Fourier components in the time domain or Dirac delta functions in the frequency domain. The continuous time correlation does not exist for discrete models when $\triangle t < \infty$ [16].

Figure 6.2 shows the basic processing blocks for the calculation of the cyclic correlation matrix. The signal is received from the antenna, then downconverted. The signal is time averaged to remove the random components, then is Fourier transformed at the cyclic frequency. This step removes all non-random interference. The final processing step combines signals from other antenna elements for the calculation of the cyclic correlation matrix which is used by the beamforming algorithm to calculate the beamweights.

The following sections will investigate how the pulse shape effects the signal model in the calculation of the cyclic correlation matrix. A discrete time model will be used to illustrate the effects of filtering on the signal. Limiting conditions with respect to the filter bandwidth, and time averaging will be presented. Finally, the implications of these findings will be summarized.

6.2.1 Unfiltered Noise Sample Model

For unfiltered time averaging, the signal waveform is periodically sampled. The ideal noise samples consist of uncorrelated delta functions of random Gaussian amplitude and uniformly distributed phase in the time domain. In the frequency domain, the signal has a constant noise power over all frequencies. The phase of the noise power is zero. This is shown in Figure 6.3.

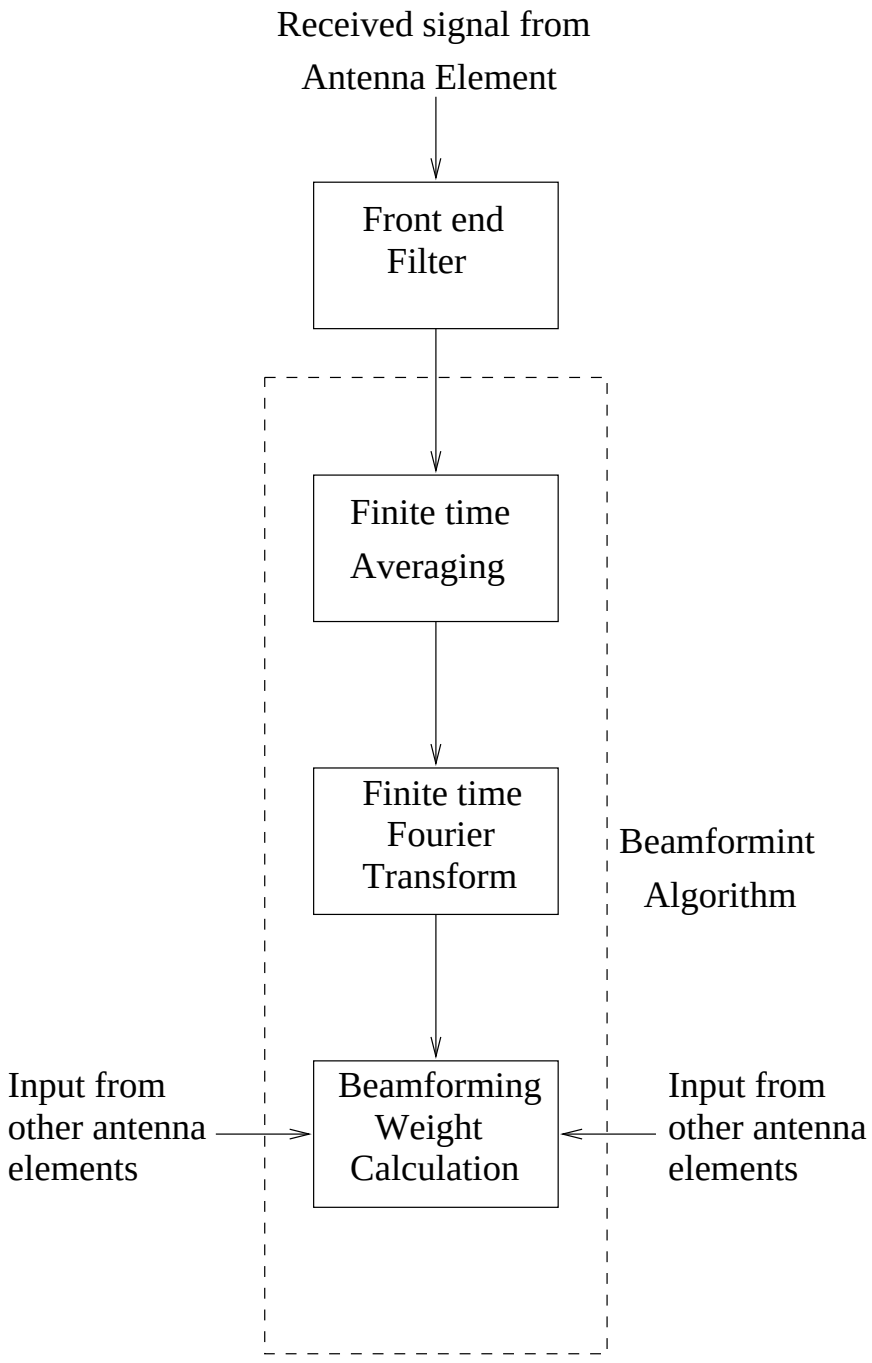

Figure 6.2: Processing Steps for Beamforming

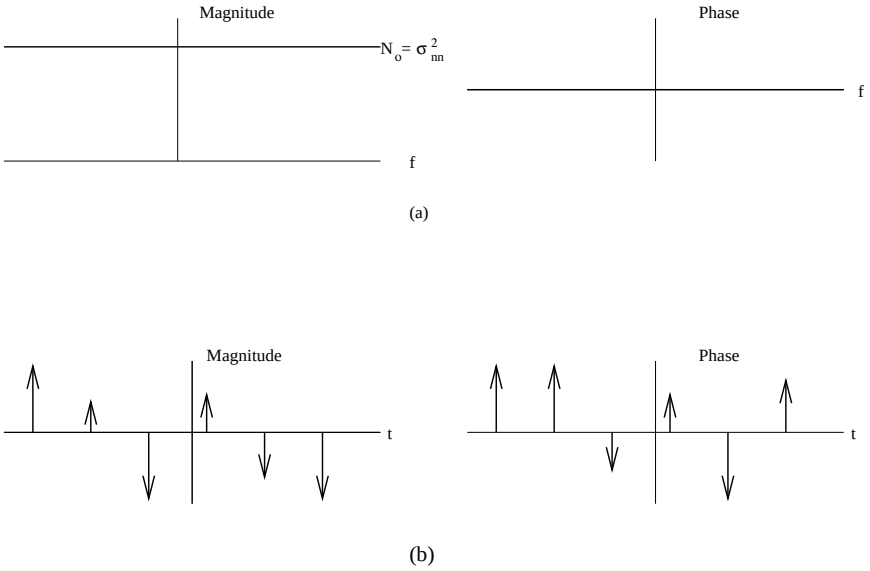

Figure 6.3: a) Frequency Domain of the Noise Variance. b) Time Domain of Noise Samples.

6.2.2 Ideal Filter Model

Equations for the ideal filter in the time and frequency domain are presented below [19]:

$$|H(f)| = \begin{cases} |A_{filt}| = 1 & W - f_c < |f| < W + f_c \\ 0 & \text{otherwise} \end{cases} \tag{6.13}$$

$$\chi(f) = \begin{cases} 2\pi t_o(f) & W - f_c < |f| < W + f_c \\ 0 & \text{otherwise} \end{cases} \tag{6.14}$$

$$h(t) = 2W sinc(2W(t - t_o)) \tag{6.15}$$

A diagram of the ideal filter pulse is shown in Figure 6.4.

6.2.2.1 Amplitude Distortion

The ideal filter is modeled as being uniform with zero attenuation in the passband from $-W \rightarrow W$ in the frequency domain. The Fourier transform for this pulse is the $sinc(u) = \sin(\pi u)/\pi u$ pulse.

6.2.2.2 Ideal Phase

The ideal phase response of the filter consists of an angle which is a linear function of the frequency. In the time domain this represents a time delay which is related to the slope of the phase in the frequency domain.

6.2.2.3 Ideal Filter Impulse Response

The time domain representation of the Fourier transform of the ideal filter is shown in Figure 6.4 (c). This sketch shows the pure time delay which results from the ideal phase. The $sinc(u)$ pulse is a consequence of the constant attenuation in the filter passband.

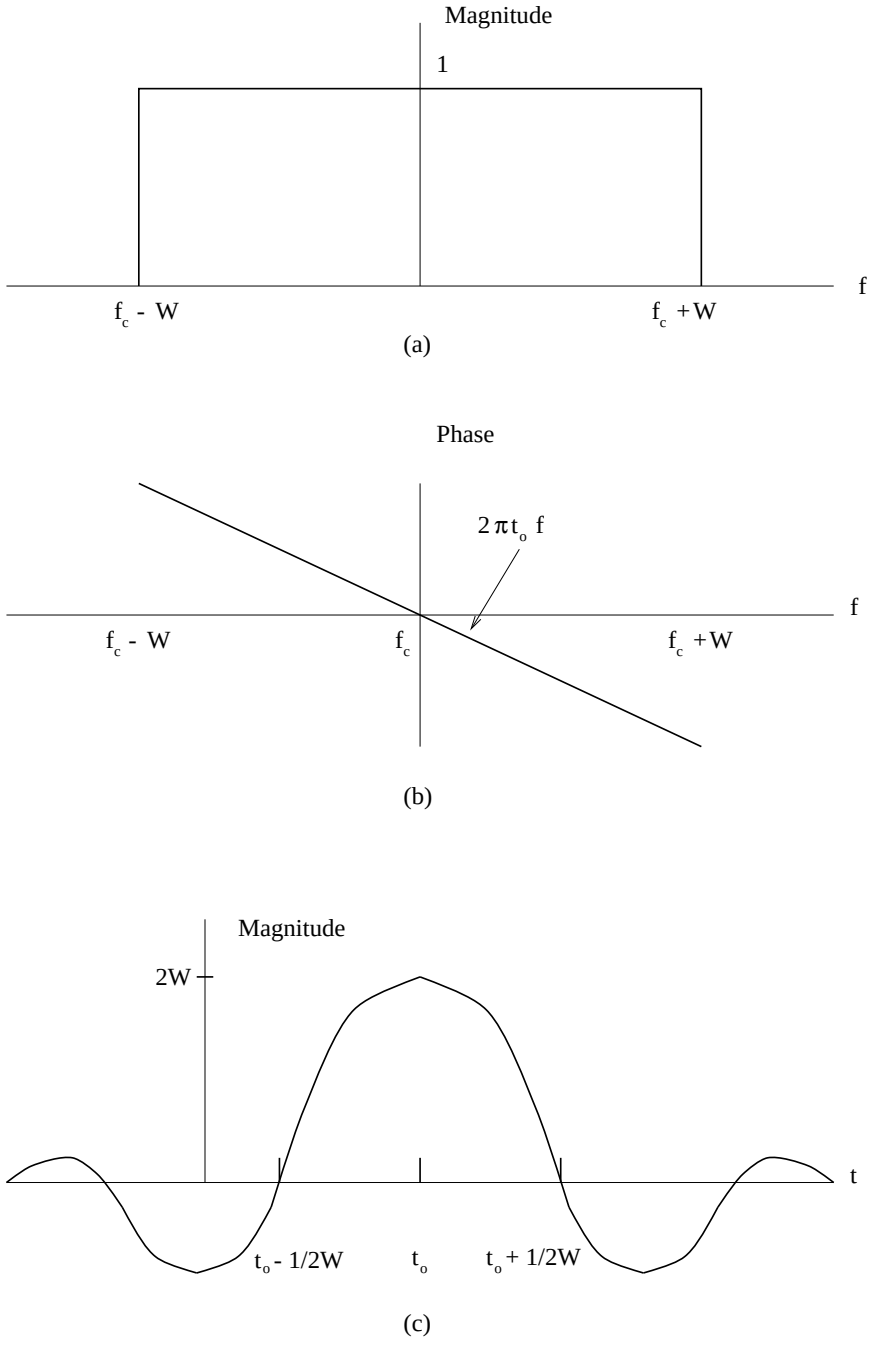

Figure 6.4: a) Frequency domain magnitude of an ideal filter pulse. b) Frequency domain phase of an ideal filter pulse. c) Time domain impulse response of an ideal filter.

6.2.3 Non-Ideal Filter Model

The effect of a non-ideal filter was derived to see how this changed the rate of convergence of the cyclic correlation calculation. The amplitude and phase in the frequency domain of the non-ideal filter are modeled as follows:

$$|H(f)| = \begin{cases} |A_{filt}| = 1 & W - f_c < |f| < W + f_c \\ 0 & \text{otherwise} \end{cases} \tag{6.16}$$

$$\chi(f) = \begin{cases} 2\pi t_o + b\sin(\pi/Wf) & W - f_c < |f| < W + f_c \\ 0 & \text{otherwise} \end{cases} \tag{6.17}$$

6.2.3.1 Amplitude Distortion

As mentioned in Section 6.2 the only known frequency needed for beamforming is the cyclic frequency f_c. This single frequency can be thought of as the message bandwidth. Therefore as long as the cyclic frequency is not attenuated, there will be no amplitude distortion of the carrier frequency.

As mentioned in Chapter 4 and simulated in [34], the cyclic temporal correlation coefficient depends on the magnitude of the cyclic correlation frequency α. This quantity in turn controls the convergence rate of the beamforming algorithm. A non-uniform amplitude attenuation which meets the condition of Equation 6.8 would have the positive effect of further attenuating the non-cyclic frequencies as compared to the ideal filter model. The ideal filter frequency magnitude is a worst-case filter amplitude scenario and is used for this derivation due to its simplicity in calculation.

6.2.3.2 Non-Ideal Phase

The effect of a non-ideal filter phase was investigated based on the model presented by [19]. The phase is shown in Figure 6.5 (b). The equation of the phase as a function of the frequency is shown in Equation 6.17. Here the constant b is assumed small such that the first order approximation $e^{j(b\sin(\pi/Wf))} = 1 + b\sin(\pi/Wf)$ is valid.

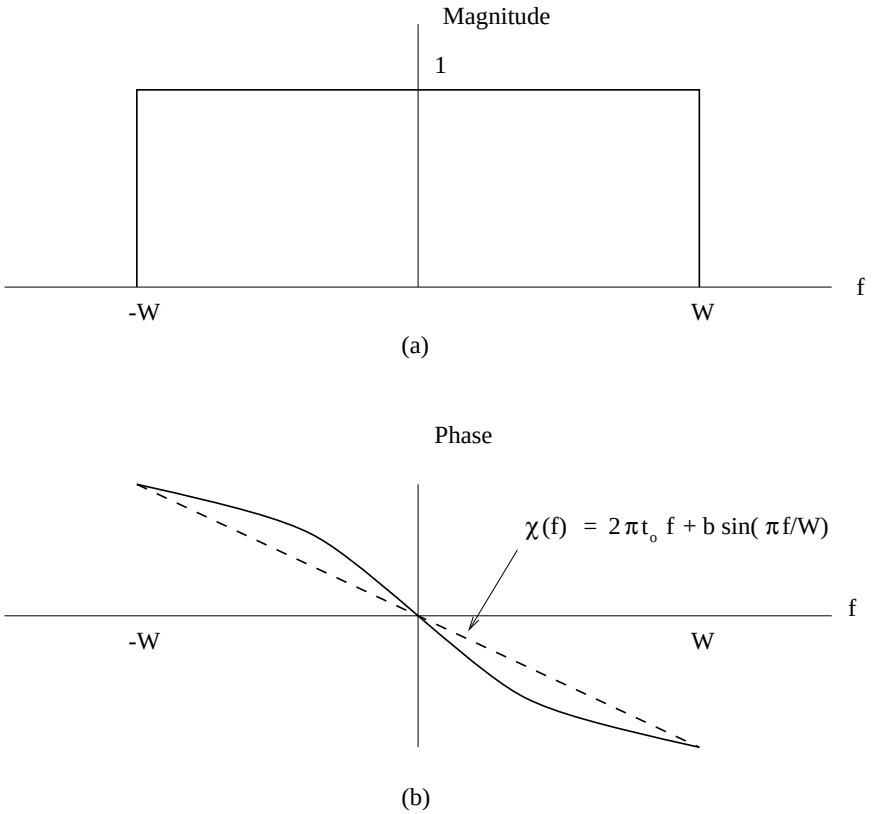

Figure 6.5: a) Frequency domain magnitude of an non-ideal filter. b) Frequency domain phase of an non-ideal filter.

6.2.3.3 Filter Impulse Response

The Fourier transform of the non-ideal pulse based on Equation 6.2.3.2 is derived as:

$$\begin{aligned} h(t) &= 2W sinc(W(t-t_o)) + \\ &\quad bW[sinc(2\pi(Wt+1/2)) + sinc(2\pi(Wt-1/2))] \end{aligned} \tag{6.18}$$

A time domain sketch of this pulse is shown in Figure 6.6 and 6.7. In comparison to the ideal filter pulse, the non-ideal phase results in a wider overall signal in the time domain.

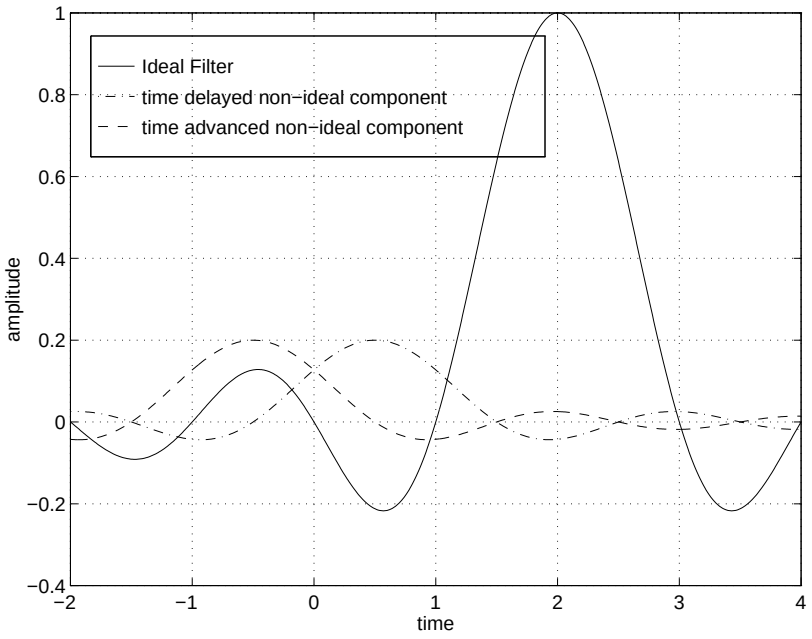

Figure 6.6: Components of a filter with non-ideal phase response

6.2.4 Time Averaging Computation

The purpose of time averaging is to eliminate the random components of the received signal. Equation 6.1 models the random noise signal in terms of two independent processes, the zero Gaussian mean and the zero mean uniformly distributed phase. These two processes are ergodic [32].

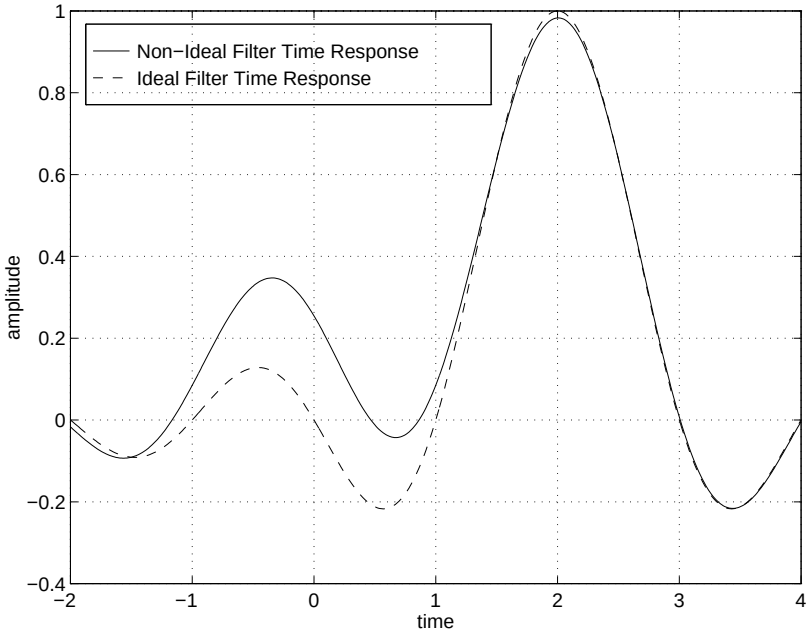

Figure 6.7: Comparison of a ideal and non-ideal filter pulse in response showing pulse widening.

6.2.4.1 Independent Time Samples

For the calculation of independent time samples, the time averaged mean may be found by [32]:

$$\overline{\mu} = \lim_{\triangle t \to \infty} \frac{1}{N_{\triangle t}} \sum_{i=1}^{N_{\triangle t}} x_i \tag{6.19}$$

$$= \mu \tag{6.20}$$

where μ is the sample mean and $N_{\triangle t}$ is the number of noise samples. The rate of convergence to the true mean is $1/N_{\triangle t}$.

The unbiased sample variance of independent signals for an unknown mean can be estimated as [32]:

$$\overline{\sigma^2_{n_l n_l}} = \frac{1}{(N_{\triangle t - 1})} \sum_{i=1}^{N_{\triangle t}} \sigma^2_{n_l n_l | i} \tag{6.21}$$

6.2.4.2 Correlated Time Samples

When the time samples are correlated, the time to convergence is affected by a factor which depends on the amount of correlation among the samples:

$$\Upsilon_{N_{\triangle t},K} \stackrel{\triangle}{=} \sum_{i=0}^{N_{\triangle t}} \sum_{k=-K}^{K} |v_c(i-k)| \tag{6.22}$$

$$\overline{\mu} = \frac{1}{N_{\triangle t}} \sum_{i=0}^{N_{\triangle t}} \sum_{k=-K}^{K} v_c(i-k) x_k \tag{6.23}$$

$$< \frac{\Upsilon_{N_{\triangle t},K}}{N_{\triangle t}} \sum_{i=0}^{N_{\triangle t}} x_i \tag{6.24}$$

where $\Upsilon_{N_{\triangle t},K}$ is the correlation coefficient sum, $2K$ is the correlation period, and $v_c(i-k)$ is the correlation between time samples i and k.

The time averaged term $\overline{\mu}$ will converge almost surely to the true mean μ in the limit as $\triangle t \to \infty$ if $\Upsilon_{N_{\triangle t},K}$ is finite.

A similar calculation may be performed for the variance of the correlated time samples which shows:

$$\overline{\sigma^2_{n_l n_l}} \quad < \quad \frac{[\Upsilon_{N_{\triangle t},K}]^2}{N_{\triangle t}-1} \sum_{i=1}^{N_{\triangle t}} \sigma^2_{n_l n_l|i} \tag{6.25}$$

6.2.4.3 Noise Sample Correlation Coefficient for the $sinc(u)$ Pulse

It can be shown that [18]:

$$sinc(u) \quad < \quad \frac{\gamma}{u^p} \tag{6.26}$$

where $p > 1$ and γ is a scaling constant, and the main lobe of the $sinc(u)$ pulse has finite width. If both functions are integrated, the $sinc(u)$ pulse is shown to be bounded by a monotonically decreasing function for the time period $0^+ \rightarrow \triangle ta$:

$$\lim_{\triangle t \rightarrow \infty} \int_{0+}^{\triangle t} sinc(u)du \quad < \quad \lim_{\triangle t \rightarrow \infty} \gamma \int_{0+}^{\triangle t} u^{-p} du \tag{6.27}$$

$$= \quad \lim_{\triangle t \rightarrow \infty} \frac{-\gamma}{p} u^{-p+1} \Big|_{0+}^{\triangle t} \tag{6.28}$$

$$= \quad \Upsilon_{\triangle t,K} \tag{6.29}$$

$$< \quad \infty \tag{6.30}$$

This result shows that pulses which are correlated by a $sinc(u)$ function will converge as the number of samples approaches infinity by Equation (6.24). The time to convergence of the $sinc(u)$ pulse is delayed by the factor $\Upsilon_{N_{\triangle t},K}$, and the main lobe width of the $sinc(u)$ function must be finite.

6.2.5 Effect of Filtering on Time Averaging

Section 6.2 shows that for the elimination of the random components in the cyclic autocorrelation calculation it is necessary to time average the inputs. In the limit as $\triangle t$ goes to infinity, all random components will be removed.

The filter has the effect of spreading out the input waveform in the time domain. Hence, the uncorrelated unfiltered noise becomes correlated after filtering. This reduces the effectiveness of time averaging and increases the required correlation time (Section 6.2.4.3).

Furthermore, for the case where the filter's phase response is given by Equation 6.17 , the pulse is spread out more. This is shown in Figure 6.7. The larger the deviation from the ideal phase response, the larger the pulse spread, and therefore the longer the required averaging time to reach convergence. It is important to note that as long as the main lobe of the $sinc(u)$ pulse is finite in the duration, the limit as $\triangle t \rightarrow \infty$ is not affected.

6.2.6 Effect of Filtering on the Noise Power

The fact that the noise is limited to the frequency band from $-W \rightarrow W$ for the filtered signal, reduces the noise power of the system. This increases the SNR of the input signal to the beamformer which improves the convergence rate. Simulations by [34] and [2] show that the higher the SNR value, the quicker the rate of convergence for cyclostationary beamforming algorithms.

6.2.7 Limit as the Filter Bandwidth Approaches Infinity

The effect of letting the filter bandwidth approach infinity is considered:

6.2.7.1 Effect on Filter Amplitude

As the filter bandwidth $W \rightarrow \infty$, the filter impulse response is more concentrated. In the limit, the filter impulse response becomes a delta function. This is the case for both the ideal and non-ideal filter model and is identical to the pulse of the non-filtered noise sample.

6.2.7.2 Effect on Filter Phase

The widening of the filter bandwidth will have the effect of reducing the slope of the filter phase in the frequency domain. This will result in a decrease in the time delay. For the non-ideal filter case, the distortion and the corresponding time pulse dilation will also be reduced. In the limit, the phase delay and distortion would be zero for both the ideal and non-ideal filter.

6.2.7.3 Effect on Time Averaging

When the filter bandwidth reaches infinity, the correlation of the different time samples is removed. Therefore there is no degradation in the time averaging performance of the algorithms. The resulting calculation is identical to the non-filtered scenario.

6.2.7.4 Effect on Noise Power

The broadening of the filter bandwidth results in a rejection of fewer noise frequency components. As a result the noise power increases. In the limit, the input noise power is identical to the non-filtered condition.

6.2.8 Limit as the Filter Bandwidth Approaches Zero

In this limit, the filter bandwidth is narrowed to reject all frequencies other than the offset carrier frequency needed for beamforming.

6.2.8.1 Effect on Filter Amplitude

As the filter's bandwidth becomes more narrow, the impulse response becomes more dilated in the time domain for both the ideal and non-ideal signal model. When the limit is reached, the filter signal is uniform for all time.

6.2.8.2 Effect on Filter Phase

The compression of the filter bandwidth will have the result of increasing the slope of the phase for the ideal filter response. This will result in the pulse having a longer delay.

For the non-ideal case, the phase distortion will become greater as the bandwidth decreases. Based on Equation 6.17, this corresponds to an increase in the magnitude of the constant b. As a result, the time domain response will be further dilated.

6.2.8.3 Effect on Time Averaging

For the ideal filter the dilation of the impulse response in the time domain will decrease the effectiveness of time averaging, as the correlation time among samples becomes longer. The pure phase delay will not affect the time averaging convergence rate.

In the case of the non-ideal filter, both the dilation due to the magnitude, and the dilation due to an increase in the phase distortion will degrade the effectiveness of time averaging on the reduction of the noise power.

When the filter frequency response reaches the limit $\delta(f - f_c)$ for both the filtered and unfiltered cases, the impulse response will be uniform for all values of time, and the period of the $sinc(u)$ pulse will be infinite. As a result, the random noise component at the carrier frequency will not be removed due to time averaging.

6.2.8.4 Effect on Noise Power

When the filter frequency response reaches the limit $\delta(f - f_c)$, only the noise which is present at the carrier frequency remains. As explained in Section 6.2.8.3, time averaging will not reduce this random component.

6.2.9 Finite Time Fourier Transform

The function of the finite time Fourier transform is to reject the non-random interference signals at frequencies other than the cyclic frequency. The finite time Fourier

transform acts much like a brickwall filter whose passband becomes more narrow as the averaging time increases.

With reference to Equation 6.10, the transform for the filtered signal at the cyclic frequency α after the random frequency components have been averaged to zero can be written as:

$$V_{l|T_{FA}}(\alpha) = |A_{sig}|e^{j\psi_l} + \sum_{k=1}^{K} |I||H(f_k)|e^{j\chi(f_k+\varrho_l)} sinc((\alpha - f_k)(T_{FA})) \quad (6.31)$$

The filter's effect does not alter the cyclic carrier frequency information and does attenuate the interference signals which would increase the rate of interference rejection [34]. The effect of the finite time Fourier transform can be compared to the case for ideal filtering where the filter passband narrows to a point about f_c.

It should be noted that the filter introduces a phase component to the interference signal. This would harm the performance of beamforming techniques which introduce beam pattern nulls to block out interferers. Since this thesis focuses on a noise-limited channel, such an investigation was not pursued.

6.2.10 Summary of Filtering's Effects on Beamforming

The goal of filtering is to reduce the input noise power into the beamformer under conditions where the signal environment is noise limited. The only signal criteria that must be preserved is the cyclic carrier frequency. Based on the preceding sections, the following statements can be made:

6.2.10.1 Noise Power Reduction

As shown in Section 6.2.6, the filter reduces the noise power input to the system. This noise power reduction increases as the bandwidth decreases, and in this manner increases the SNR of the signal input into the beamformer. The increase in the SNR will improve the convergence rate of the algorithm [34] [2]. The only condition on the filter magnitude is that the cyclic carrier frequency not be attenuated.

6.2.10.2 Effect of Filtering on Time Averaging

The cyclic correlation calculation is based on the principal of ergodicity. In the unfiltered condition, all time samples are modeled as being statistically independent. Therefore time averaging reduces the random signal's variance at a rate of $1/(N_{\triangle t}-1)$ for the condition of unknow phase [29]. Here, $N_{\triangle t}$ corresponds to the number of noise samples of the signal.

Filtering has the following two effects on the rate of time averaging:

- Limiting the input noise frequencies results in a $sinc(u)$ pulse shape (Section 6.2.2). The dilation of the noise samples in the time domain correlates the samples and in turn decreases the rate of convergence. It is possible that under low noise conditions, the correlation of the time samples will outweight the effects of noise power rejection. Therefore, filtering is predicted to be most beneficial in noise limited environments. This will be verified in the simulation tests.

- In the case of non-ideal filtering, the phase distortion also results in a dilation of the signal pulse (Section 6.2.3.2). The phase dilation increases as the filter bandwidth decreases the rate of convergence (Section 6.2.3.2).

6.2.10.3 Effect of Filtering on Convergence

In Section 6.2.5 it was shown that as long as the filter impulse response was finite, the effects of time averaging would reduce the random effects of the received signal, and the filtered and unfiltered signals would be the same in the limit as $\triangle t \rightarrow \infty$.

The rate of convergence depends on the trade-off between the filter's noise reduction (Section 6.2.6), and the input pulse's time dilation.

6.2.10.4 Motivation for Phase Compensation

An effective method of reducing the time dilation and improving the time averaged variance reduction is through phase compensation of the filtered signal. Since the

frequency response characteristics of the filter are known and deterministic, therefore phase compensation may be easily applied.

Phase compensation may take the form of conjugate multiplication of the filtered signal by the filter's phase response. A second method could be a time domain implementation where the filtered signal is passed through the filter with a reversed impulse response sequence to remove the time delay (Forward-Backward filtering).

6.2.10.5 Motivation for Adaptive Filtering

The trade-off between the pulse dilation and noise magnitude reduction which results from filtering indicates that there may be an optimum filter bandwidth to maximize the convergence rate which depends on the signal environment. The practicality of this adaptation would depend on the degree of convergence rate improvement, and the associated computational expense.

6.3 Cyclostationary Array Response Estimation

A parameter of the cyclic correlation matrix calculation which has not been directly investigated for beamforming applications is the delay parameter τ. The delay represents the relative time delay between two signals in the second-order cyclostationary cross-covariance.

$$R^{\alpha}_{x_r x_j}(\tau_{r,j}) \quad = \quad \langle x_r(t) x_j^{(*)}(t + \tau_{r,j}) \rangle_{\infty} \tag{6.32}$$

In the above equation x_r corresponds to the reference signal, and $\tau_{r,j}$ is the selected delay parameter.

For the special case where the signal of interest is a sine wave, this delay translates into a simple phase shift. If the delay parameters of each element could be found with respect to a single reference element of the antenna array, then the array response vector with respect to that element may be easily calculated.

It must be noted that the reference sinusoid must be one of the antenna elements of the array, not an independently generated sinusoid. This necessity arises from the fact that the array sinusoid is modulated according to some unknown bit sequency. If this message modulation is not present, the signals will not converge. This behavior was tested in simulations.

An algorithm for the estimation of the array response based on the relative delay among elements is proposed using a simple binary search algorithm. Two delay values corresponding to the start and end of the period of the offset sinusoid were chosen. The cyclic correlation was calculated for the upper and lower bound of the delays selected. A binary search algorithm was implemented. The delay resulting in the largest calculated value of the real component of the temporal correlation coefficient was selected as the next bound in the binary search.

When the exact delay factor is found, the real part of the temporal correlation coefficient is equal to 1.

The array response estimation technique proposed can be compared to several algorithms existing in the literature. It is most similar to the Phase estimation technique (Section 4.9.4) in that both algorithms use an antenna element as a reference signal to estimate the array response. The Phase algorithm uses a least squares cost function while the Array estimation technique performs a search of the time delay value which will maximize the real part of the temporal correlation coefficient.

The application of the cyclic array response estimation is to provide a method of calculating the array response of the antenna which may be updated dynamically, and which will be robust with respect to errors or component failures. Applications may also be used to finding direction of arrival for simple antenna geometries.

6.4 Front End Filtered SCORE Beamforming Techniques

Two basic beamforming algorithms were selected for application to the linear antenna array and for the parabolic antenna array in the $L_\alpha = 1$ environment. The least squares algorithm was chosen for its simplicity, and to give a lower bound on the performance of an algorithm with minimal computational complexity. The Cross-Score algorithm was selected based on its superior convergence rate. Many of the algorithms presented in literature aim at reducing the computational complexity of the Cross SCORE while maintaining the same convergence rate, or improving the algorithms in an interference environment.

The satellite environment is modeled as a slowly time-varying. This is supported by the condition that the earth station is stationary during transmission, and by the observation that changing weather patterns are not fast enough to result in quickly changing channel parameters. This allows the satellite environment the advantage of a relatively long convergence time as compared to the mobile signal environment. This long convergence time will be necessary in the time estimation of the cyclic correlation matrix in a high noise environment.

The sub-space constrained techniques were not applied. The first reason for this is the increase in computational complexity which would result. The second reason is that front end filtering is expected to reduce the effectiveness of the sub-space technique, though this has not been verified. Optimum implementation of the following algorithms in terms of computation and hardware will not be investigated in detail in this thesis. The main focus will be on the performance of the different algorithms under different conditions.

The following sections describe the implementation of various modifications of the SCORE algorithms. Figures 6.8 and 6.9 give a graphic representation of these schemes.

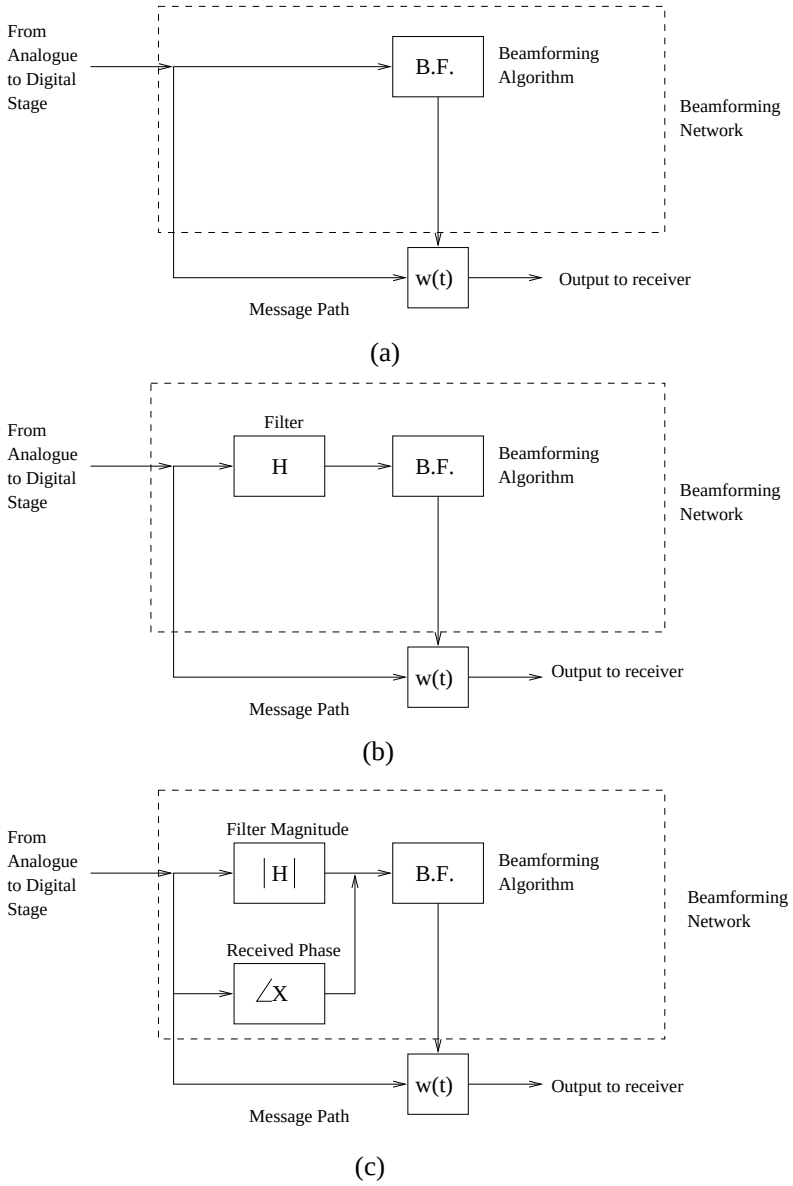

Figure 6.8: a) SCORE beamforming implementation b) F-SCORE beamforming implementation c) PC-SCORE beamforming implementation

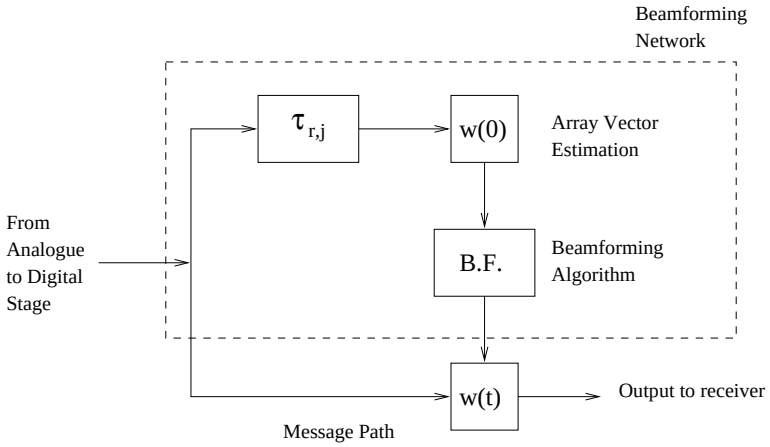

(d)

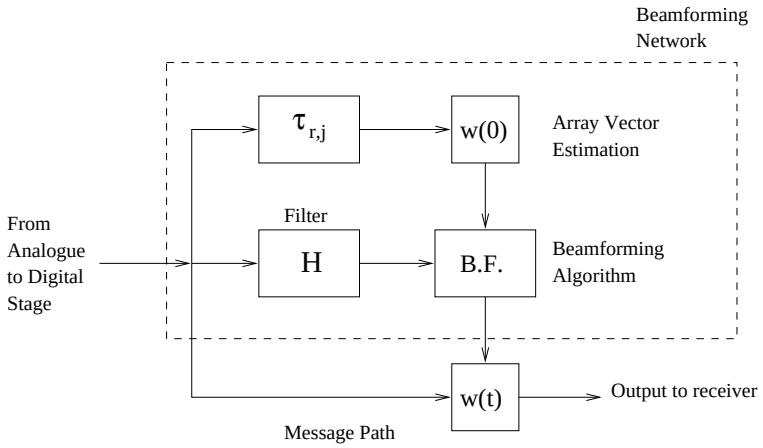

(e)

Figure 6.9: d)A-SCORE beamforming implementation e) FA-SCORE beamforming implementation

6.4.1 SCORE Algorithm (SCORE)

The first test condition used was the basic SCORE algorithm. (Least Squares or Cross Score) These algorithms were applied directly to the received signal from the antenna array. For future reference, this method will be referred to as the SCORE implementation.

6.4.2 Filtered SCORE Algorithm (F-SCORE)

The filtered SCORE algorithm consists of a the proposed front-end filter located along each antenna element array path. This filter's task is to remove the noise component of the received waveform, while preserving the offset carrier signature of the desired channel. In the simulations different filter bandwidths under different noise environments will be examined. The basic front-end filter technique has the advantage of being very easy to implement, with a minimal amount of computational complexity or hardware. This technique will be referred to as F-SCORE. (Filtered SCORE).

6.4.3 Phase Compensated SCORE Algorithm (PC-SCORE)

In this implementation, the received signal is filtered as with the F-SCORE technique, but the phase information received from the array is preserved or recovered. This may be done through storing the phase data of the digitally sampled waveform before digital filtering, and then multiplying the magnitude of the digital waveform after filtering. Other methods would include multiplying the filtered signal by the conjugate phase response, or by Forward-Backward filtering where the filtered signal is passed through the filter in reverse order to remove the time delay caused by filtering. Phase compensation filtering would be more complex and computationally expensive than the F-SCORE described above. This beamforming method will be referred to as PC-SCORE (Phase Compensated SCORE).

6.4.4 Array Estimated SCORE (A-SCORE)

The array estimated SCORE technique aims at using an estimation of the antenna array response in initializing the weight vectors to reduce the convergence time. For the purpose of simulation, the exact array response of the desired signal was used as the initial weight vector to verify if this technique would yield any improvement in performance. This technique will be called A-SCORE. (Array SCORE)

6.4.5 Filtered Array Estimated SCORE (FA-SCORE)

The filtered array estimated SCORE has the same motivation as the A-SCORE, except a digital filter is placed in the processing path as in the F-SCORE algorithm. This algorithm will be referred to as FA-SCORE. (Filtered Array SCORE)

6.5 Transitional Filter Design

This section deals with the calculations for a transitional filter. The calculations presented show the general behavior of the filter and the tradeoffs involved. Specific values are altered, and parameters are recalculated in the actual simulation section of the thesis depending on the test environment chosen.

A transitional filter was designed which combines the relatively steep roll off of a Butterworth filter with the zero phase distortion of a Bessel filter. The signal will be frequency translated to baseband before filtering.

The following steps were performed to get the transitional filter design.

- The minimum passband attenuation for a Butterworth filter was determined.
- The stopband frequency of a Butterworth filter was determined.
- The order of the Butterworth filter was calculated.
- The transfer function of the Butterworth filter was calculated, and the poles and zeros plotted.

- A Bessel filter transfer function was calculated using the same order and stop-band criteria as the Butterworth filter.
- The S-Plane locations of the Butterworth and Bessel filter's poles and zeros were averaged according to a chosen weighting function.
- The magnitude, phase, and S-Plane coordinates were graphed for each filter.

Parameter	Value
Max Passband Attenuation (dB)	3
Min Stopband Attenuation (dB)	-30
Passband Frequency (MHz, Hz)	4, 1
Stopband Frequency (MHz, Hz)	5, 1.2
Filter Order	19
Butterworth Filter Weight	1
Bessel Filter Weight	3

Table 6.1: Sample Transitional Filter Data and Calculations

Normalized and scaled plots of the magnitude, phase and S-Plane poles and zeros are plotted using the above design parameters.

The S-plane pole locations are shown in figure 6.10.

The Transitional filter shows a more gradual roll off in the transition band as compared to the Butterworth filter as shown in figure 6.11. However its attenuation characteristics are better than those of the Bessel filter. By adjusting the filter weights the transitional filter may be modified to resemble the Bessel or Butterworth filter to varying degrees.

The phase response of the transitional filter is plotted in figure 6.12. This plot shows that the phase response of the transitional filter closely follows that of the Bessel filter up to a normalized frequency of 0.8. The difference between the two plots becomes larger at the edge of the passband. Otherwise the phase distortion is below 5.0°.

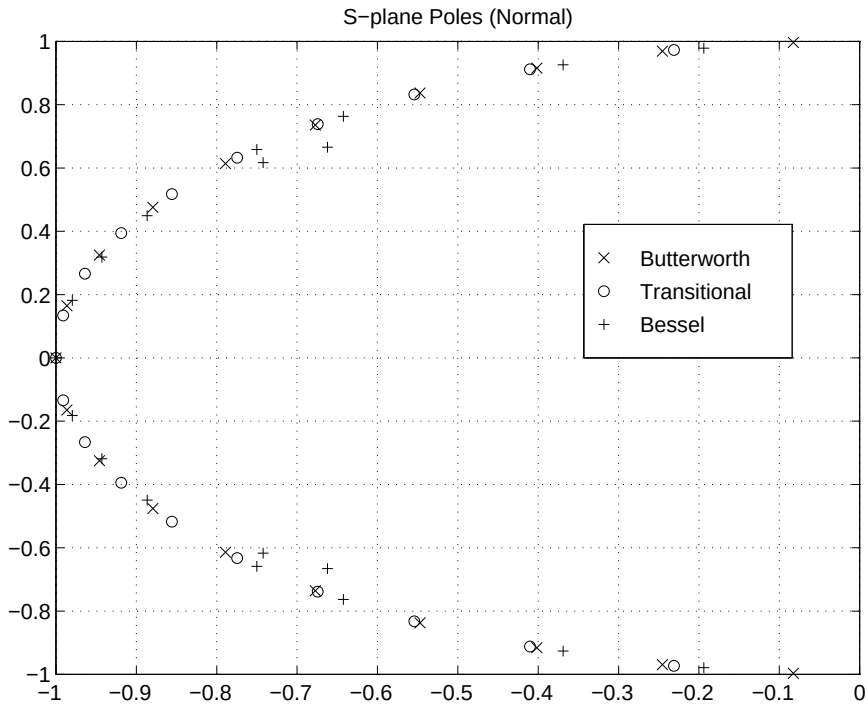

Figure 6.10: Plot of S plane Poles and Zeros for Butterworth, Bessel, Transitional Filters

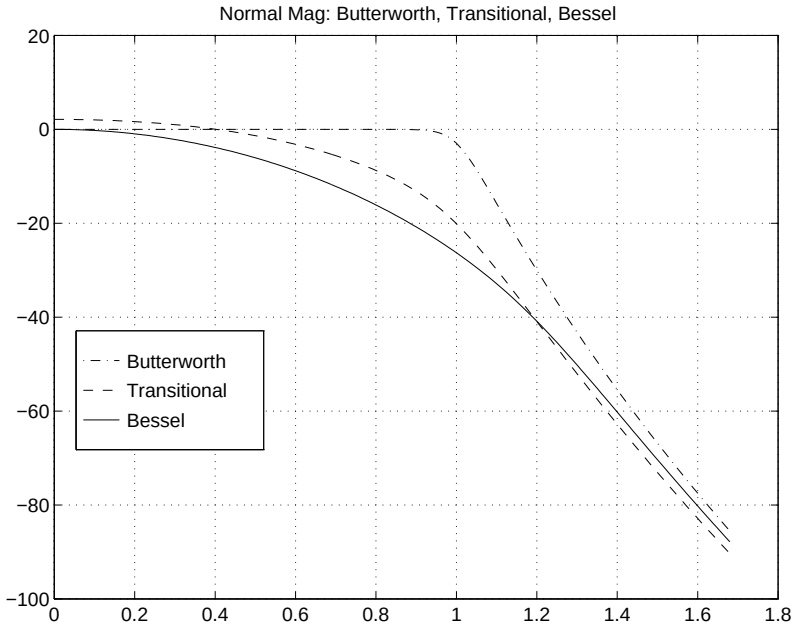

Figure 6.11: Plot of the Normalized Magnitude for Butterworth, Bessel, Transitional Filters

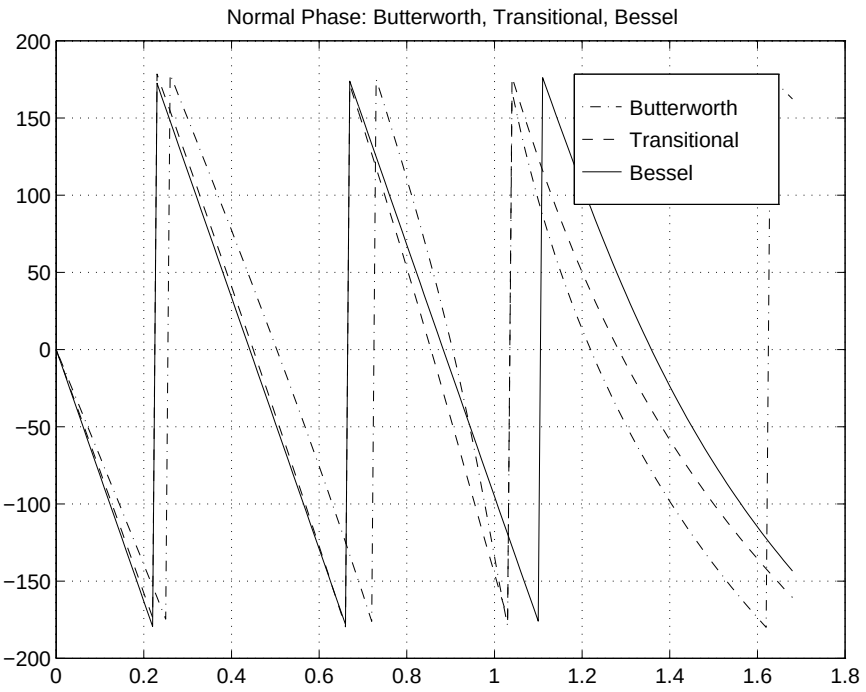

Figure 6.12: Plot of the Normalized Phase for Butterworth, Bessel, Transitional Filters

The above presented parameters produced a good realizable filter which offered adequate attenuation while preserving the phase relation of the signal. Further investigation of the tradeoff between phase and attenuation may result in filters better designed for specific noise and interference environments (Section **??**).

Chapter 7

SCORE Algorithm Simulation Results

7.1 Introduction

In this chapter the various test conditions are simulated for the different filtering algorithms. Plots of the convergence rates of each condition are made to compare the different beamforming methods. The convergence plots were done over 40 independent iterations. The number of iterations for the power method of the Cross SCORE was set to 50. Selected beam patterns are also plotted.

A plot of the convergence weights after 3000 symbols versus the noise level or filter bandwidth is made for selected conditions. The lower bound on these graphs is the SINR of a single element. For the parabolic antenna, the element with the strongest received signal strength based on the direction of arrival was chosen.

The single element performance of the parabolic system is highly dependent on the antenna geometry, the feed coordinates and the direction of arrival. Optimizing these parameters was not within the scope of this thesis.

7.2 Cyclostationary Array Estimation Performance of the Linear and Parabolic Antenna Configuration

The cyclostationary array estimation algorithm was applied for the linear array and the parabolic antenna. The linear array is not considered to have enough gain to make it applicable to the high noise satellite environment, but it does offer a familiar reference to which the algorithms' performance can be gauged.

The parabolic antenna is the antenna configuration which is most applicable to the satellite environment based on the large gain which results from the reflector.

The linear array showed a rapid convergence under low noise conditions. This indicates that the algorithm will work in a favourable environment.

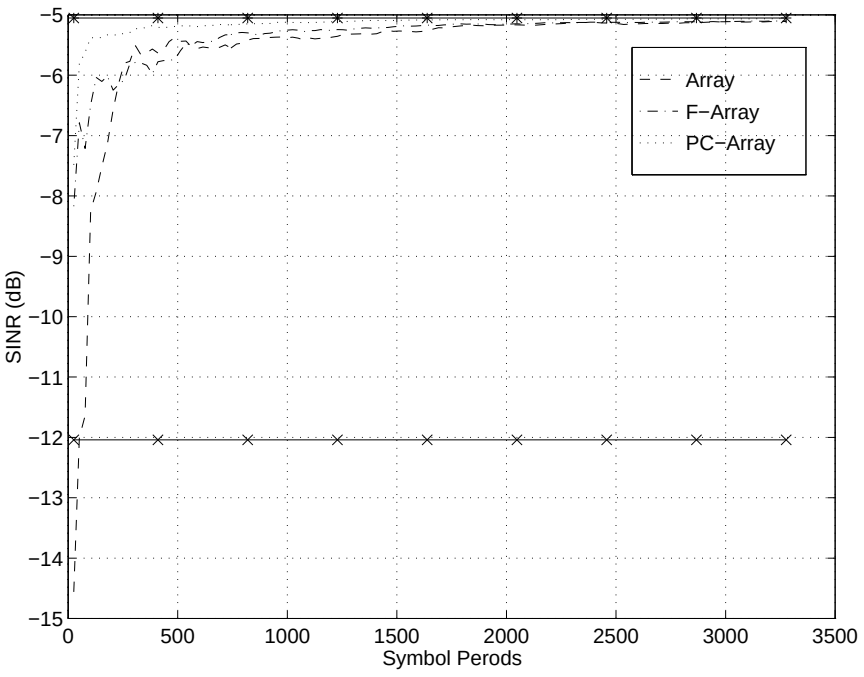

Figure 7.1: Cyclic Array Estimation Linear Array SINR Test LNNB: Received SINR=-12 dB. *-: Optimum SINR, x-:Single Element SINR.

The convergence rate of the elements to the optimal phase was plotted for elements

1 and # 5. Figures 7.2 and 7.3 show slow convergence to the desired phase under a low noise environment.

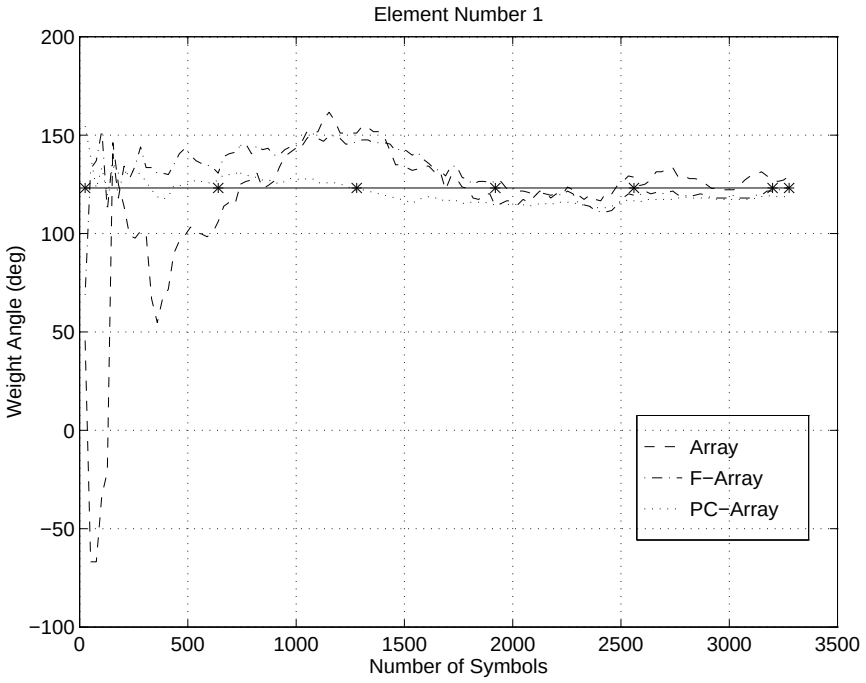

Figure 7.2: Cyclic Array Estimation: Element # 1 Phase Convergence Test LNNB: Received SINR=-12 dB. *-: Optimum Angle

The performance of the parabolic antenna array is very poor even under low noise conditions. All algorithms tend to converge very close to the SINR level of the single strongest element. This can be seen in Figure 7.4.

Convergence performance of the algorithms to the ideal phase shows very poor behavior. This can be seen in Figures 7.5 and 7.6. The fact that the weight angle fluctuates indicates that the calculation of the cyclic autocorrelation value of the reference element with the selected array element is poor. The final beam weight after 3000 symbol periods has a very large error which will greatly limit the performance of the beamformer.

One explanation for the poor behavior of the parabolic antenna is based on the fact that the antenna elements all have different received power depending on their position on the feed plane and the direction of the incoming signal. This is very

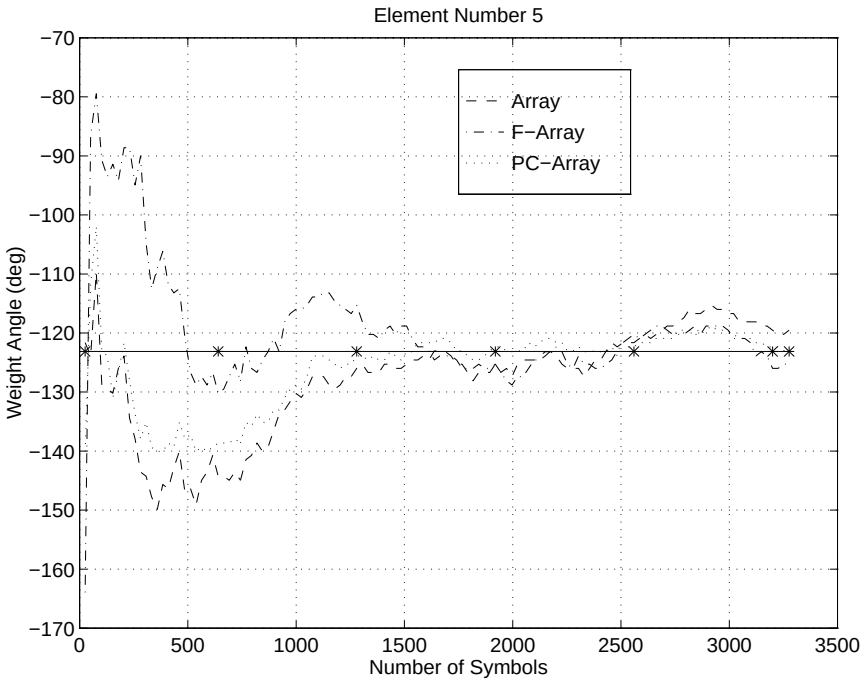

Figure 7.3: Cyclic Array Estimation: Element # 5 Phase Convergence Test LNNB: Received SINR=-12 dB. *-: Optimum Angle

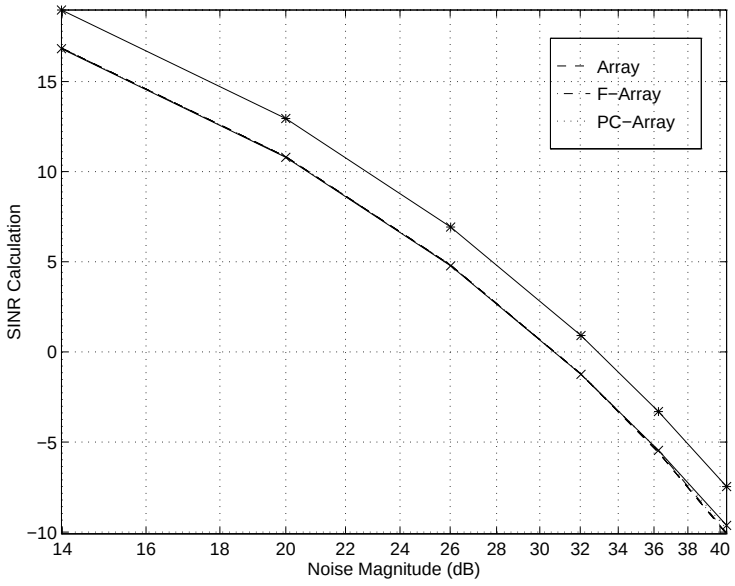

Figure 7.4: Cyclic Array Estimation Linear Array SINR Test HNNB: Received SINR=-36 dB. *-: Optimum SINR, x-:Single Element SINR.

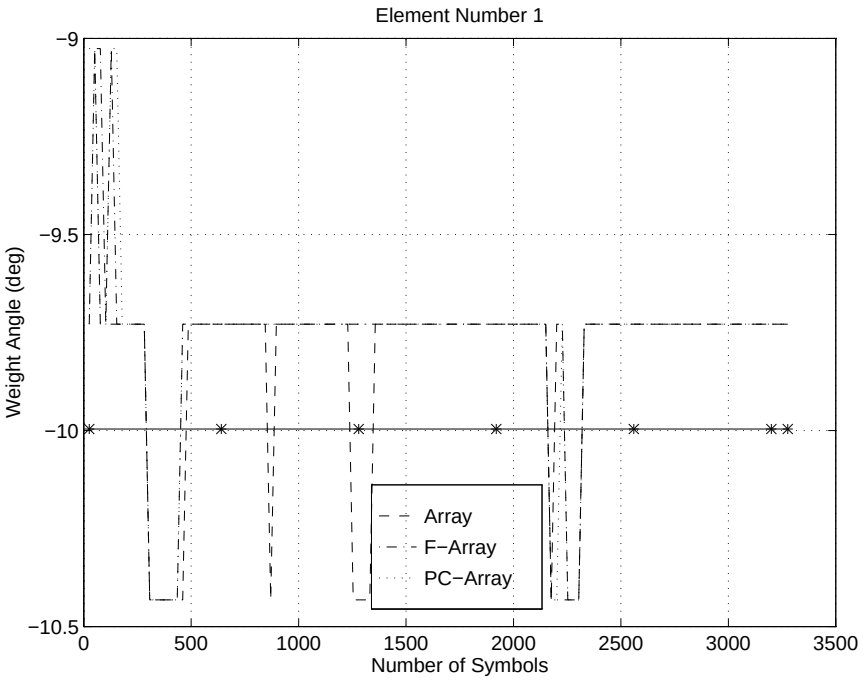

Figure 7.5: Cyclic Array Estimation Parabolic Antenna: Element # 1 Phase Convergence Test HNWB: Received SINR=-36 dB. *-: Optimum Angle

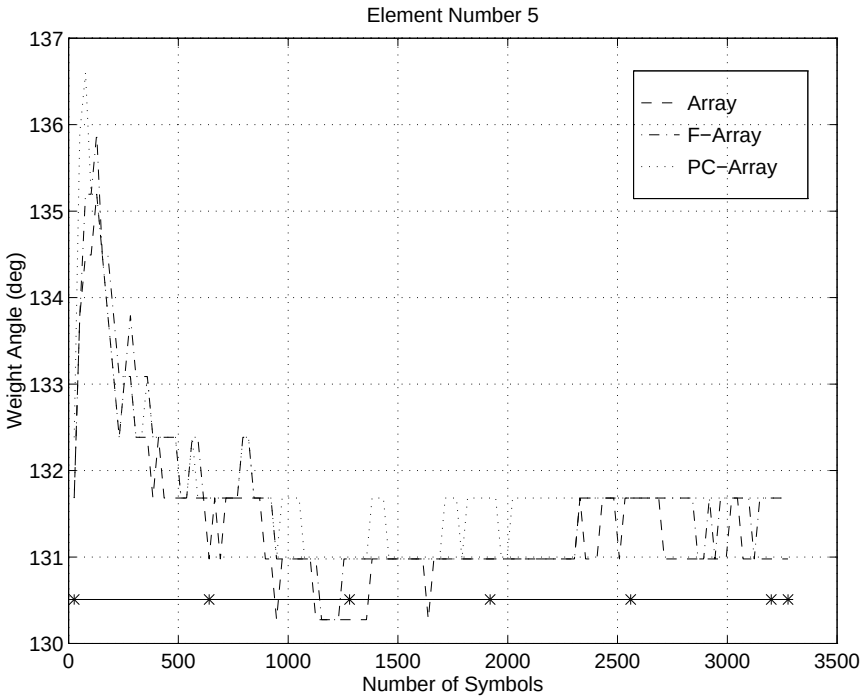

Figure 7.6: Cyclic Array Estimation Parabolic Antenna: Element # 5 Convergence Test HNWB Received SINR=-14 dB. *-: Optimum Angle

different compared to the linear array where all elements have approximately the same received signal strength. As a result of this variation in the received signal among elements, the selection of the reference element is very important in determining the convergence rate of the algorithm for the parabolic antenna. For the test conditions presented in this section, the relative gain of each antenna element can be referenced in Table 7.1. This table shows that if element 5 is selected, the signal gain on the element due to the parabolic signal would only be 12 dB. If element 3 is selected, the reflector gain would be 30.8 dB.

Another factor which significantly effects the convergence, is the fact that the element with the largest signal component will converge to the correct beam weight before the others. This may explain why the achieved SINR for the parabolic antenna is only slightly better than the SINR of the strongest single element.

The final factor which may contribute to the poor performance of the parabolic antenna array is the sensitivity of the elements with a large gain to error. A slightly incorrect temporal delay estimation could result in a large error when the power of the elements are added after beamforming. This would result in a degradation in performance.

These explanations are presented as hypotheses, and were not investigated further in this thesis.

Due to the poor performance of the cyclic array estimation technique, it was disqualified as a method for generating the array response in the high noise satellite environment. The implementation if this array estimation technique may have an application for linear arrays in a lower noise environment.

7.3 Effect of Array Initialization

For the conventional algorithms, the weights used for beamforming are set to an initial value which is not related in any way to the direction of arrival of the incoming signal. The effect of initializing the weight vector to an approximation of the direction

of arrival was hoped to reduce the convergence time of the SCORE algorithms. For the algorithms considered, the initial beam weights were those which would produce the optimal SNR.

As shown in Figure 7.28 this improvement in convergence was not observed. The performance of SCORE, A-SCORE, and F-SCORE, FA-SCORE respectively were almost identical. This behavior was observed for both Least Squares and Cross SCORE techniques, antenna configurations and all test conditions considered.

The reason for this result may be understood by referencing Equation (4.56) for the Least Squares SCORE and (4.65) and (4.66) for the Cross SCORE algorithm. The most important calculated value for determining the beam weights is the time averaged estimation of the autocorrelation matrix and the cyclic autocorrelation matrix. If estimation of these two values is poor, then any advantage gained by the initialization of the beam weights is lost.

For the implementation of the Cross SCORE algorithm in the $L_\alpha = 1$ environment, initialization of the weight vector should reduce the number of iterations necessary for the convergence of the power method implementation. This computational reduction was not expected to be significant as compared to the time average calculation of the cyclic correlation matrix.

It must be noted that cyclic array estimation weights were not applied to the received data at the antenna elements but as a part of the beamforming calculation. It is conceivable that using the cyclic array estimation directly on the received data could improve the beamforming convergence.

7.4 Performance Comparison between Cross SCORE and Least Squares SCORE

The two extremes of the SCORE family of algorithms were tested. The least squares SCORE is the least complex method using the SCORE technique, while the Cross

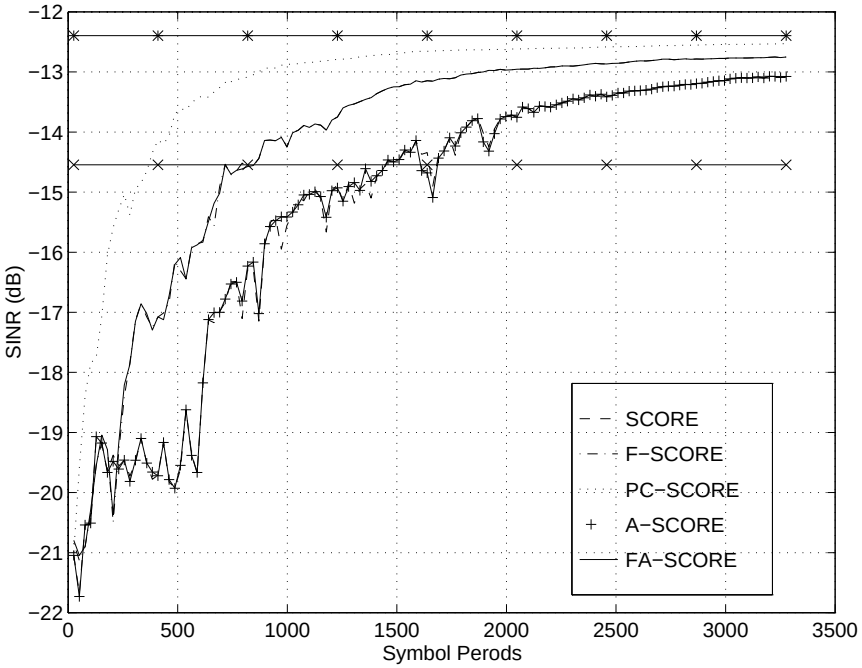

Figure 7.7: Performance Comparison of Array Initialization for SCORE Algorithms. *-: Optimum SNR, x-: Single Element SNR

SCORE technique is computationally the most expensive, and also has the best performance.

The graphs presented in this section show the relative performance of the two algorithms under a high noise environment for both the linear and parabolic configuration. The noise performance of the algorithm was considered the most crucial test in evaluating the suitability of an algorithm for the beamforming satellite environment presented in this thesis.

Linear Array

The test environment considered was test LNNB which consisted of a narrow filter bandwidth. The simulation results for the convergence rates of the least squares SCORE and Cross SCORE are presented in Figures 7.8 and 7.9 respectively.

The least squares score shows a poor convergence rate for all techniques considered as compared to the Cross SCORE technique when the SNR is low (-12 dB). As the SNR decreases, beamforming performance deteriorates further. This can be noticed by comparing the converged SINR values for the Least Squares and Cross SCORE algorithms after 3000 symbol periods. (Figures 7.10 and 7.11)

Parabolic Antenna

The Least Squares SCORE algorithm has only a slightly worse performance as compared the the Cross SCORE technique for low noise environments using the parabolic antenna array. This indicates that the Least Squares SCORE algorithm performance trade off with respect to the computational complexity may be justified for low noise environments using a parabolic antenna (Figures 7.12 and 7.18).

The noise performance of the Least Squares SCORE algorithm quickly deteriorates as the noise level increases as compared to the Cross SCORE algorithm. This shows the sensitivity of the Least Squares SCORE algorithm, and its lack of robustness. This can be seen in the Figures 7.14 and 7.15

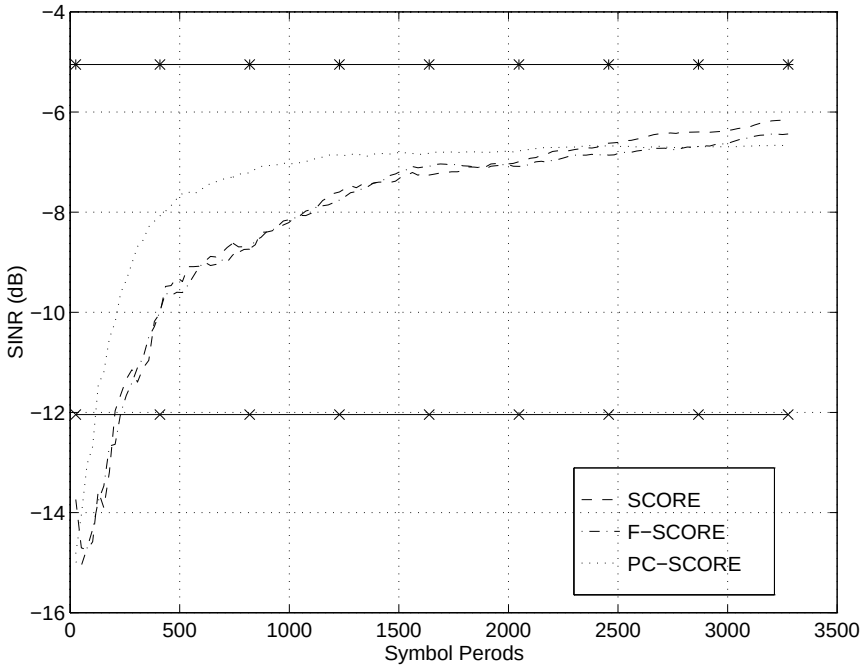

Figure 7.8: LS-SCORE Linear Array SINR, Test LNNB. Received SNR=-12 dB. *-: Optimum SINR, x-:Single Element SINR.

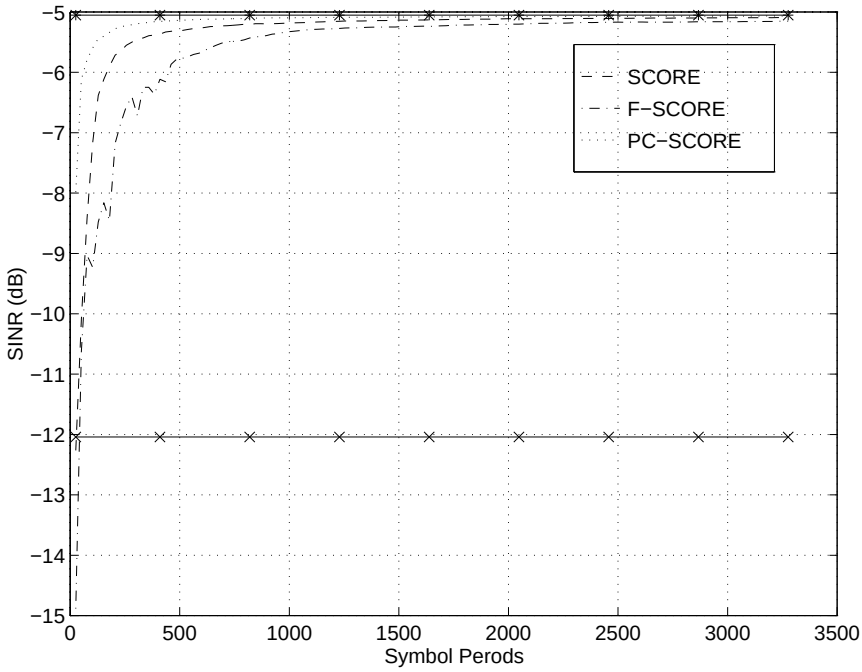

Figure 7.9: Cross-SCORE Linear Array SINR, Test LNNB. Received SNR=-12 dB. *-: Optimum SINR, x-:Single Element SINR.

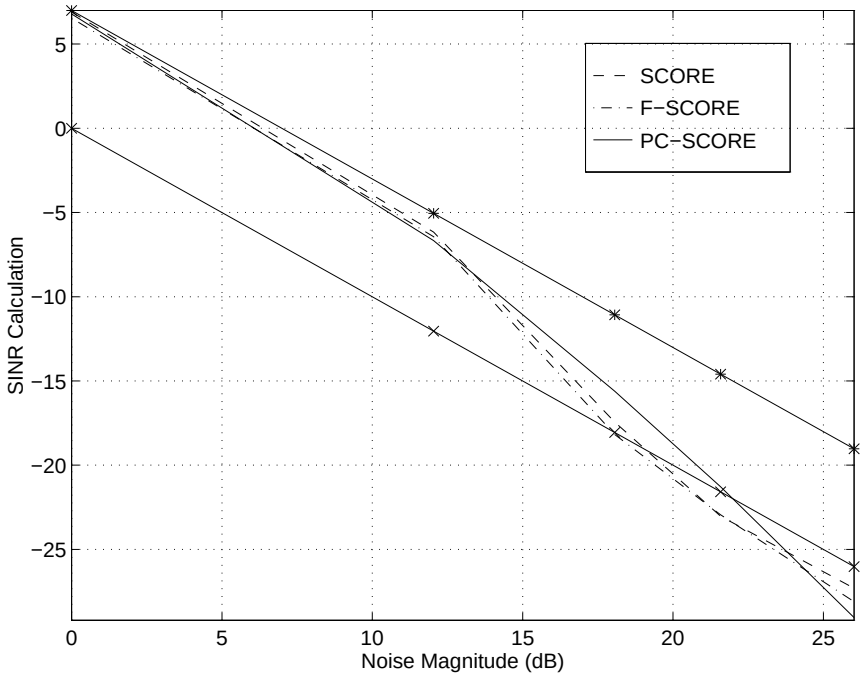

Figure 7.10: LS-SCORE Converged SINR Linear Array Noise Performance: Test LNNB. *-: Optimum SINR, x-:Single Element SINR

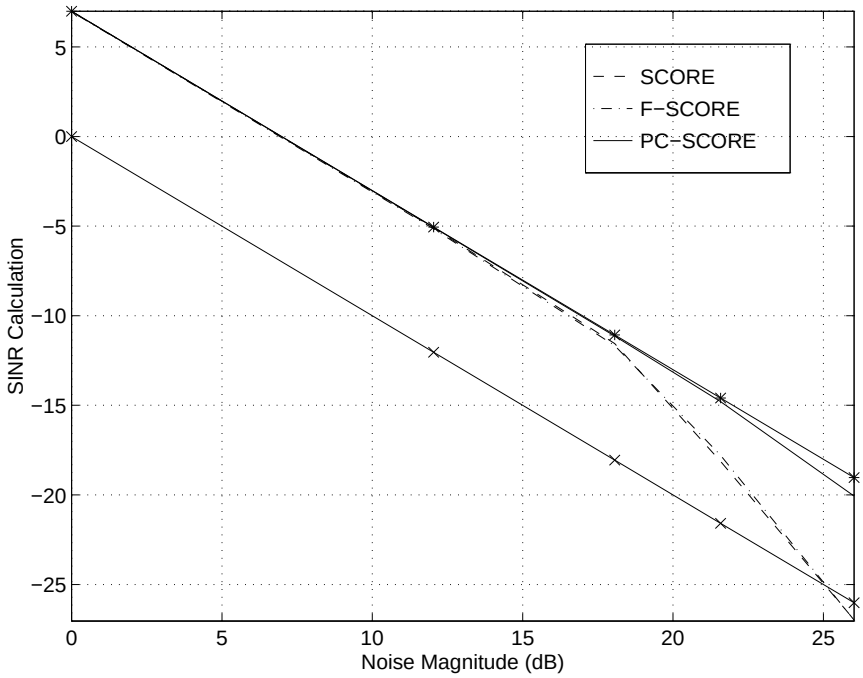

Figure 7.11: Cross-SCORE Converged SINR Linear Array Noise Performance: Test LNNB. *-: Optimum SINR, x-:Single Element SINR

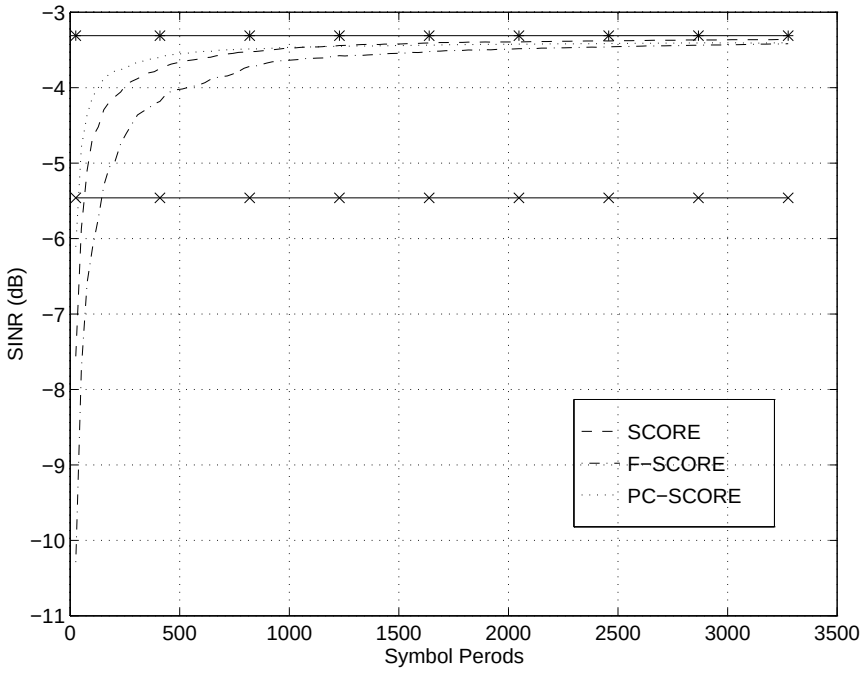

Figure 7.12: LS-SCORE Parabolic Antenna SINR, Test LNNB. Received SNR=-36 dB. *-: Optimum SINR, x-:Single Element SINR.

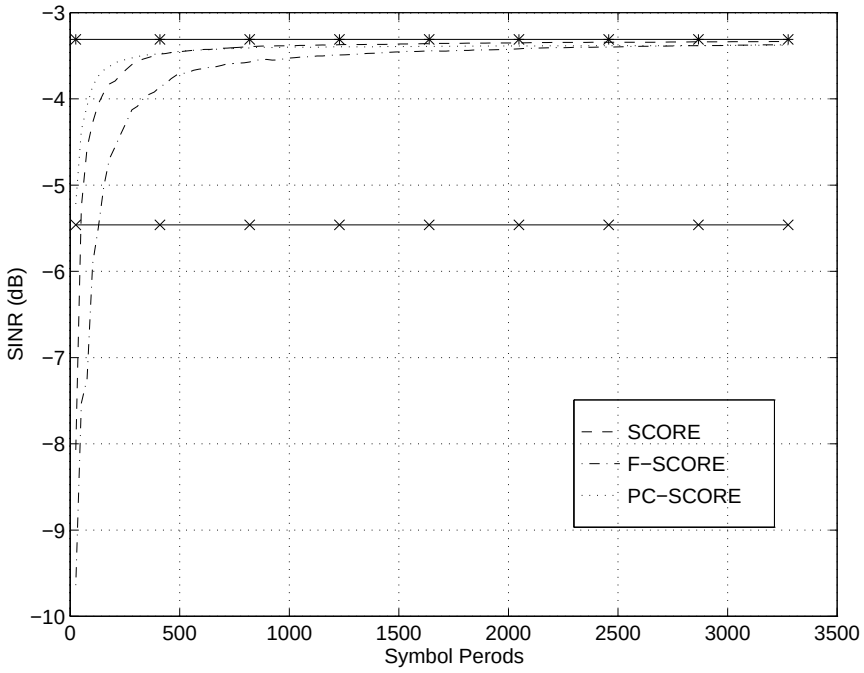

Figure 7.13: Cross-SCORE Parabolic Antenna SINR, Test LNNB. Received SNR=-36 dB. *-: Optimum SINR, x-:Single Element SINR.

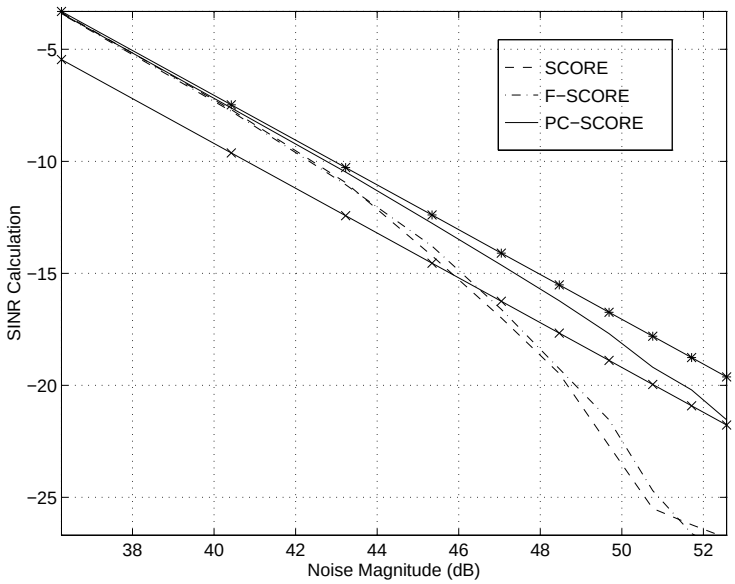

Figure 7.14: LS-SCORE Converged SINR Parabolic Antenna Noise Performance: Test LNNB. *-: Optimum SINR, x-:Single Element SINR

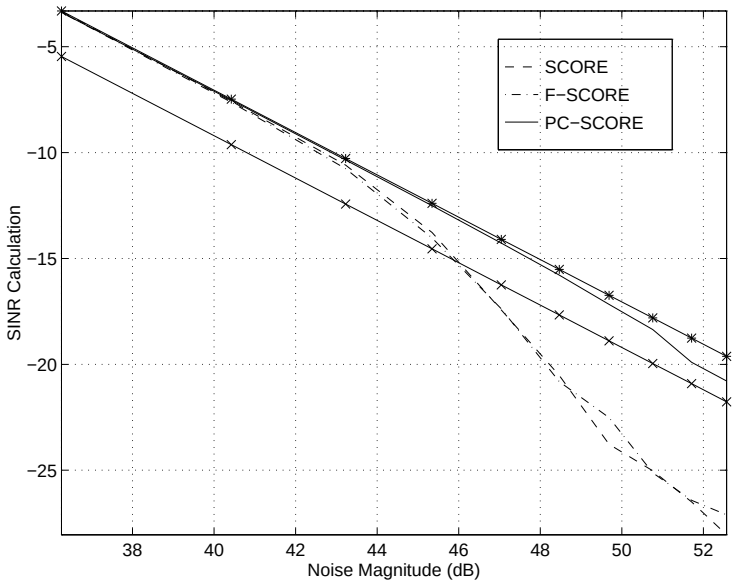

Figure 7.15: Cross-SCORE Converged SINR Parabolic Antenna Noise Performance: Test LNNB. *-: Optimum SINR, x-:Single Element SINR

7.4.1 Summary of Filtered Least Square and Cross SCORE algorithm Comparison

In all test environments considered the Cross SCORE outperforms the Least Squares SCORE algorithm. For this reason, the Cross SCORE was considered the best candidate for the satellite channel used in this thesis.

The cause of this improved performance comes from the adaptation of the control vector as well as the desired beam weight vector. This advantage is discussed in detail in Section 4.9.1.2.

Least Squares SCORE results will not be presented in subsequent sections of this thesis.

7.5 Comparison of the Parabolic and Linear Arrays

The two antenna configurations chosen for this thesis are the parabolic and the linear antenna. The linear antenna was selected as a simple implementation which could offer a familiar geometry. It is easy to build, and calculations are easy to verify.

The parabolic antenna was chosen to supply the link budget with the extra gain necessary to make the Ka band geostationary link feasible. It is the antenna design which will be presented in the remaining sections of this thesis.

The linear array was shown to have the same performance patterns as the parabolic antenna except at a much lower noise power level. This fact shows that the beamforming algorithms tested do not depend on the array geometry. Algorithms only depend on maximizing the characteristic cyclostationary frequency. Thus, cyclostationary algorithms may be developed for specific environments, and could be implemented on different antenna configurations without modification.

Comparison of the parabolic and linear array performance may be made using figures presented in Section 7.4.

7.6 Beam Pattern Performance

The beam patterns of the various antennas, test conditions and algorithms were plotted. These plots were used to verify if the beamforming algorithms produced a radiation pattern which corresponds to the direction of arrival of the desired signal. Plots are made after a correlation time of 3000 symbols.

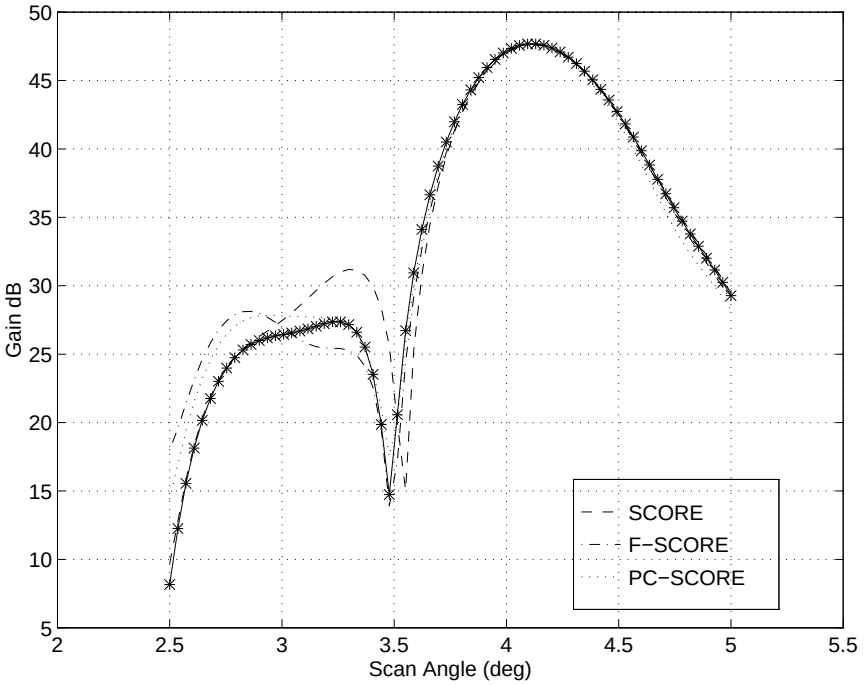

Figure 7.16: CS-SCORE Parabolic Antenna Beam Pattern, Test LNNB. Received SNR=-36 dB. *-: Optimum SINR.

Figures 7.16 and 7.17 show the degradation in performance of the beam pattern as the noise level increases. The '*-' curve shows the beam pattern based on optimum weights. The degradation was observed to correspond to the convergence performance for all test conditions and parameters. Only the effect of the reduction in gain due to imperfect beamforming was investigated in this thesis. Effects such as increased sidelobe levels and other non-idealities are an area of future investigation.

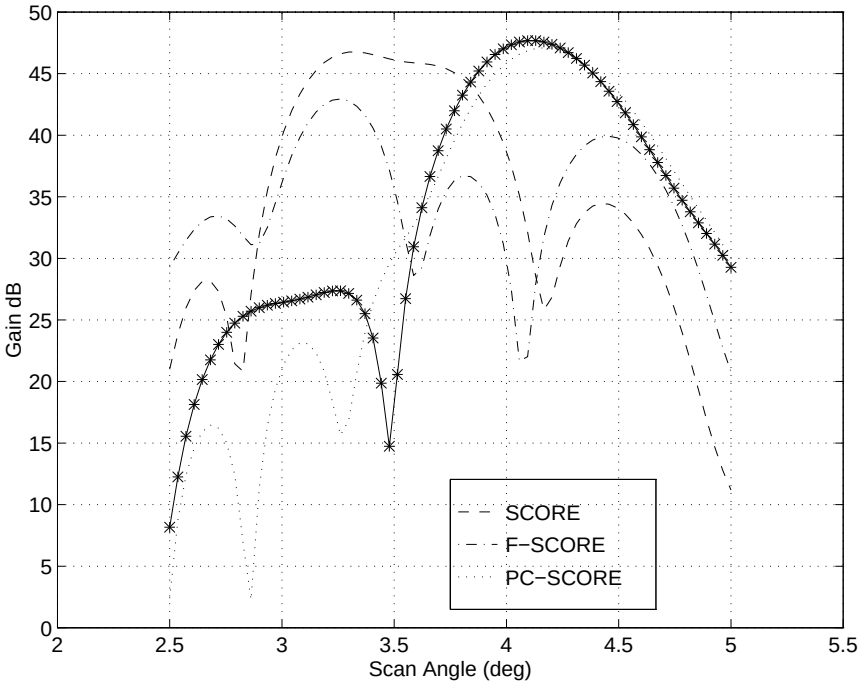

Figure 7.17: CS-SCORE Parabolic Antenna Beam Pattern, Test LNNB. Received SNR=-36 dB. *-: Optimum SINR.

7.7 SCORE Algorithm Convergence Performance

In the following pages, the convergence performance of the Cross SCORE parabolic antenna array is presented. This combination of antenna geometry and beam pattern calculation is considered most suitable to the satellite environment.

The performance of the Least Squares and linear array convergence combinations showed the same trends as for the Cross SCORE parabolic antenna combination, except at lower noise power levels. The explanation of the observations in the Cross SCORE parabolic antenna environment can be applied to the Least Squares, linear array techniques.

7.7.1 Effect of Filter Bandwidth on Convergence Performance

The filter bandwidth is aimed at reducing the noise power which is input into the beamformer. Section 6.2.10 describes the tradeoff between noise attenuation and pulse dilation in the time domain which affects the rate of convergence.

Performance comparisons in Figures 7.18 and 7.27 show that the SCORE algorithm outperforms the F-SCORE algorithm when the filter bandwidth is narrow. If the filter bandwidth is widened, the performance of the F-SCORE algorithm improves, and approaches the performance of the PC-SCORE algorithm. This improvement is more clearly seen in Figures 7.20 and 7.28 under higher noise conditions.

The degradation of F-SCORE for narrow bandwidth filters can be explained by the increase in the pulse dilation of the filtered noise which results from the non-ideal filter. This effect is shown in Section 6.2.3.2.

When the filter bandwidth becomes very large, the performance of all filtered algorithms approaches the performance of the unfiltered SCORE method as expected and shown in Section 6.2.7. This can be seen in Figure 7.22.

Figures 7.23 and 7.24 show the performance of the parabolic antenna of the different algorithms for different filter bandwidths after a convergence time of 3000 symbols.

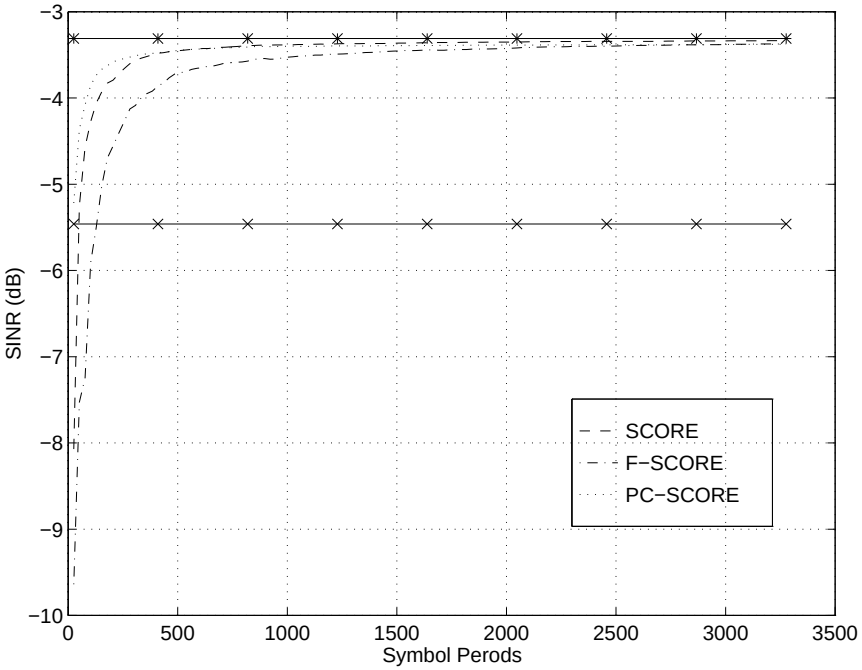

Figure 7.18: Cross SCORE Parabolic Array SINR, Test LNNB: Received SNR=-36 dB. Filter BW= .05Hz. *-: Optimum SINR, x-: Single Element SINR

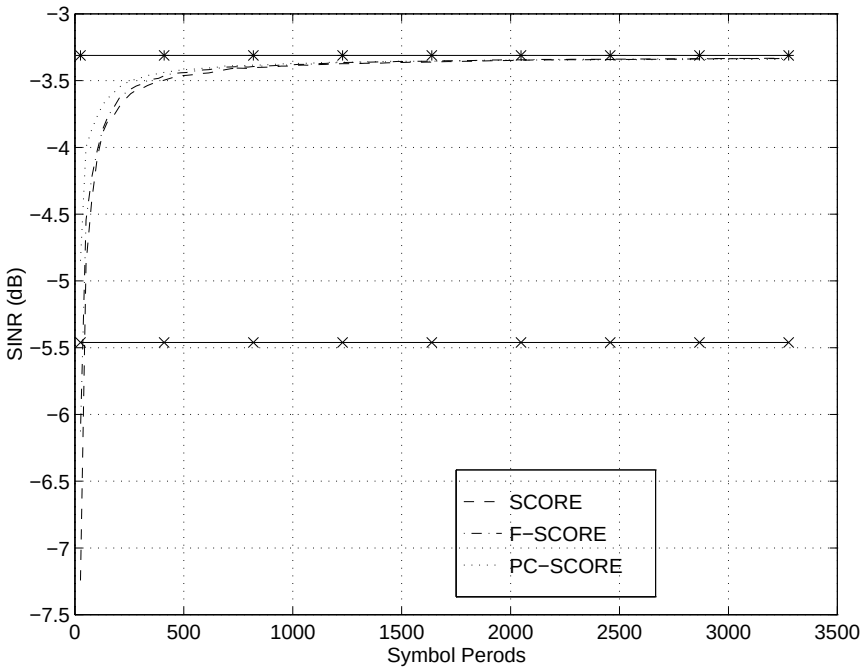

Figure 7.19: Cross SCORE Parabolic Array SINR, Test LNWB: Received SNR=-36 dB. Filter Bandwidth= .2 Hz *-: Optimum SINR, x-: Single Element SINR

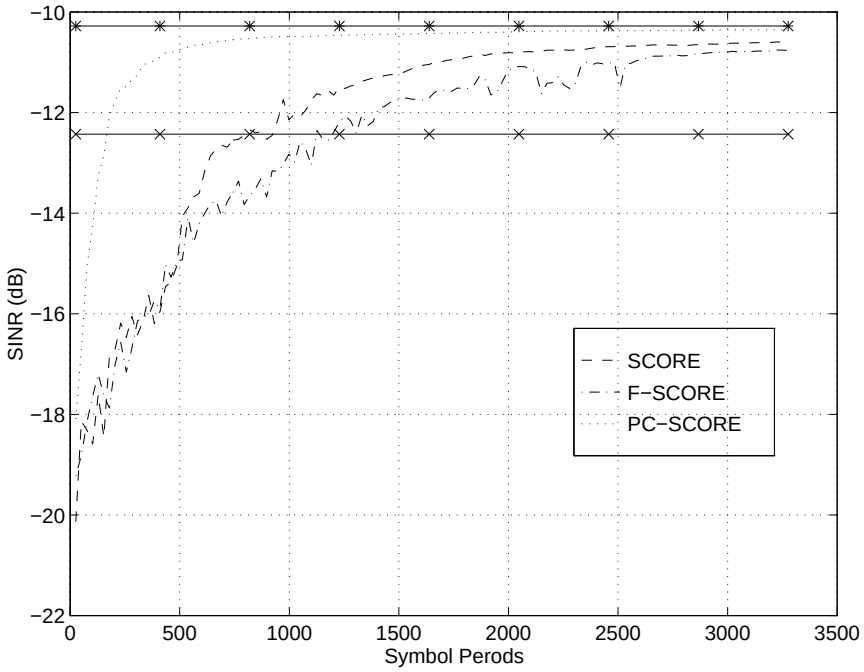

Figure 7.20: Cross SCORE Parabolic Array SINR, Test LNNB: Received SNR=-42 dB. Filter Bandwidth= .05 Hz *-: Optimum SINR, x-: Single Element SINR

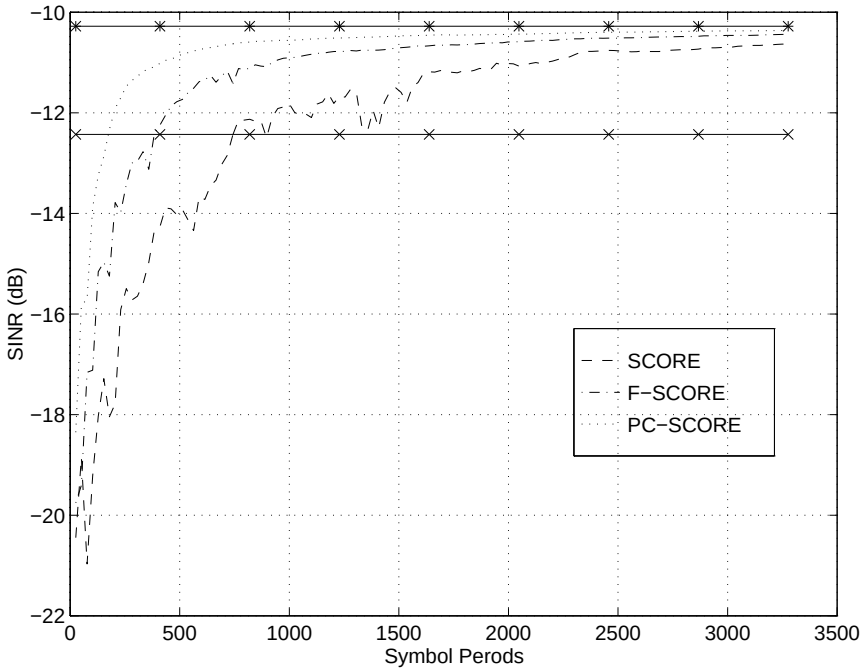

Figure 7.21: Cross SCORE Parabolic Array SINR, Test LNWB: Received SNR=-42 dB. Filter Bandwidth= .2 Hz *-: Optimum SINR, x-: Single Element SINR

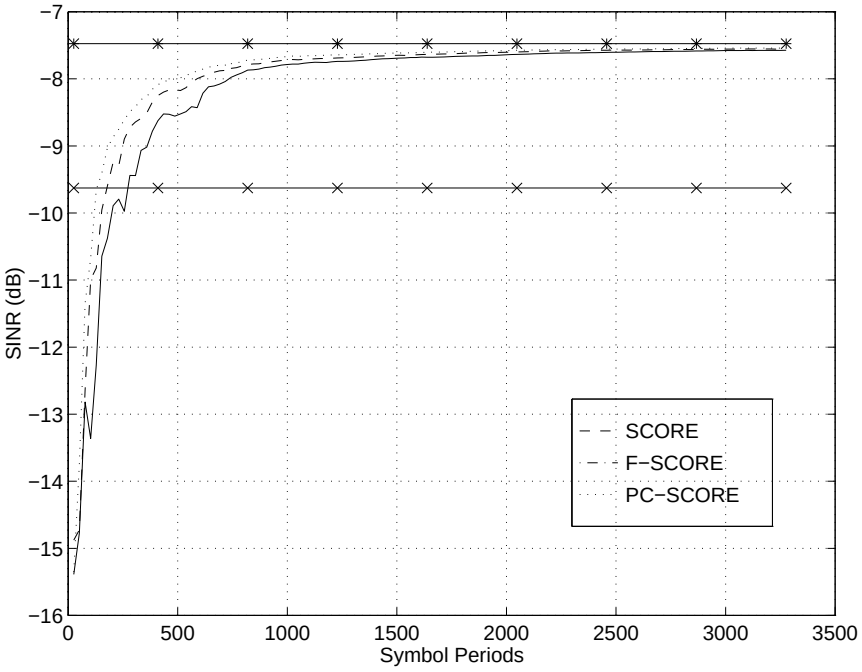

Figure 7.22: Cross SCORE Parabolic Antenna SINR, Test LNNB: Received SNR=-40.4 dB. Filter Bandwidth= .4 Hz *-: Optimum SINR, x-: Single Element SINR

The relative behavior of the PC-SCORE and F-SCORE are almost identical in the two test cases, though filtering is seen to make a significant difference in convergence performance for the high noise test condition.

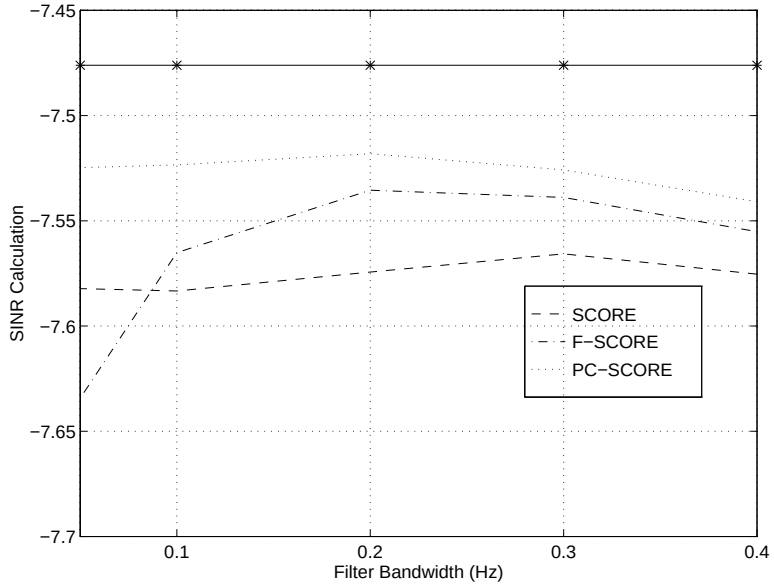

Figure 7.23: Cross SCORE Steady-State for SINR Parabolic Antenna, Test LNNB: Received SNR=-40.4 dB. *-: Optimum SINR, x-: Single Element SINR

When the converged SINR is plotted versus the filter bandwidth for the linear array after 3000 symbols, the performance dependence of the algorithms is more dramatic. The linear array shows that there is an optimal filter bandwidth which corresponds to a particular environment. For example, the optimal performance bandwidth for the F-SCORE algorithm when the received SNR level is -22 dB is close to 0.1 Hz (Test HNNB). When the received SNR is raised to -12 dB (Test LNNB), the optimal filter bandwidth is approximately 0.2 Hz. This behavior is presented in Figures 7.25 and 7.26. Again filtering has a significant effect on convergence rate performance for the linear array in a high noise environment. These trends support the theoretical predictions presented in Section 6.2.

The variation of the filter bandwidth does not result in a significant performance improvement over a large range of filter values. This can be noted in Figure 7.23 where the performance gain for F-SCORE varied by only .02 dB for a filter range of

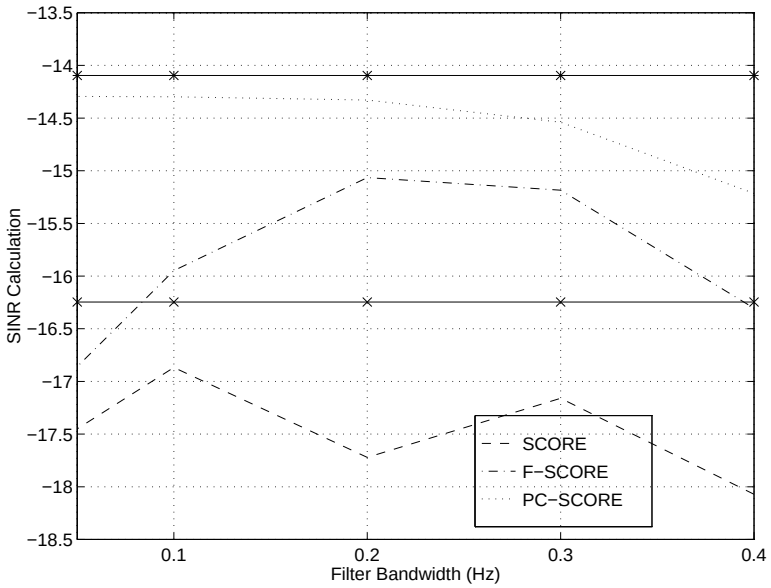

Figure 7.24: Cross SCORE Steady State for SINR Parabolic Antenna, Test HNNB: Received SNR=-47 dB. *-: Optimum SINR, x-: Single Element SINR

1.5 Hz to 3.5 Hz.

The PC-SCORE algorithm is almost flat for a bandwidth less than .3 Hz. The significance of this result shows that bandwidth optimization does not result in significant performance gains, and may not justify the necessary computational expense.

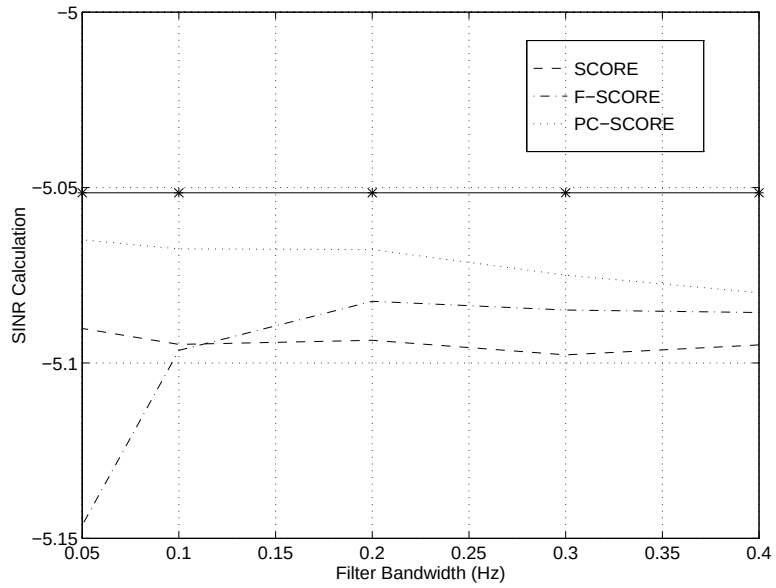

Figure 7.25: Cross SCORE Steady-State for SINR Linear Array, Test LNNB: Received SNR=-12 dB. *-: Optimum SINR, x-: Single Element SINR

7.8 Effect of Noise on Convergence Performance

The most significant environment parameter in the evaluation of the beamforming algorithms is the noise performance since the satellite system will be noise limited. This section displays the convergence of the different algorithms with the intention of characterizing the noise performance limit of the algorithms relative to the optimum SNR possible. Beamforming gains which result from these simulations may be too low for a practical system. System level changes to increase the gain would be necessary.

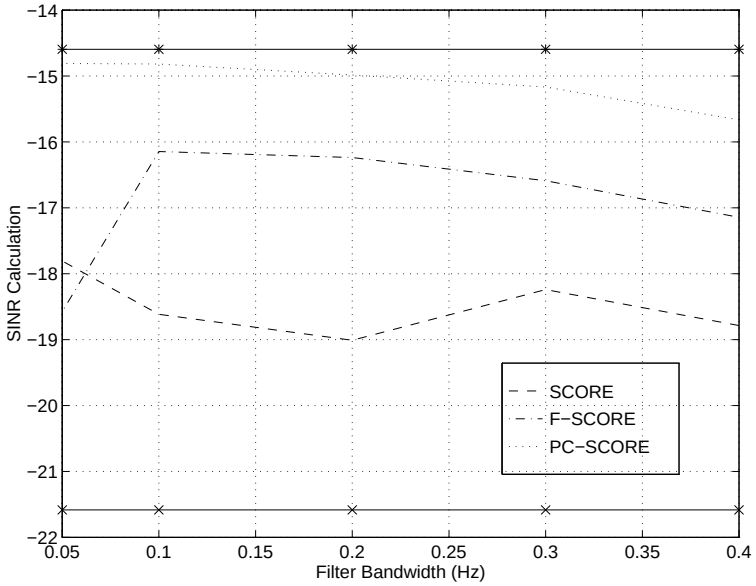

Figure 7.26: Cross SCORE Steady State for SINR Linear Array, Test HNNB: Received SNR=-22 dB. *-: Optimum SINR, x-: Single Element SINR

7.8.1 Convergence Rate Deterioration due to Noise

Figures 7.27 to 7.29 show the degradation in the convergence rate of the Parabolic antenna Cross SCORE method as the noise power increases. Noise performances were not considered above 52.5 dB where the output SINR levels of all the algorithms deteriorated below the already unsatisfactory SINR level generated by the single element configuration. All plots show that the PC-SCORE algorithm significantly outperforms all other algorithms for the test cases considered.

7.8.2 SCORE Convergence Limit due to High Noise

In Figure 7.29 the SCORE and F-SCORE show no indication of convergence after 3000 symbol periods. For the basic SCORE algorithm the poor noise performance may be explained by the need for a longer convergence time to reject the noise. For the F-SCORE algorithm the pulse dilation due to filtering may result in the poor performance. These effects are explained in Section 6.2.

The PC-SCORE technique shows a significant convergence rate performance improvement over F-SCORE. This supports the argument that the calculation of the SCORE beamforming algorithms have a critical dependence on the phase of the incoming signal data (Section 6.2.3).

The performance of the SINR convergence after 3000 symbols with respect to the noise power level is presented in Figure 7.30. This figure indicates that there is a threshold level at which the performance of the algorithms begin to deteriorate.

7.8.3 Cross SCORE Noise Performance Summary

The cross SCORE parabolic antenna configuration modeled in this thesis can provide an antenna gain of 31 dB. An optimum beamforming gain of 2 dB could be achieved at a received SNR level as low as -45 dB and -48 dB for F-SCORE and PC-SCORE respectively. This resulted in SNR levels of less than -10 dB which are too low for a reliable communications system. Therefore, a practical system would have to provide

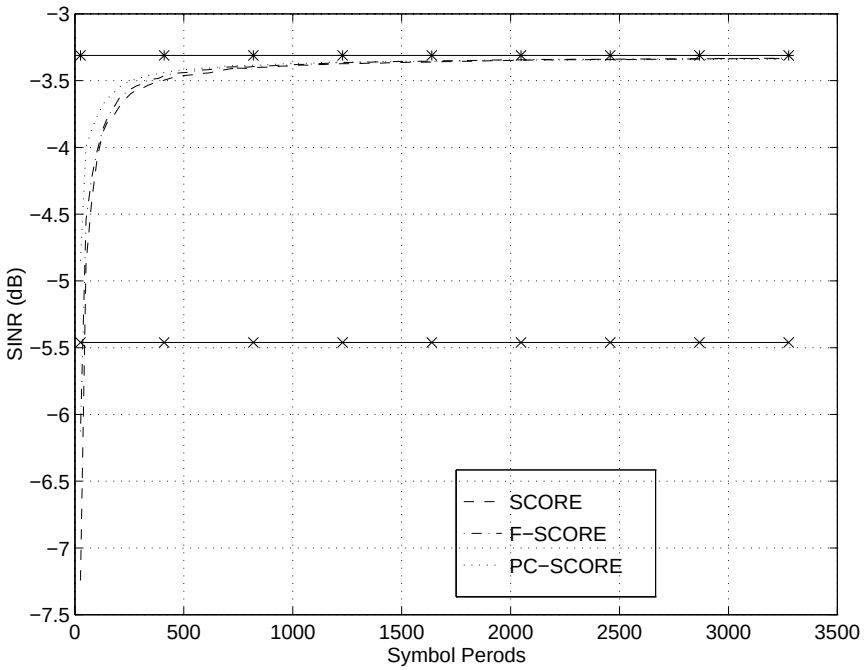

Figure 7.27: Cross-SCORE Parabolic Array SINR, Test LNWB. Received SNR=-36 dB. *-: Optimum SINR, x-: Single Element SINR

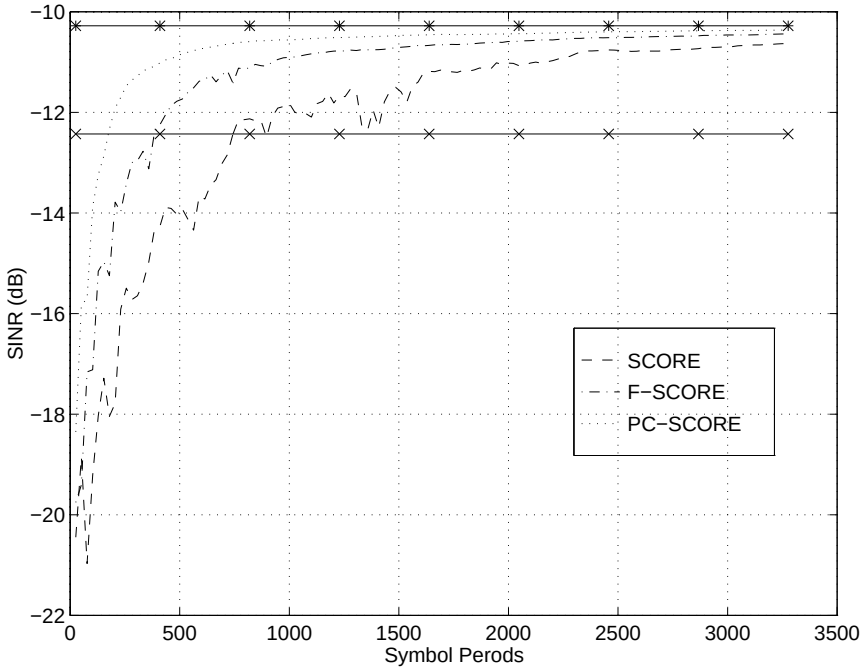

Figure 7.28: Cross-SCORE Parabolic Array SINR, Test LNWB. Received SNR=-42 dB. *-: Optimum SINR, x-: Single Element SINR

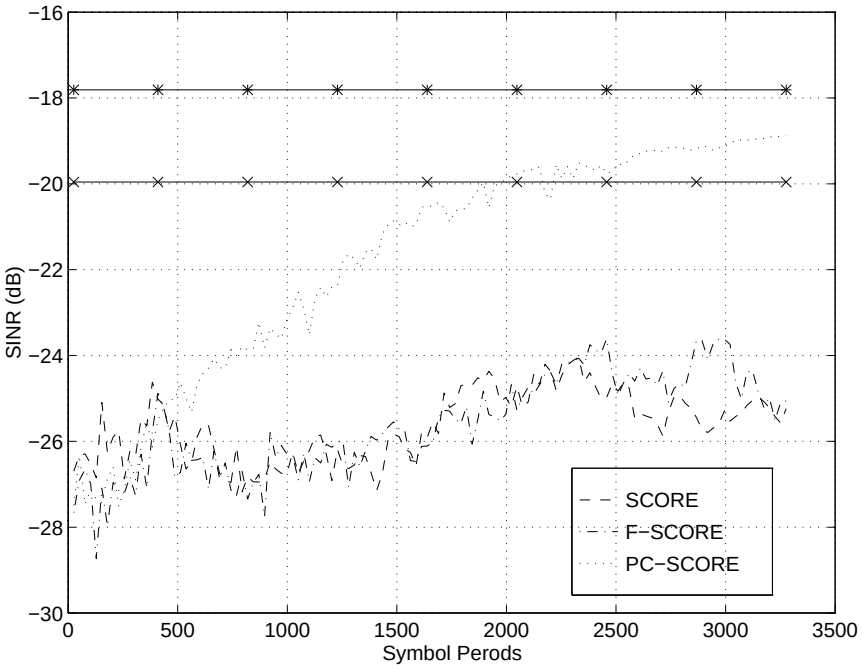

Figure 7.29: Cross-SCORE Parabolic Array SINR, Test LNWB. Received SNR=-50 dB. *-: Optimum SINR, x-: Single Element SINR

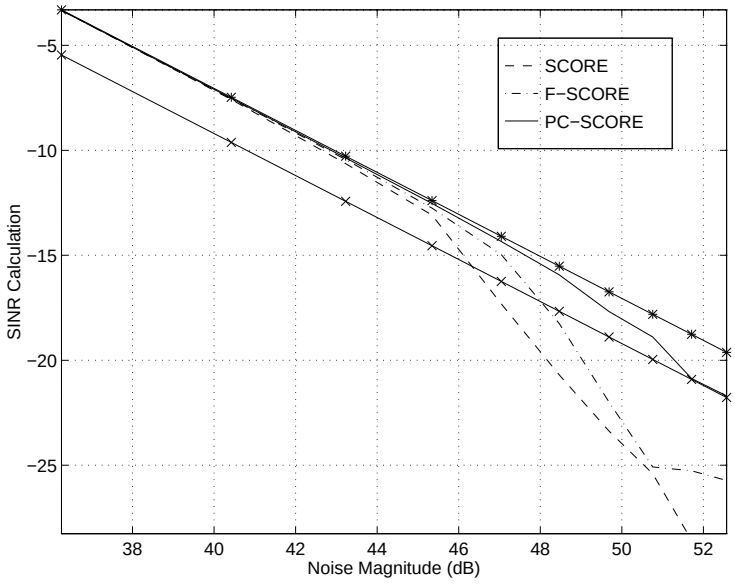

Figure 7.30: Cross-SCORE Steady State SINR Parabolic Antenna Noise Performance: Test LNWB. *-: Optimum SINR, x-: Single Element SINR

an additional 15 to 25 dB of gain. This may be obtained using higher gain antennas, or through increasing the beamforming gain by using more antenna elements.

The relatively long correlation time of 3000 symbols is possible because of the slowly time varying nature of the system modes (Section 3.2). This long convergence time is not possible with quickly changing environments such as in the case of mobile users, or interference limited channels.

7.9 Effect of Interference on Convergence Performance

The effect of interference on convergence is not expected to be significant for the test environments considered due to the fact that the interference power is much less than the noise power level. Simulations were run to verify this statement. The interferer was modeled as being in the same direction as the desired signal with the same power level. The only difference is the offset frequency.

Figures 7.31 and 7.32 show that even under narrow filtering and relatively low noise environment of test condition LNNB, there is no significant effect of introducing the interference signal on the convergence rate.

The reason for this performance may be explained by noting that the interference signal is well below the noise power of the system. Therefore the power contributed from the interference term is not significant with respect to the white noise power. Under much lower noise conditions or higher interference power levels, the effect of the interference is expected to be much more important. In these situations, the front end filter bandwidth will play an important role in interference rejection (Section 6.2.9).

7.10 Frequency Jitter Noise Performance

The frequency jitter test is aimed at evaluating the performance of the SCORE algorithms when the offset frequency is varying around the true cyclic frequency. A

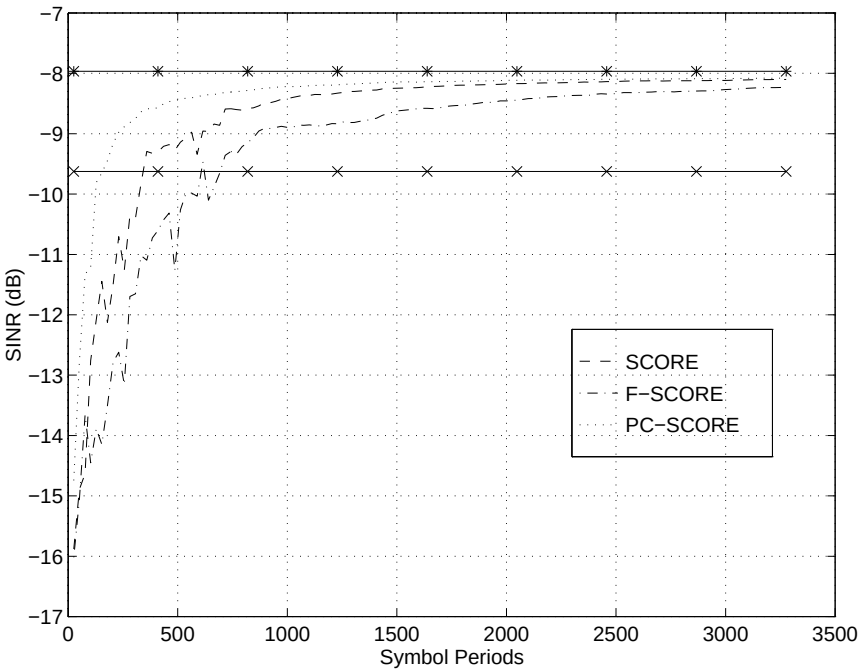

Figure 7.31: Cross SCORE Parabolic Antenna Array SINR, Test LNNB. Interference Frequency=.245 Hz with the desired offset frequency at .25 Hz. *-: Optimum SINR, x-: Single Elements SINR.

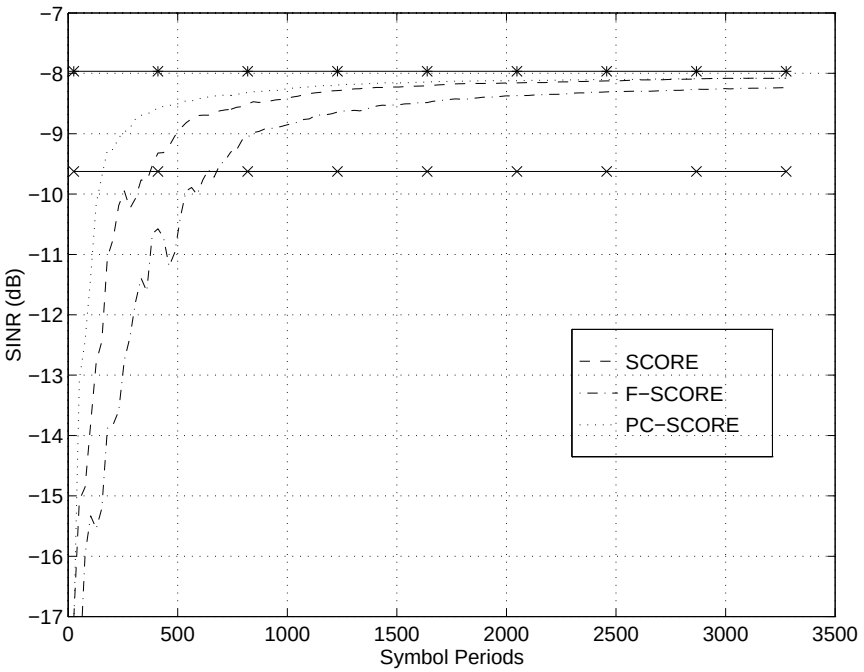

Figure 7.32: Cross SCORE Parabolic Antenna Array SINR, Test LNNB: Interference Frequency=.2 Hz with the desired offset frequency at .25 Hz. *-: Optimum SINR, x-: Single Elements SINR.

detailed description of the frequency jitter model may be referenced in Section 5.2.3.

The frequency jitter produced a significant deterioration in beamforming performance, especially as the noise level of the environment increased. This can be observed in Figures 7.33 and 7.34. The frequency jitter deviation in both of these scenarios is the same, while the noise level is increased.

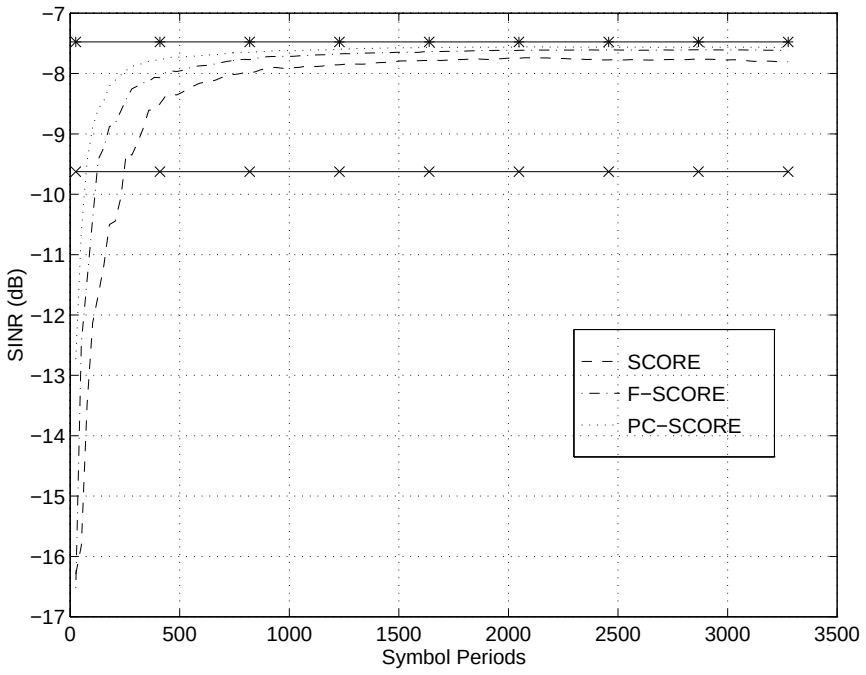

Figure 7.33: Cross SCORE Parabolic Antenna SINR, Test LNWB: Jitter Deviation= 0.04 % of Carrier Offset Frequency (2 kHz). *-: Optimal SINR, x-: Single Element SINR.

For jitter frequency deviations of 0.2 % of the carrier offset frequency (10 kHz) and greater, eventually deteriorated in SINR performance. This was observed in every test environment considered. The divergent nature of the SCORE algorithms is illustrated in figure 7.35.

This rejection of the characteristic offset frequency can be explained in terms of the frequency rejection nature of the SCORE algorithm (Section 6.2.9). When the frequency jitter is small, the effects of jitter can be averaged out as the integration time is increased resulting in only a reduction in the convergence rate.

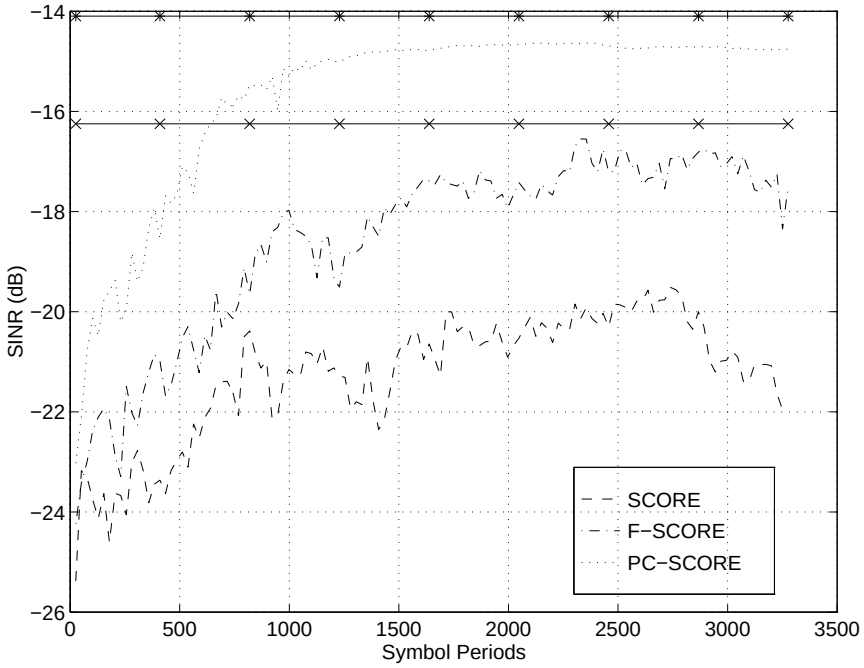

Figure 7.34: Cross SCORE Parabolic Antenna SINR, Test HNWB: Jitter Deviation= 0.04 % of Carrier Offset Frequency (2 kHz). *-: Optimal SINR, x-: Single Element SINR.

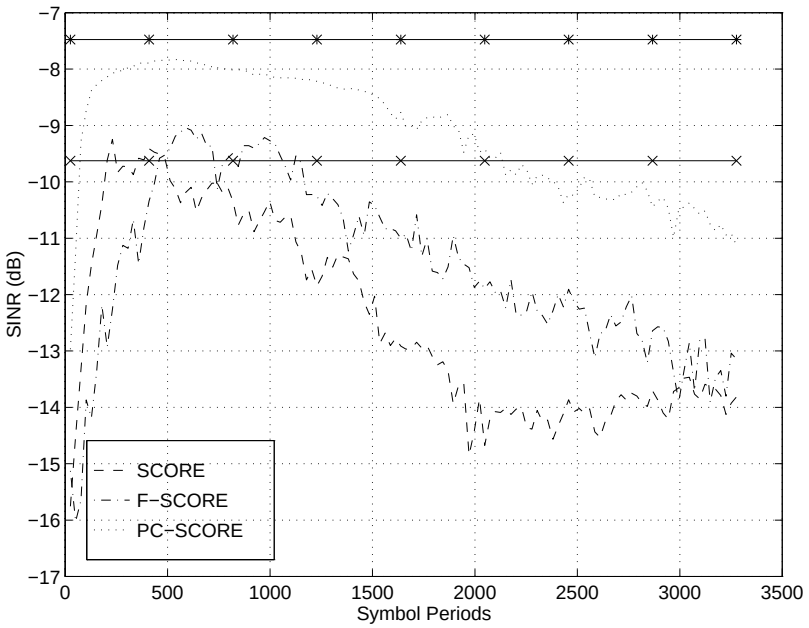

Figure 7.35: Cross SCORE Parabolic Antenna SINR, Test LNNB: Jitter Deviation= 0.2 % of Carrier Offset Frequency (10 kHz). *-: Optimal SINR, x-: Single Element SINR.

When the jitter deviation reaches a threshold dependent on the system noise power, the averaging of the frequency jitter becomes more sensitive to error. After a certain averaging time, (500 symbol periods as shown in Figure 7.35), the errors in the carrier offset eventually result in the SCORE algorithm rejecting the desired signal.

A similar type of behavior was mentioned by Agee [2], who suggested that a windowing technique be applied to the received data to improve the robustness of the SCORE time averaging to frequency error. The resulting trade-off would be a decrease in convergence rate performance. Effects of windowing, as well as finding the threshold where the desired signal is rejected due to frequency jitter are areas of future investigation.

7.11 Frequency Offset Convergence Performance

Errors in frequency offset may arise from a variety of sources including temperature fluctuations, or component mismatches.

The Figures 7.36 to 7.38 show the effects of offset frequency mismatch on the convergence rate. It can be seen that an increase from a noise power of 40.4 dB to 47.0 dB greatly degrades the performance of the SCORE algorithms.

The periodic nature of the fluctuation of the beamforming patterns can be explained in terms of the frequency rejection nature of the SCORE algorithms. The algorithm will converge to the desired beamforming weights up until the point where the time averaging will begin to reject the desired signal. After a sufficient averaging time, (1000 symbol periods for Figure 7.36), the desired signal is completely rejected, and the convergence to the desired pattern begins again. The reduction in successive maxima of the SINR is attributed to the increased sensitivity of the SCORE algorithms to the cyclic frequency error.

The periodic convergence fluctuation increases in frequency as the carrier offset error increases. This can be seen by the quick rejection of the PC-SCORE signal in

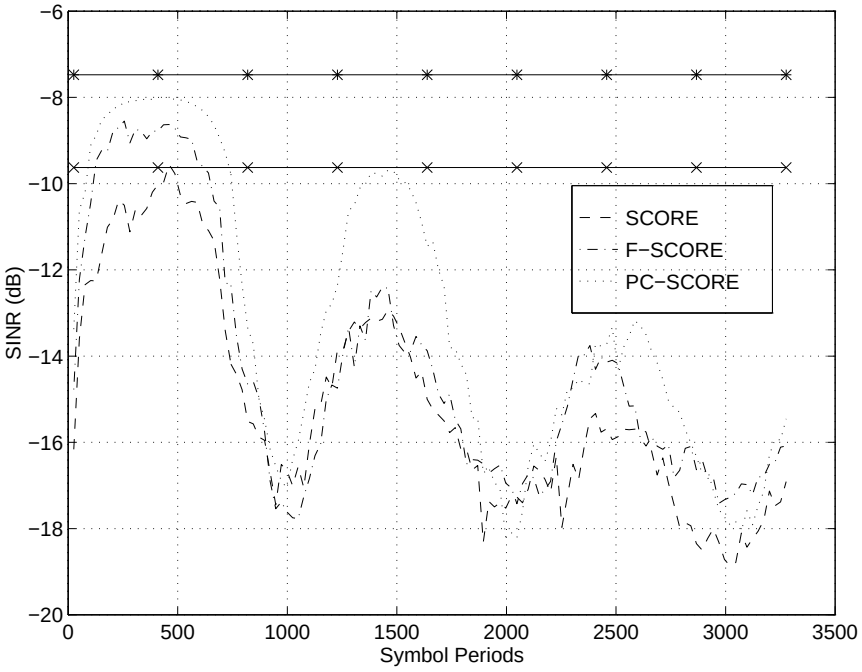

Figure 7.36: Cross SCORE Parabolic Array SINR, Test LNWB: Frequency Error = 0.04 % of Carrier Offset Frequency (2 kHz). *-: Optimum SINR, x-: Single Element SINR.

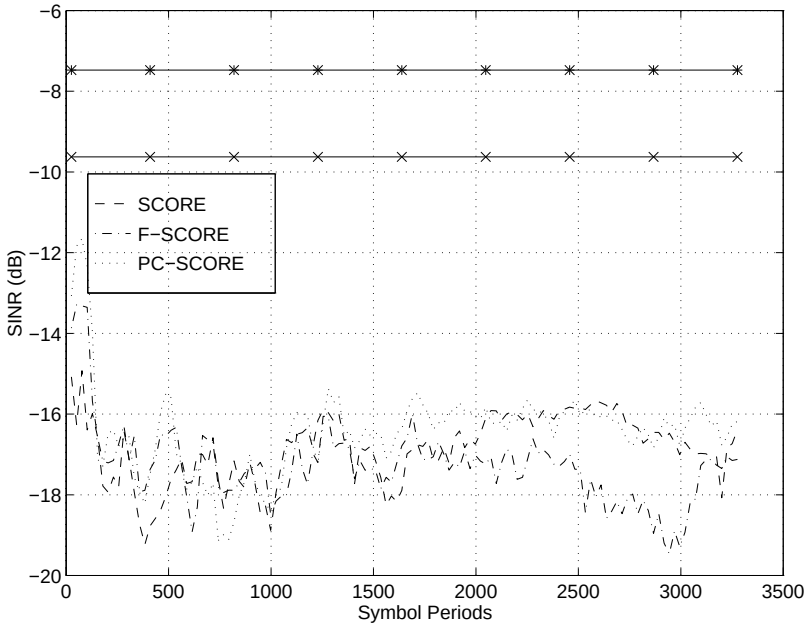

Figure 7.37: Cross SCORE Parabolic Array SINR, Test LNWB: Frequency Error = 0.2 % of Carrier Offset Frequency (10 kHz). *-: Optimum SINR, x-: Single Element SINR.

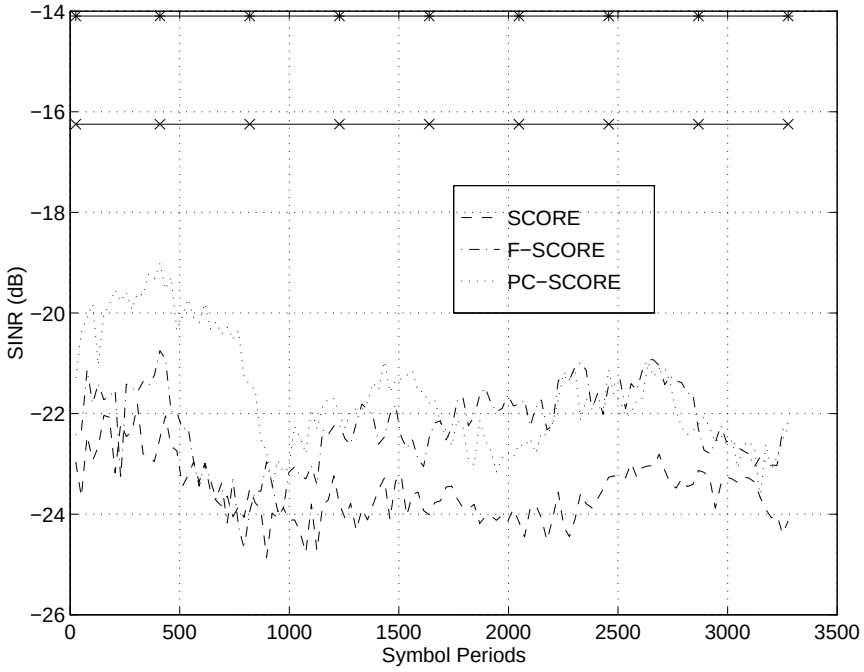

Figure 7.38: Cross SCORE Parabolic Array SINR, Test HNWB: Frequency Error = 0.04 % of Carrier Offset Frequency (2 kHz). *-: Optimum SINR, x-: Single Element SINR.

Figure 7.37

The performance of the SCORE algorithms under the frequency jitter and the carrier offset error environments are similar in terms of the mechanism of SINR degradation. The carrier offset error is considered more critical in terms of convergence performance because the carrier frequency error cannot be averaged out as seen for the jitter case in Figure 7.34. Windowing the received data points as suggested by Agee [2] would be expected to improve the robustness of SCORE to this type of error at the expense of extending the convergence time.

7.12 Direction of Arrival Effect on the Parabolic Antenna

It was observed that for the parabolic antenna the maximum theoretical gain was dependent on the direction of arrival of the desired signal. This direction determined the magnitude of the received signal and was dependent on the dimensions of the parabolic antenna and the location of the feeds.

For the above test conditions, the direction of arrival of the signal was 4.21° and the tilt angle was 0.23°. Table 7.1 shows that there are three elements that have a significant contribution with this direction of arrival.

Noise power simulations for test condition LNWB were re-run using a different direction of arrival. The received signal at the antenna elements for this new direction of arrival is displayed below in Table 7.2.

The following graphs show the result of the change of direction of the desired signal on the theoretical beamforming gain, as well as on the gain of using the single strongest antenna element.

Figures 7.39 to 7.41 can be compared with figures 7.27 to 7.29. These graphs show comparable convergence performance for the same signal environment. The only difference is in the direction of arrival of the desired signal.

Figure 7.42 shows the converged SINR value after an averaging time of 3000

Element Number	Received Magnitude	Received Angle	Gain (dB)
1	22.71	-10.00	27.12
2	15.35	-9.23	23.72
3	34.66	42.33	30.80
4	0.88	105.07	-1.12
5	4.23	130.51	12.52

Table 7.1: Direction of Arrival Information for the Parabolic Antenna: $\tau = 0.23°$ $\phi = 4.21°$

Element Number	Received Magnitude	Received Angle	Gain (dB)
1	37.66	-1.75	31.52
2	20.17	0.21	26.07
3	20.03	1.99	26.04
4	27.38	-2.44	28.75
5	20.25	-0.36	26.13

Table 7.2: Direction of Arrival Information for the Parabolic Antenna: $\tau = 0.0°$ $\phi = 3.5°$

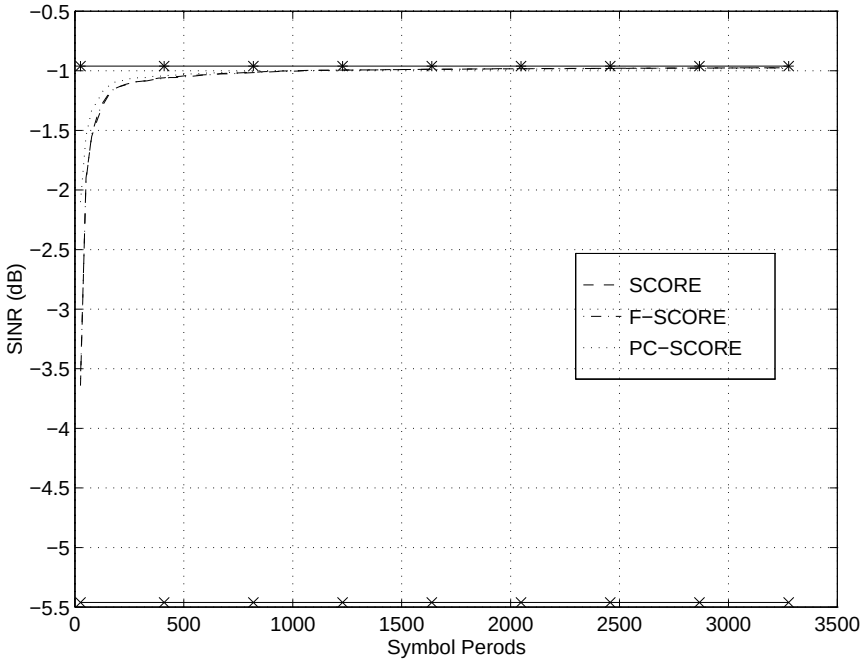

Figure 7.39: Cross SCORE Parabolic Antenna Performance: $\tau = 0°$ $\phi = 3.5°$. Received SINR=-36 dB. *-: Optimum SINR, x-: Single Element SINR.

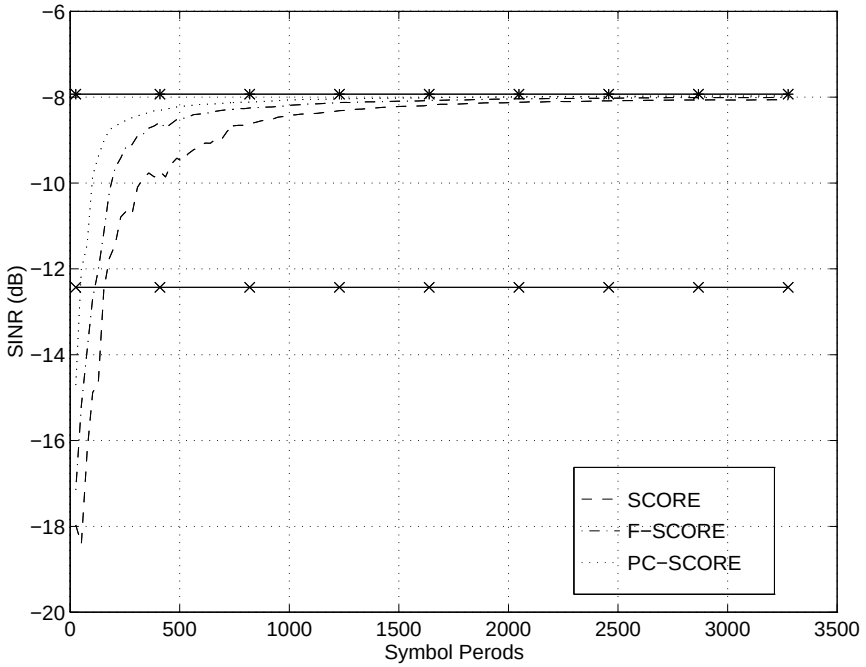

Figure 7.40: Cross SCORE Parabolic Antenna Performance: $\tau = 0°$ $\phi = 3.5°$. Received SINR=-42 dB. *-: Optimum SINR, x-: Single Element SINR.

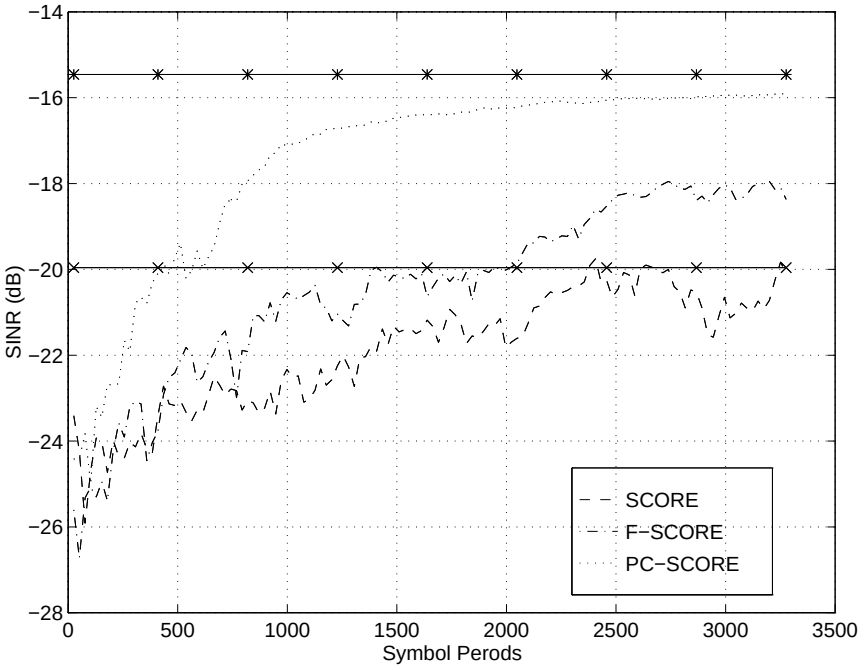

Figure 7.41: Cross SCORE Parabolic Antenna Performance: $\tau = 0°$ $\phi = 3.5°$. Received SINR=-50 dB. *-: Optimum SINR, x-: Single Element SINR.

symbols. Here the optimal and converged gain for the different scenarios, as compared to the single element case, is approximately 4 dB. For the same test conditions (test condition LNWB) Table 7.30, shows an optimum gain of approximately 2.5 dB due to beamforming.

The above comparison demonstrates the sensitivity of the performance of the parabolic antenna system on the the position of the antenna elements and the parabola geometry. The 1.5 dB difference between the two scenarios merits an investigation into the optimization of the antenna element location.

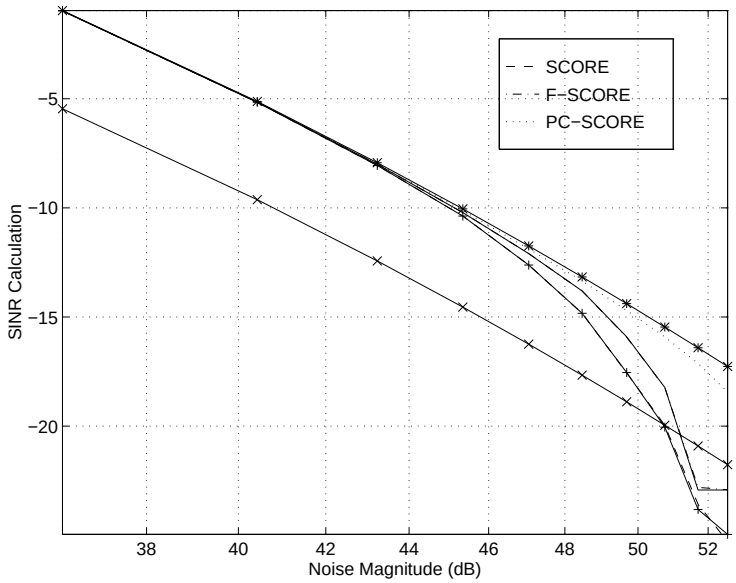

Figure 7.42: Cross SCORE Steady State SINR Parabolic Antenna Noise Performance: $\tau = 0°$ $\phi = 3.5°$. Received SINR=-50 dB. *-: Optimum SINR, x-: Single Element SINR.

Figure 7.43 shows the beam pattern of the new direction of arrival.

It is important to note that the parabolic antenna array is fundamentally different to the linear array with respect to the maximum beamforming gain possible. Each element of the linear array receives approximately the same amount of power from the desired signal. Therefore correct beamforming results in an increase in the signal power by the multiple of the number of feeds. This can be seen in the linear element simulation results (Figure 7.8) where the optimal SINR is 7 dB above the single

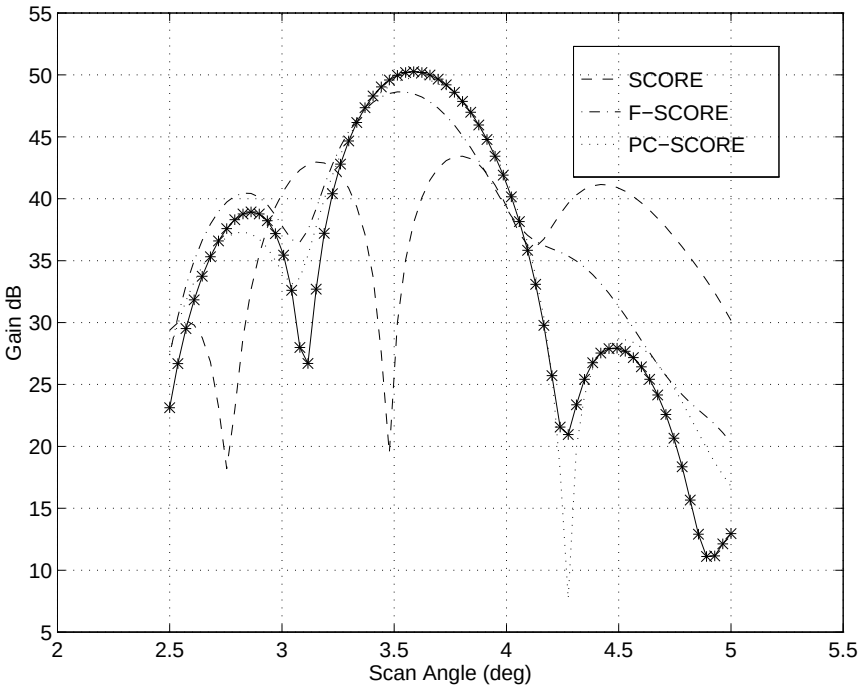

Figure 7.43: Cross SCORE Parabolic Antenna Beam Pattern: $\tau = 0°$ $\phi = 3.5°$. Received SINR=-50 dB. *-: Optimum SINR.

element SINR for a 5 element array.

The parabolic antenna acts like a "physical" beamformer. The reflector coherently adds the reflected components of the desired signal at a specific location on the feed plane. Therefore the received power of the desired signal for the parabolic antenna is dependent on its proximity to the focal point.

The reflector has much the same effect as a beamforming algorithm. A beamforming algorithm multiplies the signal received from different feeds by complex weights such that they add coherently.

Tables 7.1 and 7.2 show that only two or three antenna feeds receive a significant amount of power from the desired signal. This results in a maximum gain of only two to five dB of beamforming gain depending on the direction of arrival. More gain would be possible if the feeds were placed closer together on the feed plane, however there are physical limits to the feed density.

7.13 Performance Summary of Filtered SCORE Algorithms

The A-SCORE and FA-SCORE implementations show no significant difference from the SCORE and the F-SCORE performance respectively. This is because the initialization of the antenna weights in the A-SCORE and the FA-SCORE play no effect in the algorithm performance if the time averaged autocorrelation matrix of the signal environment is poor. Therefore the SCORE algorithm's performance would be best improved by optimizing the convergence rate as opposed to estimating the direction of arrival of the signal.

The PC-SCORE algorithm performed best in all conditions tested for the parabolic antenna array. This algorithm had significantly faster convergence rates, and showed convergence at SNR levels of -50 dB. The PC-SCORE technique also had an improved robustness performance with respect to errors in the carrier offset frequency.

The reason for this improvement is attributed to the reduction of the input noise

power to the beamformer, and the preservation of the received signal's phase information. The effects of this mechanism are detailed in Section 6.2.3.

The F-SCORE algorithm's performance was dependent on the bandwidth of the front end filter. There was an optimal filter level observed in the simulations which depended on the noise environment. The mechanism proposed for this behavior is the tradeoff between the dilation of the noise pulse in the time domain and the reduction of the noise power. The gains which result from optimization were small, and may not merit the additional computational expense.

The geometry of the parabolic antenna makes the maximum theoretical gain for beamforming dependent on the direction of arrival of the signal and the location of the feeds on the feed plane. This uneven distribution of the signal power on the feed plane means that only feed elements in close proximity to the focal point of the desired signal will contribute significantly to the beamforming gain. This is very different from linear arrays, where each element contributes the same amount to the beamforming gain.

Chapter 8

Conclusions and Future Work

Conclusions on the major areas that this thesis has investigated are presented in this chapter:

- The first area deals with the modeling of the physical conditions of the satellite environment. This area includes modeling the satellite channel, design of the antenna, and simulation of the coverage area.
- A summary of the theoretical effects of filtering is presented.
- Conclusions reached on the selection of the best SCORE technique and the most advantageous antenna array are given.
- The next section focuses on the performance of the proposed method of calculating the array response using cyclostationary techniques.
- The performance and performance comparison of the front-end filtering techniques with the Cross SCORE and the Least Squares SCORE are presented. Conclusions are drawn about the convergence rate, and the robustness of each algorithm.

A final summary is given on the feasibility of a geostationary satellite channel at the Ka band frequency using the property of cyclostationarity. In closing, suggested areas of future work are presented.

8.1 Conclusions on the Geostationary Satellite Channel

The link budget analysis of the satellite channel at the Ka frequency band for the geostationary satellite system showed that the system was noise limited (Section 3.2).

The major factors contributing to the channel attenuation were the free space loss, the thermal noise received from the wide message bandwidth, and the attenuation margin needed to account for changing atmospheric conditions. This is presented in the FDMA link budget calculation in Table 3.2. The high frequency of the channel made effects such as ionospheric distortion negligible due to their $1/f$ dependence (Section 3.3.12).

It was also noted that since the terrestrial receiver is stationary during transmission, and the channel fluctuations due to weather are slow, a long integration period for time averaging possible (Section 3.2). This makes the satellite channel potentially viable for cyclostationary beamforming using a long integration time under high noise environments.

8.2 Conclusions on Antenna Design

Based on the calculation techniques of this thesis, it is feasible to construct a high gain parabolic antenna to be used in the satellite link (Section 2.2). Present technology offers a number of candidates of feed antennas such as the Potter horn, or patch antennas which would satisfy the requirements of having a broad bandwidth, and small physical dimensions (Appendix A).

In this thesis an antenna was designed with an on focus gain of 53.4 dB. Reflector diameters were 1.67 m and 2.50 m for the uplink and downlink antennas respectively. Focal lengths were 1.21 m and 1.81 m for the uplink and downlink respectively (Table 2.7).

8.3 Conclusions on SCORE Algorithm Simulation Performance

The following sections relate the conclusions drawn about the general effect of the simulated robustness tests performed on the SCORE technique of beamforming.

8.3.0.1 SCORE Noise Performance

The front-end filtering techniques of SCORE improved the convergence rate performance of the beamforming system under high noise conditions. A summary of the conclusions based on the noise simulations of Section 7.8 are presented below:

Beamforming Convergence Rate Performance

The filtered SCORE techniques were shown to improve the convergence rate performance under high noise conditions after a correlation time of 3000 symbol periods. Filtered SCORE and PC SCORE began to show sub-optimal performance at received SNR levels of -45 dB and -48 dB under test conditions LNWB (Figure 7.30) and -43 dB and -50 dB for test conditions LNNB (Figure 7.15) respectively.

Optimum SNR Levels

High noise simulation showed that the filtering of the received signal would result in convergence of the SCORE algorithm to the optimum SNR level, as predicted in Section 6.2.10.

Optimum SNR levels for the high noise environment including antenna and beamforming gains were often below -10 dB for high noise environments (Section 7.8.2). The bulk of the optimal SNR gain for the simulations came from the antenna reflector geometry, (31 dB based on Figure 7.30), while only 2.5 dB of beamforming gain resulted for the worst case direction of arrival scenario (Section 7.8.3). This signal level is too low for reliable data performance.

For a practical system an additional gain in the optimum performance of 15 to 25 dB would be necessary. This gain could come from an increase in the parabolic antenna gain, or through the beamforming gain. The beamforming gain could be

increased using more antenna feed elements or through different antenna geometries.

8.3.0.2 SCORE Interference Performance

At low noise levels, the frequency rejection nature of the cyclostationary algorithms eliminates most of the effect of the interferer. In the channel environment modeled, the interfering signals will have a signal power well below the noise power level. Interference is therefore not expected to have a significant influence on the SINR values. It is for this reason that no significant effect of filtering was observed in the interference environment (Section 7.9).

8.3.0.3 SCORE Carrier Offset Jitter Performance

The effect of errors produced in the carrier offset frequency were observed. Based on different magnitudes of the deviation of the fluctuation it was observed that there is a threshold where a particular algorithm will converge to the optimum SINR value.

All algorithms showed a very high degree of sensitivity to this frequency jitter. Frequency deviations as low as 0.05 % (2.5 kHz) of the normalized sampling frequency at noise power levels of 40 dB and 12 dB for the parabolic and linear scenarios, respectively, resulted in a deterioration of SINR level as the averaging time increased (Section 7.10).

The mechanism for this behavior is based on the ability of the cyclostationary algorithm to correctly estimate the cyclic autocorrelation matrix. This ability degrades as the jitter increases. Furthermore, the longer the averaging time, the more sensitive the algorithm becomes to the error in the cyclic autocorrelation matrix. This resulted in the degradation of the SINR levels past approximately 500 symbol periods for the test conditions observed.

The noise level significantly effected the sensitivity of the algorithms to frequency jitter.

8.3.0.4 SCORE Offset Carrier Frequency Error Performance

All algorithms were demonstrated to be very sensitive to any error in the offset carrier frequency. The performance degradation resulted in a fluctuation in the SINR value as the time averaging period increased and eventually diverged. This periodic fluctuation increased as the offset carrier frequency error increased. The sensitivity to offset error in the carrier increased as the noise power level increased (Section 7.11).

In this test, the carrier signal appears much like an interferer to the cyclostationary algorithm which is eventually rejected by the algorithm. The frequency rejection capability of SCORE was presented in Section 6.2.

8.3.0.5 SCORE Front End Filter Bandwidth Performance

Variations of the bandwidth of the front-end filter did not have a significant effect on the convergence of the beamforming algorithms, front end filtering did have the ability to improve the performance of the SCORE algorithms especially under high noise environments. Therefore, bandwidth optimization to improve the convergence rate would be difficult to justify in terms of the computational expense in the test conditions studied.

Simulation results in relatively low noise environments showed that the SINR performance curve as a function of the bandwidth was almost flat. A wide range of filter bandwidths could therefore be selected with only a small deterioration of filter performance from the optimal parameter. Filter bandwidth design becomes marginally more important as the noise power of the environment increases (Section 7.7.1).

The positive effect of filtering reduces the noise power input into the beamformer. The draw back is that there is a pulse dilation of the input signal which results is caused by the finite noise frequency band, and any non-linear phase relationships to frequency (Section 6.2.3.2). The correlation of the noise terms in the time domain will result in an increase in the convergence time.

The PC-SCORE algorithm removes the non-ideal phase effect, and the performance deterioration was not observed for small bandwidths.

It is important to note that filtering only alters the convergence time of the algorithms, and does not affect the final convergence value. This was explained in Section 6.2 and supported by the simulation results.

8.3.1 SCORE Algorithm Performance Summary

Table 8.1 provides a summary of the SINR performance of the convergence results presented in Chapter 7. Values of the SINR convergence were taken at 500 symbol periods and 3000 symbol periods. It is important to note that these selected values do not indicate the convergence trends over the integration times.

8.4 Conclusions on Array Estimation using Cyclostationarity

The relative delay among elements for a known sinusoidal offset carrier was estimated using cyclostationarity. This information was used to calculate the array response of the antenna array. The application of array estimation to this thesis was an attempt at increasing the convergence rate of the SCORE algorithms. As shown in Chapter 7, estimating the array response did not improve the convergence rate for the SCORE algorithms under the test conditions chosen.

The effect of bandwidth, carrier frequency jitter, and carrier offset error follow the same trends as for the SCORE algorithms. The PC-Array algorithm performed the best, followed by the F-Array algorithm.

Test	Parameters	Opt SINR	Single Feed SINR	SCORE SINR dB (Symbols)					
				PC		F		SCORE	
				500	3000	500	3000	500	3000
Comparison: Cross SCORE and Least Squares SCORE									
LS	N=36, BW=.05 Hz	-3.3	-5.5	-3.5	-3.45	-4	-3.4	-3.6	-3.35
CS	N=36, BW=.05 Hz	-3.3	-5.5	-3.45	-3.44	-3.7	-3.44	-3.45	-3.35
Comparison: Filter Bandwidth									
CS	N=42, BW=.05 Hz	-10.2	-13.3	-10.8	-10.2	-14	-10.8	-14	-11
CS	N=42, BW=.2 Hz	-10.2	-13.3	-10.8	-10.2	-11.8	-10.3	-14	-10.8
CS	N=40, BW=.4 Hz	-7.5	-9.6	-8	-7.6	-8.5	-7.6	-8.2	-7.6
Comparison: Noise Power									
CS	N=36, BW=.2 Hz	-3.3	-5.5	-3.4	-3.3	-3.4	-3.3	-3.4	-3.3
CS	N=42, BW=.2 Hz	-10.2	-13.3	-10.8	-10.2	-11.8	-10.3	-14	-10.8
CS	N=50, BW=.2 Hz	-17.9	-20	-24.8	-19.2	-	-	-	-
Comparison: Frequency Jitter (Cross SCORE)									
LNWB	Dev=.04 % Hz	-7.5	-9.6	-7.8	-7.6	-8	-7.6	-8.4	-7.8
HNWB	Dev=.04 % Hz	-14.1	-16.2	-17.5	-14.8	-21	-17	-23	-21
LNNB	Dev=.2 % Hz	-7.5	-9.6	-7.8	-10.5	-9.5	-13.5	-9.5	-14
Comparison: Frequency Offset Error (Cross SCORE)									
LNWB	FErr=.04 % Hz	-7.5	-9.6	-8	-18	-9	-18	-9.5	-19
WNWB	FErr=.2 % Hz	-7.5	-9.6	-	-	-	-	-	-
HNWB	FErr=.04 % Hz	-14.1	-16	-20	-	-	-	-	-

Table 8.1: SCORE SINR Convergence Summary: Parabolic Antenna

8.4.1 Conclusions on Cyclostationary Array Estimation for the Linear Array

The linear array performs well in the estimation of the array response. Convergence rates based on symbol times are comparable to those of the least squares SCORE algorithm. All elements converge with approximately the same rate of convergence, and the convergence rate is independent of which element is chosen as the reference element.

8.4.2 Conclusions on Cyclostationary Array Estimation for the Parabolic Antenna

The parabolic antenna was observed to converge to a SINR level close to the SINR of the single element with the strongest received signal strength for the test conditions observed. This is well below the optimal level.

The reason for this poor performance arises from the gain of the reflector parabola. Each element's received signal strength depends upon its location on the feed plane relative to the direction of arrival of the signal. For this reason the selection of the reference element for the cyclostationary array estimation is critical. Selection of a reference element with a weak signal will significantly harm the convergence rate. This behavior is confirmed from the convergence plots of the individual array elements.

This dependence on array geometry and direction of arrival makes the cyclostationary array estimation technique poor for the satellite environment or for parabolic arrays in general. If some method of selecting the array element with the maximum desired signal strength could be found, then the dependence on the direction of arrival of the desired signal would be reduced.

8.5 Final System Design Proposal

Based on the simulation results in the previous chapters, and the link budget calculations, the following sections outline the design of a Ka broad band geostationary satellite system which uses cyclostationary beamforming. An FDM access scheme is assumed and no gain derived from coding is included in the link budget.

The system has been left as generic as possible and focuses exclusively on beamforming aspects of the link. No reference is made with respect to standards or protocols. Frequency reuse limits are not investigated. The goal is to provide a feasible system model that could be developed for a specific standard.

8.5.1 Phase-Compensated SCORE Algorithm

Based on the superior convergence ability and robustness of PC-SCORE (Section 7.13) this algorithm is best suited for Ka band satcom applications. The algorithm should use a front end filter with a bandwidth of .05 of the sampling frequency.

The PC-SCORE showed a significant performance improvement over SCORE and F-SCORE under high noise environments and limited convergence times (Section 7.8). It did not degrade in performance under low filter bandwidth conditions like F-SCORE (Section 7.7.1).

Based on the convergence rate performance improvement compared to F-SCORE, the increase in computation required for phase compensation was seen to be justified.

8.5.2 Link Budget

Based on the calculated link budget levels presented in Table 3.2, it is clear that for the system to have SINR levels required to achieve a bit error rate of less than 10^{-5} without coding gain and using the design parameters outlined in Table 1.1 is beyond the ability of the algorithms considered. The received SNR level of the desired signal (i.e. without the gain of the parabolic antenna) is -100.11 dB and -113.06 dB for the downlink and uplink respectively.

To overcome the noise problem, it is proposed that terrestrial systems use a highly directive antenna. This solution will increase system cost, and require some method of pointing the earth station antenna towards the satellite. Since the user is not expected to be moving during transmission, targeting the satellite is not expected to be a difficult problem.

Additional methods of increasing the link budget SNR could involve using higher gain antennas, system designs which result in higher beamforming gains (more antenna elements) or by operating at lower orbits or frequency bands. These techniques were not pursued in this thesis.

8.5.3 Receiver Antenna

The terrestrial antenna considered to improve the link budget is described in [31]. This antenna is .5 m in diameter, operates from 19 to 29 GHz, with a gain of 38.7 dB and 42.3 dB respectively. This antenna is ideal for the satellite system application.

8.5.4 Uplink System Limits

Using the antenna gain described in Section 8.5.3, the received power at the satellite based on the calculations in Table 3.2 would be -74.28 dB. This SNR is beyond the convergence capability of the beamforming algorithms studied over the 3000 symbol periods considered. If an optimal beamforming gain of 4 dB could be achieved, then using a parabolic antenna gain of 48.1 dB the final SINR would be -22.18 dB which is 32.18 dB below the SINR needed for a BER of 10^{-5}. This deficit could be made up by altering the system design.

8.5.5 Downlink System Limits

A method of providing a reference signal from the terrestrial user is required in any access scheme. This signal is needed to allow the satellite downlink to beamform on the user. Two methods of providing a reference signal could be achieved either

by using a pilot tone, or through frequency scaling the beam weights of the uplink connection. The potential source of error with frequency scaling is the need for accurate calibration of the array manifold, and accurate knowledge of the carrier frequencies being used.

Using a terrestrial antenna design such as the one presented in [31] with a 42.3 dB gain would result in a received SINR of -57.71 dB at the antenna elements. Assuming that an optimal beamforming gain of 4 dB could be achieved using a 48.1 dB satellite antenna, the final SINR would be -5.61 dB which is 15.61 dB below the SINR needed for a BER of 10^{-5}. It is conceivable that a changes in the system design could achieve the required BER.

In the down link budget, a 15 dB margin was given to atmospheric losses. From Table D.3 the down link would suffer on average only 10 fades of more than 1000 seconds per year and only 100 fades of more than 10 seconds per year.

Link Condition	Uplink (dB)	Downlink (dB)
Received SINR	-112.98	-100.01
Received SINR (Earth Antenna 38.7/42.3 dB Up/Down Gain)	-74.28	-57.71
Margin below Beamforming Threshold (-50 dB)	24.28	7.71
SINR with Satellite Reflector Gain (48.1 dB)	-26.18	-9.61
SINR assuming Optimal Beamforming (4 dB)	-22.18	-5.61
10^{-5} BER Margin	-32.18	-15.61

Table 8.2: SINR Calculations of Proposed Satellite System

8.5.6 System Robustness

As shown in Chapter 7 the cyclostationary SCORE algorithms are highly sensitive to any error in the offset carrier. The requirement for highly accurate oscillators and hardware modifications to limit temperature fluctuations etc. on the satellite and the receiver would greatly increase the cost of the system. It is unclear that even these modifications would ensure reliable performance. Other techniques such as frequency tracking may over come this problem.

8.5.7 Proposed System Specification Modifications and Performance Observations

The specifications for this thesis were chosen based on geostationary satellite communications systems which operated at lower frequencies and at lower bandwidths. The link budget calculations show that parabolic antenna beamforming alone cannot achieve the E_b/N_o required for data rate service. Additional gain will have to be provided using coding, power, or bandwidth trade-offs.

The investigation of the Ka band geostationary satellite link using parabolic beamforming did reveal several important areas to be considered in future system designs (Chapter 7). The satellite channel for a broadband service at the Ka frequency band was shown to be noise limited. The SCORE algorithms were modified to work under high noise environments. Finally, the limited application of the parabolic antenna to beamforming was characterized.

8.6 Suggested Future Areas of Investigation

In this thesis many aspects of cyclostationarity were investigated through simulation. Where possible, theoretical explanations were offered to explain the trends observed, however the focus of the thesis was more on establishing the important parameters affecting the performance of the cyclostationary algorithms in high noise environments. The following sections are a list of some of the areas which merit further investigation.

8.6.1 Channel Simulation Model

Investigation into wireless satellite communications at the Ka band is an area of ongoing research. The calculations used in this thesis combined statistical models, with empirical data from the most up to date sources available. Since this area of research constantly being updated, any future application of beamforming to Ka satellite communications must keep current with new research.

8.6.2 Antenna and Feed Plane Design

The antenna designed in this thesis was accurate to first order effects. Increased gains in antenna efficiency and performance designs may be possible using more advanced design tools which were not available to the author.

Antenna effects which should be more thoroughly investigated included element coupling, and optimization of inter-element distance to produce maximum gain (Section 2.3.6).

Techniques need to be investigated to maximize the gain of the received signal while minimizing the number of elements, and effect of user location on beamforming performance. These gains would depend on the pattern of the feeds on the feed plane, and antenna beam width optimization.

8.6.3 Noise Performance Limit

The beamforming ability of the different SCORE algorithms should be characterized with respect to noise performance. Simulation results indicate that the different algorithms begin to degrade at a certain received SNR level. The factors which contribute to this degradation threshold should be characterized in terms of the channel, and the filter specifications.

8.6.4 Interference Performance

It was shown that the presence of a single interferer in a noise limited environment does not significantly affect the performance of the algorithms. The effect of the interference on the convergence of different algorithms should be investigated for lower levels of noise power relative to the desired signal power and interference power. While this characterization is not relevant to this satellite channel model, it would be relevant to terrestrial systems or satellite systems operating at lower frequencies.

8.6.5 Frequency Jitter Performance

Simulations showed a high degree of sensitivity of the algorithms to frequency jitter at the cyclostationary frequency. Research in this area should focus on more realistic models of frequency jitter. Techniques which may make the algorithms more robust to jitter should also be investigated. This might include methods of weighting the values of the received signal samples based on the time of arrival.

It was also observed in the simulations that there might be a threshold at which the algorithms investigated will converge to a stable level. This threshold appears to depend on the noise power level, as well as the jitter deviation. A theoretical explanation of this behavior should be investigated.

8.6.6 Offset Frequency Error

All algorithms were very sensitive to any error in the offset cyclostationary frequency. This was noted by a periodic fluctuation of the SINR which depends on the magnitude of the frequency error. A relation between the frequency error, noise power level, and magnitude and period of the SINR fluctuations should be investigated.

8.6.7 Filter Optimization

Only one filter type was investigated in this thesis. Different parameters for the transitional filters should be investigated, as well as other filter types which trade off

attenuation with phase distortion.

Section 6.2 offers an explanation as to the mechanism of how filtering is advantageous to beamforming in high noise environments. This model should be explored further to characterize the significance of the phase errors and noise power reduction introduced by the filter. Such a relation could possible offer a method of adaptively selecting an optimal filter bandwidth depending on the noise conditions.

8.6.8 Cyclostationary Array Estimation

Theoretical relationships for the performance of the proposed cyclostationary array estimates should be found. This would include the effect of the convergence rate with the selection of reference elements with varying signal strengths, robustness and the sensitivity of the array estimation with respect to the error in the calculated array response. This result would indicate to which environment this array estimation technique could be applied.

The binary search algorithm used to find the delay among elements is simple but lacks robustness. The performance of the cyclostationary array estimation may be improved by a more robust technique, and one that converges faster.

A method of estimating the antenna element with the highest received power of the desired signal should be found. This would minimize the dependence on the parabolic configuration on the direction of arrival of the desired signal, and is expected to improve the convergence rate performance.

8.6.9 Low Earth Orbit Satellite Applications

The large amount of attenuation which results from the geostationary orbit is a major cost in the link budget calculation. A low earth orbit application may improve the link budget, and make the satellite system more robust. There would be an increase in complexity in the system which would require tracking of the target location due to the asynchronous orbit of the satellite with the earth.

8.6.10 Terrestrial Applications

The linear array as well as the least squares SCORE technique showed convergence trends at lower noise power levels. An investigation should be made into the application of these techniques to lower noise environments such as for terrestrial applications. Terrestrial applications would require simpler algorithms and array configurations which are satisfied by the least squares SCORE and the linear array respectively.

8.6.11 Algorithm Optimization

This thesis neglected any attempt to calculate the computational complexity of the algorithms. To complete the investigation, more cyclostationary beamforming techniques should be compared to the SCORE methods presented here on the basis of convergence and complexity. In particular, the sub-space constrained SCORE techniques should be compared to the front end filtering techniques. It is expected that constraining the weight vector to the signal sub-space will have a similar effect as front end filtering.

Appendix A

Antenna Design and Simulation Methods

This appendix outlines the methods followed to calculate the offset parabolic antenna used in the link budget calculation and the beamforming simulation of the satellite system. Background on antenna feed elements and filter design methods are also presented.

A.1 Calculation of the Offset Parabolic Reflector Dimensions

The formulas for the design of a Parabolic Reflector are give by Lee and Rahmat-Samii. [26] They can be used to provide approximate dimensions for a parabolic antenna which satisfies certain parameters. These dimensions may then be modified using a more accurate antenna simulation program developed by Duggan to meet the exact specifications. Figure A.1 shows the design geometry for the offset reflector antenna.

The basic equation for the parabolic reflector surface can be found using:

$$z = \frac{x^2 + y^2}{4F} - F \tag{A.1}$$

The feed radiation pattern is modeled for offset feeds using:

$$g(\theta') = (\cos(\theta'))^q \tag{A.2}$$

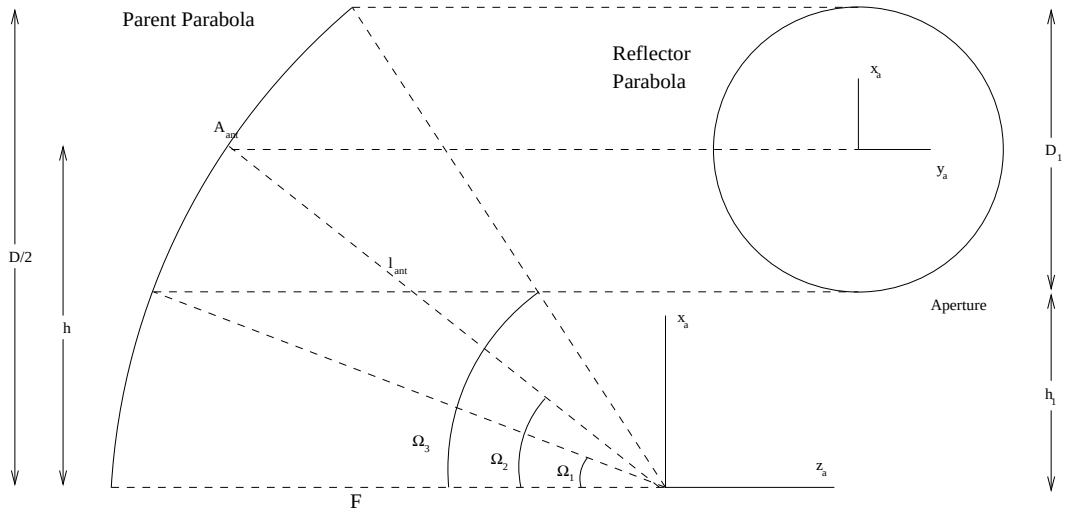

Figure A.1: Offset Parabolic Antenna Schematic

$$q = \frac{\log(1-\triangle)}{\log(\cos(\frac{1}{2}(\Omega_2 - \Omega_1)))} \tag{A.3}$$

The feed employed in the thesis is symmetric in its electric and magnetic components. $\triangle$ is the aperture taper.

The edge taper (ET) is used to measure the electromagnetic distribution of radiation across the reflector. This quantity may be used to find the antenna's efficiency.

$$ET = |20\log_{10}(1-\triangle)| \tag{A.4}$$

The geometry of the reflector is completely determined by the focal length, the reflector diameter and the offset height. To arrive at these dimensions, the following design information must be given.

- The sidelobe level of the secondary pattern must be determined.
- The half power beamwidth must be defined.
- The maximum scan angle in the z-y, and z-x plane must be calculated.
- The offset height of the reflector must be decided.

Calculated and specified parameters must satisfy the following conditions in order for the equations which are presented to be valid.

$$
\begin{aligned}
0 &< \triangle &< 0.85 \\
0 &< GL &< 3 \\
(\tfrac{F}{D}) &< 1.5 & \\
\Omega_3 &< 30 \text{ deg} & \\
\theta_3 &\approx \tan(\theta_3) &
\end{aligned}
$$

A.2 Design Procedure

The following steps outline the design procedure for finding the geometry of the offset parabola according to [26]

- The aperture taper is found using the following equation:

$$\triangle = \sum_{n=0}^{3} \alpha_n (\frac{SL}{10})^n \tag{A.5}$$

  The coefficients for the offset feed location are:

  α_0 = -8.87 α_1 = 9.32 α_2 = -3.00 α_3 = 0.32

- The aperture efficiency for the offset feed location may be determined graphically based on the edge taper value (ET) or the aperture taper ($\triangle$). The optimum efficiency occurs at an edge taper value of 11.00 dB [26].

- The diameter for the parent parabola is calculated below. The reflector parabola is the circular portion of the parent parabola to which the feed plane is directed.

$$\frac{D_1}{\lambda} = \frac{1}{\pi \sin(\theta_1)} \sum_{n=0}^{3} \gamma_n \triangle^n \tag{A.6}$$

$$D = 2(h_1 + D_1) \tag{A.7}$$

  The coefficients used in calculating the diameter are:

  γ_0 = 1.61 γ_1 = 0.57 γ_2 = -1.43 γ_3 = 1.47

- The focal length of the antenna is determined by the allowable gain loss (GL) and the furthermost scan angle θ_1. This length may be found for gain losses less than 3 dB using

$$\frac{F}{D} = \frac{\pi(\sin(\theta_3)/\sin(\theta_1))}{190\kappa\cos^{-1}[1-(GL/5)]} \quad (A.8)$$

$$k = 1-\exp(-0.12\sqrt{D_1/\lambda}) \quad (A.9)$$

- The length from the reflector focus to the reflector center is given by:

$$l = F[1+(\frac{h}{2F})^2]^{\frac{1}{2}} \quad (A.10)$$

- The required angles needed for subsequent calculations including the angle and orientation of the feed plane may be obtained using:

$$\Omega_1 = (\frac{h_1}{F})[1-\frac{1}{4}(\frac{h_1}{F})^2]^{-1} \quad (A.11)$$

$$\Omega_2 = (\frac{D}{2F})[1-\frac{1}{4}(\frac{D}{2F})^2]^{-1} \quad (A.12)$$

$$\Omega_3 = (\frac{h}{F})[1-\frac{1}{4}(\frac{h}{F})^2]^{-1} \quad (A.13)$$

- The actual direction of the beam aimed at the focus is altered slightly due to the reflector geometry. The amount that the beam deviates from the true ray is determined by the Beam Deviation Factor (BDF) It may be calculated as follows:

$$BDF = \tau[1-.72\exp(-3.2\frac{F}{\tau D_1})] \quad (A.14)$$

$$\tau = \frac{\cos(\Omega_3)+\cos(\Omega_3-\Omega_1)}{1+\cos(\Omega_3-\Omega_1)} \quad (A.15)$$

$$\theta_2 = \frac{1}{2}\tan^{-1}[(BDF)\frac{d}{l}] \quad (A.16)$$

Where θ_2 is the actual direction of the ray. d is the element spacing on the feed plane.

- The criteria to insure no feed blockage is to specify the height of the offset reflector such that the lower edge of the reflector clears the feed array plane. This condition is satisfied if

$$h_1 \quad > \quad d_{max|ant}[1 - (\frac{h}{l_{ant}})^2]^{\frac{1}{2}} \tag{A.17}$$

In order to determine the number of elements required for the antenna feed, the following calculation is performed. [33]

$$N \quad \approx \quad \frac{Area}{2764(\lambda/D_1)^2} \tag{A.18}$$

The area is calculated in terms of degrees squared and represents a circular disk defined by the maximum scan angle θ_{max}. The elements are assumed to be placed in a hexagonal pattern.

The maximum size of the feed element aperture can be calculated using Equation (A.19) [33]. This formula is based on the need for low cross polerization levels for a multiple beam antenna. The result was derived for circular polerization using horn feeds and giving cross polerization levels below 20 dB. The numbers generated by this formula will be used as a guideline for antenna element spacing. This feed size approximation assumed Potter horn feeds which provided low cross polar radiation levels in the antenna designed in [33].

$$\frac{d}{\lambda} \quad \approx \quad 1.25 * (F/D_1) \tag{A.19}$$

A.3 Approximate Radiation Pattern

The following formula presented in [26] can be used to approximate the radiation pattern produced by the calculated reflector geometry. The patterns calculated using matlab were found to produce a radiation pattern close to the design parameters specified. The final radiation pattern used in the model system will be calculated from [11]. The variable λ' ranges from 0 to 2π.

$$g(u) = \frac{1}{1-0.5\triangle}\left(\frac{2J_1(u)}{u} + \triangle\left[\frac{2J_2}{u^2} - \frac{2J_1(u)}{u}\right]\right) \quad (A.20)$$

$$u = \pi D_1 \sin(\lambda') \quad (A.21)$$

A.4 Antenna Pattern Program

To accurately perform beamforming calculations, it was necessary to get a more detailed calculation of the antenna beam pattern. It was necessary to find a program that would accurately account for design parameters such as feed location, feed polerization, feed plane geometry, and which would accurately calculate the electrical and magnetic fields based on physical equations.

This program was provided by Duggan in his master's thesis [11], and has been used with his permission. The program was modified to allow the selection of a tilt angle which would give beam pattern calculations in a direction off the horizontal plane of the satellite antenna. Below is a brief summary of the principles upon which the program was developed. For an account of the formulas used, refer to [11]

A.4.1 Parabolic Antenna Theory and Approximations

The electric field pattern is found through the solution of the radiation integral. This integral is simplified using far field approximations. The program numerically calculates the integral using the Fourier-Bessel Method.

In order to model the scattering of the electric field on the parabola, the physical optics approximation is used. This assumes that scattering takes place as if there was an infinite tangential plane at the point of intersection of the antenna. It has been shown that this method is accurate for the main beam, but the accuracy decreases for successive sidelobes.

A.4.2 Parameter Specification

The following parameters must be specified to calculated the antenna's radiation pattern.

Focal length	Radius of parabola
Offset height	Number of feeds
Polerization Magnitude X	Polerization Magnitude Y
Phase offset of Polerization	Number of iterations (2*)
Order of Bessel Function	

Table A.1: Antenna Parameters for the Offset Parabolic Antenna Program

These parameters are selected based on the system to be simulated, and through the geometric calculations based on the specifications as computed by the simplifying formulas presented in [26]. The output of the antenna program is compared to the desired specifications and modifications are made to meet the original specifications. Dimensions are also bounded by the physical limits of existing systems referenced in the literature search.

Feed plane X coordinate	Feed Plane Y coordinate
Angle with Antenna X Axis (α)	Angle with Y Axis (γ)
Angle with Antenna Z Axis (β)	Electric field Directivity of feed
Magnetic field Directivity of feed	

Table A.2: Feed Parameters for the Offset Parabolic Antenna Program

A.5 Feed Design

A design of an antenna feed that would accurately model all of the electromagnetic properties is beyond the scope of this thesis. Instead, some of the more significant design considerations are presented, along with some references from specific satellite projects.

The antenna feeds needed in this thesis will have to support a frequency range of approximately 2 GHz. The transmit frequency will be either 20 or 30 GHz. This requires that the feed have a frequency bandwidth of 10% and 6.7% respectively. It is also necessary that the feeds be small in size to allow for a large antenna gain while insuring thorough coverage of the proposed service area. Using recent developments in microwave technologies and the formulas presented in [33], these goals can be achieved.

A.5.1 Maximum Theoretical Efficiency of Multiple Beam Antennas

The electromagnetic interaction of the antenna feed matrix causes mutual interference which can limit the efficiency of the overall antenna. In the paper by DuFort [10] he shows that the maximum efficiency for a multiple beam antenna is approximately 50 % for large antenna arrays. This proof is based on the Stein Limit [39] which shows that the maximum efficiency possible is the ratio of the average to the peak value of the aperture power distribution. [10] shows this to be approximately 50 %. DuFort goes on to prove that the efficiency limit can be achieved by selectively attenuating the signal in the aperture.

In the antenna feed plane design for this thesis, the maximum efficiency is assumed to be achieved and the limit of 50 % efficiency is used in the link budget calculation. The specific details in the feed design to achieve the 50 % limit are not derived. For more detail on optimal feed plane efficiency design, [10] may be referenced.

A.5.2 Beamwidth of Antenna Feed Elements

Antenna feed elements have a characteristic bandwidth of operation. As a result, it was necessary to insure that today's technology could provide antenna elements that could operate at Ka band frequencies, while providing a bandwidth that would allow complete recovery of the message signal for processing.

In Kraus [22] a formula is presented for finding the half power bandwidth of an antenna feed. This may be calculated as follows:

$$\triangle f_{hp} = \frac{f_o}{Q} \tag{A.22}$$

Q $\Rightarrow$ Quality factor

f_{hp} $\Rightarrow$ Half power frequency

f_o $\Rightarrow$ Center frequency (Hz)

Where the quality factor of the feed Q can be calculated from the following formulas:

$$Q = \frac{2\pi f_o L}{R_f + R_l + R_r} \tag{A.23}$$

R_f $\Rightarrow$ Resistance of the feed Ω

R_l $\Rightarrow$ Loss Resistance Ω

R_r $\Rightarrow$ Radiation Resistance Ω

f_o $\Rightarrow$ Center frequency (Hz)

The resistance value calculations can be very involved depending on the geometry of the feed selected. Often these parameters are determined through empirical measurements.

As an antenna becomes small in terms of electrical wavelength, the following effects take place:

- The frequency bandwidth becomes narrow.
- Radiation efficiency becomes low.
- The Voltage Standing Wave Ratio (VSWR) becomes high.

Hirasawa [20] presents detailed design formulas for electrically small antennas and patch antenna design which use a variety of techniques to compensate for these trends. Some of these techniques are outlined below.

A.5.3 Wide Band Techniques for Antenna Feeds

A.5.3.1 Patch Antenna

The patch antenna is typically characterized by a ground plane covered with a dielectric material. A conductor is placed on top of the substrait in accordance to some design specification A.2. The dimensions of the patch antenna can be of the order of a wavelength or smaller.

Patch Antenna

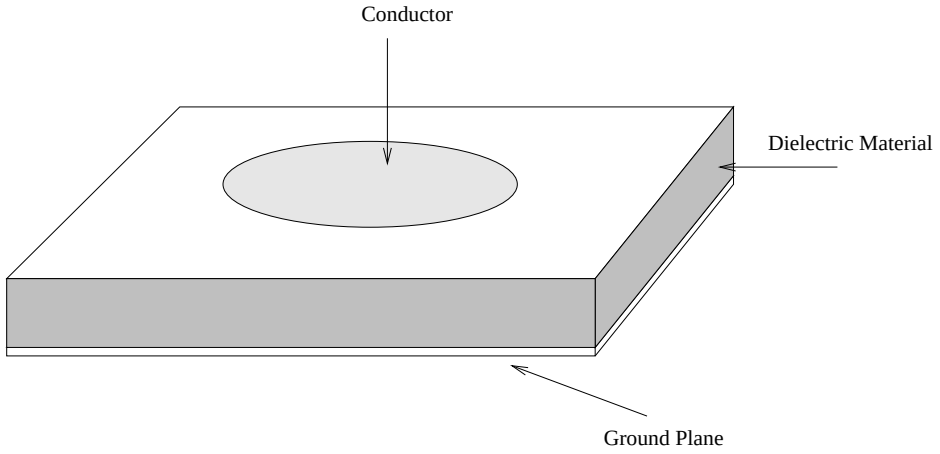

Planar F Antenna

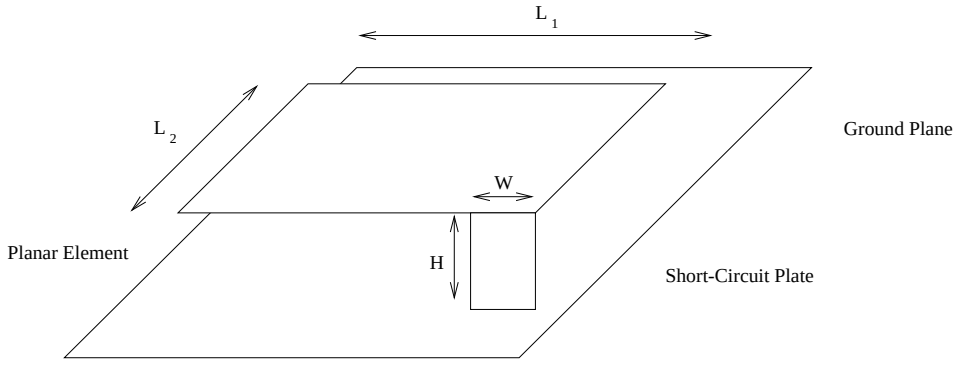

Figure A.2: Simple Diagram of a Patch and Planar F Antenna

The patch antenna has the following advantages, depending on the design chosen:

[20]

- Low profile and conformal structure.
- Suitable for mass production (low cost).
- Easy for miniaturization and light weight.
- Structurally robust.
- Integration of a radiator and feeding system is possible.

The standard bandwidth of a patch antenna is 1 - 2 %. [20]

The small size and light weight of the patch antenna make it a good candidate for a satellite antenna feed, and the offset design of the parabolic antenna would overcome the interference of the received signal which might be caused by the feed plane. The standard patch antenna would have a bandwidth that is several percent too small for the broadband application, however [20] presents methods for increasing the patch antenna bandwidth. Some of these techniques are presented below.

- Low Unloaded Q Substraight:

  By selecting a substraight that results in a low Q value, the band width of the patch antenna may be increased to approximately 8.75 % of the modulating frequency.

- Double Resonance Phenomenon

  This technique uses a parasitic element to creat a second resonant frequency. The result is an increase in bandwidth of up to 8.5 % of the modulating frequency.

- Wideband Impedance Matching Network.

  Through the use of transmission line broadband impedance matching techniques the bandwidth of the patch antenna can be increased to 9.1 % of the modulating frequency.

To increase these bandwidths further, a combination of techniques can be employed.

A.5.3.2 Planar Inverted F Antenna

The Planar inverted F typically consists of a rectangular planar element, ground plane, and a short circuit plate [20] (Figure A.2). These antennas are low profile, and have been designed for various portable communication applications.

This type of antenna can be designed to have dimensions less than a wavelength. The bandwidth of the antenna can be increased by increasing the height dimension up to a maximum of 14% of the modulating frequency.

A.5.3.3 Planar Spiral Antennas

The text by Elliott [12] contains the design formulas for planar spiral antennas. These antennas provide a very large bandwidth and a low profile by using micro strip techniques. The drawback is that the antenna's physical dimensions are large, which may make dense clustering of feeds difficult.

A.5.3.4 Potter Horn Antenna

In the work done by Rao et. al. [33] a 45 GHz multi-beam antenna was designed. The design used 121 Potter horn feeds to achieve coverage in an 8° diameter. Physical modeling and theoretical calculations showed that the system operated well within 43.5 to 45.5 GHz. This corresponds to 4.5 % of the modulation bandwidth. The the Potter Horn antenna can achieve a 30 dB side lobe level of suppression which makes it a good candidate for the feed antenna required.

A.6 Filter Implementation

It is expected that the satellite system will be noise limited, and therefore selective filtering is expected to improve the performance of the system.

Two filter designs operating on two parallel branches are required. The first branch will filter out all noise and message components except for the known carrier frequency. This path will be used for calculating the antenna weights based on the cyclostationary properties of the carrier. A schematic of the proposed scheme can be referred to in A.3

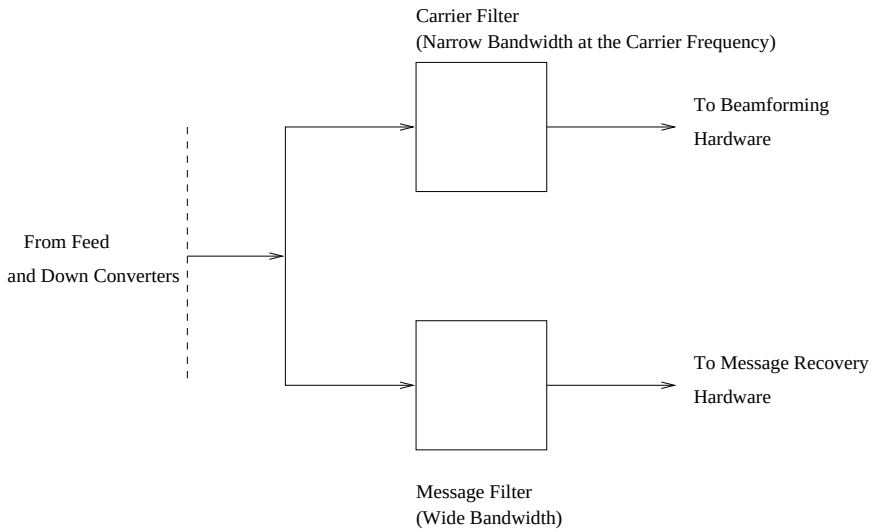

Figure A.3: Broad and Narrow band Filter Schematic for Message and Carrier Recovery

The second filter will be a wide band filter, which will pass only the information on the desired channel. This filtered branch will be used to recover the message data. Either filter may be implemented using analogue or digital techniques, depending on the resources available on the satellite. The chosen filters must also preserve phase information necessary for beamforming and signal combining as much as possible while providing a large attenuation in the stop band.

The critical filter for the investigation of beamforming is the filter on the cyclostationary branch. The message filter is expected to improve performance of the system through out of band noise rejection, but would not affect the performance of the cyclostationary algorithms. For this reason, only the cyclostationary filter is designed and simulated in this thesis.

A transitional filter will be used to achieve the tradeoff between passband and

phase distortion of the cyclostationary information path. [23] The design of this filter is presented below.

A.7 Transitional Filter Design

The transitional filter combines the relatively high attenuation of the Butterworth filter with the ideal phase response of the Bessel filter. This is done through a weighting of the pole location of the two filters on the complex plane. The maximum number of poles for the filter was limited to 25 due to software simulation limitations. The following method was used to find the Transitional filter poles:

- The Butterworth filter poles were calculated according to the required specification.
- The Bessel filter poles were calculated according to the required specification.
- The pole location of the Transitional filter was found by weighting the poles of the Butterworth and Bessel pole locations and averaging the weighted values.

$$P_{trans} = \frac{W_{Btt}P_{Btt} + W_{Bss}P_{Bss}}{W_{Btt} + W_{Bss}} \tag{A.24}$$

$P_{trans} \Rightarrow$ Complex Poles of the transitional filter
$P_{Btt} \Rightarrow$ Complex Poles of the Butterworth filter
$P_{Bss} \Rightarrow$ Complex Poles of the Bessel filter
$W_{Btt} \Rightarrow$ Weighting factor of the Butterworth filter
$W_{Bss} \Rightarrow$ Weighting factor of the Bessel filter

A.8 Butterworth Pole Location

The Butterworth poles provide the transitional filter with the necessary attenuation needed to achieve the specification. The design is done with respect to normalized frequencies. The pole locations may be found as follows:

$$|k_{Btt}(j\omega)| = \epsilon_{Btt}\omega^N \quad \text{(A.25)}$$

Here $k_{Btt}(j\omega)$ is the characteristic polynomial of the filter transfer function, ϵ_{Btt} is a scale factor, and N is the order of the filter.

$$A_{Btt}(\omega) = 10\log[1 + |k_{Btt}(j\omega)| \quad \text{(A.26)}$$

$$= 10\log[1 + \epsilon_{Btt}^2\omega^{2N}] \quad \text{(A.27)}$$

$A_{Btt}(\omega)$ represents the attenuation at a specific frequency. If the maximum attenuation at the normalized passband frequency is specified as A_{max}, and the minimum stopband attenuation is specified as A_{min}, then ϵ_{Btt} and N may be solved. Let Ω_s be the stopband frequency.

$$\epsilon_{Btt} = \sqrt{10^{A_{max}/10} - 1} \quad \text{(A.28)}$$

$$N_{Btt} = \frac{\log\sqrt{\frac{10^{A_{min}/10}-1}{10^{A_{max}/10}-1}}}{\log(\Omega_s)} \quad \text{(A.29)}$$

The pole location on the complex plane may be found as follows:

$$P_{Btt} = (\frac{1}{\epsilon_{Btt}})^{\frac{1}{N}} \cdot \exp^{j[\frac{-\pi}{2}+\frac{\pi}{2N}+\frac{k\pi}{N}]} \quad \text{(A.30)}$$

Where $k = [0, 1...2N-1]$ The poles are symmetric about the complex axis. Only those poles on the left half plane are stable.

A.9 Bessel Pole Location

The Bessel poles provide the transitional filter with a constant phase shift over a specified frequency required for correct performance. The design is done with respect to normalized frequencies. The pole locations may be found as follows:

The Bessel transfer function is

$$H_{Bss}(s) = \frac{a_o}{M_{Bss|2} + N_{Bss|2}} \tag{A.31}$$

$$\triangleq M_{Bss}(s) + N_{Bss}(s) \tag{A.32}$$

$$M_{Bss|2}(s) = q_0 + q_2 s^2 + ... \tag{A.33}$$

$$N_{Bss|2}(s) = q_1 s^1 + q_3 s^3 + ... \tag{A.34}$$

$$M_{Bss}(s) = \frac{q_0 M_{Bss|2}(s)}{M^2_{Bss}(s) - N^2_{Bss|2}(s)} \tag{A.35}$$

$$N_{Bss}(s) = \frac{-q_0 N_{Bss|2}(s)}{M^2_{Bss}(s) - N^2_{Bss|2}(s)} \tag{A.36}$$

The quantity of interest in the Bessel filter is the delay over the passband which is ideally uniform. The delay may be calculated using the following formula:

$$\tau_{Bss}(\omega) = \frac{M_{Bss2}(\omega)N'_{Bss2}(\omega) - N_{Bss2}(\omega)M'_{Bss2}(\omega)}{M^2_{Bss2}(\omega) - N^2_{Bss2}(\omega)} \tag{A.37}$$

Where the prime denotes differentiation with respect to ω. The solution to the above equation for delay may be approximated using Bessel polynomials from which the Bessel filter poles may be found.

Appendix B

Satellite Footprint Calculations

The satellite footprints are contour plots of lines of equal power which originate from the satellite and intersect the earth. This information is needed to determine the location of the feed element with the appropriate coverage area on the ground. A simple method of calculating the main lobe footprints of a geostationary satellite was derived by Spy and Haakinson [38]. The the technique is limited by the following restriction.

- No consideration is given to the interaction of antenna radiation with atmosphere.
- The small variation of received power due to slightly differing distances from the different transmitter locations within a footprint are ignored. This power variation is due to the curvature of the earth, and is small for small beam footprints.
- The earth is assumed to be perfectly spherical.
- Only the main lobe pattern is calculated.

This technique requires knowledge of the satellite longitude location μ_{es}, the aim point location (μ_{eA}, ρ_{eA}), and the beam width θ_{bw}. The program finds a cone of constant power density which corresponds to the main lobe of the antenna pattern.

Once this cone is defined from the satellite position , a locus of intersection of points with the earth are calculated.

The satellite location for geosynchronous orbit is defined as

$$s = (\frac{GMP^2}{4\pi^2})^{\frac{1}{3}} \quad \text{(B.1)}$$

$$= 6.62R \quad \text{(B.2)}$$

The formulas required for the calculation of the intersection of a line from the satellite with the earth are presented below. The beam footprint was found by iteratively performing the calculation for the beam for different ϕ_{bw} values.

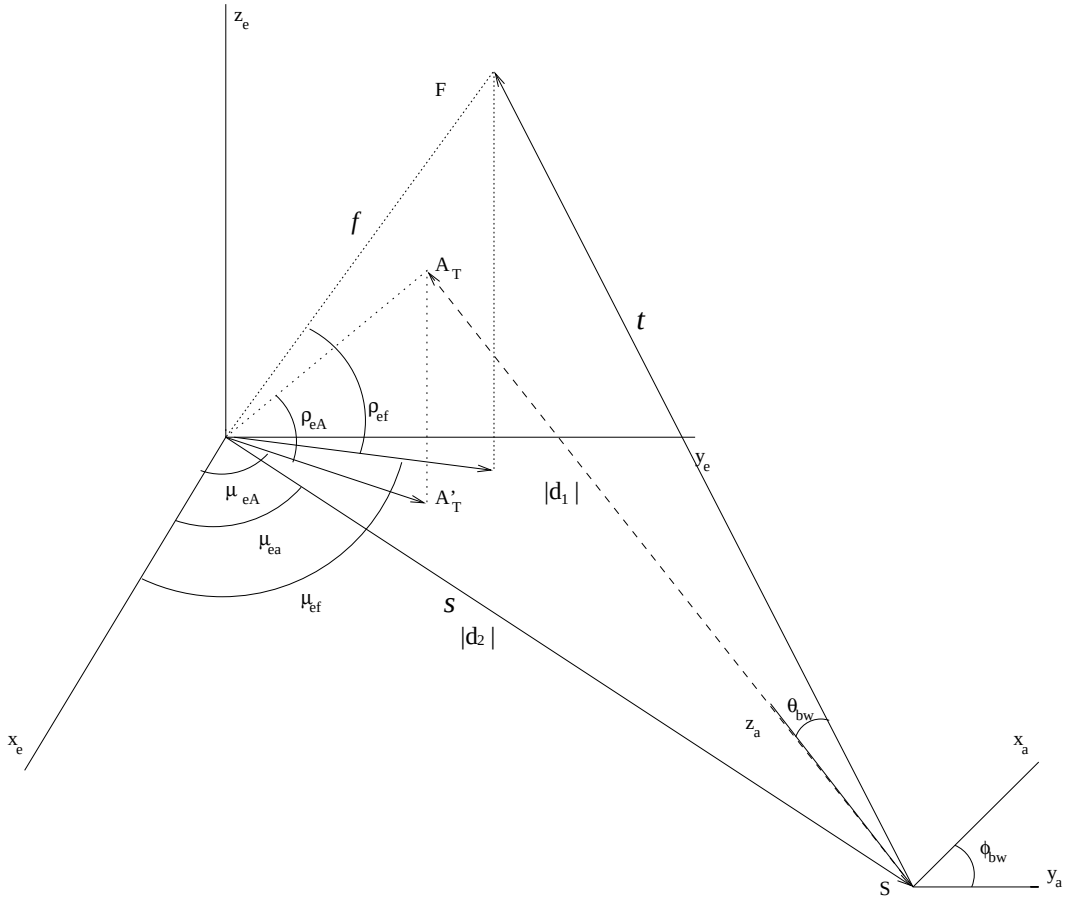

Figure B.1: Earth-Satellite Geometry for the Calculation of Beam Footprints

- The coordinate system used for the earth is specified in Appendix E. All distances are expressed in earth radii.

- The aim point is the point on the earth to where the satellite's z axis is directed. The satellite geometry and orientation relative to each other are specified in Appendix E. The aim point is a know location on the earth and corresponds to the beam center for a particular antenna element.

- As seen in the diagram B.1, the intersection point of the satellite ray with the earth may be found by solving the following relation.

$$\vec{f} = \vec{s} + \vec{t} \tag{B.3}$$

Where $\vec{f}$ is the intersection point of the ray from the satellite with the earth, $\vec{t}$ is the ray from the satellite to the intersection point F, and $\vec{s}$ is the ray from the earth center to the satellite. In this equation the only unknown is the vector $\vec{t}$.

For the calculation of the unknown parameters d_1, d_2, and $\vec{t}$ the following procedure is used.

Applying the cosine law to the satellite geometry, it can be shown that:

$$d_1 = [|s|^2 + |s|\cos^2(\rho_{ea})\cos(\mu_{ea} - \mu_{es})]^{1/2} \tag{B.4}$$

$$d_2 = [|s|^2 + 1 - 2|s|\cos^2(\rho_{ea})\cos(\mu_{ea} - \mu_{es})]^{1/2} \tag{B.5}$$

From these values the components of $\vec{t}$ may be calculated in the earth centered coordinate system.

$$\begin{aligned} \frac{t_x}{t} = \frac{1}{d_1 d_2}[&(\cos(\rho_{ea})\cos(\mu_{ea}) - |s|\cos(\mu_{es})) \cdot \\ &(d_2\cos(\theta_{bw}) - \sin(\rho_{ea})\sin(\theta_{bw})\cos(\phi_{bw})) + \\ &(\cos(\rho_{ea})\sin(\mu_{ea}) - |s|\sin(\mu_{es})) \cdot (d_1\sin(\theta_{bw})\sin(\phi_{bw}))] \end{aligned} \tag{B.6}$$

$$\frac{t_y}{t} = \frac{1}{d_1 d_2}[(\cos(\rho_{ea})\sin(\mu_{ea}) - |s|\cos(\mu_{es})) \cdot \tag{B.7}$$

$$
\begin{aligned}
& (d_2\cos(\theta_{bw}) - \sin(\rho_{ea})\sin(\theta_{bw})\cos(\phi_{bw})) - \\
& (\cos(\rho_{ea})\cos(\mu_{ea}) - |s|\cos(\mu_{es})) \cdot (d_1\sin(\theta_{bw})\sin(\phi_{bw}))] \\
\frac{t_z}{t} &= \frac{1}{d_1}(\sin(\rho_{ea})\cos(\theta_{bw}) + (d_2\sin(\theta_{bw})\cos(\phi_{bw})) \qquad \text{(B.8)}
\end{aligned}
$$

To find the magnitude of $\vec{t}$, it can be shown that

$$
\begin{aligned}
\vec{f}\cdot\vec{f} &= (\vec{s}+\vec{t})\cdot(\vec{s}+\vec{t}) \qquad \text{(B.9)} \\
&= 1
\end{aligned}
$$

This leads to the following quadratic equation:

$$
|t|^2 + B_1|t| + B_2 = 0 \qquad \text{(B.10)}
$$

The constants B_1 and B_2 may be found by:

$$
\begin{aligned}
B_1 &= \frac{2|s|}{d_1 d_2}[(\cos(\rho_{ea})\cos(\mu_{ea}-\mu_{es}) - |s|) \qquad \text{(B.11)} \\
& (d_2\cos(\theta_{bw}) - \sin(\rho_{ea})\sin(\theta_{bw})\cos(\phi_{bw})) + \\
& (d_1\cos(\rho_{ea})\sin(\mu_{ea}-\mu_{es})\sin(\theta_{bw})\sin(\phi_{bw}))] \\
B_2 &= |s|^2 - 1 \qquad \text{(B.12)}
\end{aligned}
$$

The following physical situations occur under these range of values for the discriminant of equation B.10.

- The beam from the satellite does not intersect the earth at all when

$$
B_1^2 - 4B_2 < 0 \qquad \text{(B.13)}
$$

  This solution gives a complex solution to the equation for $\vec{t}$.

- The beam from the satellite intersects the earth at two locations when

$$
B_1^2 - 4B_2 > 0 \qquad \text{(B.14)}
$$

  The smaller magnitude of the two possible solutions corresponds to the physical projection of the satellite contour on the earth.

In conclusion, the Cartesian and angular coordinates for the intersection point f in earth center coordinates can be calculated using:

$$f_{ex} = s_{ex} + (\frac{t_x}{|t|})|t| \tag{B.15}$$

$$f_{ey} = s_{ey} + (\frac{t_y}{|t|})|t| \tag{B.16}$$

$$f_{ez} = (\frac{t_x}{|t|})|t| \tag{B.17}$$

$$\rho_{ef} = \tan^{-1}(\frac{f_z}{(f_x^2 + f_y^2)^{\frac{1}{2}}}) \tag{B.18}$$

$$\mu_{ef} = \tan^{-1}(\frac{f_y}{f_x}) \tag{B.19}$$

Computer simulation programs have been created which uses this technique for finding the beam footprints. For the circular aperture, the variable ϕ_{bw} ranges over 2π radians, which results in a closed contour of points of intersection with the earth for a specified beamwidth θ_{bw} and target location A_T.

Appendix C

Beam Patterns for Off Focus Feeds

This appendix presents the degradation which results from moving the feed from the center of the focus. The feed locations were based on the coordinates in table 2.9. The beam patterns were calculated using the parabolic antenna program developed in [11].

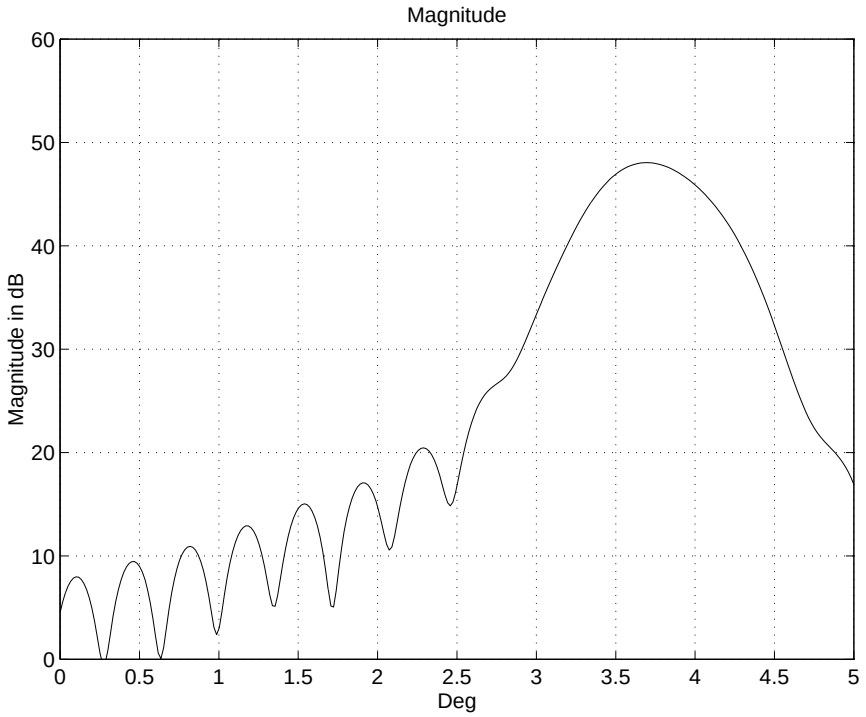

Figure C.1: Beam Pattern of Feed 1

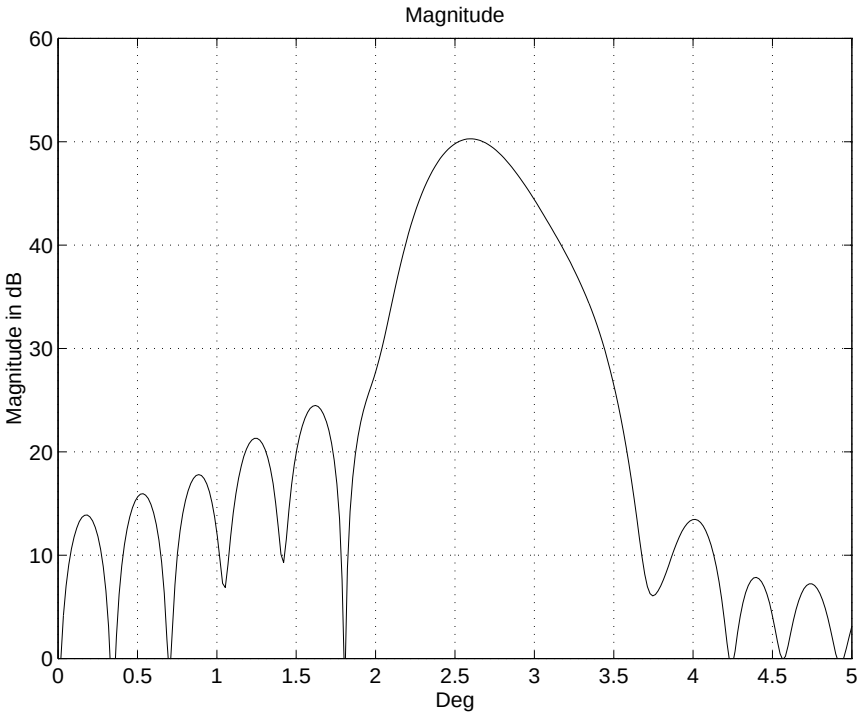

Figure C.2: Beam Pattern of Feed 2

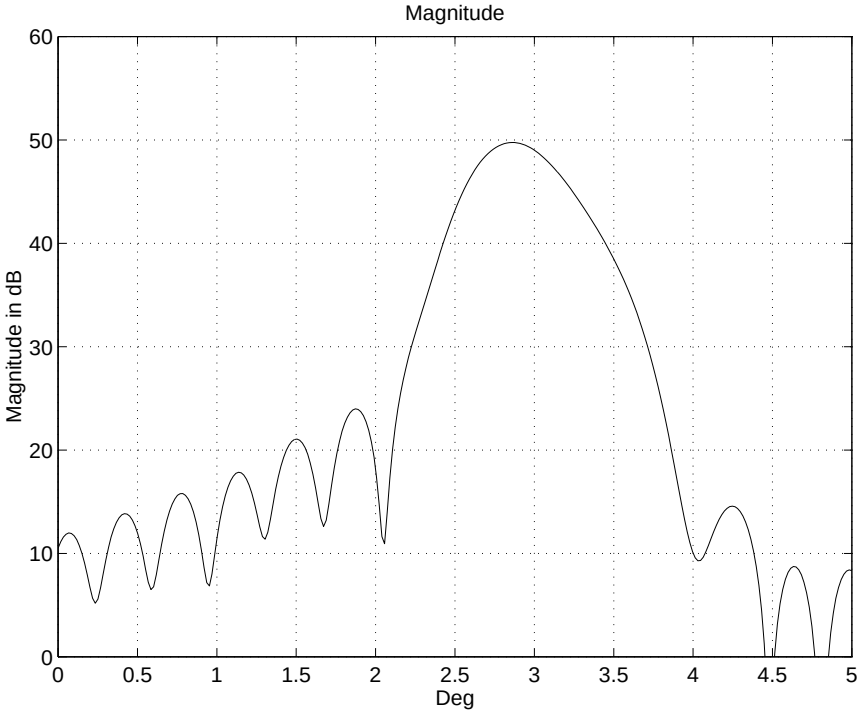

Figure C.3: Beam Pattern of Feed 3

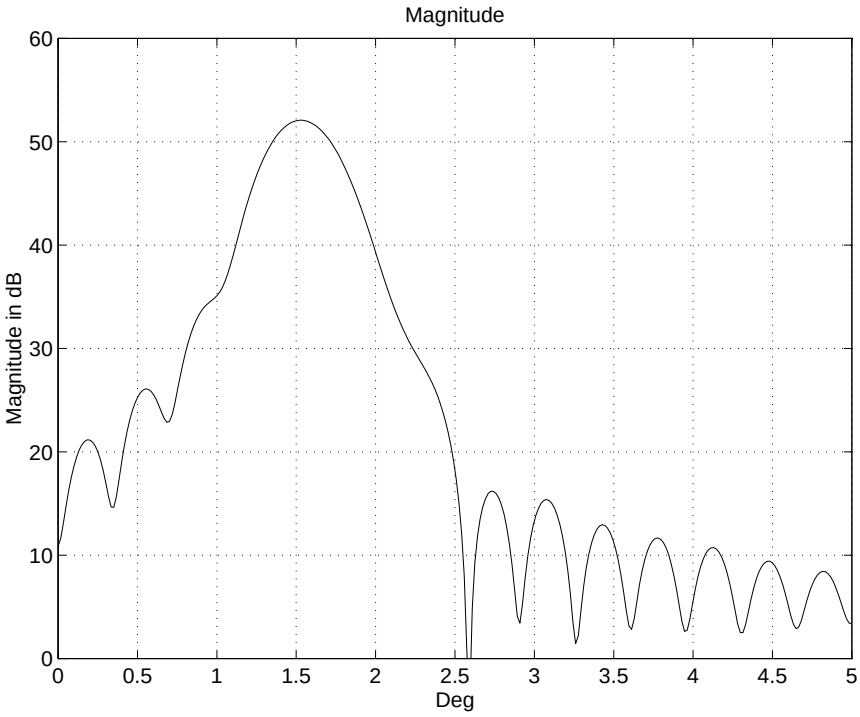

Figure C.4: Beam Pattern of Feed 4

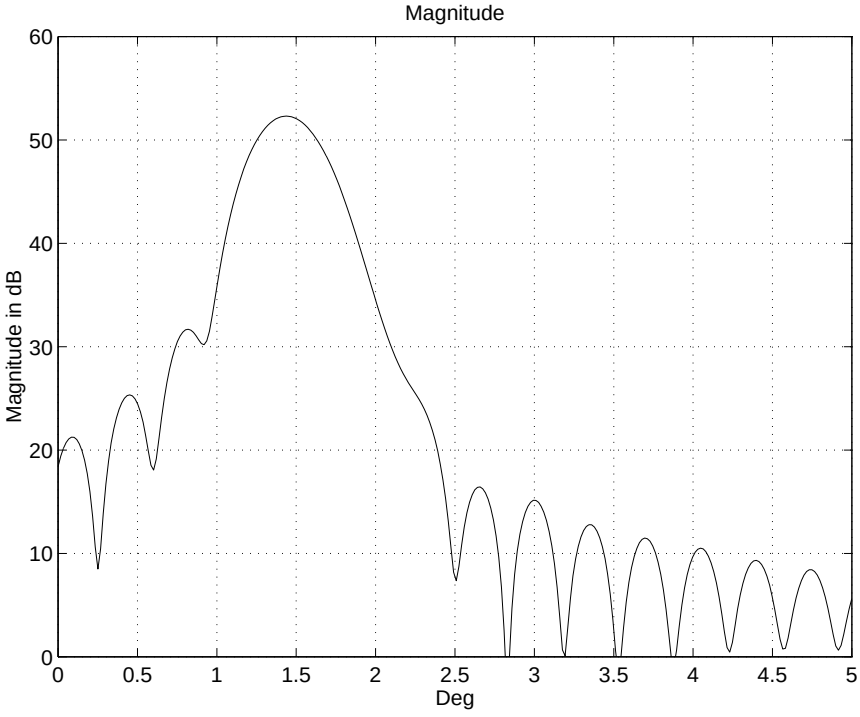

Figure C.5: Beam Pattern of Feed 5

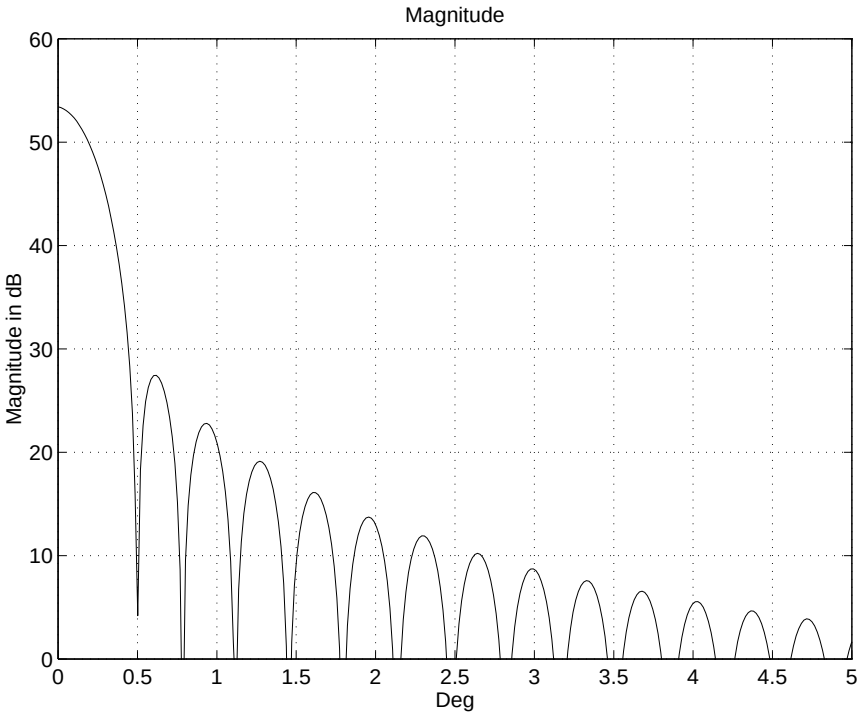

Figure C.6: Beam Pattern of Feed 6

Appendix D

Communications Model Background

This appendix gives a detailed account of the models used in determining the parameters to be used in the link budget analysis, and the effects of different variables on the attenuation models used. Only the most significant of these effects are presented in the final calculation for the link budget.

The recent interest in satellite communications using the Ka frequency band has lead to a study of the effects of atmospheric conditions on the propagation of these service links. Empirical studies have revealed a lot of variation among sites, due to variables such as temperature, elevation angle, relative humidity and other site specific phenomenon. Much has yet to be satisfactorily modeled.

The atmospheric communication link for this thesis has been developed based primarily on the empirical statistical data collected by Loo [27], and the Olympus Satellite experiment performed by Warren et.al. [42], the CCIR model, and the models presented by Allnutt [3] which are developed using experimental and theoretical calculations.

Atmospheric attenuation due to Ionospheric conditions, Tropospheric conditions, and Rain attenuation were investigated. Where possible, other atmospheric effects were incorporated into the model based on the data available. Channel modeling of the Ka band is an area of on going research, and there is relatively little long term empirical data available which can be used for simulation. The channel model presented here incorporates the most significant influences on the Ka band frequency

link, and where possible pessimistic values were used to give a upper bound on the attenuation. Other factors are omitted from the model and the justification for these omissions are presented.

D.1 Statistical Channel Model of the Carrier at the Ka Frequency Band

In order to determine the conditions under which the beamforming algorithms must perform, it is first necessary to develop an accurate channel model. The goal of this model is to predict the amount of attenuation of the signal at the Ka frequency band, and the necessary gain needed to achieve the system goals. This information will also be used in designing the parabolic antenna used to receive the signal.

The paper by Loo [27] collects signal strength and phase measurements from the Olympus satellite for both mobile and stationary signals. The test measurements were taken from the region around Ottawa Ontario Canada. This locality had an elevation angle of 14.2° with respect to the satellite. A continuous wave signal was used to make the measurements at a signal frequency of 28.07 GHz for the stationary measurement. This system used a 4.2 m receiving parabolic antenna.

Statistical data was collected under a variety of weather conditions. This information was analyzed, and a trial and error approach was attempted to find the best distribution fit with the empirical data. It was found that for the stationary receiver, the communication's channel depended only on the weather conditions. A Gaussian distribution for phase and amplitude was found to accurately predict the empirical data. This model was usually reliable up to the 99 % confidence level for both amplitude and phase models. The distribution of the model under rain conditions had the largest variance of the weather patterns observed. Thunder showers and cumulus cloud had the next largest variances respectively. Below is a reproduction of the statistical results. [27]

These statistics show that the mean envelope is attenuated significantly depending

Weather Conditions	Envelope Model Parameters		Phase Model Parameters	
	Mean*	Variance	Mean	Variance
clear sky	0.413	0.00087	0.0072	0.00357
cloudy	0.498	0.00025	0.0086	0.00405
cumulus cloud	0.346	0.00272	0.0154	0.00864
overcast	0.440	0.00041	0.0274	0.00414
intermittent light rain	0.483	0.00003	0.0088	0.00546
thunder shower	0.436	0.01386	0.0068	0.00414
light snow	0.488	0.00034	0.0088	0.00442
overcast with snow	0.458	0.00039	0.0082	0.00459
blowing snow	0.500	0.00021	0.0089	0.00435
ice pellets	0.482	0.00062	0.0094	0.00544
rain	0.662	0.02000	-0.0089	0.03077

nominal signal envelope level is 1. volt

Table D.1: Statistical Data on Carrier Envelope Under Various Weather Patterns

on the weather conditions, while the energy of the sinusoid remains relatively constant as indicated by the low variance of the envelope. Due to this low variance, the channel will be modeled as a non-time varying system for the purposes of simulation. Other models will be used to calculate the amount of attenuation of the signal.

D.2 Ionospheric Effects

The ionospheric effects are due to the charged particles in the atmosphere which result from a number of sources, the most significant of which is the solar wind. These charged particles may cause attenuation and multipath effects that can degrade the transmitted signal. An account of the ionospheric effects are presented below.

D.2.1 Refraction/Direction of Arrival Variation

The effects of refraction are not significant for frequencies above 10 GHz. The beamforming algorithms used in the thesis are not dependent on knowing the direction of arrival of the information. Average values for the direction of arrival variation due to the ionosphere may be calculated in an actual design of a satellite system, but this factor is considered unimportant for the purpose of simulating the effects of beamforming on a satellite channel.

D.2.2 Faraday Rotation

Due to the anisotropy of the medium which results from the distribution of ionized particles, linear polerized waves will suffer an angular rotation according to the following formula

$$\phi_{fd} = \frac{2.36 \cdot 10^4}{f^2} B_{av} \int N dl \qquad \text{(D.1)}$$

Where

f $\Rightarrow$ frequency (Hz)

N $\Rightarrow$ number of electrons $/m^3$

B_{av} $\Rightarrow$ average strength of earth's magnetic field (Wb/m^3)

dl $\Rightarrow$ incremental distance through plasma. (m)

TEC $\Rightarrow$ Total Electron Content (electrons$/m^2$)

The TEC is calculated for a zenith path having a cross-section of 1 m^2. Typical values of TEC vary between 10^{16} and 10^{18}. To minimize the effect of Faraday rotation on the signal, circular polerization will be used in transmission. The Faraday effect would make frequency reuse using polerization to provide signal isolation difficult for other communications systems, especially those operating at lower frequencies where the Fariday rotation effect becomes more significant.

D.2.3 Group Delay

The frequency dependent nature of the medium will result in parts of the signal reaching the target at different times. The group delay between the highest and lowest component of the transmitted bandwidth may be calculated using:

$$\triangle t_i = \frac{1.34 \cdot 10^{-7}}{f^2} \cdot TEC \quad \text{(D.2)}$$

$$\delta t_{gd} = \triangle t_2 - \triangle t_1 \quad \text{(D.3)}$$

The inverse frequency relationship of the group delay makes it a secondary factor at Ka band frequencies.

D.2.4 Phase Advance

The delay of arrival of the signal in the time domain, can be modeled as a phase advance in the frequency domain. The phase advance for a specific frequency is calculated as follows:

$$\triangle \phi_{pa} = \frac{(8.44 \cdot 10^{-7})}{f^2} \cdot TEC \quad \text{(D.4)}$$

$$\frac{d\phi_{pa}}{dt} = \frac{(-8.44 \cdot 10^{-7})}{f^2} \cdot TEC \tag{D.5}$$

The inverse relationship of the phase advance with respect to frequency makes its impact on the overall signal a secondary effect. The phase advance phenomena demonstrate a potential problem for broad band digital signals at lower frequencies which would be affected by pulse smearing.

D.2.5 Doppler Frequency

The atmospheric conditions are time dependent in nature. Therefore the rate of change of the phase advance results in a frequency fluctuation. This may be calculated as follows:

$$f_D = \frac{1.34 \cdot 10^{-7}}{f} \frac{d(TEC)}{dt} \tag{D.6}$$

For the system studied in this thesis, the target station is assumed to be stationary during transmission, therefore there is no Doppler shift due to the earth station unit. The Doppler frequency with respect to the ionosphere is not considered significant at the Ka band frequency range due to the inverse frequency relationship. This assumption is also supported by Loo's empirical statistical model presented in section D.1.

D.2.6 Dispersion

The rate of change of the time delay with frequency is the dispersion of the signal due to time delay. This quantity may be modeled as follows:

$$|\triangle \phi_{pd}| = \frac{(8.44 \cdot 10^{-7})}{f^2} \cdot B \cdot TEC \tag{D.7}$$

The variable B is the bandwidth of the signal transmitted. the dispersion angle is again an inverse function of frequency which makes the effect of dispersion on the signal relatively small for the Ka band frequencies.

D.2.7 Ionospheric Scintillation

Ionospheric scintillation is caused by variations in the electron density. This will cause a variation in focusing effect due to changes in Fresnel zones. The fluctuations are usually seen as a rapid variation in amplitude of the signal around a mean level. For regions away from the geomagnetic equator, which have an elevation angle of approximately 10 degrees or greater, and with a frequency above 10 GHz, the effects of ionospheric scintillation are negligible.

D.2.8 Summary of Ionospheric Effects

Below is a table of the effects of ionospheric factors on a 20 GHz signal. These results were scaled from data presented in [3]

Effect	Frequency Dependence	20 GHz
Faraday Rotation	$\frac{1}{f^2}$	0.28°
Propagation delay ns	$\frac{1}{f^2}$	0.625
Refraction	$\frac{1}{f^2}$	$< 0.09''$
Variation in direction of arrival	$\frac{1}{f^2}$	$0.03''$ of arc
Dispersion ps/Hz	$\frac{1}{f^2}$	$0.5 \cdot 10^{-7}$

Table D.2: Calculation Summary of Ionospheric Effects

The high frequency effects of Ka band frequencies makes ionospheric effects on the signal secondary as shown by the above table.

D.3 Clear Air Effects

Clear air effects primarily deal with the effects that the lower atmosphere has on the radio signal. It has been presented in [3] that the most significant influence on the magnitude of clear air interference comes from the elevation angle. For elevation angles above 5 degrees, the effect of the atmosphere are usually only a secondary consideration. The ray bending due to the troposphere is not considered relevant for the channel model being developed in this thesis due to the blind beamforming algorithms being considered.

D.4 Tropospheric Scattering

Tropospheric scattering is a result of turbulence in the lower earth atmosphere which causes variations in the medium's density and composition. This becomes a significant for the signal when the elevation angle is below approximately 1 degree. Tropospheric scattering was not modeled in this thesis.

D.5 Antenna Gain Reduction

The apparent reduction in the gain of an antenna increases as the effective aperture increases. The effect of antenna gain reduction becomes larger as the frequency increases. Allnutt [3] has presented a relation based on empirical data which gives regions of antenna gain reduction based on the elevation angle and the beamwidth of the reflector. The gain reduction is primarily a result of the phase distortion of the received electric field. This results in a nonuniform phase incident on the antenna aperture. For a beamwidth of 0.2°, and an elevation angle of 20° , the antenna gain is reduced by a factor of 0.5 dB. This gain reduction was incorporated in the link budget analysis.

D.6 Absorptive Effects

Polerized molecules will cause an increase in the complex component of the dielectric permutivity. This will in turn absorb power in frequencies which are around the resonating frequency of that molecule. The most abundant polar molecules in the earth's lower atmosphere are oxygen and water vapour. The effect of gaseous absorption is a function of temperature and pressure of the atmosphere. Some of the effects of these gasses are outlined below.

D.6.1 Absorption due to Oxygen

The resonant absorption line of oxygen occurs at 118.74 GHz, and it has a collection of smaller absorption frequencies around 60 GHz. A model for the prediction of the attenuation due to the absorption of oxygen is presented in [3] This model assumes a standard atmospheric pressure of 1013 mb and a temperature of 15 C°.

$$\gamma_o = [7.19 \cdot 10^{-3} + \frac{6.09}{f^2 + 0.227} \tag{D.8}$$

$$+\frac{4.81}{(f-57)^2 + 1.5}] \cdot f^2 \cdot 10^{-3} \text{ dB/km} \tag{D.9}$$

$$f < 57 \text{ GHz} \tag{D.10}$$

The correction factor for temperature can be found using:

$$\gamma_{o|Temp} = \gamma_{o|15^{\circ}C} \cdot [-0.01(Temp - 15^{\circ}C)] \text{ dB/km} \tag{D.11}$$

$$-20^{\circ}C < Temp < 40^{\circ}C \tag{D.12}$$

The height of dry oxygen is calculated by integrating along the path from the earth station to the satellite, taking into account the change of pressure and temperature. An approximation to this method is used by assuming that a fixed height for the dry oxygen.

$$h_o = 6 \tag{D.13}$$

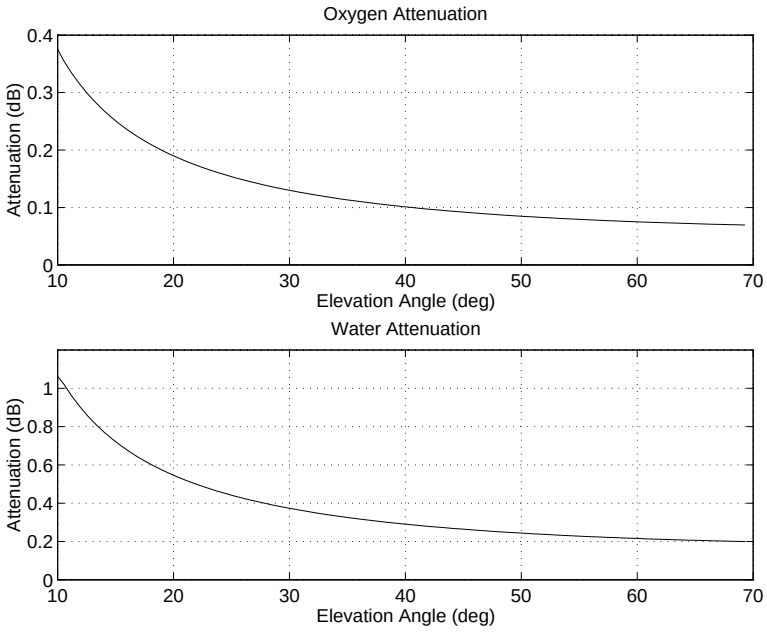

Figure D.1: Effect of Elevation Angle on Oxygen and Water attenuation at = 20 GHz

h_o is given in km, and is valid for $f < 57$ GHz.

The effect of Oxygen attenuation due to elevation angle and frequency are given in figure D.1. These figure show that as the elevation angle decreases the oxygen attenuation rises significantly.

Frequencies around 50 GHz show high attenuation due to the resonant frequency of oxygen. Oxygen does not display any dominant resonant frequencies in the 20-30 GHz range.

D.6.2 Absorption due to Water

The resonant frequencies of water occurs at 22.3, 183.3 and 323.8 GHz. This is significant because one of the absorption lines occurs in the frequency band of the proposed system. Formulas are presented in [3] for a pressure of 1013 mb and 15 degrees C. The attenuation coefficient due to water may be calculated using:

$$\gamma_w = [0.5 + 0.0021\rho_w + \frac{3.6}{(f - 22.2)^2 + 8.5} \quad \text{(D.14)}$$

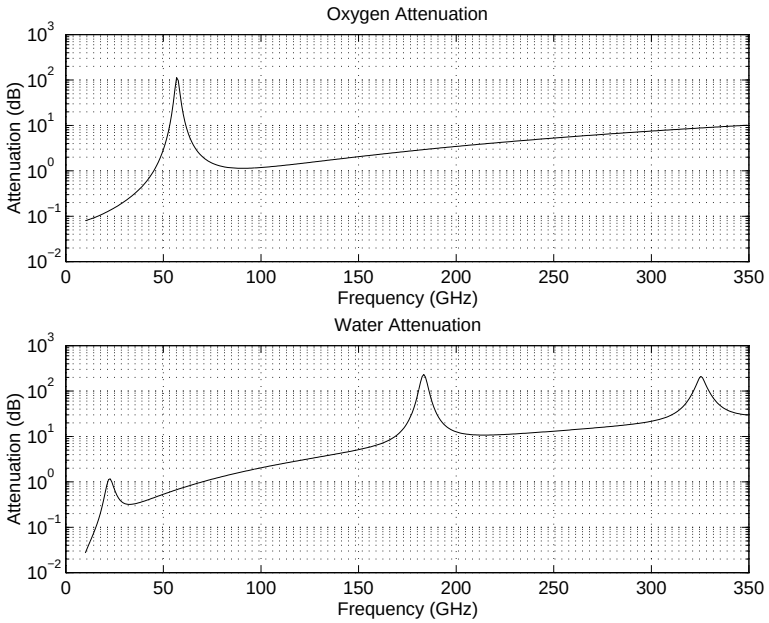

Figure D.2: Effect of Frequency on Oxygen and Water attenuation

$$+\frac{10.6}{(f-183.3)^2+9.0}+\frac{8.9}{(f-325.4)^2+26.3}]f^2\rho_w 10^{-4} \qquad \text{(D.15)}$$

The correction factor for temperature can be found using:

$$\gamma_{w|Temp} \quad = \quad \gamma_{w|15^\circ C}\cdot[-0.006(Temp-15^\circ C)] \text{ dB/km} \qquad \text{(D.16)}$$

$$-20^\circ C < \quad Temp \quad < 40^\circ C \qquad \text{(D.17)}$$

This formula is accurate to within 15 % over the range of measured water vapour density ρ_w of 0-50 g/m^3.

The equivalent height for water vapour may be calculated by:

$$h_w \quad = \quad h_{wo}[1+\frac{3.0}{(f-22.2)^2+5}+\frac{5.0}{(f-183.3)^2+6}+\frac{2.5}{(f-325.4)^2+4} \qquad \text{(D.18)}$$

h_{wo} has a value of 1.6 km in clear weather, and 2.1 km in rain. It is measured in km and is valid for $f < 350$ GHz.

D.6.3 Total Gaseous Attenuation due to Absorption

The total zenith attenuation A_g due to atmospheric gasses may be found as follows.

$$A_g = \frac{\gamma_o h_o e^{-h_s/h_o} + \gamma_w hw}{\sin(\theta_{el})} \quad \text{(D.19)}$$

This formula is valid for slant angles θ_{el} greater than 10 degrees, and $f < 50$ GHz. The variable h_s is the earth station's height above sea level.

D.7 Tropospheric Scintillation Effects

The effect of wind on the lower earth atmosphere tends to mix up the different stratification layers of gas which causes a variations in the refractive index to occur over small intervals at a rapid rates. Amplitude and phase variations due to the change in the refractive index appear as amplitude variations at the receiving antenna. Studies have shown [3] that the effect of the tropospheric scintillations increases with frequency and with decreasing elevation angle.

The empirical data collected by Loo [27] shows that for a sinusoidal frequency operating at the Ka frequency band, the variation in the signal amplitude is not very large. The cyclostationary algorithms which will be employed depend only on the preservation of the known carrier sinusoid, and should not be degraded by the slight carrier envelope variations. (Section D.1). For this reason, the tropospheric scintillation effects were not modeled in the channel. For a method on the modeling of tropospheric scintillation refer to [3].

D.8 Attenuation Effects

The attenuation on the satellite signal is the most significant effect in the link budget analysis. The attenuation is a result of two main mechanisms which are absorption and scattering.

The first form of attenuation results when the medium absorbs some of the signal energy. This energy is then retransmitted through thermal vibrations. The result observed is an increase in the thermal noise of the system.

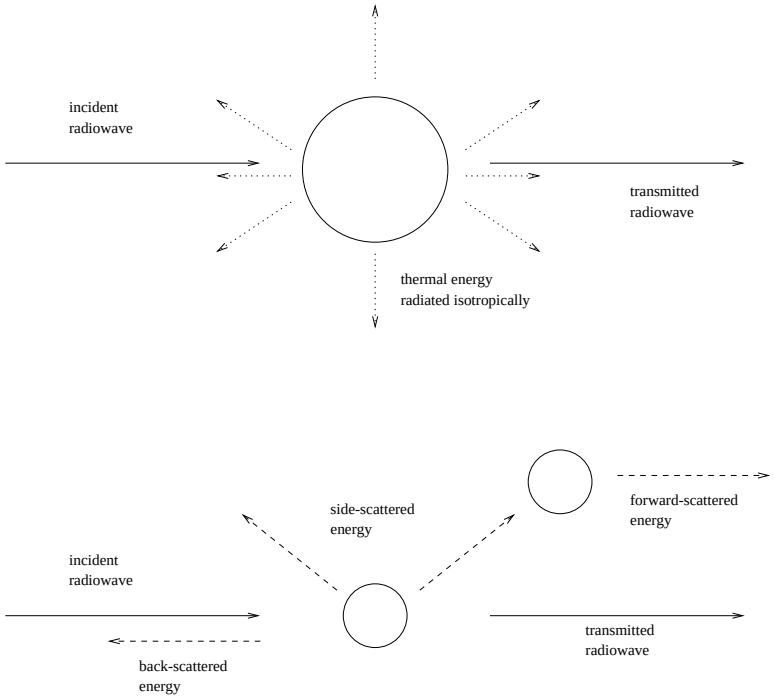

Figure D.3: Schematic of Absorption Mechanisms

The second method of attenuation is in the form of scattering. In this mechanism the energy is redirected and not absorbed by the medium. The scattering effects of radio signals above 1 GHz becomes quite complex due to the fact that at these frequencies the wavelength of the carrier is smaller than the drop size of most water vapour particles. A detailed account of scattering is found in [3], and will not be dealt with explicitly in the simulation model. The effects of the two types of attenuation mechanisms are accounted for in the attenuation prediction models presented below. a Schematic representation of absorption and scattering is shown in figure D.3.

D.8.1 Attenuation Prediction Models

The most significant amount of attenuation is cause by rain. It is therefore necessary to choose an appropriate rainfall model for the region in question. The rain model chosen for this thesis is the standard CCIR prediction model. It was chosen for several reasons. The attenuation predicted using this model has shown a good correlation for most typical long term rainfall patterns for frequencies below $f < 30$ GHz. The

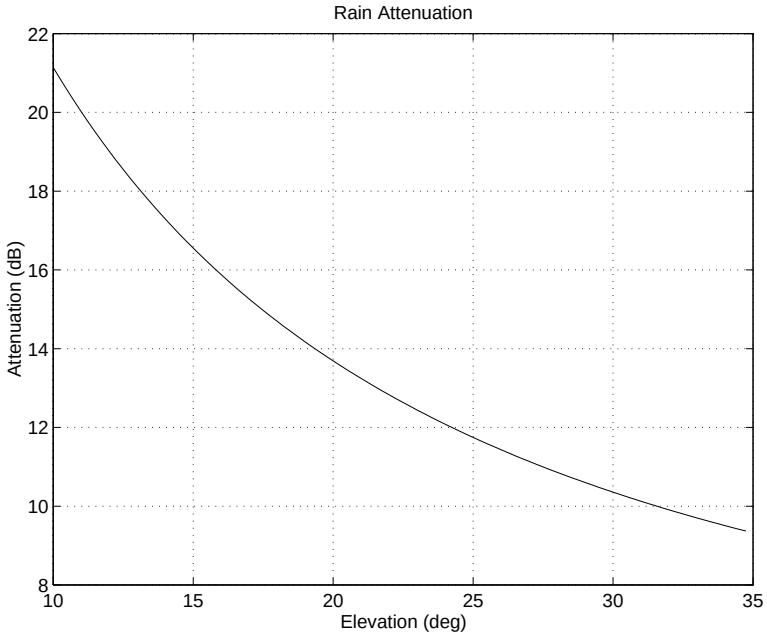

Figure D.4: Effect of Elevation on Rain Attenuation

model is simple, and needs only a few parameters for its calculation. It is widely used and accepted as a standard method of rain attenuation calculation in satellite systems for design and comparison.

The CCIR model determines an outage percent based on a statistical prediction of rain fall for a region.

The following terms are used in the attenuation model.

$R_{0.01}$ $\Rightarrow$ Point rainfall rate for the location
for 0.01 percent of an average year mm/hr.

h_s $\Rightarrow$ height above mean sea level of the earth station (km)

θ_{el} $\Rightarrow$ elevation angle (degrees)

ϕ_{elat} $\Rightarrow$ latitude of earth station (degrees)

The method for predicting the attenuation that is exceeded 0.01 percent of the time is presented below. A modification is also included for predicting other percent outage levels. Parameters affecting some of the significant contributions to the attenuation model are plotted based on the equations found in [3]. All plots are based on a 20 GHz carrier frequency, and a selected outage percentage of .01

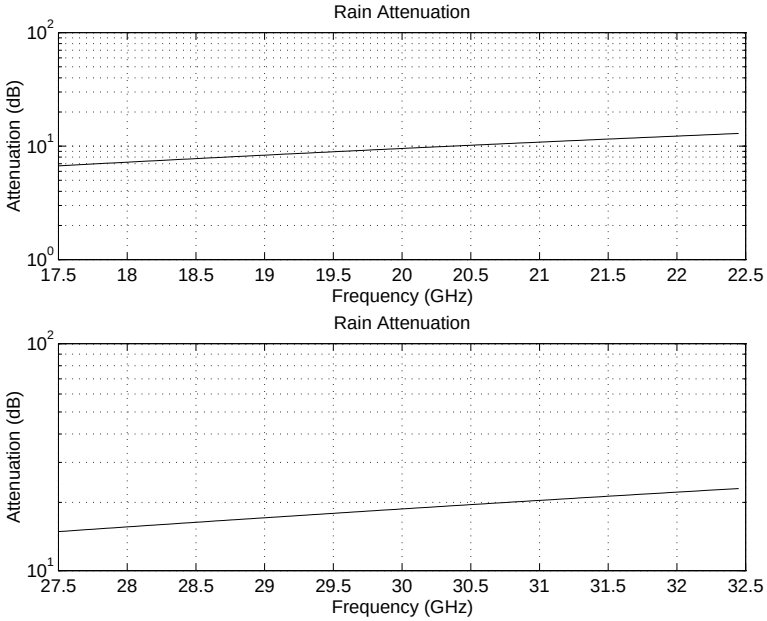

Figure D.5: Effect of Frequency on Rain Attenuation

Figure D.4 shows that as the elevation angle decreases, the attenuation due to rain increases significantly. This behavior will affect the the selection of the target location on the earth of the parabolic antenna.

Figure D.5 shows that as the frequency increases so does the attenuation due to rain. It can be observed that the attenuation at 30 GHz is approximately 10 dB higher than at 20 GHz. For this reason the downlink channel was chosen to be at 20 GHz due to the power limitations on the satellite.

The attenuation due to the height above sea level decreases with elevation as shown in figure D.6. Locations closer to sea level receive more attenuation which is a result of a thicker layer of precipitation.

The effect of the selected outage percent on the attenuation margin is also plotted. This shows a steep rise in the attenuation margin for confidence levels of greater than 0.01 % per year. Therefore the cost of decreasing the outage percent below 0.01 % would be very expensive in terms of hardware or power.

The following collection of equations outline the calculation of the attenuation parameters for the CCIR attenuation model as presented in [3]

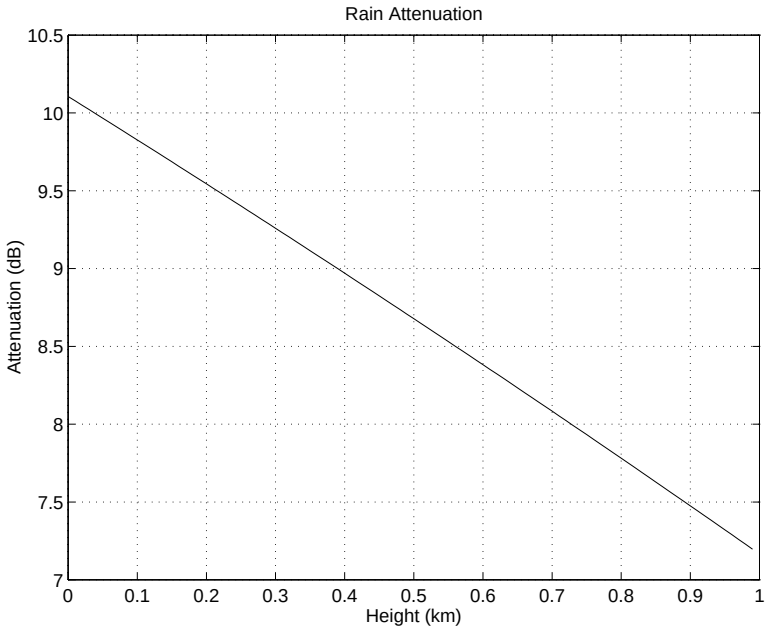

Figure D.6: Effect of Height Above Sea Level on Rain Attenuation

- The rain height h_R is calculated from the latitude of the station, and is in units of km.

$$h_R = \begin{cases} 4.0 & 0 < \phi_{el} < 36^\circ \\ 4.0 - 0.075(\phi_{el} - 36) & \phi_{el} > 36^\circ \end{cases} \tag{D.20}$$

- The slant path for angles above $\theta_{el} > 5^\circ$ can be found using the following equation. L_s is calculated in km.

$$L_s = \frac{(h_R - h_s)}{\sin(\theta_{el})} \tag{D.21}$$

- The horizontal projection of the slant path is

$$L_G = L_s \cos(\theta_{el}) \tag{D.22}$$

- The reduction factor $r_{0.01}$ for 0.01 % outage time can be calculated from

$$r_{0.01} = \frac{1}{1 + 0.045 L_G} \tag{D.23}$$

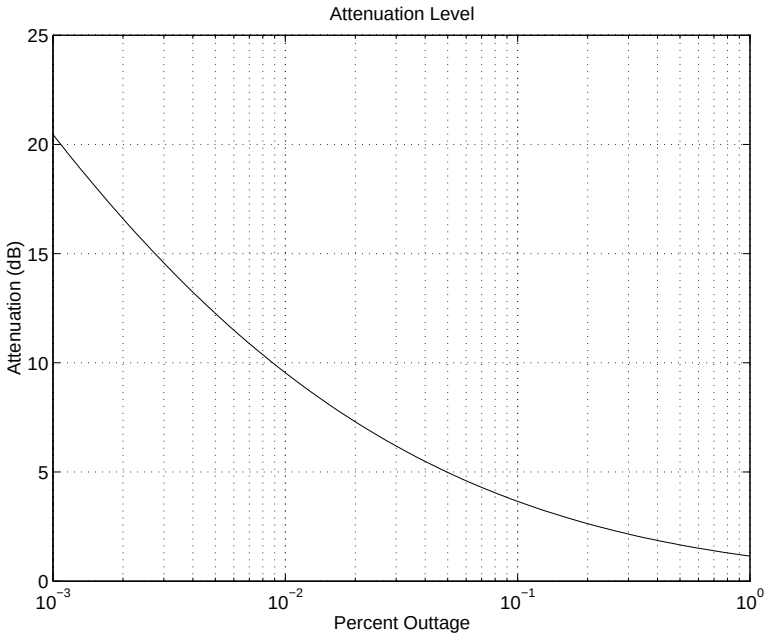

Figure D.7: Effect of Percent Outage Level on Rain Attenuation

- The value for the rain intensity (integration time of one minute) is obtained. The standard CCIR map of rain climate is used to obtain $R_{0.01}$ for the region in question. [3]

- The specific attenuation γ_r is obtained by using the coefficients given in [3]. The following equation finds the specific attenuation in dB/km.

$$\gamma_r = k(R_{0.01})^{\alpha} \tag{D.24}$$

$$\begin{aligned} \alpha_{30GHz} &= 1.021 \\ \alpha_{20GHz} &= 1.099 \\ k_{30GHz} &= 0.187 \\ k_{20GHz} &= 0.0751 \end{aligned}$$

- The attenuation in dB exceeded for 0.01 percent of an average year may be predicted from

$$A_{0.01|R} = \gamma_r L_s r_{0.01} \tag{D.25}$$

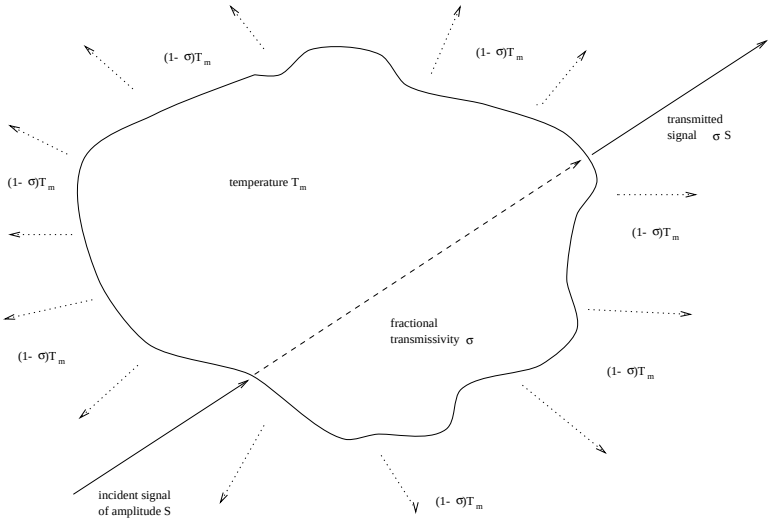

Figure D.8: Down Link Degradation Mechanism

- The attenuation to be exceeded for other percentages of an average year in the range 0.001 to 1.0 percent may be estimated from the attenuation to be exceeded for 0.01 percent for an average year by using:

$$\frac{A_p|R}{A_{0.01}|R} = 0.12p^{-(0.564+0.043\log(p))} \quad \text{(D.26)}$$

D.9 Downlink Degradation

The energy that is absorbed by rain is retransmitted in the form of thermal energy. This increase in temperature of the environment can have a significant effect upon the total noise in the system.

The satellite antenna used for the uplink is pointed towards the earth, and for this reason there is a high level of thermal noise incident upon the antenna due to the warm earth . The thermal noise lost by the signal and absorbed by rain is not significant to the total noise radiated by the earth on the uplink.

The downlink antenna however is pointed towards the "cool" sky. As a result the thermal noise temperature is much lower, and the increase in thermal noise due to the rain can be significant. The downlink degradation factor is a measure of the increase in attenuation due to the thermal noise absorbed from the signal by the water vapour.

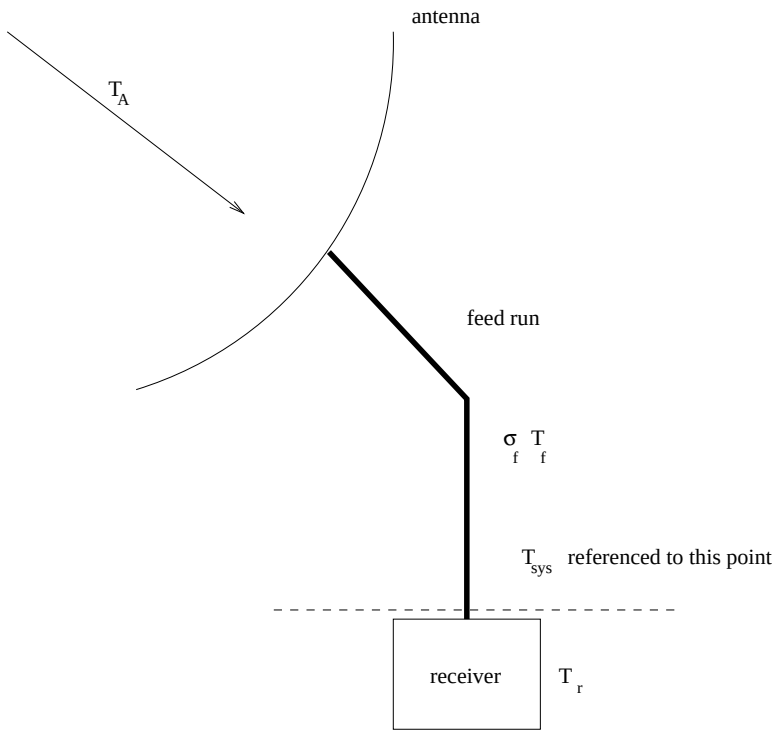

Figure D.9: Antenna Noise Schematic

Figure D.8 depicts schematically this mechanism.

To calculate the downlink degradation factor (DND), the following variables must be defined. The variables are represented schematically on the diagram D.9

T_{sys} $\Rightarrow$ System noise temperature. ($^\circ K$)

T_A $\Rightarrow$ Noise temperature incident on antenna. ($^\circ K$)

T_r $\Rightarrow$ Receiver noise temperature ($^\circ K$)

T_c $\Rightarrow$ Cosmic noise temperature ($^\circ K$)

T_m $\Rightarrow$ Temperature of the medium ($^\circ K$)

σ_f $\Rightarrow$ Feed transmission factor

A_{sky} $\Rightarrow$ Total atmospheric attenuation (dB)

A_g $\Rightarrow$ Gaseous attenuation (dB)

A certain amount of the energy received by the antenna is absorbed by the feed line to the receiver. The receiver in turn transmits some thermal noise which is proportional to its temperature. The DND factor may be found using the following steps.

- The total system noise temperature must be found. This can be done using:

$$T_{sys} = T_r + (1 - \sigma_f)T_f + \sigma_f T_A \quad \text{(D.27)}$$

- It is necessary to find the clear sky attenuation with and without attenuation due to rain.

$$T_{A|clear\,sky} = T_m(1 - 10^{-A_g/10}) + T_c \cdot 10^{-A_g/10}) \quad \text{(D.28)}$$

$$T_{A|rain} = T_m(1 - 10^{-A/10}) + T_c \cdot 10^{-A/10}) \quad \text{(D.29)}$$

  A_g may be calculated from equation D.19.

- The downlink degradation factor is then calculated as follows:

$$DND = A + 10\log(\frac{T_{sys|rain}}{T_{sys|clear\,sky}}) \quad \text{(D.30)}$$

The DND can have a significant affect on the level of received noise seen by the earth station. For example, the following values were used:

A_g=0.5 dB T_c=2.7°K T_m=280°K A=5.0 dB σ_f= 0.95 T_f=280°K T_r=200°K

Here the resulting temperatures calculated were:

$T_{A|clear\,sky}$=39.2°K $T_{A|rain}$=192.3°K $T_{sys|clear\,sky}$=245.3°K $T_{sys|rain}$=396.7°K

From this the DND was found to be:

$$DND = 5 + 2.1 \quad \text{(D.31)}$$

$$= 7.1 \quad \text{(D.32)}$$

The additional increase of 2.1 dB in attenuation is significant in the total link budget calculation for system performance and capacity.

D.10 Frequency Scaling

The transmitted frequency band proposed is has a large bandwidth. For this reason it was necessary to develop an accurate model that would frequency scale the attenuation at the band edges. This was significant in determining if the signals on the

edge of the frequency channel would suffer significantly more or less than channels closer to the target frequency. An empirical statistical model was used to achieve the attenuation scaling parameters. The attenuation of a radio beacon at the frequencies of 12.5, 20 and 30 GHz were measured over one year. Data was collected by a research group in Blacksburg Virginia from the Olympus satellite at an elevation angle of 14 degrees. This angle provides a worst case scenario for coverage in Canada with a geostationary satellite. The data in this experiment is unique due to the fact that measurements were made simultaneously at all three frequencies. Using this data, the following frequency scaling principle was derived based on the frequency scaling power law. [25]

$$RAS_n(f_L, f_U) = \frac{ACA(f_U)}{ACA(f_L)} \quad \text{(D.33)}$$

$$= (\frac{f_U}{f_L})^n \quad \text{(D.34)}$$

Where ACA is the attenuation due to clear sky conditions, and RAS is the statistical attenuation ratio.

Analysis of the averaged data ratios for the factor n showed that the best value to match the data when scaling from 20 to 30 GHz was 1.72. The average value for n was found to be 1.9 for general frequency scaling across the Ka/Ku frequency bands.

This relation for the attenuation scaling is accurate 50 % of the time. For example, if the attenuation at the lower frequency is exceeded 1 percent of the time per year, then the frequency scaled result is exceeded 0.5 percent of the time. (50 percent of one percent)

For a more accurate frequency scaling prediction, presented an empirical model based on collected data. This model is accurate 99 percent of the time for attenuation in the Ka/Ku band.

$$A(f_U)_{99\%} = (\frac{f_U}{f_L})^{2.65} A(f_L) - 0.00138(\frac{f_2}{f_1})^{6.98} A(f_L) \quad \text{(D.35)}$$

The prediction model presented above showed a significant improvement in performance as compared to other frequency scaling attenuation models.

D.11 Fading Statistics

In the paper by [42] secondary statistics are presented using data obtained from the Olympus Satellite program using beacons at frequencies of 12.5, 20 and 30 GHz. The most interesting secondary statistic is the fade duration statistics for a given attenuation. These measurements were taken under the same conditions as [25] described above.

The experiment set threshold levels of at various levels of clear air attenuation and then calculated the time during a particular fade that the attenuation was below this level. The raw data was smoothed using a 30 sec block averaging window to remove scintillations. Fade events were grouped into durations ranging from 1 sec to 1 hour. Generally it was found that with an increase in the carrier frequency, the number of fades, and the fade duration increased.

The following data was obtained which gives a bound to the type of service provided for a given threshold level for clear air attenuation. Clear air attenuation is primarily a result of rain.

Frequency (GHz)	$>$ 10 sec	$>$ 100 sec	$>$ 1000 sec
20	100	70	8
30	300	200	30

Table D.3: Fading Duration Statistics: 15 dB Attenuation Threshold

The clear air properties of the weather in Virginia is assumed to be close enough to the weather in Canada such that the empirical data developed here is relevant in providing some indication of the fading environment.

Frequency (GHz)	$>$ 10 sec	$>$ 100 sec	$>$ 1000 sec
20	70	30	10
30	200	100	30

Table D.4: Fading Duration Statistics: 20 dB Attenuation Threshold

The fading statistics give a measure of the type of performance that subscribers to the system would have to deal with under worst case scenarios.

Appendix E

Coordinate System Transformations

Throughout this thesis it was necessary to use a variety of coordinate systems to aid in calculations and for visualization of the physical geometry. This appendix contains a summary of the coordinate systems used, under what conditions, and how to transform among them.

The reference "Generation and Display of Satellite Antenna Patterns" by Cook et. al. [8] provided the transformation formulas and the reference models needed.

E.1 Earth Centered System

The earth centered system is used in calculation of the beam foot prints and the target position of the main beams. It is also used to output the maps corresponding to the coverage location.

This coordinate system has its origin located at the center of the earth. The positive z axis points to the north pole, the positive x axis intersects the Greenwich Meridian and the positive y axis points 90° east according to the right hand rule. [8]

The following formulas are used to define the spherical and Cartesian coordinates for the earth centered system.

$$x_e = R_e \cos(\rho_e) \cos(\mu_e) \tag{E.1}$$

$$y_e = R_e \cos(\rho_e) \sin(\mu_e) \tag{E.2}$$

$$z_e = R_e \sin(\rho_e) \tag{E.3}$$

To transform from Cartesian to spherical coordinates:

$$R_e = 6371km \tag{E.4}$$

$$\rho_e = \sin^{-1}(z_e/R_e) \tag{E.5}$$

$$\mu_e = \tan^{-1}(y_e/x_e) \tag{E.6}$$

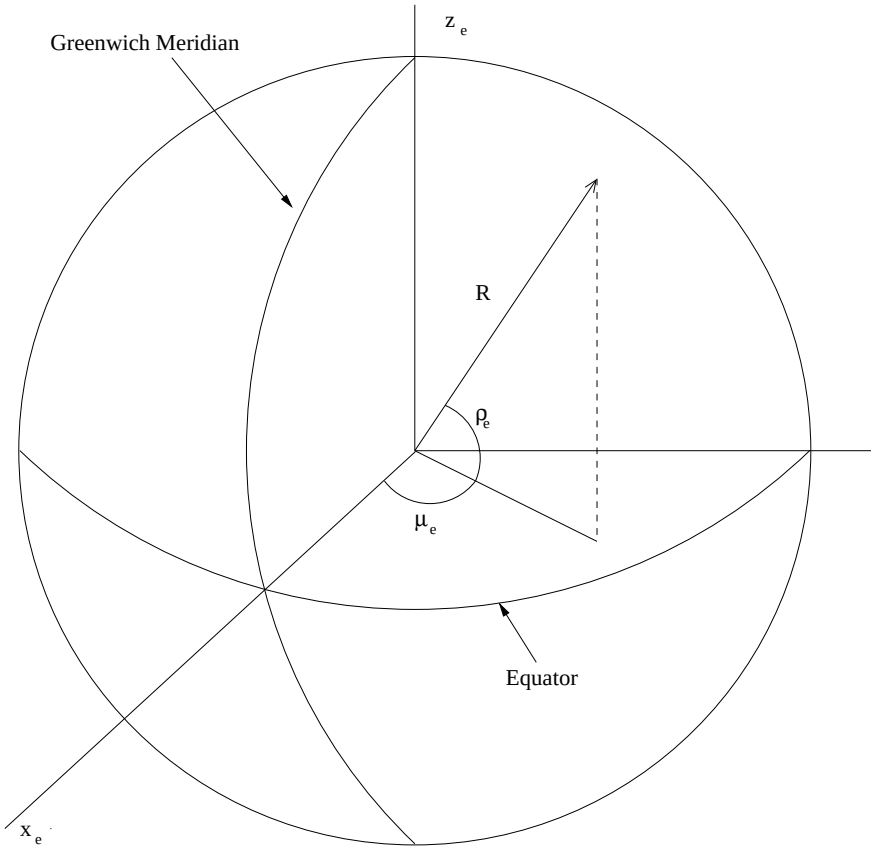

Figure E.1: Earth Coordinate system Geometry

Here, the subscript "e" denotes the earth centered system, and the constant R_e refers to the earth's radius. A geometric representation of the coordinate system is shown in figure E.1.

E.2 Satellite Centered System

The satellite centered system has the z-axis pointing towards the center of the earth, and the x-axis is oriented towards the north pole of the earth. The y-axis corresponds to the orientation of a right handed coordinate system. Here the subscript "s" denotes the satellite system. A geometric representation is shown in figure E.2.

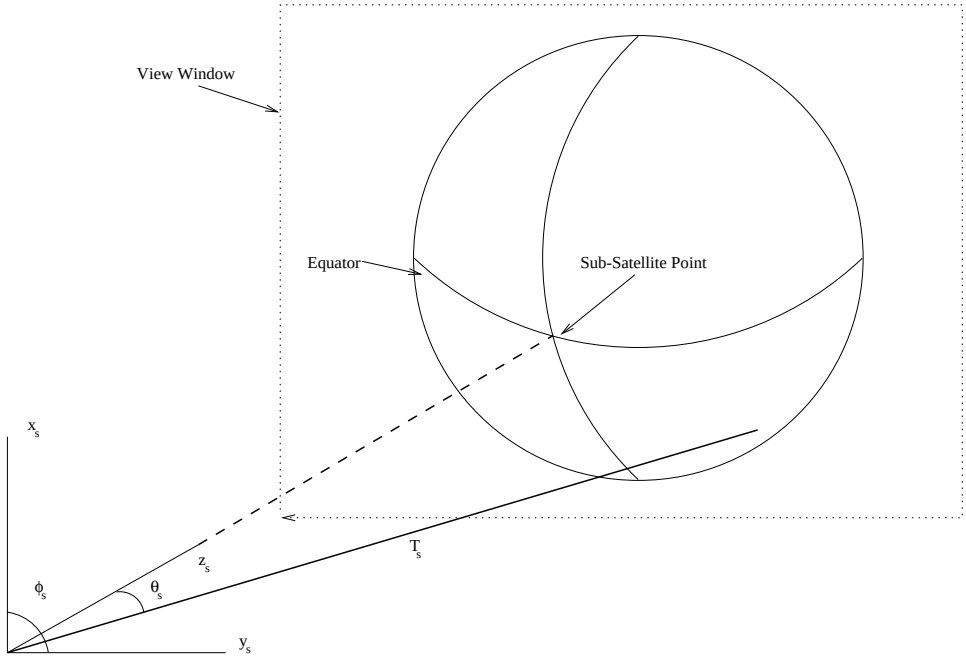

Figure E.2: Satellite Coordinate system Geometry

$$x_s = T_s \sin(\theta_s)\cos(\phi_s) \quad \text{(E.7)}$$

$$y_s = T_s \sin(\theta_s)\sin(\phi_s) \quad \text{(E.8)}$$

$$z_s = T_s \cos(\phi_s) \quad \text{(E.9)}$$

E.3 Perspective Projection View of the Earth

There are a variety of ways of viewing a circular earth on a two dimensional surface. The method that was chosen for this thesis was the perspective projection. The earth

is seen in perspective as viewed from a specific location in space. This method was implemented using matlab's three dimensional graphics capabilities. The viewing window is represented by the dotted box in figure E.2.

E.4 Coordinate Transform

In order to transform coordinates among the different reference system, the following vectors were defined. A graphical representation of the system is depicted in figure E.3.

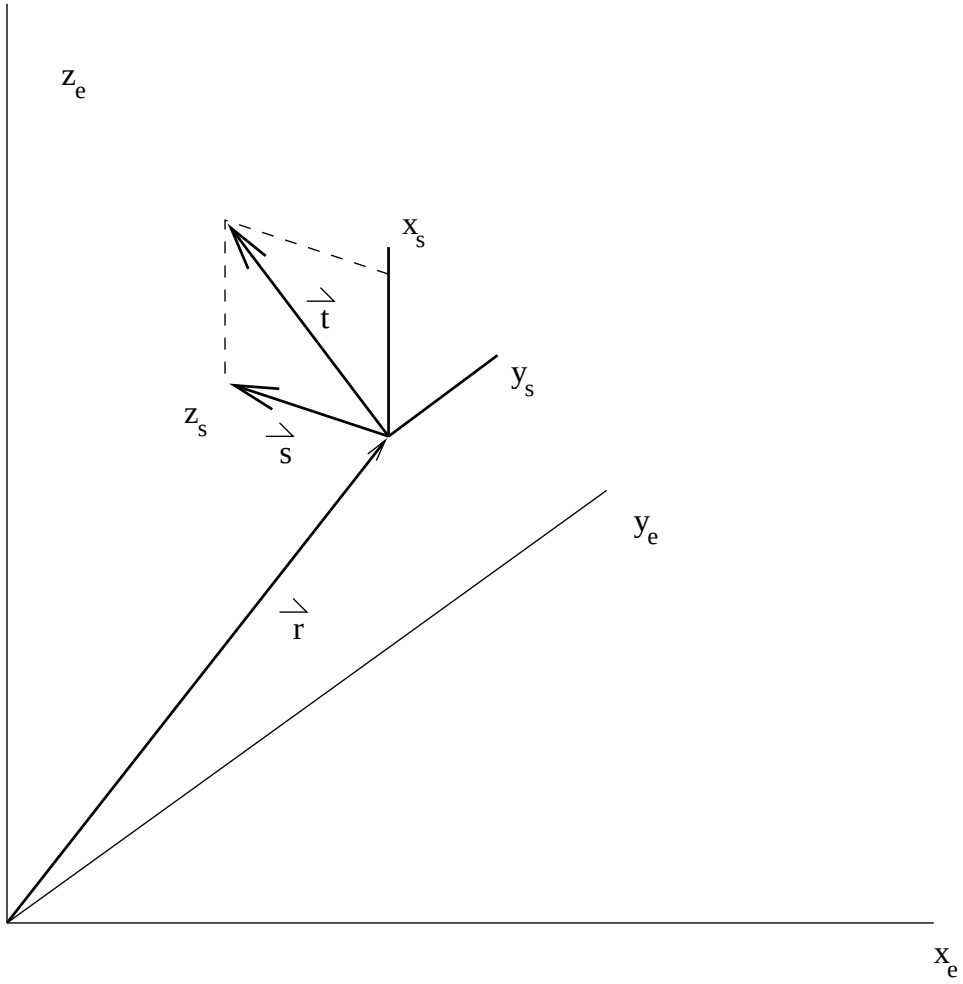

Figure E.3: Satellite Coordinate system Geometry

$$\vec{r} = r_1\vec{i} + r_2\vec{j} + r_3\vec{k} \quad \text{(E.10)}$$

$$\vec{s} = s_1\vec{i} + s_2\vec{j} + s_3\vec{k} \quad \text{(E.11)}$$

$$\vec{t} = t_1\vec{i} + t_2\vec{j} + t_3\vec{k} \quad \text{(E.12)}$$

Here $\vec{i}$, $\vec{j}$, and $\vec{k}$ are the unit vectors of the earth coordinate system. $\vec{r}$ originates from the center of the earth system and points towards the center of the local system. $\vec{s}$ points in the direction of the positive z-axis. $\vec{t}$ lies on the x-z plane.

The unit vectors in the local system may be defined as follows:

$$\vec{l} = a_1\vec{i} + a_2\vec{j} + a_3\vec{k} \quad \text{(E.13)}$$

$$\vec{m} = a_4\vec{i} + a_5\vec{j} + a_6\vec{k} \quad \text{(E.14)}$$

$$\vec{n} = a_7\vec{i} + a_8\vec{j} + a_9\vec{k} \quad \text{(E.15)}$$

The elements a_* form the transformation matrix **A**. These elements may be calculated using the following formulas [8]

$$a_1 = [(s_3t_1 - s_1t_3)s_3 - (s_1t_2 - s_2t_1)s_2]/M_1 \quad \text{(E.16)}$$

$$a_2 = [(s_1t_2 - s_2t_1)s_1 - (s_2t_3 - s_3t_2)s_3]/M_1 \quad \text{(E.17)}$$

$$a_3 = [(s_2t_3 - s_3t_2)s_2 - (s_3t_1 - s_1t_3)s_1]/M_1 \quad \text{(E.18)}$$

$$a_4 = (s_2t_3 - s_3t_2)/M_2 \quad \text{(E.19)}$$

$$a_5 = (s_3t_1 - s_1t_3)/M_2 \quad \text{(E.20)}$$

$$a_6 = (s_1t_2 - s_2t_1)/M_2 \quad \text{(E.21)}$$

$$a_7 = s_1/M_3 \quad \text{(E.22)}$$

$$a_8 = s_2/M_3 \quad \text{(E.23)}$$

$$a_9 = s_3/M_3 \quad \text{(E.24)}$$

The scalar vectors M_i are computed from the vectors $\vec{s}$ and $\vec{t}$ as follows:

$$M_1 = \vec{s} \times \vec{t} \times \vec{s} \tag{E.25}$$

$$M_2 = \vec{s} \times \vec{t} \tag{E.26}$$

$$M_3 = \vec{s} \tag{E.27}$$

The transformation from the satellite system (x_s, y_s, z_s) to the earth centered system (x_e, y_e, z_e) is calculated by:

$$\begin{Bmatrix} x_e \\ y_e \\ z_e \end{Bmatrix} = \begin{bmatrix} a_1 a_4 a_7 \\ a_2 a_5 a_8 \\ a_3 a_6 a_9 \end{bmatrix} \begin{Bmatrix} x_s \\ y_s \\ z_s \end{Bmatrix} + \begin{Bmatrix} r_1 \\ r_2 \\ r_3 \end{Bmatrix} \tag{E.28}$$

The transformation from the earth centered system (x_e, y_e, z_e) to the satellite centered system (x_s, y_s, z_s) is found as follows:

$$\begin{Bmatrix} x_s \\ y_s \\ z_s \end{Bmatrix} = \begin{bmatrix} a_1 a_2 a_3 \\ a_4 a_5 a_6 \\ a_7 a_8 a_9 \end{bmatrix} \begin{Bmatrix} x_e \\ y_e \\ z_e \end{Bmatrix} - \begin{bmatrix} a_1 a_2 a_3 \\ a_4 a_5 a_6 \\ a_7 a_8 a_9 \end{bmatrix} \begin{Bmatrix} r_1 \\ r_2 \\ r_3 \end{Bmatrix} \tag{E.29}$$

E.5 Local Coordinate System

The local coordinate system is primarily used in calculation of the azimuth and elevation angle of the satellite with respect to the target location on the earth. This information is needed for the link budget calculation.

The local coordinate system has its origin at an arbitrary location in space. Typically this is a position on the earths surface corresponding to a target position of the main beam. The z-axis points perpendicular to the earth's surface, the x-axis points towards the north pole, and the y-axis corresponds to the orientation for a

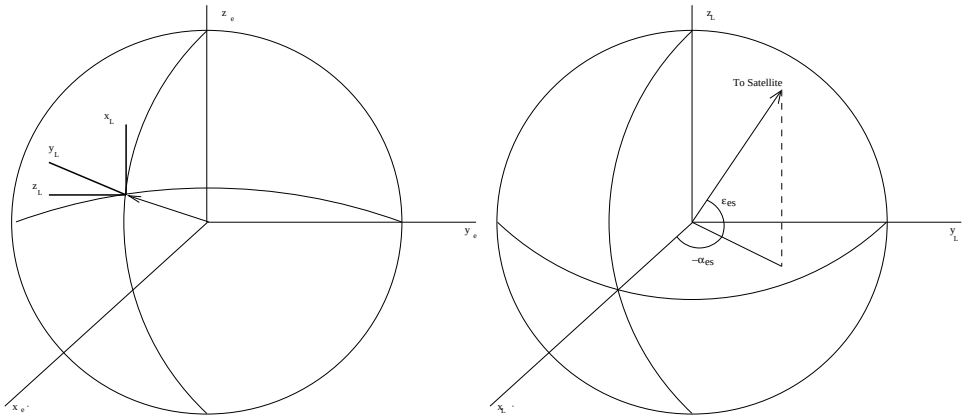

Figure E.4: Local Coordinate system Geometry

right handed coordinate system. A geometric representation of the Local coordinate system is represented in figure E.4. Here the subscript "L" denotes the local system.

The azimuth angle is denoted α_{es}, and may be found using:

$$\alpha_{es} = -\tan^{-1}(y_s/x_s) \tag{E.30}$$

The elevation angle is denoted ϵ_{es}, and may be found using:

$$\epsilon_{es} = \sin^{-1}[\frac{z_s}{\sqrt{(x_s^2+y_s^2+z_s^2}}] \tag{E.31}$$

The satellite system (x_s, y_s, z_s) may be represented with respect to the local system (x_L, y_L, z_L) as follows:

$$x_L = (R_e + S_{es})\cos(\rho_e)\cos(\mu_e) \tag{E.32}$$

$$y_L = (R_e + S_{es})\cos(\rho_e)\sin(\mu_e) \tag{E.33}$$

$$z_L = (R_e + S_{es})\sin(\rho_e) \tag{E.34}$$

Where R denotes the radius of the earth and S denotes the height above the earth's surface of the satellite.

For the special case where a point lies on the earth's surface, the vectors $\vec{s}$, $\vec{t}$ and $\vec{r}$ take on the following values:

$$\begin{aligned} r_1 &= s_1 = x_e & t_1 &= 0 \\ r_2 &= s_2 = y_e & t_2 &= 0 \\ r_3 &= s_3 = z_e & t_3 &= 1 \end{aligned}$$

E.6 Satellite / Earth Geometry

The geometric relationship of a satellite positioned at the same latitude as the equator with respect to a point on the earth is depicted in Figure E.5.

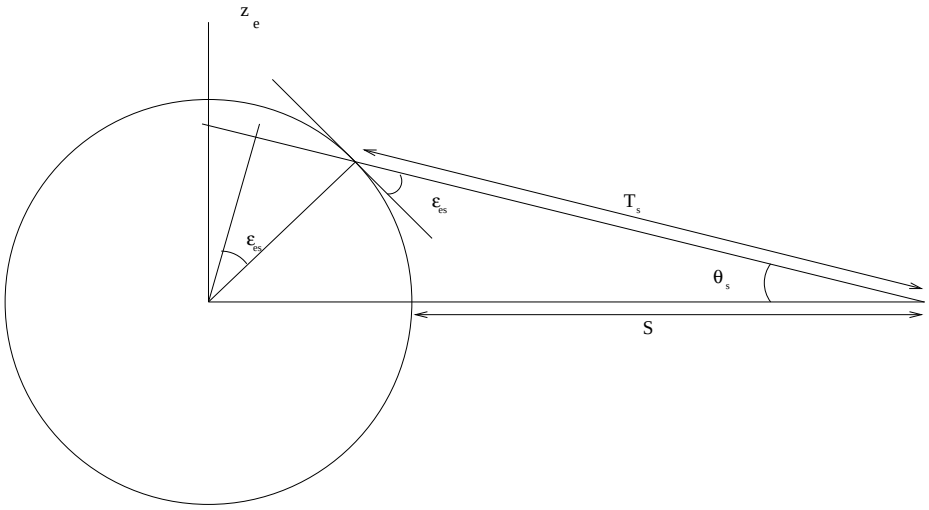

Figure E.5: Satellite-Earth Geometric relationship

The target position of a beam on the earth may be represented by the variables $(T_{es}, \theta_s, \phi_s)$ which are shown in the figure E.5.

$$T_{es} = (S_{es} + R_e)\cos(\theta_s) - \sqrt{R^2 - (S_{es} + R_e)^2 \sin^2(\theta_s)} \quad \text{(E.35)}$$

$$R_e \cos(\epsilon_{es}) = (S + R)\sin(\theta_s) \quad \text{(E.36)}$$

$$R_e \sin(\epsilon_{es}) = \sqrt{R_e^2 - (S_{es} + R_e)^2 \sin^2(\theta_s)} \quad \text{(E.37)}$$

Appendix F

Calculation of Satellite Feed Coordinates

The following method was developed to find the coordinates of the satellite feed positions which correspond to different target locations on the earth. Figure F.1 shows the physical modeling of the problem. The satellite must be positioned at 0 degrees latitude to maintain a geostationary orbit. The longitude position of the satellite is stationed in the center of the coverage area.

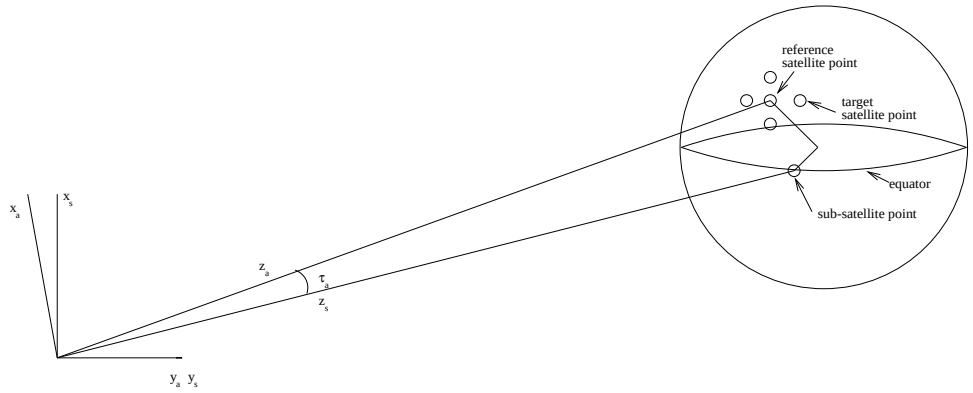

Figure F.1: Earth-Satellite Target Geometry

The antenna is aimed at a point on the earth which is ideally in the center of the coverage area. This point on the earth corresponds to the on focus feed position, and is defined as the reference target location or reference beam. This beam lies parallel to the z axis of the antenna coordinate system which is used to calculate the feed locations for the other target beams.

All coordinates are transformed into the satellite antenna reference system. The

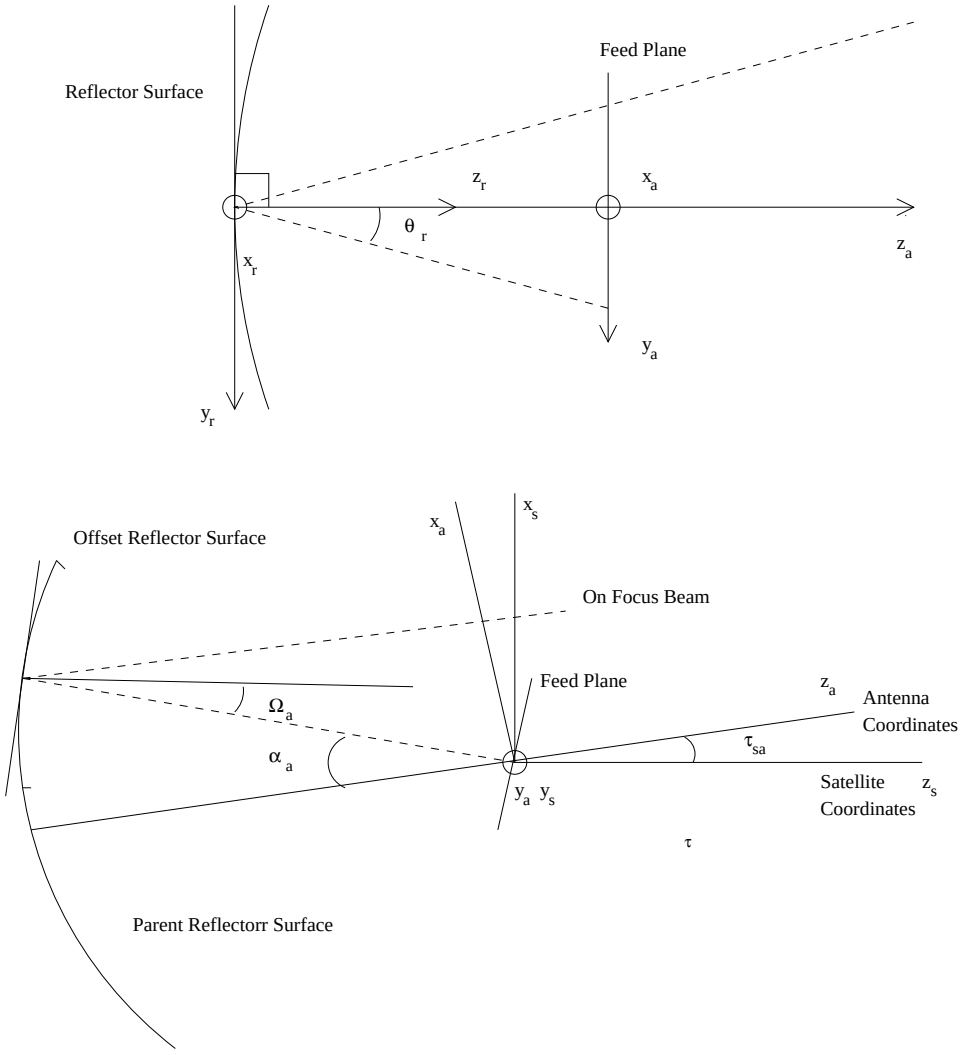

Figure F.2: Antenna Feedplane Geometry, Y-Plane

angle τ_{sa} specifies the angle the antenna axis makes with the satellite system in the xz plane. There is no offset angle in the zy plane because the satellite and the antenna are located directly above the target on the earth in the longitudinal coordinate. See F.2 for a detail of the geometry. The incoming angle of a target beam is broken up into two components, the xz component and the yz component.

The reflected angle in the yz component can be found using simple angle of incidence equals the angle of reflection principle. This angle is specified by θ_r All feeds are assumed to be aimed towards the geometric center of the offset parabola.

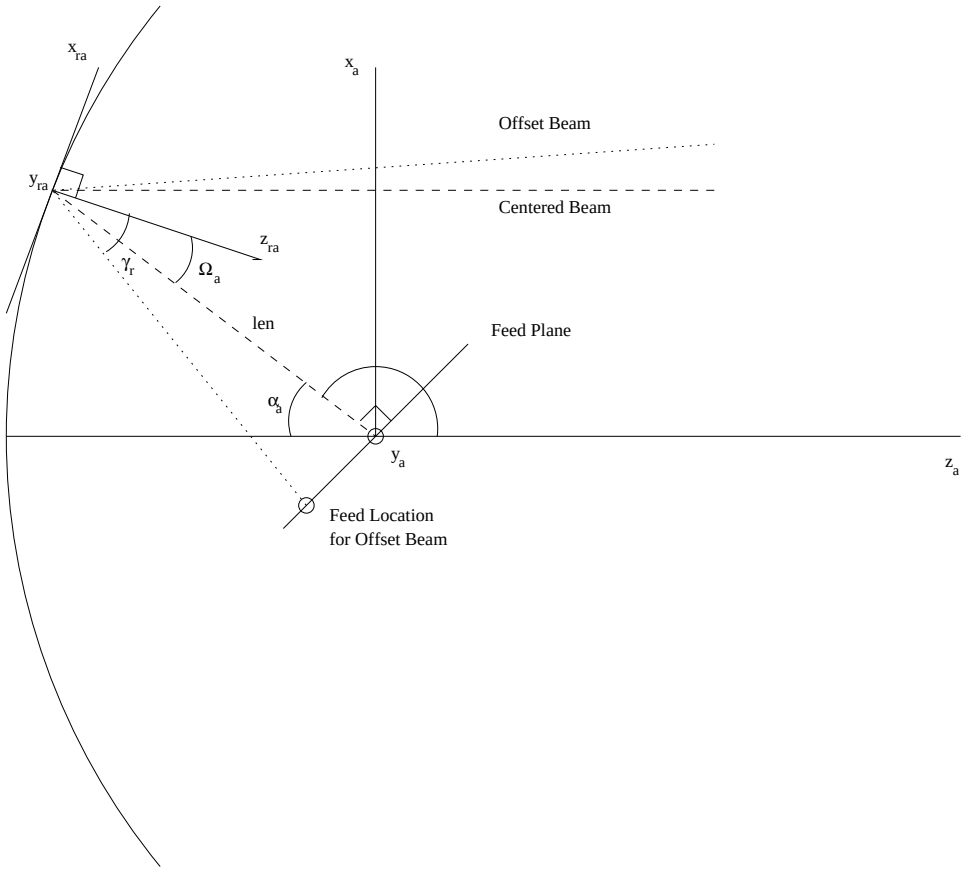

Figure F.3: Antenna Feed Plane Geometry, XZ-Plane

The reflected angle in the xz plane is depicted in figure F.3 This angle can be calculated as follows:

- Ω_a is calculated for the system by dividing the known angle α_a by two. α_a was

found in the calculation of the reflector geometry.

$$\Omega_a = -\alpha_a/2 \tag{F.1}$$

The reflected angle is therefore the negative of the incident angle and the line parallel to z_a. Here the subscript ta refers to the target's Cartesian coordinates in the antenna reference system.

$$\gamma_r = -(\tan^{-1}(x_{ta}/z_{ta}) + 2\Omega_a) \cdot BDF \tag{F.2}$$

- The coordinates of the reflector center is calculated with respect to the antenna coordinate position. Since the satellite is positioned above the reference beam location in longitude, the coordinates may be found using:

$$x_{ra} = len \sin(\alpha_a) \tag{F.3}$$

$$y_{ra} = 0 \tag{F.4}$$

$$z_{ra} = len \cos(\pi - \alpha_a) \tag{F.5}$$

$$\vec{V_r} = (x_{ra}, y_{ra}, z_{ra}) \tag{F.6}$$

- The normal of the feed plane is found with respect to the antenna coordinate system as follows:

$$x_{nf} = \sin(\alpha_a) \tag{F.7}$$

$$y_{nf} = 0 \tag{F.8}$$

$$z_{nf} = \cos(\pi - \alpha_a) \tag{F.9}$$

$$\vec{N_f} = (x_{nf}, y_{nf}, z_{nf}) \tag{F.10}$$

- A direction vector for each target location from the offset reflector's center to the feed plane is calculated. The constant M_d is the magnitude of the direction vector, and is used to normalize the cartesian coordinates.

$$x_{da} = \sin(\gamma_r) \tag{F.11}$$

$$y_{da} = \sin(\theta_r) \tag{F.12}$$

$$z_{da} = \cos(\pi - \theta_r) \tag{F.13}$$

$$M_d = \sqrt{x_{da}^2 + y_{da}^2 + z_{da}^2} \tag{F.14}$$

$$\vec{V_d} = (x_{da}, y_{da}, z_{da})/M_d \tag{F.15}$$

- A parametric method is used to calculate the intersection of each direction vector with the feed plane. [4]

$$t_{feed} = \frac{-\vec{N_f} \cdot \vec{V_r}}{\vec{V_d} \cdot \vec{N_f}} \tag{F.16}$$

- The parameter t_{feed} is used to calculate the length of the direction vector necessary for the intersection with the feed plane.

$$x_f = x_{ra} + x_{da}t \tag{F.17}$$

$$y_f = y_{ra} + y_{da}t \tag{F.18}$$

$$z_f = z_{ra} + z_{da}t \tag{F.19}$$

$$\vec{V_f} = (x_f, y_f, z_f) \tag{F.20}$$

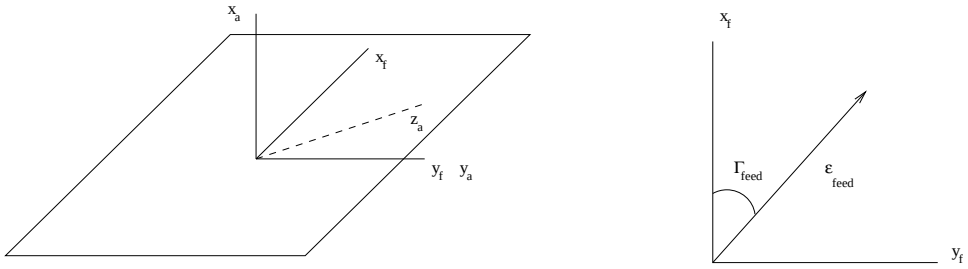

Figure F.4: Geometry of Polar Coordinate Transform

The z_f component for the intersection always resulted in a zero value.

- The points of intersection are transformed into polar coordinates on the feed plane. The geometry of this transform is depicted in figure F.4.

$$\epsilon_{feed} = \sqrt{x_f^2 + y_f^2} \tag{F.21}$$

$$\Gamma_{feed} = \tan^{-1}(y_f/x_f) \tag{F.22}$$

Bibliography

[1] B.G. Agee. *The property restoral approach to blind adaptive signal extraction.* PhD thesis, University of California, 1989.

[2] B.G. Agee, S.V. Schell, and W.A. Gardner. Spectral Self-Coherence Restoral: A New Approach to Blind Adaptive Signal Extraction Using Antenna Arrays. *IEEE Proceedings*, 4:753 – 766, April 1990.

[3] J.E. Allnutt. *Satellite to ground radiowave propagation.* Peter Peregrinus Ltd., 1989.

[4] H. Anton. *Elementary Linear Algebra.* John Wiely and Sons, 4 edition, 1984.

[5] T.E. Biedka. Subspace-constrained SCORE algorithms. In *Proceedings of the Asilomar Conference on Signals, Systems and Computers*, pages 716 – 720, November 1993.

[6] E. Bodewig. *Matrix Calculus.* North Holland Publishing Company, Amsterdam, Holland, 1956.

[7] L. Castedo, A.R. Figueiras-Vidal, C.Y Tseng, and L.J Griffiths. Linearly constrained adaptive beamforming using cyclostationary signal properties. In *IEEE International Conference on Acoustics, Speech and Signal Processing*, volume IV, pages 249 – 252, 1994.

[8] W.L. Cook, D.D Opiedun, and L.R. Karl. Generation and Display of Satellite Antenna Patterns. *Comsat Technical Review*, 19(2):259–297, 1989.

[9] J. Cui, D.D. Falconer, and A.U.H. Sheikh. A phase algorithm for blind adaptive optimum diversity combining. In *Vehicular Technology Conference Proceedings*, June 1995.

[10] E.C. DuFort. Optimum Low Sidelobe High Crossover Multiple Beam Antennas. *IEEE Transactions on Antennas and Propagation*, 33(9):946 – 954, 1985.

[11] J. Duggan. Parabolic Antenna Beamforming. Master's thesis, Queen's University, 1996.

[12] R.S. Elliott. *Antenna THeory and Design.* Prentice-Hall, 1981.

[13] R.J Fang. *Lecture Notes in Control and Information Sciences 182: Advanced Methods for Satellites and Deep Space Communications.* COMSAT Corporation, 1992.

[14] W.A. Gardner. *Representation and Estimation of Cyclostationar Processes.* PhD thesis, University of Massachusetts, Amherst, MA, 1972.

[15] W.A. Gardner. Spectral correlation of modulated signals: Part I - Analogue modulation. *IEEE Transactions on Communications*, 35:584 – 594, June 1987.

[16] W.A. Gardner. *Statistical Spectral Analysis: A Non-Probabilistic Theory.* Prentice-Hall, Englewood Clifs, NJ, 1987.

[17] W.A. Gardner. Cyclic Wiener filterint: theory and method. *IEEE Transactions on Communications*, 41:151 – 163, January 1993.

[18] S. Grossman. *Calculus.* Academic Press Inc., 3 edition, 1984.

[19] S. Haykin. *An Introduction to Analog and Digital Communications.* John Wiley & Sons, Toronto, 1989.

[20] K. Hirasawa. *Analysis, design and measurement of small and low-profile antennas.* Artech House, 1992.

[21] J. Karimi. Personal Han-Held Communications Via L-Band CDMA-Based Geostationary Beamforming Satellites. Master's thesis, Queen's University, 1996.

[22] J.D. Kraus. *Antennas.* McGraw-Hill, 1988.

[23] H. Lam. *Analogue and Digital Filter Design: Design and Realization.* Prentice-Hall Inc., 1979.

[24] P. Lam, S. Lee, C. Donald, Chang, and Lang. Directivity Optimization of a Reflector Antenna with Cluster Feeds: A Closed-Form Solution. *IEEE Transactions on Antennas and Propagtion*, 33(11):1163 – 1473, 1985.

[25] J.D. Laster and L.S. Warren. Frequency Scaling of Rain Attenuation for Satellite Communication Links. *IEEE Transactions on Antennas and Propagation*, 43(11):1207 – 1216, 1995.

[26] S.W. Lee and Y. Rahmat-Samii. Simple Formulas for Designing an Offset Multibeam Parabolic Reflector. *IEEE Transactions on Antennas and Propagation*, 29(3):472–478, 1981.

[27] C. Loo. Statistic Models for Land Mobile and Fixed Satellite Communications at Ka Band. In *IEEE Vehicular Technology Conference*, 1996.

[28] R.A. Monzingo and T.W. Miller. *Introduction to Adaptive Arrays.* Wiley, New York, 1980.

[29] A. Papoulis. *Probability, Random Variables, and Stochastic Processes.* Mc Graw Hill, 2 edition, 1989.

[30] R.A. Pearson, Y. Kalatidazeh, B.G. Driscoll, G.T. Philippou, B. Claydon, and D.J Brain. Application of Contoured Beam Shaped Reflector Antannas to Mission Requirements. In *IEE 8th International Confrence on Antennas and Propagation*, pages 9 – 13, United Kingdom, March 1993.

[31] C.J. Pike. EHF(28/19 GHz) Suitcase Satellite Terminal. In *Proceedings of the Olympus Utilisation Conference*, pages 203 – 207, Sevilla, Spain, April 1993.

[32] J.G. Proakis. *Digital Communicaions.* Mc Graw-Hill, Montreal, 1989.

[33] K.S. Rao, G.A. Morin, M.Q. Tang, and S. Richard. Development of a 45 GHz Multiple Beam Antenna for Millitary Satellite Communications. *IEEE Transactions on Antennas and Propagation*, 43(10):1036 – 1046, 1995.

[34] M.E. Rollins and C Loo. Cyclic Beamforming Algorithms for Future Broad-band Satellite Communications Systems Employing On-Board Processing. Technical report, Communications Research Center, Ottawa, December 1995.

[35] S.V. Schell and B.G. Agee. Application of the SCORE alogrithm and SCORE extensions to sorting in the rank-L spectral selfcoherence environment. In *Proceedings of the 22nd Asilomar Conference on Signals, Systems and Computers*, pages 274 – 278, 1988.

[36] R.O. Schmidt. *A Signal Subspace Approach to Multiple Emitter Location and Spectral Estimation.* PhD thesis, Stanford University, November 1981.

[37] J. Shynk and R. Gooch. The Constant Modulus Array for Cochannel Signal Copy and Direction Finding. *IEEE Transactions on Signal Processing*, 44(3):652 – 660, March 1996.

[38] K.P. Spy and E.J. Haakinson. *Calculation of Geostationary Satellite Footprints for Certain Idealized Antennas.* U.S. Department of Commerce, October 1980.

[39] S. Stein. On cross coupling in multiple-beam antennas. *IRE Transactions on Antennas and Propagation*, 10:548, 1962.

[40] W. Tranter and R. Ziemer. *Principles of Communications.* John Wiley and Sons, 4 edition, 1995.

[41] B. Van Veen and K.M. Buckley. Beamforming: A versitile approach to spatial filtering. *IEEE ASSP Magazine*, pages 4 – 23, April 1988.

[42] L.S. Warren, T. Pratt, A. Safaai-Jazi, P.W Remaklus, J. Laster, B. Nelson, and H. Ajaz. Results for the Virginia Tech Propagation Experiment Using the Olympus Satellite 12, 20 and 30 GHz Beacons. *IEEE Transactions on Antennas and Propagation*, 43(1):54 – 62, 1995.

[43] T.R. Waterfield. Design Features of the Orion Satellite Antenna Subsystem. In *IEE 8th International Confrence on Antennas and Propagation*, pages 95 – 98, United Kingdom, March 1993.

[44] J.H Winters. Optimum combining in digital mobile radio with cochannel interference. *IEEE journal on Selected Areas in Communications*, 2(4):528 – 539, July 1984.

[45] Q Wu. Fast algorithm for adaptive beamforming of cyclic signals. *IEE Proceedings on Radar, Sonar and Navigation*, 141(6):312 – 318, December 1994.

[46] Q. Wu and K.M. Wong. Adaptive beamforming of cyclic signal and fast implementation. In *IEEE International Conference on Acoustics, Speech and Signal Processing*, volume IV, pages 157 – 160, 1994.

[47] A.R. Zieger, D.W. Hancock, G.S. Hayne, and C.L. Purdy. NASA Radar Altimeter for the TOPEX/Poesidon Project. *Proceedings of the IEEE*, 79(6):810 – 826, 1991.

Vita

Paul James Lusina

EDUCATION

M.Sc (1995–1997), Electrical & Computer Engineering, Queen's University

B.Sc. (1990–1995), Engineering Science: Electrical Option, University of Toronto

International Baccalaureate Diploma (1988–1990), Victoria Park Secondary School

LANGUAGES

- Two Ontario Academic Credits in French and three summer work terms in French speaking communities.
- One year of introductory German in preparation for the Ontario/Baden-Württemberg exchange program at the University of Ulm. (97-98)

EXPERIENCE

Queen's University, Kingston, Ontario (Sept 95 – Present)

Teaching Assistant (Image Processing & Communications Lab)

Teleste Antenni Oy, Littionen Finland (May/95 – Aug/95)

Design Engineer

Northern Telecom: Product Assurance Component Evaluation Lab.

Ottawa, Ontario (May/93 – Aug/94)

Test Engineer

General Comminution Inc, Toronto, Ontario (May/92 – Aug/92)

Test Technician

Ministere Des Telecommunications, Ste. Foy, Quebec (May/91 – Aug/91)

Research Technician

PUBLICATIONS

Lusina, Karimi, Blostein, "Broadband Satellite Coverage of Canada Using Parabolic Antennas and Beamforming", Proceedings for the CITR Conference, pp83-84. August 1996, Montebello, Quebec, Canada.